AD-A284 494

N PAGE

Form Approved
OMB No. 0704-0188

1. AGENCY USE ONLY (Leave blank)	2. REPORT DATE	3. REPORT TYPE AND DATES COVERED
	Aug 94	

4. TITLE AND SUBTITLE
Meteorological Investigation of Ozone Anomalies During the Artic Boundary Layer Experiment (ABLE 3A)

5. FUNDING NUMBERS

6. AUTHOR(S)
David A. Smarsh

7. PERFORMING ORGANIZATION NAME(S) AND ADDRESS(ES)
AFIT Students Attending:
Georgia Institute of Technology

8. PERFORMING ORGANIZATION REPORT NUMBER
AFIT/CI/CIA
94-034D

9. SPONSORING/MONITORING AGENCY NAME(S) AND ADDRESS(ES)
DEPRTMENT OF THE AIR FORCE
AFIT/CI
2950 P STREET
WRIGHT-PATTERSON AFB OH 45433-7765

10. SPONSORING/MONITORING AGENCY REPORT NUMBER

11. SUPPLEMENTARY NOTES

12a. DISTRIBUTION/AVAILABILITY STATEMENT
Approved for Public Release IAW 190-1
Distribution Unlimited
MICHAEL M. BRICKER, SMSgt, USAF
Chief Administration

12b. DISTRIBUTION CODE

13. ABSTRACT *(Maximum 200 words)*

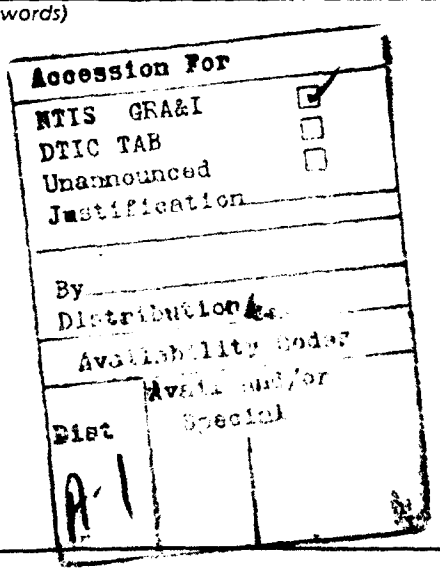

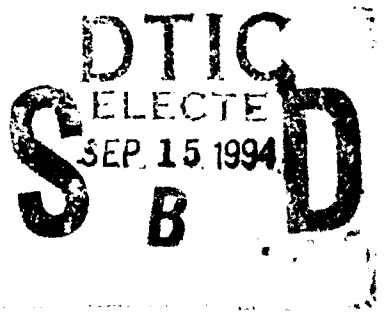

DTIC QUALITY INSPECTED 3

14. SUBJECT TERMS

15. NUMBER OF PAGES
231

16. PRICE CODE

17. SECURITY CLASSIFICATION OF REPORT	18. SECURITY CLASSIFICATION OF THIS PAGE	19. SECURITY CLASSIFICATION OF ABSTRACT	20. LIMITATION OF ABSTRACT

METEOROLOGICAL INVESTIGATION OF OZONE ANOMALIES DURING THE ARCTIC BOUNDARY LAYER EXPERIMENT (ABLE 3A)

A THESIS
Presented to
The Academic Faculty

by

David Anthony Smarsh

In Partial Fulfillment
of the Requirements for the Degree
Doctor of Philosophy in Atmospheric Sciences

Georgia Institute of Technology
August 1994

METEOROLOGICAL INVESTIGATION OF OZONE ANOMILIES

DURING THE ARCTIC BOUNDARY LAYER EXPERIMENT (ABLE 3A)

APPROVED:

Carl G. Justus, Chairman

Robert G. Roper

Fred N. Alyea

John D. Bradshaw

Gerald W. Grams

Date Approved by Chairperson 8/17/94

DEDICATION

I dedicate this thesis to my wife Jean and daughter Tara for their patience and support. Successful completion of the thesis was made possible through their understanding of the complexity of the task and time sacrifice.

ACKNOWLEDGMENTS

The contributions of many people made this thesis possible by providing understanding, encouragement, guidance, and support.

- To my thesis advisor, Dr. Carl G. Justus for his advice, guidance, and support especially his procurement of a SUN workstation.
- To Dr. John D. Bradshaw for investing his time and effort in the many discussions and recommendations and for providing the avenues to develop the research tools.
- To Dr. Robert G. Roper for guidance and encouragement.
- To Dr. Fred N. Alyea for the many discussions on isentropic trajectories and computer support.
- To Mark Shipham and Scott Bachmeier at the NASA-Langley Research Center for the program support.
- A special thanks to Nicole Shumaker, Christy Robb, and Kathy Plummer for administrative support.
- To others including Bill Murphey and Glenn Stone

TABLE OF CONTENTS

LIST OF TABLES

LIST OF ILLUSTRATIONS

SUMMARY

The enhancements in tropospheric ozone that were found during the Arctic Boundary Layer Experiment (ABLE 3A) have been investigated to determine the ozone's origin and the physical mechanisms involved in producing the observed summertime high latitude distributions. These meteorological analyses of potential vorticity, isentropic trajectories, time-series plots, cross-sections, parcel time-series and total ozone column values describe the mechanisms responsible for the observed ozone enhancements. Based on the analysis, a meridional structure is proposed for the Arctic summer. Two ideal case scenarios are developed to describe the major mechanisms for producing tropopause folds over the summertime high latitudes. This analysis is then used to estimate the summertime high latitude flux of ozone due to tropopause folding, high pressure-induced subsidence, and the relocation of the tropopause during the dissipation of the polar vortices. These estimates indicate that the mechanism for the stratospheric exchange over these regions is from tropopause relocation in polar vortices. This source mechanism's estimated 1.2×10^{11} molecules/cm^{2}s flux almost completely offsets *Jacob et al.*'s estimated losses due to net photochemical destruction (8.0×10^{10} molecules/cm^{2}s) and surface depositional loss (8.2×10^{10} molecules/cm^{2}s). In addition, this high latitude summertime mechanism could potentially contribute as much as 25% of the yearly average global

ozone flux from the stratosphere. Understanding this mechanism in more detail should be a high priority for future assessments of the factor controlling ozone's summertime tropospheric distribution over these regions.

CHAPTER I

INTRODUCTION

Ozone values, as large as 284 parts per billion by volume (ppbv), compared to a background value of 75 ppbv were measured at relatively low altitudes, as low as 4.5 km, during the Arctic Boundary Layer Expedition (ABLE 3A). This thesis conducts a meteorological investigation into the enhanced ozone regions during ABLE 3A. Results of this investigation suggest that the majority of the enhanced ozone regions originated from higher altitudes, at times from the stratosphere. This thesis uses analyses of potential vorticity, isentropic back trajectories, meteorological cross-sections and time-series plots, parcel time-series, total ozone, constant pressure charts, skew-t logP plots, tropopause heights, and vertical velocities to describe the origins of the enhanced ozone regions and associated physical mechanisms. Figure 1.1 displays each of the techniques and the uses regarding the systematic approach of analyzing each ozone event.

Ozone plays an important role in our atmosphere. Ozone acts as a stratospheric filter to harmful solar ultraviolet radiation. Without this filter, many plant and animal species could perish, upsetting the Earth's food chain. Ozone also

affects the upper atmosphere by absorbing the ultraviolet, visible, and thermal infrared radiation creating the stable temperature profile in the stratosphere. Without the stable temperature regime, dramatic climate changes would likely occur including droughts, severe storms, etc.. Of direct environmental concern is the destruction of ozone in the stratosphere caused by the tropospheric-stratospheric exchange or upward mixing of tropospheric air containing ozone-controlling HO_x, NO_x, and Cl_x (*Molina and Rowland*, 1974; *Crutzen*, 1971; and *Hampson*, 1965). Recent measurements over Canada (*Kerr and McElroy*, 1993) have revealed record high amounts of ultraviolet radiation corresponding with a decline in total ozone. Ozone is also important in the troposphere as an initiator of photochemical chain oxidation (*Levy*, 1971). Sources of ozone to the troposphere include both the *in situ* photochemical production (*Crutzen*, 1973; *Chameides and Walker*, 1973; *Fishman and Crutzen*, 1978) and exchange from the stratosphere. Because ozone is so important to many regions of and processes within the atmosphere, understanding the factors controlling its budget is of major concern.

Understanding the troposphere's ozone budget will require an examination of the complex interaction between chemical, radiative, and dynamical processes. This includes considering the chemical processes controlling the troposphere, exchange of mass and constituents across the tropopause, and emission of gases from the biosphere. In this thesis, meteorological investigation into the physical

mechanisms responsible for the ozone enhancements will help to further assess how ozone is distributed.

The Arctic Boundary Layer Expedition (ABLE 3A) investigated the sources, sinks, and distribution of trace gases and aerosols during July and August 1988. ABLE 3A concentrated on polar and arctic areas of Alaska, Northern Canada and Greenland. The primary objectives during this program included studying the atmospheric interactions that influence the tropospheric ozone budget over these regions. A total of 33 missions were flown (see Table 1.1) during this program. Each mission measured data ranging from the surface to the mid-troposphere with some measurements made up to the tropopause level. *In situ* measurements included ozone, temperature and dew point. A differential absorption lidar (DIAL) system (*Browell et al.*, 1983; *Browell*, 1989, *Browell et al.*, 1992) was used to provide vertical profiles of ozone from near the surface to above the tropopause along the flight tracks of the NASA Wallops Electra aircraft. Simultaneous zenith and nadir lidar measurements were made from a range of about 750 m above and below the aircraft to slightly above the tropopause in the zenith and to about 300 m above the surface in the nadir. This instrument had an ozone measurement accuracy of less than 10% or 3 ppbv (parts per billion by volume), whichever was larger, with a vertical resolution of 210 m and a horizontal resolution of about 6 km (assuming an aircraft speed of 100 m s^{-1}) [*Browell et al.*, 1983; *Browell et al.*, 1983, 1985*a*, *b*].

The airborne DIAL system used two frequency-doubled Nd: YAG lasers to

pump two high-conversion-efficiency, frequency-doubled, tunable dye lasers. One of the frequency-doubled dye lasers is operated at 286 nm for the DIAL on-line wavelength of ozone, and the other one is operated at 300 nm for the off-line wavelength. The DIAL wavelengths are produced in sequential laser pulses with a time separation of ~300 μs to ensure that the same atmospheric scattering volume is sampled at both wavelengths during the DIAL measurement. Half of each ultraviolet laser beam is transmitted in the zenith and nadir directions. The output beams are transmitted through 40-cm-diameter fused silica windows out of the aircraft in a coaxial geometry with the 36-cm receiver telescopes. After a pulse is transmitted, the receiver collects the backscatter from the laser providing a temporal record of the event. The back scattered signal nominally decreases by the square of the distance of the pulse from the receiver due to the normal loss of the solid angle of collection for isentropic scattering as a function of distance for the fixed aperture collector. In addition, factors that attenuate the UV laser pulses (e.g., absorption by O_3 and attenuator to the Rayleigh and Mie scattering) are also more effective at reducing net signal strength as the total roundtrip path (i.e., twice the distance from the receiver) increases. Therefore, since the DIAL data reduction algorithm requires using the signal differences between two points to obtain a range cell measurement, then the farthest point becomes more attenuated and at some distance closer to the limiting noise of the system (e.g., solar flux). This can create artifacts in the data near the limit of detection of the DIAL system (e.g., note the white area- see Figure

3.24). Data can also be absent due to attenuation by optically thick clouds.

The *in situ* ozone data used in this study were taken using an ethylene chemiluminescence instrument on the aircraft. This instrument had an ozone mixing ratio measurement accuracy of 5 ppbv or 5%, whichever was larger, with a 2 second response time [*Gregory et al.*, 1983, 1988, 1990]. The ozone mixing ratio values were averaged over 10 second intervals. Total air temperature was measured on the aircraft with a platinum resistance probe. The probe had a measurement accuracy of $\pm 0.05^{\circ}C$ with a response time of one second. Dew point temperature was determined with a cooled-mirror hygrometer, which had a measurement accuracy of $\pm 2^{\circ}C\ s^{-1}$. Temperature and dew point measurements were used to provide information on the characteristics of layers observed in the atmosphere.

To date, 24 research papers have been published on ABLE 3A. Of these, five (*Shipham et al.*, 1992; *Browell et al.*, 1992; *Sandholm et al.*, 1992; *Gregory et al.*, 1992; *Harriss et al.*, 1992) included limited discussions on enhanced ozone regions and the physical mechanisms responsible. In these papers, the investigations of the ABLE 3A enhanced ozone regions were limited to primarily preliminary analyses that connected air mass back trajectory tracing methods to the chemical signatures found in suspecting layers in order to draw conclusions of ozone origins. *Shipham et al.* (1992) provided a limited analysis using isentropic back trajectories and constant level charts. *Harriss et al.* (1992) summarized the results of the program which concluded that the stratosphere was the dominant source region of ozone to

lower troposphere in the Arctic summertime. This conclusion was based on the air mass characterization of *Browell et al.* 1992 and on estimates of net losses due to photochemical destruction (*Jacob et al.*, 1992) and deposition (*Gregory et al.*, 1992).

The stratosphere to troposphere exchange of ozone can occur primarily through tropospheric folds where a tropospheric fold is defined as a crimp in the tropopause (*Bluestein*, 1992, uses the description "the tropopause is being crimped at some point and pulled down"). In this thesis, the term "tropopause fold" is taken to include stratospheric-tropospheric exchange of air (ozone). The term ozone intrusion will have a similar physical characteristic as a fold, but with negligible net stratospheric-tropospheric exchange[1]. The term ozone intrusion will refer to a polar vortex with no large vertical motions taking place across the tropopause. By comparison, a tropopause fold consists of a wave plus a polar vortex which has strong vertical motion that allows stratospheric-tropospheric exchange to occur.

The research carried out thus far on the ABLE 3A data has generally lead to somewhat substantiated conclusions about the enhanced ozone regions found over these investigated areas. Generally, in these earlier studies, ozone intrusions were identified with the assumption that stratospheric-tropospheric exchange took place. For example, *Browell et al.* (1992) determined that the role of stratospheric-tropospheric exchange greatly influenced the large-scale distribution and variability

[1] An exception to this is when the troposphere relocates in an intrusion during the dissipation of polar vortex. This dissipation process takes place on a time scale of a week.

of ozone in the troposphere. Their analysis gave two examples of well-defined stratospheric-tropospheric exchange in Missions 19 and 30. However, as will be shown subsequently in the text, these cases actually represented a depressed tropopause in association with a polar vortex with negligible stratospheric-tropospheric exchange. Other ABLE 3A papers identified ozone maximums, but did not attempt to draw definite conclusions on the origin of enhanced ozone areas. For example, the analysis of *Sandholm et al.* (1992) on the Mission 8 enhanced ozone region resulted in an indefinite conclusion even though the largest mixing ratios in ABLE 3A of ozone were measured. Their analysis indicated that lidar soundings did not detect a tongue of stratospheric air, or other signs of tropopause folding. Their calculations of potential vorticity resulted in values less than the threshold for stratospheric air. Based on a back trajectory analysis of potential vorticity, their conclusion for this enhanced ozone region was that the mechanism responsible for the ozone maximum could be any of the following: a remnant of a cutoff low, an area influenced by a jet streak, or the production by downward transport following tropospheric relocation. They recommended that a complete meteorological analysis capable of providing a detailed characterization of mechanisms affecting these and other ABLE 3A case studies is needed.

In this thesis, selected ozone and enhanced ozone regions are investigated through meteorological analyses to determine the origins of the ozone maximums. The enhanced ozone regions were identified from aircraft measurements, lidar

profiles, and *in situ* ozone profiles. A preliminary analysis[2] using isentropic back trajectories, constant pressure level charts, rawinsondes, and potential vorticity was completed to determine which case studies warranted further development. Several cases were not used due to lack of data, especially those with upwind locations north of the data-sparse Arctic circle. Of the 33 missions, nine produced candidates for major case studies based either on having regions of enhanced ozone in the lidar profiles or on measured *in situ* ozone values significantly above the background values. Of these nine cases, three were in locations where isentropic back trajectory analysis indicated that the air had resided near atmospheric rawinsonde sites. These cases would have the augmented data needed for a more in-depth analysis. Other ozone enhanced regions were also identified and investigated using ozone profiles. In most of the ozone enhanced regions investigated, isentropic back trajectories indicated sinking motion could explain the higher than normal values.

This thesis is aimed at completing a detailed analysis for the selected case studies. The methods of meteorological analysis are discussed in Chapter II. These selected case studies are introduced by categorizing the particular enhanced ozone regions found in several missions (Chapter III). The expanded analyses are presented for Mission 8, Mission 19, Mission 3, and enhanced ozone regions found in lidar soundings and profiles. These analyses not only cover the area in the vicinity of the ozone enhancement but follow the enhanced ozone region back in time until a

[2]The methods of analysis are discussed in the next chapter.

conclusion can be reached either about the origin of the ozone in the air parcel or the limitation of the analysis techniques in defining the origin of the ozone. These analyses are made both vertically and horizontally around the parcel path. Each analysis uses various methods including those described earlier for the preliminary analysis plus skew-t LogP diagrams, parcel-time series, time-series plots, total ozone, cross-sections, tropopause heights and vertical velocities. Along with determining the origins of each enhanced ozone region, the physical mechanisms responsible for transporting the enhanced ozone region are identified.

Chapter IV brings together these analyses in order to develop and discuss the stratospheric-tropospheric exchange's physical mechanisms responsible for the observed ozone enhancements in the Arctic summertime. The analyses compare and contrast the behavior of the large-scale polar vortex (about 2000 km across) in the Arctic summer. From the case studies, a meridional structure theory is developed for the Arctic in summer. Two cases are then presented demonstrating the meridional structure theory. This theory for the Arctic summertime has similarities to the model proposed by *Shapiro et al.* (1987) for the mid-latitudes.

Table 1.1 Summary of flights conducted during the ABLE #3A Expedition (from Harriss, 1992)

Mission Number	Flight Date	Departure		Arrival		Purpose
		Time	Location	Time	Location	
1	July 7	1312	NASA Wallops Island	1700	Thunder Bay	Mid-troposphere distributions
2	July 7	1813	Thunder Bay	2108	Churchill	Mid-troposphere distributions
3	July 8	1356	Churchill	1845	Thule	Mid-troposphere distributions
4	July 9	1250	Thule	1844	Fairbanks	Mid-troposphere distributions
5	July 10	1951	Fairbanks	2329	Barrow	Mid-troposphere distributions
6	July 12–13	2332	Barrow	0304	Barrow	Correlations
7	July 13–14	1945	Barrow	0043	Barrow	Boundary layer composition
8	July 15–16	2033	Barrow	0046	Barrow	Boundary layer composition
9	July 17	1756	Barow	2309	Barrow	Vertical distributions
10	July 18–19	1925	Barrow	0048	Barrow	Flux measurements
11	July 19–20	2024	Barrow	0153	Barrow	Vertical distributions
12	July 21–22	2303	Barrow	0349	Barrow	Vertical distributions
13	July 24	1801	Barrow	2343	Bethel	Mid-troposphere distributions
14	July 26–27	2007	Bethel	0033	Bethel	Vertical distributons
15	July 27–28	2351	Bethel	0503	Bethel	Vertical distributions/correlations
16	July 28–29	1955	Bethel	0107	Bethel	Flux measurements
17	July 29–30	1859	Bethel	0016	Bethel	Land-sea interface
18	July 31	1707	Bethel	2214	Bethel	Flux measurements
19	Aug. 2–3	1855	Bethel	0010	Bethel	Land-sea interface
20	Aug. 3	1800	Bethel	2220	Bethel	Vertical distributions
21	Aug. 4	0001	Bethel	0404	Bethel	Vertical distributions
22	Aug. 7	1902	Bethel	2157	Cold Bay	Mid-troposphere distributions
23	Aug 7–8	2329	Cold Bay	0419	Cold Bay	Vertical distributions
24	Aug. 8	2206	Cold Bay	2331	Bethel	Mid-troposphere distributions
25	Aug. 9	0131	Bethel	0645	Bethel	Land-sea interface
26	Aug. 9–10	2057	Bethel	0156	Bethel	Flux measurements
27	Aug. 11–12	2136	Bethel	0015	Barrow	Mid-troposphere distributions
28	Aug. 12	1723	Barrow	2224	Thule	Mid-troposphere distributions
29	Aug. 13	1330	Thule	1836	Thule	Mid-troposphere distributions
30	Aug. 15	1200	Thule	1636	Frobisher Bay	Mid-troposphere distributions
31	Aug. 15	1719	Frobisher Bay	2108	Goose Bay	Mid-troposphere distributions
32	Aug. 16	1333	Goose Bay	1750	Portland	Mid-troposphere distributions
33	Aug. 17	1340	Portland	1708	NASA Langley	Mid-troposphere distributions

Time is GMT.

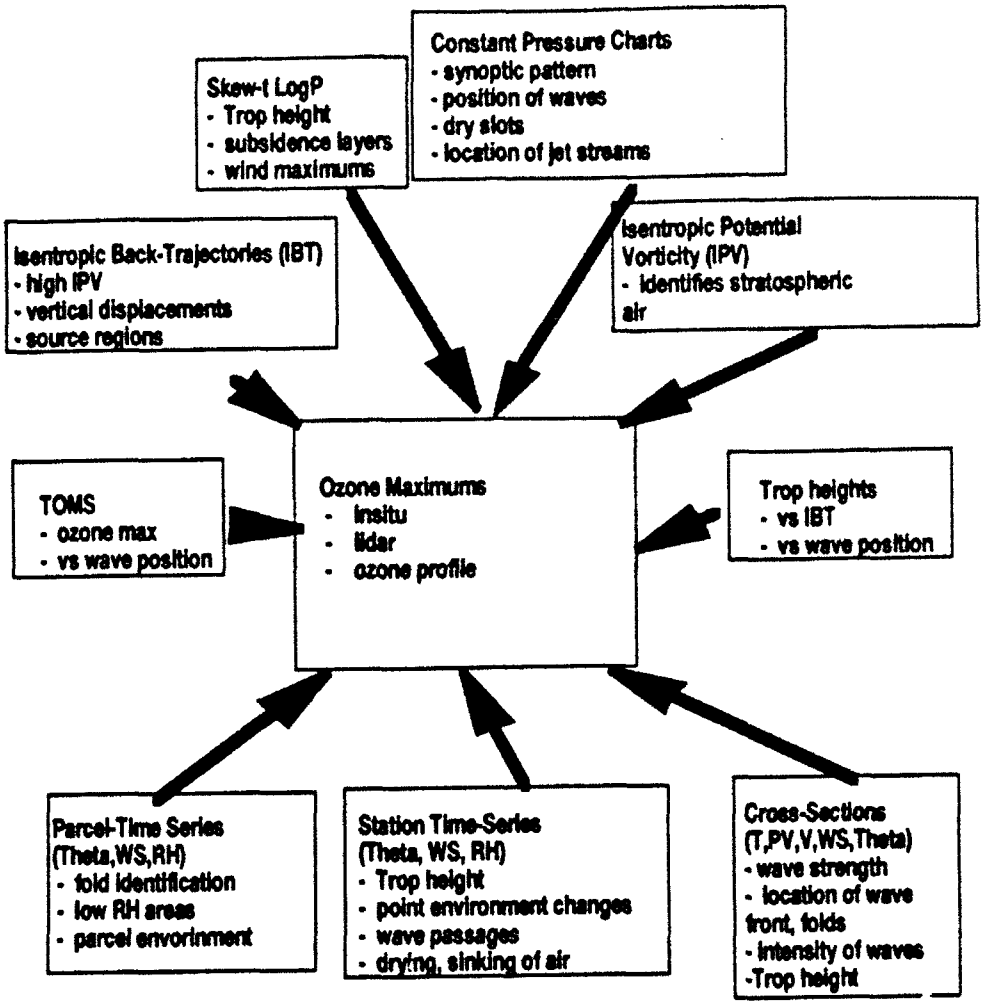

Figure 1.1 Analysis techniques applied to ozone enhancements in ABLE 3A.

CHAPTER II

METHODS OF ANALYSIS

The methods of analysis used in this thesis include isentropic back trajectories, parcel-time series, potential vorticity analysis, constant level charts, meteorological soundings, time-series plots, total ozone, tropopause height analysis, and tropopause vertical velocities (see Figure 1.1). This section will describe how each method is applied to the identification of a particular physical mechanism. All of the methods used, except for the TOMS ozone measurements, are based on rawinsonde data. Figure 2.1 depicts the rawinsonde locations for the ABLE 3A areas impacting the study region. These cover the northern portions of Russia, Alaska, Canada, Greenland, and the Northeastern United States. A listing of the rawinsonde stations is given in Table 2.1. The rawinsonde locations will serve as reference points in this chapter and later when the specific analysis is discussed for each case study.

1. Isentropic Back Trajectories. The isentropic assumption is the basis for many of the analyses and is discussed further in the section on isentropic potential vorticity. Back trajectories can be computed by three different methods: isentropic, isobaric, and isosigma. The isentropic method is favored because of the inherent conservation principle (i.e., contours of potential temperature represent equal

amounts of specific entropy). If all motions are adiabatic, thus excluding diabatic processes, then the potential temperature is conserved as the wind moves the constant potential temperature surfaces. Confidence in the back trajectory can be assumed by looking at how the potential vorticity changes along the trajectory path. This confidence factor for the isentropic trajectory is obtained from the known physical mechanisms that change potential vorticity equation (*Pedlosky*, 1979). This equation identified two important physical mechanisms that change potential vorticity: heating gradients and mixing, turbulent or shear-induced. Heating and mixing affect potential temperature in a similar way. So when the isentropic assumption is made and potential vorticity is changing, then potential temperature is also changing and the isentropic assumption is violated. *Lamarque et al.* (1994) recently modeled a simulated tropopause folding event in which diabatic processes dominated over mixing processes. Heating rates in excess of 3 degrees per day (or around -1 PVU per day) were found near the tropopause. This diabatic heating acted to decrease the potential vorticity and increase sinking motions near the tropopause (*Lamarque et al.*, 1994). Therefore, in this area of changing potential vorticity, uncertainty is introduced in the trajectory. The back trajectory analysis program used here (*Haagenson and Shapiro*, 1979) forces isentropic movement, and, if conserved, the potential vorticity should also stay the same. However, diabatic effects (as well as spatial and temporal) can cause errors. Usually, these can be considered small for time-periods of less than a few days (*Haagensen et al.*, 1987;

Kahl et al., 1989; *Kuo et al.*, 1985) except near jet stream (i.e., tropopause folding, fronts, and clouds). Research completed on uncertainties of trajectory methods indicates that errors due to temporal and spatial scales can reach 1000 km after five days (*Haagenson et al.*, 1987). During the Cross Appalachian Tracer Experiment (CAPTEX '83), their study compared the isentropic, isobaric, and isosigma methods of transport using perfluorocarbon tracer data. Their results revealed that the isentropic and isosigma transport methods were more accurate than isobaric. Errors in the isentropic and isosigma methods in the boundary layer were on the order of 200 km after 24 hours. However, in the boundary layer, larger errors can be expected because of the stronger diabatic heating and larger friction values. Above the boundary layer, *Kahl et al.* (1989) compared an omega, an isobaric, and an isentropic model and concluded that the usefulness of these three methods after five days is limited to the identification of source regions with dimensions on the order of 1000 km. *Kuo et al.* (1985) compared the accuracy of these methods by limiting the temporal and spatial resolution of data. This study used the PSU/NCAR model for the actual atmospheric data. This data was then degraded to simulate actual rawinsonde measurements. Their study found that the isentropic model gave considerably better results. Further, *Kou et al.* (1985) found for horizontal transport that the isentropic method was only slightly better than the isobaric and isosigma methods (after three days, an error of 400 km vs. errors of 500-600 km). For vertical transport, the isentropic method was considerably better (after three days, error of

60 mb vs errors of 100 and 120 mb). *Danielsen* (1961) found the isentropic trajectory deviated only slightly from the actual for average values of stability and diabatic rates. *Kahl and Samson* (1988, 1986) also studied the uncertainties in trajectory models based on observed distributions of spatial and temporal interpolation errors. Based on the current National Weather Service 12 hour resolution, their analysis gave similar findings, concluding that errors in 3-day back trajectories contained a 50 percent chance of exceeding horizontal displacement errors of 350 km.

The isentropic back trajectory analysis scheme used in this thesis consists of five programs. The scheme itself was first developed by *Danielson* (1961) and *Danielson and Bleck* (1967) and further modified by *Haagenson and Shapiro* (1979). For this thesis, the programs have been modified to run on the SUN workstation and to ingest NMC gridded data.

All air motions are assumed dry adiabatic, thus air parcels move along isentropic or potential temperature surfaces that obey the equation:

$$\theta = T\left(\frac{1000}{P}\right)^{\frac{r_d}{c_p}}$$

where θ is the potential temperature, T is the absolute temperature, r_d is the specific gas constant for dry air, and c_p is the specific heat at constant pressure.

The first two programs (traj1 and traj2) read and decode NMC-gridded (145X37 points) data. The NMC grid horizontal resolution is about 2.5 degrees

longitude by 2.5 degrees latitude. Vertical resolution varies as standard pressure levels are used. Temperature, u/v component of wind, relative humidity and pressure are specified at ten levels (1000, 850, 700, 500, 400, 300, 250, 200, 150 and 100 mb). The grid on the constant pressure (isobaric) surfaces is interpolated using a 16-point overlapping parabolic fit (*Koehler*, 1977). These two programs also read and decode rawinsonde data using both significant and mandatory levels. The programs then transform the data using the Duquet method (*Duquet*, 1964). In this method, the NMC gridded data is transformed from pressure to isentropic coordinates using a multiple linear regression technique determining values for pressure, height, and stability (change of potential temperature with respect to pressure and winds), creating a vertical resolution of potential temperature of one degree. The Montgomery stream function[3], the change of potential temperature with respect to pressure, height, and pressure values are computed at each potential temperature surface. The output produces a first guess potential temperature grid field and tests output values for errors.

The third program (traj3) takes the now transformed potential temperature grid fields (called the first guess potential temperature field) and adds the radiosonde data to improve the grid. This program computes differences between the first guess potential temperature grid and rawinsonde data and identifies the eight nearest

---

[3]Equation is defined by $M = C_pT + gz$, where M is the Montgomery Stream Function, C_p is the specific heat at constant pressure, T is the absolute temperature, g is gravity, and z is the geopotential height.

rawinsonde locations to each grid point. The program then calculates weights using the auto-correlation function. The procedure is referred to as the Optimum Interpolation (OI) method. These weights are then used to correct the first guess grid values. The corrected grid values are then filtered with a five-point method and are used to produce the final balanced Montgomery stream values of pressure, winds, and the change of potential temperature with respect to pressure.

The fourth program (traj4) actually computes the trajectory. The starting point and time, the ending point and time, and the potential temperature level are additional input information. Using these inputs and the output of traj3, the program computes potential vorticity fields at a given potential temperature level from which it calculates the trajectory and computes change in potential vorticity for each 12 hour time-step along the trajectory. The trajectory path "r" is computed by relating to the wind by:

$$\frac{d\bar{r}(t)}{dt} = \bar{V}(\bar{r}, t)$$

After a time interval (t_1), the position of the parcel will be:

$$\bar{r}(t_1) = \bar{r}(t_0) + \int_{t_1}^{t_0} \bar{V}[\bar{r}(t), t]\, dt$$

However, the normal time interval is 12 hours (the temporal resolution of

meteorological sounding data). But if this time-step is used, unacceptably large errors in the trajectory path will occur. To minimize this error, a smaller time-step of one hour is used here. Since time-steps of one hour are taken, the trajectory is computed from:

$$\overline{r}(t_1) = \overline{r}(t_0) + \frac{1}{n}\Delta t \sum_{n-1}^{k=0} \overline{V}(\overline{r_k}) ,$$

which gives the exact location of each interpolated (one hour) value. This program also calculates pressure, location, and potential vorticity for each point on the trajectory every six hours from start time to finish time.

The final program (trajf) takes the output from traj4 and actually produces a graphics file to plot. The boundaries of maps, grid size, and other attributes are defined for final processing. Trajectories are then plotted using the NCAR Graphics software package. The path of the trajectory is plotted along with a graph denoting the vertical position of the trajectory.

2. Total Ozone Mapping Spectrometer (TOMS). TOMS data is used with other analysis techniques (vertical velocity, tropopause heights, constant pressure level charts) to aid in the identification of those physical mechanisms responsible for enhancing tropospheric ozone levels. The combination of an increase in total ozone along with a lowering of tropopause height and downward vertical motion identifies where a tropopause fold could have developed.

The TOMS instrument is mounted onboard NASA's polar orbiting Nimbus-7 weather satellite. This instrument measures the backscatter of ultra-violet radiation at 312.5 and 331.2 mm. From this information, the total column can be calculated based on differential absorption at these two wavelengths (WMO, 1988). The TOMS instrument scans the globe once each day (see Figure 2.2 for illustration for the instrument geometry) making about 200,000 measurements a day. Overpass data for any particular area is observed near local noon. TOMS data are unavailable at low sun angles and during the polar night. Missing data can also occur due to equipment malfunction or near the international date line.

When comparing TOMS data with other meteorological data, a "lag-time" must be considered. Since the TOMS measurements occur at local noon, an adjustment time should be noted, especially near the international date line. For the purpose of this thesis, TOMS will be used over specific areas of Canada where local time (LT) equals Z - 6 hours[4], in Alaska where local time equals Z - 10 hours, and in Russia where LT equals Z + 9 hours. In a few instances, actual locations considered will differ from above but will only change by one or two time zones. This difference is not significant for the time scales on which the meteorological data and the TOMS ozone are compared. For Canada, TOMS can be compared to the

[4]Greenwich Mean Time (GMT) is equal to Zulu, or Z, time zone, which is also called Universal Time (UT) based on local time in Greenwich, England.

meteorological data at 12Z of the same day or 00Z of the next day[5]. Likewise for Alaska, compared to 00Z meteorological data of the next day and for Russia, TOMS can be compared to 00Z meteorological data of the same day. Because TOMS data is archived on a day-by-day basis, then an apparent discontinuity occurs at the date line where data east of the dateline is actually about 24 hours older than displayed.

The TOMS data for each day is processed and analyzed onto a regular global grid with a resolution of one degree latitude and 1.25 degrees longitude. TOMS satellite observed ozone values have been found to vary on the order of 30 percent for synoptic scale systems and 3-4 percent for tropospheric folds (*Krueger et al.*, 1981). TOMS data has been shown to agree with the ground-based Dobson spectrometer data within 1-2 percent (*Bhartia et al.*, 1984). Thus, changes in TOMS derived total ozone column values due to tropopause folds can be within the measurement precision limit of the instrument. An additional uncertainty in TOMS can occur due to the instrument not being able to see through clouds, an effect identified by *Clancy et al.* (1992). Here a correction is applied for the climatological average values of ozone below cloud level. This correction method has estimated total ozone column values that are in error by as much as 20 DU or 6% of the total column (*Thompson*, 1993). For tropospheric residual or daily total ozone column differences, which are only a fraction of the total column value, the effects of clouds become more important as the residual or difference value diminishes toward zero.

---

[5]Meteorological data is measured at OOZ and 12Z daily.

Time-series, total ozone and difference analysis were conducted using information from the gridded NASA data that is available on CD-ROM. Two types of total ozone data are available from NASA. The first presents TOMS data as a series of time loops of global false color imagery maps. This format uses map scales that are too large to be useful in discerning small scale events such as tropopause folds. A second technique is developed using gridded data from the gridded CD-ROM disk. By using a modified version of a program "toms.pro", and Interactive Data Language (IDL), TOMS total ozone can be displayed on essentially any map scale and contour interval down to the resolution of the instrument. This latter analysis enables ozone features related to the polar vortex and a wave to be more easily discerned. This technique uses a 3-point interpolation scheme with data resolution of one degree latitude and 1.25 degrees longitude. Following this technique, other programs such as "toz.pro" were developed to indicate how ozone changes with time. The idea here is to be able to detect the small changes of ozone that could be due to tropopause folds. *Reed et al.*(1950), estimated changes in total ozone due to a wave can be as high as 24 Dobson Units[6] (DU) for a well developed wave and for a tropopause fold up to 10 DU (WMO, 1988).

3. Parcel-Time Series. The "Parcel-Time Series" method developed in this thesis demonstrates how a parcel moves in the atmosphere with time. From actual

---

[6]Total column ozone is measured in Dobson Units (Dobson, 1968) (DU, atm-cm x 1000). For example, 300 DU is equal to 3 nm of total ozone column.

rawinsonde data, this technique uses locations and times along the isentropic back trajectories. Vertical transport of the parcel can be easily visualized as well as can other parameters such as humidity and temperature. Following the path of a parcel in this way helps identify any grid-scale physical mechanisms responsible for enhanced ozone levels, such as tropospheric folds as will been seen in Mission 8. Being able to examine what the air parcel's environment is from above and below is equally important as a tool to help identify the mechanisms controlling a parcel's motion (jet streak, drying, cooling, etc.). Errors associated with this analysis depend on how well the rawinsonde data represent the paths along the trajectory and how well the scheme interpolates between data points. This method cannot be used in places where rawinsonde data do not exist. The Parcel-Time Series approach takes the rawinsonde data and applies the Lagrangian interpolation scheme. In this scheme, input points are taken three at a time and used to compute the three coefficients of the Lagrange interpolating quadratic polynomial. The computed coefficients are then applied to the interpolation between points by using a linear distance weighting of quadratic Lagrange polynomials. The output of the computed data is then graphed using the NCAR Graphics package. The program, called "PTS" uses parts of a program originally developed by John Klassa at NASA's Langley Research Center.

4. Station Time-Series Plots. Station Time-Series plots, at a reporting station, enable an Eulerian view of how the atmosphere changes over a specific

point. Analysis of meteorological parameters include potential temperature, absolute temperature, relative humidity, and wind. These analyses are useful in determining general aspects of air parcel behavior. For example, a lowering potential temperature surface can indicate sinking air. Temperature changes along with changing relative humidity and wind shift can denote a frontal passage, wind increases can indicate jet streaks, and changes in potential temperature gradient can indicate changes in the height of the tropopause. Station Time-Series plots use actual rawinsonde data at a specified location. As in the Parcel-Time Series, this method requires rawinsonde data as input, and errors can arise from the interpolation scheme that is used between the data-timed points. The Station Time-Series uses the same interpolation scheme as is used in the Parcel-Time Series method. Data times used in the program are chosen by the user and are usually spaced 12 hours apart. The Station Time-Series program, called "TS", is a modified version originally developed at NASA's Langley Research Center and has been modified for use on the SUN workstation. Rawinsonde data used is archived data from National Climatic Data Center (NCDC).

5. Cross-Sections Plots. Cross-sections plots are used to slice the atmosphere in order to identify the strength of waves, stratospheric-tropospheric exchange, and frontal zones. Cross-sectional analysis of temperature, vorticity, winds, potential temperature and isentropic potential vorticity surfaces can be computed. Of special interest is the cross-section of isentropic potential vorticity, which can be used to

identify tropopause folding events as previously discussed. Cross-sections of the other parameters can be used to indicate the strength of waves, location of frontal zones and intensity of the polar vortex. Data for this analysis can be retrieved from the NMC grid or actual rawinsonde data. The method using rawinsonde data (called "CS") uses all mandatory and significant levels by linearly interpolating to 40 reference levels. By using these reference levels, neighboring points can be determined for computation of certain partial derivatives required for potential vorticity. This method assumes a flat Earth and centers the cross-section in a three-dimensional Cartesian coordinate system. All latitude and longitude points are converted to x,y,z coordinates with the center of the cross-section at 0, 0, mean-radius of the earth. All values of z are ignored, which is a good assumption over moderately-sized regions of the Earth. The method then interpolates into the plane of the cross-section. All data in the Northern Hemisphere are considered for generating the cross-section. Output is produced via NCAR Graphics package in the form of a graphics file.

The method using NMC grids (called nmc_xs) incorporates data from the NMC grid and computes the desired parameter at each grid point. Since neighboring points are known, partial derivatives can be easily computed in order to construct potential and absolute vorticity plots. The output calculations are then plotted using the NCAR graphics package.

6. Isentropic Vertical Velocities at the Tropopause. Isentropic vertical velocities are computed at the tropopause to indicate areas of stratospheric-tropospheric exchange. The methods used to compute is the same as previously discussed in the isentropic back trajectory section. The interaction of waves with the polar vortex is believed to be the major cause of stratospheric-tropospheric exchange at high latitudes. To analyze for this effect, first station skew-t logP diagrams are plotted in the area of interest annotating the potential temperature height of the tropopause. Isentropic trajectories are then run on these points giving an isentropic vertical velocity in units of mb per hour. These isentropic vertical velocities are then plotted using the NCAR graphics package.

7. Isentropic Potential Vorticity. Isentropic potential vorticity charts constructed at different potential temperature levels indicate locations and levels where stratospheric air exists. Isentropic potential vorticity (P_θ) is a quasi-conservative scalar derived from the equation of motion, energy and continuity equations. Isentropic potential vorticity is calculated from the equation:

$$P_\theta = -g(\zeta_\theta + f)\frac{\delta\theta}{\delta p}$$

where

$$\zeta_\theta = \left(\frac{\delta v}{\delta x} - \frac{\delta u}{\delta y}\right)$$

is the local vorticity, f is the coriolis parameter, g is the acceleration of gravity, θ is the potential temperature, p is pressure. The partial derivative of θ with respect to p represents a vertical thermal stability parameter. The symbols u and v are the horizontal x and y components of the wind (on a potential temperature surface). *Danielsen* (1984) and others conducted research correlating isentropic potential vorticity with ozone. *Danielsen* (1984), *WMO* (1988) and others, indicate that values of greater than 1.5 PVU[7] suggest stratospheric air. Isentropic potential vorticity charts are computed as an output to the isentropic trajectory program (traj3). Isentropic potential vorticity cross-sections are produced by the cross-section program.

8. Constant Pressure Charts. Constant pressure level charts can be used to identify synoptic scale enhancements of ozone over an entire region. The location, strength, and movement of Rossby waves can be determined and used as the basis for other finer scale cross-sectional analyses. The constant pressure level charts were plotted using a modified version of a NASA Langley program "heights.f". Parameters plotted include absolute temperature, relative humidity, and winds. These products can be used to further characterize an air parcel. For example: Temperature gradients can identify frontal zones, especially at the 850 and 700 mb levels, warm pockets in the upper levels (500 and 300 mb) can indicate ridges, and cold pockets can identify waves or the polar vortex. In addition, wind maximums can indicate the

[7]Potential Vorticity (PVU) has units of deg K m^2 kg^{-1} s^{-1} x 10^{-5}.

intensity of waves, and minimums of relative humidity suggests sinking air, whereas relative humidity maximums suggest lifting air.

9. Skew-T Plots. Rawinsonde data (pressure, temperature, dew point, winds) are plotted on a Skew-T logP diagram. Using this tool identifies the structure of the atmosphere above the sounding location. This tool helps to identify the location of fronts, the tropopause, dry slots, wind shifts and inversions. Indication of vertical motions also can be inferred. Along with other meteorological tools, Skew-Ts help to determine physical mechanisms such as tropopause folding, jet streaks and intensification of weather systems. Data from the rawinsonde is accurate to about 1°C, 2 mb, five percent relative humidity below about 500 mb, and a 3 ms^{-1} wind vector error. The error in relative humidity increases above the 500 mb height in the polar summer regions due to the inability of dew point sensors to accurately measure frost points less than -30°C (*US Navy*, 1969; *Elliot et al.*, 1991).

Table 2.1 Rawinsonde locations used in analysis of ABLE 3A depicted in Figure 2.2.

Sation		Lat		Lon		
04202	THU	76	31 N	68	50	W
20046		80	37 N	58	03	E
20069		79	30 N	76	59	E
20107		78	04 N	14	12	E
20274		77	30 N	82	13	E
20292		77	43 N	104	17	E
20353		76	57 N	68	35	E
20667		73	20 N	70	02	E
20674		73	30 N	80	14	E
20744		72	23 N	52	44	E
20891		71	59 N	102	28	E
21358		76	09 N	152	50	E
21432		76	00 N	137	54	E
21504		74	40 N	112	56	E
21647		73	11 N	143	56	E
21824		71	35 N	128	55	E
21965		70	38 N	162	24	E
21982		70	58 N	178	32	W
24125		68	30 N	112	26	E
24266		67	33 N	133	22	E
24343		66	46 N	123	24	E
24507		64	10 N	100	04	E
24641		63	46 N	121	37	E
24688		63	16 N	143	09	E
24726		62	33 N	114	00	E
24817		61	16 N	108	01	E
24908	NKI	60	20 N	102	16	E
24944		60	24 N	120	25	E
24959	EEE	62	05 N	129	45	E
25042		69	55 N	167	58	E
25123		68	48 N	161	17	E
25173		68	55 N	179	29	W
25399		66	10 N	169	50	W
25400		65	44 N	150	54	E
25428		65	14 N	160	30	E
25551		64	41 N	170	25	E
25563		64	47 N	177	34	E
25594		64	26 N	173	14	W
25677	HMR	63	03 N	179	19	E
25703		62	55 N	152	25	E
25822		61	57 N	160	22	E
25913		59	35 N	150	47	E
25954		60	21 N	166	00	E
70026	BRW	71	18 N	156	47	W
70086	BTI	70	08 N	143	38	W
70133	OTZ	66	52 N	162	38	W
70200	OME	64	30 N	165	26	W
70219	BET	60	47 N	161	48	W
70231	MCG	62	58 N	155	37	W
70261	FAI	64	49 N	147	52	W
70273	ANC	61	10 N	150	01	W
70308	SNP	57	09 N	170	13	W
70316	CDB	55	12 N	162	43	W
70326	AKN	58	41 N	156	39	W
70350	ADQ	57	45 N	152	30	W
70361	YAK	59	31 N	139	40	W
70398	ANN	55	02 N	131	34	W
70414	SYA	52	43 N	174	06	E
70454	ADK	51	53 N	176	39	W
71000	AIR	50	00 N	70	00	W
71043	YVQ	65	17 N	126	48	W
71051	YSY	72	00 N	125	16	W
71072	YMD	76	14 N	119	20	W
71081	YUX	68	47 N	81	15	W
71082	YLT	82	30 N	62	20	W
71109	YZT	50	41 N	127	22	W
71115	WVK	50	14 N	119	17	W
71119	YED	53	33 N	114	06	W
71399	WOS	43	43 N	65	15	W
71600	YSA	43	56 N	60	01	W
71722	YMW	46	22 N	75	58	W
71801	YYT	47	37 N	52	45	W
71811	YZV	50	13 N	66	15	W
71815	YJT	48	32 N	58	33	W
71816	YYR	53	18 N	60	22	W
71823	YAH	54	00 N	73	00	W
71836	YMO	51	16 N	80	39	W
71848	WTL	53	50 N	89	52	W
71867	YQD	53	58 N	101	06	W
71896	YXS	53	53 N	122	40	W
71906	YVP	58	06 N	68	25	W
71907	YPH	58	27 N	78	07	W
71909	YFB	63	45 N	68	33	W
71913	YYQ	58	45 N	94	04	W
71915	YZS	64	12 N	83	22	W
71917	WEU	80	00 N	85	56	W
71924	YRB	74	43 N	94	59	W
71925	YCB	69	06 N	105	07	W
71926	WBK	64	18 N	96	00	W
71934	YSM	60	02 N	111	56	W
71945	YYE	58	50 N	122	36	W
71957	YEV	68	19 N	133	32	W
71964	YXY	60	43 N	135	04	W
72518	ALB	42	45 N	73	48	W
72520	PIT	40	32 N	80	14	W
72528	BUF	42	56 N	78	44	W
72532	PIA	40	40 N	89	41	W
72553	OMA	41	22 N	96	01	W
72562	LBF	41	08 N	100	41	W
72572	SLC	40	47 N	111	58	W
72576	LND	42	49 N	108	44	W
72583	WMC	40	54 N	117	48	W
72597	MFR	42	22 N	122	52	W
72606	PWM	43	39 N	70	19	W
72637	FNT	42	58 N	83	45	W
72645	GRB	44	29 N	88	08	W
72654	HON	44	23 N	98	13	W
72655	STC	45	33 N	95	04	W
72662	RAP	44	03 N	103	04	W
72681	BOI	43	34 N	116	13	W
72694	SLE	44	55 N	123	00	W
72712	CAR	46	52 N	68	01	W
72734	SSM	46	28 N	84	22	W
72747	INL	48	34 N	93	23	W
72764	BIS	46	46 N	100	45	W
72768	GGW	48	13 N	106	37	W
72775	GTF	47	29 N	111	22	W
72785	GEG	47	38 N	117	32	W
72797	UIL	47	57 N	124	33	W
74494	CHH	41	40 N	69	58	W

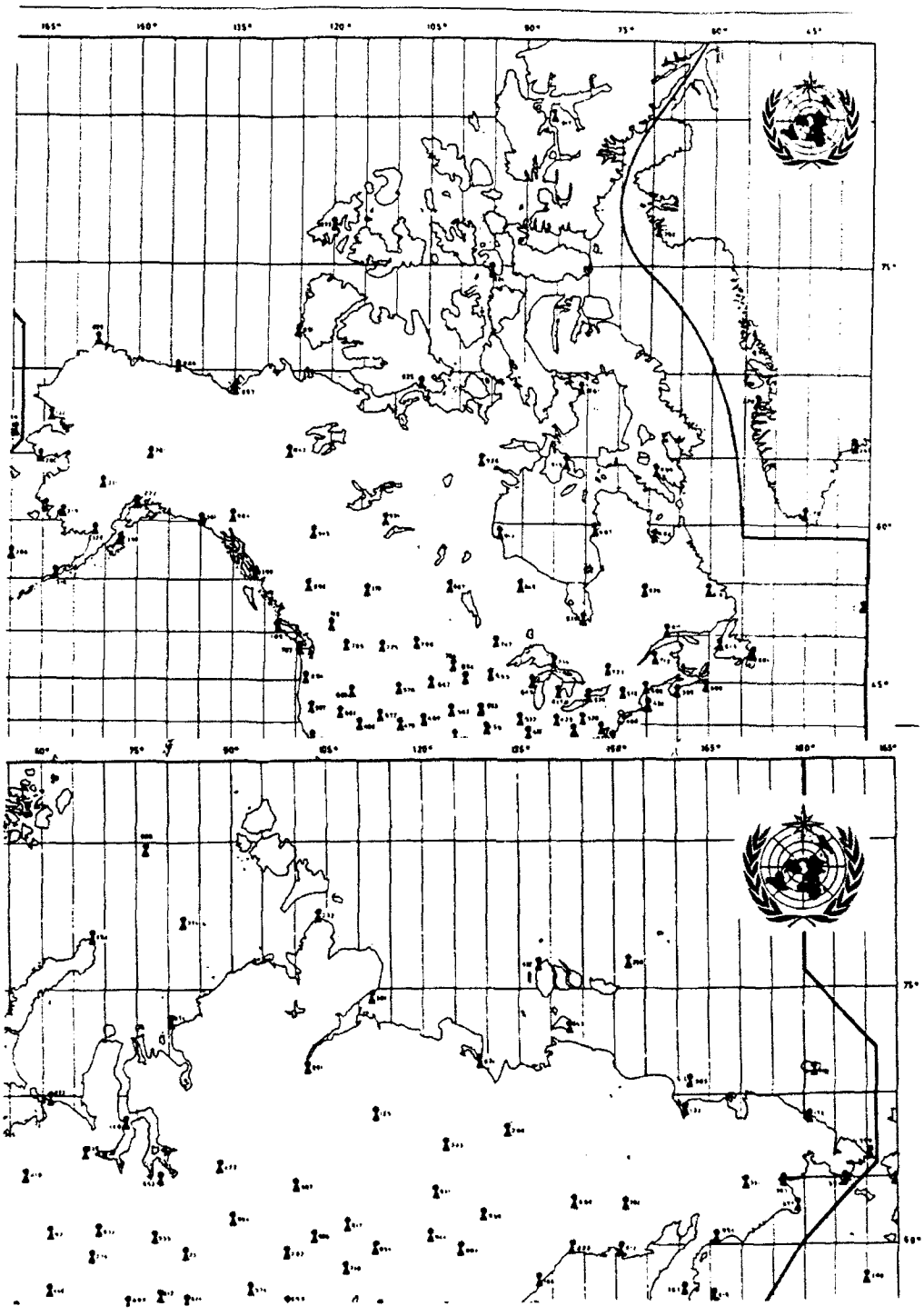

Figure 2.1 Rawinsonde location over ABLE 3A area. Soundings taken at 00Z and 12Z daily. Stations identified by a three digit identifier. A listing of locations is included in Table 2.1

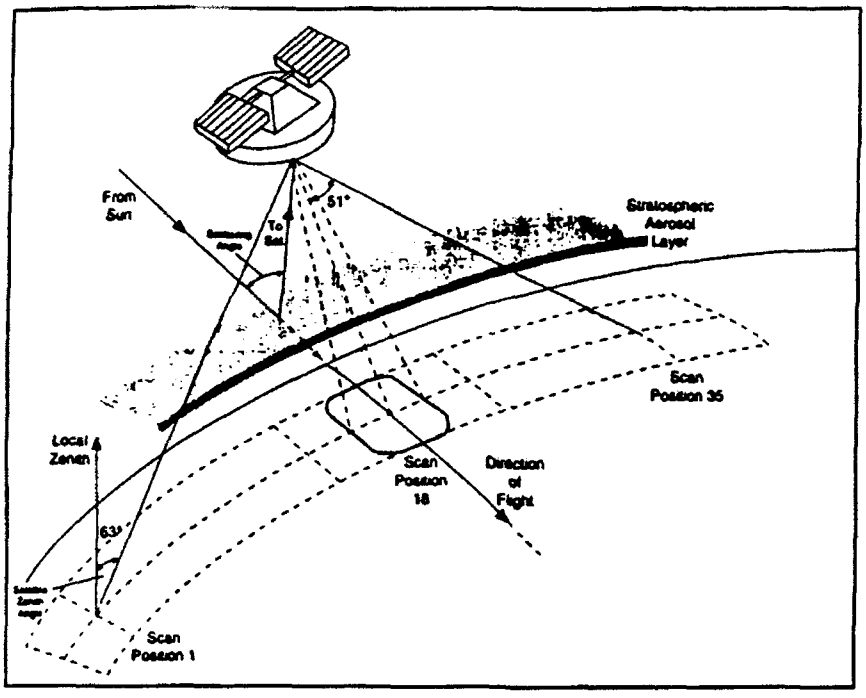

Figure 2.2 TOMS scanning properties (from WMO, 1988)

CHAPTER III

ENHANCED OZONE REGIONS INVESTIGATED

Three types of enhanced ozone regions are investigated from the ABLE 3A data set: tropospheric fold events, existing pools of ozone in a polar vortex, and enhanced ozone regions found in ozone profiles. Mission 3 and 8 cases show how the polar vortex and smaller waves combined to cause tropopause folding and the stratospheric-tropospheric exchange of ozone. The Mission 19 case documents how the ozone structure changes on the northwest side of the polar vortex. The regions of enhanced ozone within the profiles are shown to have been caused by the gradual sinking of ozone enhanced air. One case was associated with a tropopause fold and another with the existing polar vortex. In many of the enhanced regions in the ozone profiles, the increase in ozone can be explained by vertical transport of air. In each of the cases studied, the isentropic trajectory is the major tool used in determining the origin of parcels in the vicinity of the enhanced ozone regions. The meteorological techniques used are important in determining the atmospheric conditions around these ozone enhancement regions. Since the lifetime of ozone was about 46 days in the summertime, upper troposphere over these regions (*Jacob et*

al.,1992), exchanged ozone should have maintained its value above normal background levels for long periods (on the order of weeks). Thus, enhanced ozone areas could be transported long distances and still be detectable.

(1) The Mission 8 Case Study. Aircraft *in situ* measurements recorded ozone values greater than 255 ppbv over Alaska at 4.5 km and represent the highest values measured during the entire ABLE 3A experiment. A meteorological analysis has now been completed to determine where the parcel of air originated. This analysis includes isentropic trajectories, constant level charts, meteorological soundings, potential vorticity analysis on isentropic surfaces, cross-sections of potential temperature and vorticity, cross-sections of specific humidity, time series analysis over certain points, and TOMS ozone information. This analysis provides evidence suggesting that this air originated in the stratosphere near a cutoff low over Siberia and was transported to Alaska following a dynamic disturbance. The parcel, which was tracked back toward a tropopause fold, subsided nearly 76 mb in a 36 hour period. Potential vorticity of the parcel was conserved back to the vicinity of the tropopause fold as values held steady back to 24 hours at 0.84 PVU. The dynamic disturbance responsible for the tropopause fold contributed to a 30 Dobson Unit (DU) increase in ozone.

Mission 8 was flown north and east of Barrow, Alaska on July 15-16, 1988 from 2033Z to 0046Z. Measurements onboard the aircraft included O_3, CO, CH_4,

and H_2O, among other trace gases. The flight path began around Barrow and traversed to a point approximately 200 km east along the coast and north of Barrow to over the ice shelf. The objective was to measure boundary layer differences in trace gases over land-sea and sea-ice transitions.

The aircraft measured ozone (*in situ*) and with lidar. A graphic view of altitude and ozone measurements (Figure 3.1) clearly shows a maximum 284 ppbv at time 22:06:30, July 15, 1988 at location 72.61N, 158.007W. Note that the normal ozone background level is around 70 ppbv. Just after this time, the aircraft descended from 4.5 km to near the surface.

Meteorological evidence is presented using various methods to study the origin of the parcel of air. The most conclusive evidence will be presented first.

(a) Potential Vorticity Back Trajectory on Isentropic Surfaces. The altitude of the aircraft at 4.5 km along with the ambient air temperature of -12.5 °C converts to a potential temperature of approximately 309K. To find the origins of this parcel, a 2-day isentropic back trajectory was calculated using the 309K potential temperature surface (Table 3.1). Note the low value of potential vorticity of 0.86 PVU at the point the air parcel was encountered. *Danielson* (1984) correlated values of greater than 1.6 PVU with stratospheric air. At first look, the small values of potential vorticity appear out of place with the high ozone values (see discussion by *Sandholm et al.*, (1992). However, by examining the trajectory, it is easy to speculate on the origin of the enhanced ozone in this air parcel. A potential vorticity plot in

Figure 3.2b clearly shows the high values of potential vorticity from which the parcel originated. Values as high as 1.45 PVU were calculated at the -48 hour point. If the height of the 309K potential temperature level is plotted (Figure 3.2a), the parcel is found to descend from near the tropopause at 490 mb at the -48 hour point to near 566 mb at 15/12Z[8] at the initial point, a descent of nearly 76 mb. Above the 309K potential temperature level, the 322K potential temperature level demonstrates even stronger indications of a fold (Figures 3.3a and b). The parcel in this trajectory descends 37 mb in just 6 hours between 14/18Z and 15/00Z (Figure 3.3a) with the potential vorticity falling from near 2.7 PVU to 0.9 PVU (Figure 3.3b). The PVU change here indicates the parcel being influenced by diabatic heating as discussed earlier. The back trajectory's use is limited at times earlier than 14/18Z at the 322K potential temperature level and 15/00Z at the 309K potential temperature level.

To have moved that much vertically, the parcel must have passed near a strong dynamical system. Figures 3.4a-e display a series of plots of the 309K potential temperature surface every 12 hours along the back trajectory beginning at the -12 hour point or 15/12Z and going back to -60 hours on 14/00Z. Refer to these plots for the specific discussion that follows. On each plot, the entire path of the parcel has been plotted with corresponding times next to the path. At the 0 hour point, the values of potential vorticity at the 309K potential temperature level (not shown) remained below 1.0 PVU throughout the area. Compare this with the high

[8]15/12Z stands for the day of the month (15th) at 1200Z or GMT, or universal time.

values found in Figure 3.4d at the -48 hour point (14/00Z). At the 0 hour point (16/00Z), the parcel is located east of Barrow, Alaska (73.2N, 150W) at a pressure height of 526 mb and with a potential vorticity value of 0.86 PVU.

At the -12 hour point (15/12Z), the parcel had traveled nearly 22 degrees in longitude in the previous 12 hours, now located at 72.5N, 172.9W. The only northern high latitude potential vorticity maximum at this potential temperature surface is located on the other side of the globe near 0 degrees longitude east of Greenland. At the -12 hour point, the parcel was at its lowest altitude at pressure height 566 mb with a vorticity value of 0.84 PVU near Wrangel Island (73N, 179W).

At the -24 hour point (15/00Z), a center of positive vorticity did appear near the New Siberian Islands (72.3N, 164.5E) as the parcel traveled nearly 27 degrees in the previous 12 hours. During these next 12 hours the parcel followed a downward descent along a path from the 542 mb level with a potential vorticity of 1.01 PVU.

At the -36 hour point (14/12Z), an area of enhanced potential vorticity was close to the back trajectory path and was increasing in intensity. A region of potential vorticity with values greater than 3 PVU was also found over the eastern Taymyr Peninsula (near 75N, 120E). During the 12 hours prior to the -36 hour point, the parcel maintained the quick pace traveling 23 degrees and descending as much as 44 mb in 6 hours, while reaching a potential vorticity value as large as 1.47 PVU. During this time, the back trajectory becomes limited near 14/12Z due to the trajectory path being in the vicinity of the tropopause folding event that is indicated

by the strong gradient in potential vorticity along the path. Even so, the general position or path is still believed to be basically valid but with lower confidence in the accuracy of the trajectory path.

The -48 hour point (14/00Z) marks where the trajectory indicates that the parcel exited out of the cyclonic flow. At this point the potential vorticity on the 309K potential temperature surface was greater than 4 PVU for the system centered near the Taymyr Peninsula (75N, 120E). During the preceding 12 hours, the parcel's speed dramatically slowed with a travel of only 16 degrees in 12 hours. As might be expected, the parcel continued to descend 8 mb with a potential vorticity of 1.06 PVU.

At the -60 and -72 hour points (not shown), the parcel moved to a position to be under the influence of the cyclonic system from the northwest. Not much change in altitude or potential vorticity occurred.

Since the trajectory analysis is somewhat limited near the tropopause folding event, another approach can be used to understand why potential vorticity decreased from the near stratospheric values (e.g., at the 309K potential temperature surface, changed from 1.45 PVU to 0.84 PVU along the trajectory) while ozone remained at high levels (284 ppbv). An estimation of this parcel's original potential vorticity can be obtained from a simple atmospheric dilution scheme and the conservation of ozone and potential vorticity relationship in the stratosphere. Taking H_2O as a conservative tracer can give the simple dilution equation

$$[H_2O]_S V_S + [H_2O]_t V_t = [H_2O]_T V_T$$

Where $[H_2O]$ is the mixing ratio of water, and V is the volume of air at s (taken here as the stratosphere), before the air was mixed, t, the air mixed with background air (taken here as the tropospheric background), and T, after mixing (taken here as the intercepted region of enhanced ozone).

If it is assumed here that the water's concentration in the air parcel is much less than that of the background, then the above equation can be solved for a dilution factor:

$$DF = \frac{V_S}{V_T} = [1 - \frac{[H_2O]_T}{[H_2O]_t}]$$

where DF is the dilution factor or the ratio of the volume of air before to that of air after mixing. This dilution factor can be applied to the same relationship for ozone:

$$[O_3]_T V_T = [O_3]_S V_S + [O_3]_t V_t$$

where $[O_3]$ is the ozone mixing ratio and V is the volume of air at s, before the air was mixed, t, the air mixed with background air, and, T, after mixing.

Solving this equation for $[O_3]_s$ and substituting the DF, the dilution factor obtained from above:

$$[O_3]_s = \frac{[O_3]_T - [O_3]_t(1-DF)}{DF}$$

This relationship can be used to estimate the original amount of ozone in the air parcel based on a water dilution ratio. The information needed for this estimate is the water and ozone mixing ratios present in the parcel after mixing and the background values in the tropospheric air that is being mixed. During Mission 8 water mixing ratios were obtained from rawinsonde data for the average background dewpoints for the average pressure level of 537 mb. The average dewpoint of the background was 243K, which converts to 614 ppmv water. The dewpoint of the parcel after mixing was obtained from aircraft measurements. The measured dewpoint for this parcel was 228K, which converts to 122 ppbv water. Thus, the initial assumption that $[H_2O]_T >> [H_2O]_S$ appears valid based on the nominal 10 ppmv water found in the lower stratosphere (*Kelly et al.*, 1991). Ozone's background values of 700 ppbv can be obtained from the data shown in Figure 3.1, and ozone's level after mixing can be taken from the aircraft data as 284 ppbv. Computing the ozone mixing ratio before the air mixed yields: $[O_3]_s$ equal to 337 ppbv. A potential vorticity value that equates with this ozone value is 4.83 PVU (*Gidel and Shapiro*, 1980). Based on this approach, the parcel's ozone mixing ratio was diluted from 337

ppbv to 284 ppbv after mixing with the tropospheric air, while the potential vorticity decreased from 4.83 PVU to 0.84 PVU based on the analysis (i.e., 4.83 PVU value) and the meteorological grid scale 0.84 PVU derived from the trajectory analysis. This analysis strongly suggests that physical mechanisms changed the potential vorticity values much faster than simple dilution changed the ozone mixing ratio. This change in potential vorticity is due to the physical mechanisms discussed earlier or due to the 0.84 PVU value being too spatially large.[9]

(b) Constant Level Charts. The 200 mb, 300 mb, 500 mb, 700 mb, and 850 mb charts show evidence of a weather system passing over Barrow near the time (15/22Z) that the high ozone values (greater than 255 ppbv) were measured. Constant level charts derived from the NMC grids were used and were available at the 12Z and 00Z times daily. On 16/00Z, the 300 mb chart (see Figure 3.5a) analysis shows a strong west-east zonal jet with an embedded upper wave. The position of the upper wave had a slight curl starting at 80N, 152W that curled in an anticyclonic manner to 70N, 158N[10], several degrees east of Barrow, Alaska. At the flight time, by extrapolation, the wave was still just east of the flight position. Likewise, the 200 mb, 500 mb, and 700 mb charts (not depicted) show a similar pattern with the wave nearly vertically stacked.

---

[9]The ozone enhancement at the 0.84 PVU location had a spatial scale of 0.64 degrees compared to the grid scale of 2.5 degrees.

[10]Wave locations are identified by two points that the wave is between (See Figure 3.5 a).

The strength of this wave can also be determined by the relative humidity fields. The stronger the wave, the stronger the gradient of moisture that will occur across the wave. At 500 mb on July 16 at 00Z (see Figure 3.6a), a strong gradient of relative humidity existed near the wave. Just east of the wave, a center of maximum relative humidity of greater than 70 percent existed near 70N, 140W, while a minimum of less than 20 percent existed west in the trough that was centered near 72N, 175W. This field in itself suggests that strong vertical motions were associated with the system. The presence of moist air infers the upward push of warm moist air from the surface, whereas and the dry air infers descending air from aloft. Near the point of the flight, the relative humidity was approximately 45 percent and under a steep gradient with lower values to the west. On the 500 mb temperature chart (not shown) a trough of cold air is evident signifying the wave's passage near Barrow, AK.

To see if the trajectory analysis makes sense, a back track of the wave can be examined. Since the parcel remained between the 500 mb and 300 mb levels, they will be on it. In addition, this treatment will also include the 500 mb relative humidity. At -12 hours (approx 15/12Z), the parcel (marked by the X in Figure 3.5) was located at 72.5N, 172.39 at 566 mb and 7-8 degrees upstream of the wave that is depicted by a dark curved line just east of Wrangel Island (72N, 180E) at 300 mb (see Figure 3.5b). The positioning of the wave at the 300 mb level in Figure 3.5b suggests an area of sinking motion to the west of the wave. The sinking motion is also supported by the 500 mb relative humidity chart, Figure 3.6b, which shows the

center of a minimum of less than 20 percent relative humidity (~35%) just to the west of the parcel. In contrast, to the east of the trough, an area of greater than 90 percent relative humidity is observed at 75N, 177W. This indicates that the system was stronger than it was at the trajectory's initial point on 16/00Z. A trough of cold air is also evident on the 500 mb temperature chart (not shown) that indicates a somewhat stronger wave.

At -24 hours (approx 15/00Z), the parcel was located at 71.9N, 165.5E at 542 mb. The 300 mb chart on 15/00Z (see Figure 3.5c) depicts the wave position 4-5 degrees ahead of the parcel. A polar vortex now can be noted at this level located at 78N, 170E and at a minimum height of 8928 m. Thus, a conclusion here would be that the parcel of interest is in an area of descending air. The 500 mb relative humidity chart (see Figure 3.6c) depicts the parcel in a general minimum area centered to the east where the relative humidity is less than 40 percent. The wave can still be identified by a trough of cold air on the 500 mb temperature chart (not shown).

At -36 hours (approx 14/12Z), the enhanced ozone parcel was located at 69.7N, 138E at 498 mb. The 300 mb chart at this time (see Figure 3.5d) depicts a broad flow around a polar vortex. The wave is not yet evident in the strong jet rotating around the low. Even so, the parcel is estimated to be 5-10 degrees behind the wave and the parcel is just exiting a cyclonic flow into a broad west-east flow pattern. The closed low is centered at 75N, 150E with a minimum height of 8916 m,

slightly lower than previously noted at the -24 hour point. The most likely scenario here is that this trough is acting to deepen the closed low. Since the parcel is now under the influence of the polar vortex, the 500 mb relative humidity can be used to indicate vertical transport. Since the parcel is bordering a region of higher humidities at around 50 percent (see Figure 3.6d) and moving towards a developing dry area (compare with Figure 3.6c), the air must be sinking. Supplementing the 300 mb pressure analysis, the wave is still noticeably identified by a cold trough in the 500 mb temperature (not shown).

At -48 hours (approx 14/00Z), the parcel was located at 67.2N, 115.6E at 387 mb. The 300 mb chart at this time (see Figure 3.5e) depicts the parcel traveling around the polar vortex. The center of the low is located at 74N, 120E with a center of 8850 m, the lowest height yet. The parcel should still be behind in the wave (best guess noted by the heavy line).

At -60 hours (approx 13/12Z), the parcel was located at 78.0N, 109.3E at 385 mb. The 300 mb chart (Figure 3.5f) depicts the parcel at its entry point for travel around the polar vortex. The center of the low is located at 74N, 125E with a center of 8840 m, the lowest height yet.

(c) Tropopause Potential Temperature Heights and Tropopause Vertical Velocity. An analysis of tropopause potential temperature heights and vertical velocity, along with the plot of the trajectory path (similar to Figures 3.4a-e) will help to established where the air was exchanged. Figures 3.7a-c display tropopause

heights in degrees K. These heights show how the 309K potential temperature parcel rotated around what appears as a "bowl" of stratospheric air. In Figures 3.7a-c at times 16/00Z, 15/12Z, and 15/00Z, the tropopause remained between 325K and 330K potential temperature levels. At 14/12Z (not shown), the tropopause at the parcel's location was near the 330K potential temperature level. Between these two time periods, the parcel passed through a trough of lower tropopause heights of less than the 320K potential temperature level. At 14/00Z (not shown), the parcel was rotating around the polar vortex with a tropopause height of around the 315K potential temperature level.

The tropopause vertical velocity at 15/12Z and 15/00Z (Figures 3.8b-c) indicates a broad maximum of descending air to the northeast of the parcel. However, the 14/12Z in Figure 3.8a indicates strong upward motions of 5 mb/hr at 72N, 145E and sinking motions of 7 mb/hr at 65N, 145E. The strong vertical motions are being produced by the wave interacting with the polar vortex.

(d) Meteorological Soundings for Barrow were plotted for 15/12Z and 16/00Z. The 15/12Z (Figure 3.9a) shows a moist sounding except for a dry slot at 536 to 532 mb. Noticeably, a wave had passed by 16/00Z (see Figure 3.9b) as the sounding had dried out above 700 mb with subsidence noted from 700 to 630 mb. This supports the fact that a trough did pass through near the time of Mission 8. Even before the wave passed, dry air started moving in at around the 535 mb level. The drying at this level represents the air that was transported from the vicinity of

the tropopause folding event that occurred 36-48 hours earlier.

(e) Time-Series (TS) Plots. Barrow soundings were plotted to construct a Time-Series using data from 15/00Z every 12 hours until 16/12Z. Plots were made using potential temperature, winds, and relative humidity. A passing wave was indicated by a wind shift in the lower levels before the 16/00Z sounding and in the upper levels after the 16/00Z sounding (see Figure 3.10a[11]). Lowering of the 309K potential temperature level can be noted throughout. On the relative humidity plot (see Figure 3.10b), a drying out of the atmosphere is noticeable at the 570 mb level just before 15/12Z. This drying area expanded and by 16/00Z values of less than 10 percent existed from 620 to 350 mb. The drying signifies that the air was transported from the upstream tropopause fold region and from the wave's passage in which dry air resided behind the wave.

Other Time-Series plots can indicate the strength of the short wave as it exited the polar vortex and moved east. Around 14/00Z, the parcel was exiting the polar vortex low behind the wave. Station 20891 (see Figure 3.11a). Time-Series analysis shows the wave passing several hours before 14/00Z as indicated by a wind shift and the elevated values of potential temperature. Similar results are obtained from stations plotted downstream, including station 24125 (see Figure 3.12a) which the parcel passed near at approximately 14/06Z. At station 24125, notice how the

[11]Times below the cross-section are DD/MM/YY/TT where DD is the day, MM is the month, YY is the year, and TT is the time in GMT.

tropopause dipped to 500 mb by 14/12Z in association with the relative humidity drying out significantly at nearly all levels indicating sinking air.

(f) TOMS Ozone Charts. Daily plots of ozone from July 14-15 (see Figures 3.13a-c) show a band of enhanced total ozone column near Barrow (location 71.3N, 156.7W) on July 15th in Figure 3.13c. Note that the July 15th TOMS ozone measurements over Alaska corresponded to primary features on the meteorological charts at 16/00Z (see discussion in Chapter 2 under TOMS ozone for more details). The position of this ozone maximum agrees well with the Figure 3.5a 300 mb position of the wave that was just east of it. The ozone maximum was on the rearward side of the wave. The 300 mb wave can be followed back and compared in good agreement with enhanced values of total ozone. Comparing Figure 3.13c (July 15 total ozone) with Figure 3.5c (300 mb at 16/00Z), the band of ozone continued to be on the backside of the 300 mb wave. Comparing Figure 3.13a (July 14 total ozone) with Figure 3.5e (300 mb at July 14 at 12Z) shows a band of ozone near longitude 125E in the region where the short wave is just beginning to react with the polar vortex. Total column ozone time-series were also run at the wave's other positions. These time-series also show that an ozone maximum occurred on July 15 at location 71.5N, 155W.

In an attempt to better understand the factors affecting ozone's temporal evolution, trend data were examined to see if this wave could be followed through time with respect to changes in day to day ozone. TOMS ozone trends were

calculated and plotted for the 15/14 July, 1988 (Figure 3.14b-c) and 14/13 July, 1988 (Figure 3.14a). Figure 3.14c shows a 20-30 DU increase over the Barrow area when the wave passed over. Compare this increase with the 16/00Z 300 mb chart in Figure 3.5a. The position of the wave's axis (around 155W) corresponds with the region of maximum ozone enhancement. In Figures 3.14a and 3.14b, the same trend is evident. Comparing Figures 3.14b with 3.5c, the 20-30 DU enhancement near 70N, 175E is coincident with the position of the wave's axis. In Figures 3.14a and 3.5e, the 40-50 DU increase near 70N, 110E is coincident with the wave's interaction with the polar vortex. This agrees well with the position of the wave and the daily total ozone plots discussed in the last section. In the total ozone plots, the centers of enhanced ozone lag behind the wave. In the total ozone differences, the axis of maximum positive difference lies close to the wave axis. In these cases, the enhancement in total ozone column is due primarily to a lowering of the tropopause height and in part to the tropopause fold.

(g) Summary of Trajectories. At the 309K and 322K potential temperature surfaces (see Figure 3.15a-b), a 2-day back trajectory is given. At the 309K potential temperature level (Figure 3.15a, top chart), the trajectory indicates the parcel maintained approximately the same potential vorticity and height back to the -30 hour position. At the 322K potential temperature level (Figure 3.15b, bottom chart), the parcel maintained approximately the same potential vorticity and height back to the -24 hour position (15/00Z). The dashed trajectory path at earlier times before

15/00Z represent the portion of the path that becomes uncertain due to the large change in potential vorticity that is associated with the tropopause fold that occurred in the area near 72N, 150-135E . As discussed earlier, the changes in potential vorticity in the area were primarily due to diabatic heating in the vicinity of the troposphere fold. For comparison, trajectories on the 300K and 340K potential temperature surfaces were also computed to see if parcels starting from much lower or higher heights would conserve potential vorticity. In both the 300K and 340K potential temperature level trajectories (Figure 3.16), the potential vorticity values remained nearly constant (i.e., potential vorticity was conserved), varying from 0.9 to 1.2 PVU along the 300K tropospheric potential temperature surface and 8 to 9 PVU along the 340K stratospheric potential temperature surface. Since the potential vorticity was nearly conserved and the direction of the paths are similar to that calculated for the 309K and 322K potential temperature surfaces, then it is not unreasonable to assert that this analysis has generated a vertical corridor that defines the boundaries within which the a parcel's ingestion must have followed.

(h) Parcel Time Series. By plotting a time series of meteorological soundings near the path and time of the isentropic trajectory, an actual history of the parcel's path can be visualized. Figures 3.17 and 3.18 depict the path of the parcel along the 309K and 322K potential temperature levels. Meteorological sounding stations used along the path have been listed in Table 3.2. Figure 3.17 shows the soundings plotted in a time series diagram with indicated potential temperature and

tropopause levels plotted. Figure 3.17a shows how the tropopause varied along the parcel's path. A lowering in the tropopause over the time 14/00Z indicates where the tropopause fold was located. At this point, the parcel went through a wind maximum of 25 m/s. The parcel traveled along the 309K potential temperature level descending between 14/00Z and 15/12Z. This is further supported by Figure 3.17b, which shows the relative humidity decreasing along the 309K potential temperature level especially between 14/12Z and 15/00Z. This is taken as a strong indicator of sinking air. Figure 3.17c depicts a plot of potential temperature and vorticity along the same path. Note the strong potential vorticity gradient along the 309K potential temperature level between 14/18Z and 15/06Z. This gradient represents where the parcel was influenced by the tropopause fold. This supports the air around Barrow at 16/00Z having been exchanged around 14/18Z and transported to Barrow.

At the 322K potential temperature level (Figure 3.18), the tropopause fold is better defined. The break in the line over the time 14/12Z indicates where the tropopause fold is located. Since the parcel moves along the 322K level, it is important to notice how this level descends between 14/12Z and 15/12Z. In the bottom Figure 3.18b, the relative humidity also decreased rapidly at the same time the parcel descended. Figure 3.18c depicts a plot of potential temperature and vorticity along the same path. Note the strong potential vorticity gradient along the 322K potential temperature level between 14/06Z and 14/18Z. This gradient represents where the parcel was influenced by the tropopause fold. This supports the

air around Barrow at 16/00Z having been exchanged from the stratosphere around 14/12Z and transported to Barrow.

In Figures 3.17 and 3.18, the tropopause, denoted by a thick line, has also been plotted based on soundings. The height of the tropopause at each point is based on using the soundings to locate the temperature inversion near the region of maximum wind. Notice how the 322K potential temperature level crosses the tropopause between 14/12Z and 15/00Z. This suggests that a tropopause fold took place here with stratospheric air being brought down into the troposphere. Cross-sections were generated in this vicinity in order to reveal if a break in the tropopause had actually occurred. At 14/12Z the air parcel in figure 3.18 is near the 24125 sounding location. The station 24125 sounding on 14/12Z (Figure 3.19) also suggests a tropopause fold has occurred. Two tropopause inversions are noted in this sounding with the strongest winds associated with the lowest inversion. In this sounding, temperature inversions occurred at the 480 mb and 340 mb levels with the wind maximum at the 500 mb level.

Plotting the relative humidity field on the parcel-time series diagram reveals a dry slot. Figures 3.17b and 3.18b display the potential temperature field along with relative humidity. Following the 309K and 322K potential temperature levels in figures 3.17 and 3.18, it is seen that moist air existed at 14/12Z with relative humidities of 75 percent and 50 percent, respectively. A dry slot developed at 15/00Z indicating the development of the tropopause fold. Values of 40 percent

relative humidity existed at the 309K and 322K levels at 15/00Z and decreased to less than 10 percent by 16/00Z. This relative humidity field gives a different perspective of the time scale of this event in contrast to the spatial scale depicted in the 500 mb relative humidity charts given in Figures 3.6a and 3.6b.

(i) Cross-sections. The wave can also be followed by plotting a cross-section parallel to the wind flow. Figures 3.20a-c depict cross-sections plotted for 14/00Z, 14/12Z, and 15/00Z for stations 24125, 24266, 21965, 21982, and 70026. The wave can be seen near station 24266 (near 300 mb) at 14/12Z in Figure 3.20a, near station 21965 (500 mb - 300 mb) at 15/00Z in Figure 3.20b, and east of station 70026 on the 15/12Z plot in Figure 3.20c. The forming of the tropopause fold near 70N, 140E can also be shown by plotting the relative humidity cross-sectional charts. Low relative humidity can be associated with sinking motion and can represent the influence of stratospheric air. Figures 3.21a-c depict the atmosphere at 70N, 110-180E for times 14/12Z, 15/00Z and 15/12Z. At 14/12Z (Figure 3.21a), the back trajectory of the parcel is located at 69.7N, 138E (marked on diagram with an x), at a height of 430 mb. The 14/12Z plot shows that a dry slot had begun to develop along with the parcel movement. The parcel's location is in a small area of minimum relative humidity. In contrast, an area with relative humidity of greater than 90 percent existed at 132E around 600 mb. This combination signifies the advection of moisture ahead of the polar vortex that was centered back around 120E and is also indicated by the change in the wind from southwest to northwest. Also noted on the chart is

the position of the wave located near 150E that is associated with a moist area ahead and dry intrusion behind. By 15/00Z (Figure 3.21b), the enhanced ozone parcel was located at 71.9N, 165.5E at a pressure height of 483 mb. The parcel was near an area of minimum relative humidity, which formed and expanded around 140E at the 400 mb level. Two areas of moisture existed around the parcel, one at 180E centered near the 500 mb level and the second at 135E near the surface. By 15/12Z (Figure 3.21c), the parcel was located at 72.5N, 172.9W or just off the right side of the plot. The parcel was in an area of extremely low relative humidity of less than 10 percent. This minimum existed at 180E at the 580 mb level extending back to 145E at the 520 mb level. Figures 3.22a and b are plotted near Alaska for 15/12Z and 16/00Z to represent the atmosphere near the point of interest (72.6N, 158W) and to give continuity with the earlier plot over Russia (Figures 3.21a-c). In Figure 3.22a, at 15/12Z, the parcel location is 72.2N, 176W at 566 mb, which is right in the center of the dry slot having less than 10 percent relative humidity. The wave can be noted just to the east of 170W by noting the warm advection (winds from the south in the lower levels (not shown) and the slight turning of the wind around 170W (winds not shown). Relative humidity values are higher ahead of the wave that was centered at approximately 165W. By 16/00Z (Figure 3.22b), the parcel was at the location 72.6N, 150W at 526 mb level where the aircraft measured the high values of ozone. At this time a large area of low humidity near 0 percent existed over the nearby point at 72N, 159W.

To see how the potential vorticity field changes with time and movement with the wave, potential vorticity cross-sections were plotted for 14/00Z (Figure 3.23a), 14/12Z (Figure 3.23b), 15/00Z (Figure 3.23c), and 15/12Z (Figure 3.23d). At 14/00Z (Figure 3.23a), an absolute vorticity maximum of greater than 22 AVU[12] can be found just off to the left of the plot in a region where potential vorticity varies only slightly with longitude. At 14/12Z (Figure 3.23b), strong fields of both potential and absolute vorticity had developed where values greater than 1 PVU were folded into the lower troposphere at the 650 mb level near 70N, 125E. Strong absolute vorticity was centered at the 400 mb level near 70N, 118E. By 15/00Z (Figure 3.23c), the higher values of potential vorticity had penetrated to 140E at the 700 mb level and to 145E at the 400 mb level. The wave of interest for Mission 8 had now moved out of the polar vortex and was now near 72N, 165E at the 300 mb level. By 15/12Z (Figure 3.23d), the high values of potential vorticity had weakened and moved to 172W where values of potential vorticity greater than 1 PVU could be found down to the 420 mb level.

The Mission 8 case study analysis represents an excellent example of a tropopause folding event. This folding event was identified by running isentropic back trajectories from the point where stratospheric values of ozone (255 ppbv) were measured in the mid-troposphere (4.5 km). The parcel time series documented the environment of the parcel along the trajectory path as it became under the influence

[12]Absolute vorticity has units (AVU) of 10^{-5} s^{-1}

of the folding event. A 322K parcel-time series plot indicated a break in the tropopause and descent into the troposphere by the downward slope of the potential temperature and a gradient of potential vorticity values. These changing potential vorticity values identify the tropopause folding event. Other analysis to include isentropic potential vorticity, tropopause vertical velocity, 500 mb relative humidity, TOMS ozone and differences, and 300 mb heights identified the positioning of the wave that caused this fold as it rotated around the polar vortex. Relative humidity minimums, total ozone maximums, daily ozone increases, and 300 mb wave positioning all coincide to identify the location of the fold itself. Cross-sections run across the trajectory path and skew-t logP diagrams helped to identify the atmospheric characteristics as the parcel passed through an area of strong subsidence. Thus, this case describes a nearly perfect setup for stratospheric-tropospheric exchange of ozone as a wave interacted with a polar vortex.

(2) Mission 19 Case Study. The Airborne lidar instrument recorded a dramatic shift in ozone mixing ratios. High values exceeding 100 ppbv were recorded near 5.8 km and above east of longitude 167W. This enhanced ozone region receded to 8 km west of 167W. *Browell et al.* (1992) indicated that this was a "well-defined" stratospheric intrusion. This section describes a more detailed meteorological analysis that has been carried out in order to find the origin of this enhanced ozone region. This analysis includes isentropic trajectories, constant pressure level charts, meteorological soundings, potential vorticity analysis on isentropic surfaces, cross-

sections of potential temperature, vorticity and relative humidity, time series, and TOMS ozone information. From the analysis, evidence suggests that the lidar record represents the western edge of a polar vortex where the tropopause had eroded from 5.8 km up to 8 km.

Mission 19 was flown from near Bethel, AK southwest over the North Pacific Ocean on August 2-3, 1988 from 1855Z-0010Z. *In situ* measurements by the aircraft included O_3, CO, CH_4, and H_2O, among other trace gases. The flight path started from just northwest of Bethel and traversed southwestward to a point 300 km over the Kuskokwim Bay (near 58N, 163W). Two spiral profiles were flown, one near Bethel and one over the ocean. The objective of the mission was to measure changes in trace gases at the land-sea interface.

Ozone was measured both *in situ* and with lidar. A graphic view of the ozone values from lidar (Figure 3.24) clearly shows values of ozone exceeding 100 ppbv down to 6 km at 166.5W, which abruptly recedes to 8 km at 167W longitude. In Figure 3.24 the ozone mixing ratios are shown in parts per billion by volume (ppbv) defined at the top of the display. Black areas represent values greater than the maximum level given on the color scale. The white areas are an artifact that occurs at the end of the lidar's range due to a loss of return signal as previously discussed. Geometric altitudes are given in km above sea level. Local time is shown at the top of the display. Location (latitude and longitude in degrees) is shown below the display. Figure 3.25 depicts a time series profile of altitude, ozone, temperature, and

dew point measurements from *in situ* measurements onboard the aircraft. At the aircraft altitude of 4 km (636 mb), a maximum in ozone of 180 ppbv occurred at 20:14:30Z, at 61.095N and 161.947W, which was near Bethel. Note also that the normal background ozone values were approximately 75 ppbv near 4 km.

Meteorological analyses are presented that lead to the conclusion that a movement of the polar vortex was responsible for the erosion of the tropopause. Further, it is shown that the presence of the polar vortex was not accompanied by strong vertical motions. This lack of vertical motion leads to the conclusion that a tropopause fold was not active in the region and during the time period of interest, and the small amounts of exchanged ozone is most likely due to a small relocation of the slowly rising tropopause.

(a) Constant Level Charts. Since the lowest altitude of the enhanced ozone in Figure 3.23 is around 6 km, or 470 mb, the 500 mb level will be used to represent the background environment of the ozone. Figures 3.26a-c depict the 500 mb chart for 2/00Z, 2/12Z, and 4/00Z in August 1988. Figure 3.26a gives the 500 mb heights with the flight path corresponding to Figure 3.25 annotated by a solid line. On August 3 at 00Z, the 500 mb chart depicts the center of the polar vortex, which was moving East, over the Kuskokwim Bay. This polar vortex formed as a result of a strong upper-level wave rotating around another polar vortex that was located over Northeast Russia on July 29. The polar vortex first formed at the 500 mb level on July 30 at 00Z with the 500 mb central pressure occurring at 5520 m, and with the

lowest height occurring on August 1 at 12Z with the 500 mb central pressure at 5510 m. By 2/12Z (Figure 3.26), the center of the low had moved East to 60N, 155W and had began filling in with the 500 mb central pressure at 5600 m. Note the location of the flight path (from 61N, 162W to 59N, 169W) in comparison with the polar vortex. The low was now to the East of the flight path, which allowed warmer air to move in and begin raising the tropopause. On August 4 at 00Z (Figure 3.26c), the low had moved to the Gulf of Alaska and was no longer completely closed off at the 500 mb level. The axis of the high pressure ridge was now over the flight path.

(b) TOMs Ozone Charts. Daily plots of total ozone column from August 1-3 (see Figures 3.27a-c) show an area of enhanced ozone that correlates well with the polar vortex. The enhanced region of ozone moved east in conjunction with the movement of the center of the low at the 500 mb level as shown in Figures 3.26a-c. Notice as the low decreased in intensity, that the total ozone also decreased (compare center of low on 500 mb chart in Figures 3.26a-c with Figures 3.27a-c). The increase in pressure of the center as well as the decrease in total ozone signifies what is called the de-intensification or "filling" of the low pressure system. Now compare Figure 3.24 with Figure 3.27b noting the position of the enhanced ozone region (near 59N, 167W). A strong gradient of ozone existed at the point in Figure 3.27b that corresponds to the western edge of the polar vortex in Figure 3.26b.

Total ozone column differences between August 1st and 2nd (see Figure 3.28) show increasing values over the Gulf of Alaska that extend back to the northern

Alaska Peninsula, whereas decreasing values cover southwest Alaska and the Kuskokwim and Bristol Bays. At the point 59N, 167W, ozone differences of 30-40 DU occur. This one day decrease in total ozone levels signifies the influence of the polar vortex moving to the East of the point. As expected, a time series of the total ozone column at 59N, 167W reveals a steady decrease. Total ozone column values are on August 1, 371.2 DU, on August 2, 340.5 DU, and on August 3, 322.9 DU. This rapid decrease in ozone signifies the movement of the polar vortex to the East.

(c) Meteorological Soundings. The closest sounding stations to the point 59N, 167W are Bethel (station 70219) at 60.78N, 161.8W to the east-northeast and St. Paul Island (station 70308) at 57.15N, 170.22W to the southwest. Both stations have been plotted on a skew-t logP diagram in Figures 3.29a-c for station 70219 every 12 hours from August 2 at 00Z to August 3 at 00Z and Figures 3.30a-d for 70308 from August 1 at 12Z to August 3 at 00Z. Both sets of skew-Ts show a subsidence layer developing in the mid levels. A drying trend can be seen in the sounding by looking at Figures 3.29a and 3.29b and comparing them with 3.29c. Figures 3.29a and 3.29b show a relatively moist sounding with distinct drying noted in 3.29c from 620 mb to 400 mb. The same can be seen for station 70308 by looking at Figures 3.30a-c and comparing them with Figure 3.30d. Figures 3.30a and 3.30b show a moist sounding with drying shown in 3.30c and especially 3.30d. Tropopause heights show an increase in altitude with time with the greatest change occurring near the enhanced ozone region in Figure 3.24. The tropopause height (indicated

on the sounding as a temperature inversion near the region of maximum wind) over station 70308 (St. Paul Island) increased from 10 km (263 mb) on Aug 2 at 00Z to 11.2 km (217 mb) on August 2 at 12Z and to 12.1km (200 mb) by August 3 at 00Z. At station 70219 (Bethel), Figure 3.29a-c, the tropopause height rose from 9.85 km (271 mb) on August 2 at 00Z to 104 km (240 mb) by August 3 at 00Z. Winds at the 500 mb level over St. Paul Island (station 70308) shifted from the north on August 2 to the southwest on August 3 indicating the polar vortex had moved off to the east as a ridge began to influence the area. Winds over Bethel (station 70219) gradually weakened at the 500 mb level and turned more to the north with time. This wind shift supports the movement of the polar vortex off to the east from its position at 59N, 167W (see Figures 3.26a-c).

(d) Time-Series Plots. Bethel (station 70219) and St. Paul Island (station 70308) Time-Series plots of potential temperature and wind in Figures 3.31a and b clearly show changes in the atmosphere as the polar vortex moved away from the stations. Figure 3.31a shows station 70219 plotted from August 1 at 00Z to August 3 at 00Z and Figure 3.31b shows station 70308 plotted from August 1 at 12Z to August 3 at 00Z. Both plots show the rising of the tropopause with time, highlighted by a darkened line. The time of interest, for the aircraft interception, in both Figures 3.31a and 3.31b is August 2 at around 20Z when the lidar sounding was taken (see Figure 3.24). Both in Figures 3.31a and 3.31b, the tropopause is seen to rise in

conjunction with a slow backing[13] of the wind. This again signifies the movement of the polar vortex to the east. Potential temperatures also warm with time due to the sinking of air (i.e. adiabatic compression) and advection of warm air into the area.

(e) Potential Vorticity Back Trajectory on Isentropic Surfaces. Back-trajectories were computed at specified points and levels to determine the origins of certain parcels. After examining Figure 3.24, points on the eastern edge and just west of the enhanced ozone region were picked for further analysis. At 7 km the back trajectory along the 321K potential temperature surface[14] for the eastern, ozone enhanced, point 61.1N, 162W (see Figure 3.32a), shows the parcel descended along its trajectory while maintaining a high potential vorticity value of 2.12 PVU. The eastward parcel's path is seen to rotate counterclockwise around the polar vortex. For the western point 57.2N, 170.2W, low ozone, at the same altitude, the back trajectory along the 311K potential temperature level (see Figure 3.32b) indicates the parcel remained near the same height during the initial 36 hours. At this time the back trajectory ascended while the parcel's potential vorticity remained nearly constant, ranging from 0.76 PVU to 0.85 PVU, back to -96 hours. This latter, low-ozone parcel also came from the west over Russia and not around the polar

[13]Backing is a meteorological term referring to a decrease in the wind azimuth with time.

[14]The 312K potential temperature value was picked from the station 70219 sounding at 02/12Z.

vortex. This is in contrast to the back trajectory for the parcel with enhanced ozone (180 ppbv) that was encountered at the point 61.1N, 162W. Figure 3.32c shows an ascending motion of this ozone enhanced parcel, of 203 mb, during its travel in the previous 72 hours. During this time, the potential vorticity of this parcel varied between 0.83 and 1.28 PVU. This trajectory path conflicts with what is normally expected in order for vertical transport alone to explain the 180 ppbv of ozone measured at the point 61.1N, 162W. A possible explanation for this discrepancy could include terrain features or subgrid scale. The Kilbruck Mountains (peaks at 0.8 km) and the terrain over the Alaskan Peninsula (peaks to 1.5 km) could have influenced the trajectory path (path at 4.5 km). The scale of this event is 0.4 degrees compared to a grid scale of 2.5 degrees. This area of enhanced ozone, having values to 180 ppbv at 61.1N, 162W, was most likely caused by a small, subgrid scale event.

(f) Cross-sections of Meteorological Parameters. Cross-sections of potential and absolute vorticity for approximately the path in Figure 3.24 are given in Figures 3.33a-c. The potential vorticity values (Figure 3.33b) agree well with the location of the enhanced ozone region. Note the 1.5[15] PVU value is known to be representative of stratospheric air and the tropopause . This agrees well with the

[15]Note here that the potential vorticity units plotted here have units of deg K $m^2 kg^{-1} s^{-1} X 10^{-6}$. Therefore these units here plotted on the cross-section need to be divided by 10 to equal the PVU. Also note that latitude increases from right to left in Figure 3.33, whereas it increases from left to right in Figure 3.24.

lidar ozone sounding shown in Figure 3.24,[16] where a gradient in potential vorticity, near 59N, 167.5W was located where the change in ozone occurred. The gradient in potential vorticity at 59N, 167.5W represents the point where the polar vortex ended. The cross-sections of absolute vorticity also help to determine the position of the polar vortex. Taking the point of 59N, 167.5W (point of interest from Figure 3.24), Figures 3.33a-c can also be used to demonstrate how these fields changed with time. The east-west cross-section (Figure 3.33a) at 02/12Z shows the polar vortex's influence on an area of positive absolute vorticity that was centered at 59N, 163W at 300 mb. However, by 03/00Z (Figure 3.33b, especially near 59N, 167.5W), a transition zone becomes evident as the center of positive absolute vorticity moved to the east, nearly off the chart, while maintaining approximately the same altitude. By 03/12Z (Figure 3.33c), the entire 300 mb level was influenced by the ridge of high pressure with its associated minimum in absolute vorticity that was found over the area.

The Mission 19 case study analysis represents an excellent example of an intrusion. A lidar sounding measured the structure of the northwest side of a polar vortex. Isentropic back trajectories for parcels in the vortex indicate that little vertical movement of the air occurred along the trajectory paths. Meteorological analysis of 500 mb pressure heights, cross-section, station time-series, and skew-t logP

[16]Note that latitude increases from right to left in Figure 3.33, whereas it increases from left to right in Figure 3.24.

as well as TOMs total ozone column charts revealed the position and movement of the polar vortex clearly identifying the feature in Figure 3.24 as an intrusion. The edge of the vortex shows up well in the potential vorticity cross-sections. The skew-t information that yielded an evaluation of the height of the tropopause reveals little vertical change occurring until after 3/00Z at which point the average tropopause began to rise in association with the dissipation of the polar vortex. Little exchange of ozone occurred during the time of the lidar sounding. However, after 03/00Z, there are stronger indications of the polar vortex's dissipation suggesting that the beginning of the tropopause erosion was taking place.

(3) Mission 3 Case Study. Aircraft *in situ* measurements recorded enhanced ozone values from 150 to 170 ppbv at 5.5 km altitude over Alaska when background values of 80 ppbv existed nearby. A meteorological analysis has been completed to locate the origins of the high ozone values. This analysis included isentropic trajectories, constant level charts, meteorological soundings, potential vorticity on isentropic surfaces, cross-sections of potential temperature, vorticity, relative humidity, specific humidity, time series analysis over certain points, and TOMS total ozone information. From the analysis, the evidence suggests that this air originated in the stratosphere near a cutoff low over Northern Canada, and passed through a tropopause fold and ended up at a 5.5 km height at 63.6N, 91W.

Mission 3 was flown from Churchill, Canada to Thule, Greenland on July 8 from 1356-1846Z. Measurements onboard the aircraft included O_3, CO, CH_4, and

H_2O, among other trace gases. The flight path started at Churchill and made an almost straight line path to Thule, Greenland at a nearly constant altitude of 4.8-5.5 km. Ozone was measured *in situ* and with Lidar. The most interesting enhanced ozone regions were found at flight level. A graphic view of altitude and ozone measurements (Figure 3.34) shows three regions of enhanced ozone along the flight track. A maximum of 170 ppbv was recorded at 1514Z at altitude 4.8 km (313K potential temperature level or 521 mb) located at 63.6N, 91W. Another region having 150 ppbv ozone was found at 1644Z at altitude 5.3 km (311K potential temperature level or 528 mb) located at 68.6N, 81.5W. A third region with ozone values of 168 ppbv was found at 1722Z at altitude 5.3 km (313K potential temperature level or 526 mb) located at 71.3N, 79.2W. Background levels for this altitude were about 80 ppbv. Note that the dew points in these ozone enhanced air parcels are dry in comparison to surrounding air for all three points suggesting that these three enhanced ozone areas may have had a stratospheric or upper tropospheric origin.

Meteorological Analyses are presented using various methods to conclude the origin of the parcel of air. Evidence is presented with the most conclusive first.

(a) Isentropic Back Trajectory. Isentropic back trajectories were run for each of the three points. For the first point at 63.6N, 91W, the back trajectory was run along the 313K potential temperature surface (see Figure 3.35). During the 60 hour period preceding the flight, this enhanced ozone parcel descended 163 mb while the

potential vorticity value decreased from 1.17 to 0.83 PVU. The potential vorticity values here do not indicate an origin in the stratosphere. Figure 3.35 shows the path of the trajectories. A back trajectory was run for the second point starting at 68.6N, 81.5W on the 313K potential temperature level (see Figure 3.35). This enhanced ozone parcel also followed a descending path of 84 mb during the previous 60 hours while its potential vorticity decreased from 2.03 PVU to 0.83 PVU. The back trajectory for the third point at 71.3N, 79.2W was run at the 313K potential temperature level (see Figure 3.35). During the previous 60 hour period, this enhanced ozone parcel descended 64 mb while the potential vorticity value decreased from 2.19 PVU to 0.88 PVU, a strong indicator of stratospheric origin.

(b) Parcel-Time Series. By plotting a time series of meteorological soundings along the path and time of the isentropic trajectory, an actual history of the parcel's path can be visualized. The back trajectory paths for two of the points discussed above went through a data sparse area, therefore, the construction of Parcel-Time Series was not possible. The ozone maximum located at 63.6N, 91W was the only point for which a Parcel-Time Series could be plotted (see Figure 3.36). The meteorological sounding stations used are listed in Table 3.3. The parcel traveled along the 313K potential temperature surface, which descended between July 7 at 00Z and July 8 at 00Z. A tropopause fold can be seen above the

trajectory's altitude along with a jet maximum.[17] In this regard, the Mission 3 case is similar to the Mission 8 case. Isentropic trajectories indicate that the parcel's of interest path descended as potential vorticity changed in the vicinity of a tropopause fold. The parcel-time series for one of the enhanced ozone features indicate the position of the tropopause fold. The situation depicted describes another good example for the stratospheric-tropospheric exchange of ozone and subsequent transport to the point of measurement within the troposphere.

(4) Enhanced Ozone Regions from Lidar Soundings. Enhanced ozone regions identified from lidar were investigated. Discussion of these enhanced ozone regions will be brief since the other major case studies already have been shown as examples of this type of enhanced ozone region. The lidar enhanced ozone regions are categorized into two different areas: ozone intrusions and minor ozone enhancements.

(a) Ozone intrusions with similar characteristics to that of Mission 19 are found in Missions 4 and 30. The Mission 4 lidar sounding (Figure 3.37) shows an intrusion of ozone existed down to 8 km with enhanced ozone values near 200 ppbv at 8 km. Comparing the location of the intrusion to the 500 mb chart at 09/12Z (Figure 3.38), the intrusion was located on the southwest corner of a polar vortex. The center of the polar vortex was located near the north pole, to the northeast of

[17]A jet maximum is an isotach maximum embedded within a jet stream (Palmen and Newton, 1969). A jet stream is an intense, narrow, quasi-horizontal current of wind that is associated with strong vertical shear (Reiter, 1961).

the lidar profile. The influence of the polar vortex can also be visualized by plotting the potential and absolute vorticity cross-sections that intercept the enhanced ozone region at 76N, 110W. These cross-sections, plotted from 86N, 100W to 66N, 120W (Figure 3.39), indicate a decrease in altitude of a given potential vorticity value from the point 76N, 110W, at 8 km, and to the northeast (i.e., left of the point). An enhanced absolute vorticity area is also found northeast of the point 76N, 110W with values greater than 18 AVU at 10.5 km. However, due to the location of this ozone enhanced area in a data-sparse area in northern Canada, further analysis is limited.

The ozone intrusion found in Mission 30 also has similarities to the Mission 19 case. Mission 30 was conducted on 15 Aug 88 (see Table 1.1). The Mission 30 lidar sounding (Figure 3.40) depicts a small-scale intrusion 1.5 degrees latitude in width protruding down from 9 km to 7 km at 69.5N, 68.5W. At this same location, on the 500 mb chart at 15/12Z (Figure 3.41), a weak polar vortex was centered at 72N, 80W. This polar vortex extended to the southeast and crossed the flight track where the lidar sounding was taken. The position where the two intersect (near 69.5N, 68.5W) is where the ozone intrusion is found to occur. Cross-sections further support this. Cross-sections of potential and absolute vorticity (from 80N, 69W to 60N, 69W) that include the same path as the ozone profile (Figure 3.42a) show large values of potential vorticity (1.5 PVU) down to 6 km at 69N, 68.5W and a center of maximum absolute vorticity above the same point. This analysis does not depict the exact shape of the ozone intrusion due to the resolution of the meteorological data.

To determine the structure of the polar vortex, relative humidity and potential temperature cross-sections (Figure 3.42b) were also plotted along this path. A strong gradient of relative humidity is evident in the 6 to 7 km region above the point. This gradient corresponds to a point crossing the tropopause and encountering larger values of ozone. The decrease of relative humidity from 50 percent at 6 km to less than 20 percent at 8 km further suggests that the air was sinking. The sinking of the air above this point is further supported by the temperature cross-section shown in Figure 3.42c. At 7 km, the temperature over this point was cooler than the adjacent air to the north and south, but warmer than the air aloft at 8.5 km, as shown by the separation of constant temperature surfaces at 8 km over the point at 69N, 68.5W. The cross-section of potential temperature (Figure 3.42b) also depicts the presence of the typical atmospheric structure of a polar vortex. This structure exhibits the inverted potential temperature values that indicate cool air below the low (below 7 km) and warm air above. Mission 30 can be classified as an intrusion based on the meteorological cross-sections and the analysis 500 mb pressure heights, which indicate that it is similar to the Mission 19 case analysis.

(b) Other minor ozone enhancements were also found in the lidar ozone soundings and were investigated in order to see if the origins could be determined from the trajectory analysis of vertical transport or the analysis of meteorological variables. These ozone enhancements were located using two methods. The first method compared the ozone measurements to the local background level, which can

often be taken directly from the lidar sounding. The second method compared local ozone measurements to the average background levels for the study period. These average background values for continental polar air masses were obtained from an average profile determined by *Browell et al.* (1992). They obtained an average background ozone vertical distribution with a value of 30 ppbv at 500 m that increased with altitudes by a gradient of 7.4 ppbv km^{-1} up to 8 km.

The Mission 6 lidar sounding (Figure 3.43) depicts pockets of ozone enhancements at low altitudes. Mission 6 was flown on July 12, 1988 (see Table 1.1). Ozone values near the surface, 70 ppbv, were markedly enhanced compared to the average background value of 30 ppbv for this altitude. These near surface, values were close to background values at an altitude near 4.5 km. Meteorological conditions near this region of enhanced ozone favored sinking air. At the 500 mb level at 13/00Z (Figure 3.44), northern Alaska was under the influence of high pressure. This high pressure pattern persisted in this area for several days. To better evaluate the conditions around the area of enhanced ozone, cross-sections of potential vorticity, relative humidity, and winds coinciding with the lidar sounding were plotted between the points 76.6N, 147W and 66.6N, 157W (Figure 3.45). These cross-sections reveal generally stagnant conditions with light winds, little horizontal change of potential vorticity and a very dry air mass over the point 71.62N, 152W. The relative humidity was 15-20 percent at altitudes form 1 to 6 km, and dry air of near 0 percent existed at 4 km to the northeast at 74N, 149.5W. To help identify the

origins of this air, isentropic back trajectories (not shown) were run from the point 71.62N, 152W along the 296K (1.5 km) and 300K (2.5 km) potential temperature surfaces. In the previous 48 hour period, the parcel on the 296K potential temperature surface ascended 22 mb, its the potential vorticity only changed from 0.47 to 0.40 PVU. For the same 48 hour period, the parcel on the 300K surface descended only 13 mb, and its potential vorticity also changed little, going from 0.62 to 0.56 PVU. However, these trajectories may be of limited use because of the light winds (~5 m/s) at all altitudes. *Sandholm et al.* (1992) conducted a study in this same area and concluded that the haze layers that existed in this air mass could have been from fires burning in the southwest portions of the Brooks range. During a spiral descent over this point sporadic ozone enriched parcels were measured onboard the aircraft. These results indicate that of a combination of factors may account for the origin of the enriched ozone. Meteorological conditions favored subsidence while haze layers were encountered. Trajectory methods were limited because of light winds.

The Mission 7 lidar (Figure 3.46) shows fairly low levels of ozone near 30 ppbv at 8 km. In comparison, the nominal altitude for an ozone background level of 30 ppbv should be near 0.5 km. In order to explain this area of depressed ozone by a simple vertical transport mechanism, ascent of the air parcel should have occurred. Meteorological conditions favored ascending air near the region where the depressed ozone levels were found. However, the isentropic back trajectory

analysis for the air parcel indicates descending air. The 500 mb chart for 14/00Z (Figure 3.47) shows a wave nearly over the point. This wave is better depicted in the cross-sections of potential temperature and absolute vorticity (Figure 3.48a) constructed from 70.5N, 175W to 70.5N, 135W. At the 400 mb level, above the ozone depressed parcel, absolute values of the vorticity reached a maximum of 18 AVU at the point 70.5N, 155W, where potential vorticity was also enhanced. This analysis indicates an unstable atmosphere, which is further supported by the cross-sections of potential temperature, relative humidity and wind (Figure 3.48b) for the same area. The relative humidity fields over this location (70.5N, 155W) indicate that moisture was increasing at altitudes below 5 km. The potential temperature and wind fields indicate a cyclonic turning of winds over this area and a wave to the west. These indications suggest the ascent of air over the location 70.5N, 153.3W. The back trajectory run on the 316K (6.5k m) potential temperature surface (Figure 3.49), from the point 70.3N, 153.3W, shows the parcel followed a 81 mb descending path during the previous 48 hours while the potential vorticity changed little from 0.83 to 0.79 PVU. The Brooks range could have influenced the trajectory here as the trajectory path passed over higher terrain of 1.5 km. Whereas ascent was expected from meteorological conditions, descent occurred due to downsloping terrain. A trajectory at the same level just to the west at 70.3N, 160W, where terrain would not have been a factor, indicated a 108 mb ascent over the same 48 hour period. Mission 7 is an example of depressed ozone levels at higher altitudes. Results from

meteorological analysis supports the ascending air in the area while the descending path from the trajectory may be explained by the path crossing the leeward side of the Brooks range.

The Mission 13 lidar sounding (Figure 3.50) shows an area of ozone enriched air near 2.5 km. This enhanced ozone region had ozone values of 60 ppbv at 2 km and 70 ppbv at 2.5 km. These levels of ozone are more typical of background values at higher altitudes (3.5 km for 60 ppbv and 4.4 km for the 70 ppbv). In order to explain this deviation from nominal background conditions by vertical transport alone, descent of air should have occurred. Meteorological conditions did favor descending air near the enhanced ozone region. The 500 mb chart at 25/00Z (Figure 3.51) and previous upper air charts indicate an anticyclonic turning of the atmosphere over southwest Alaska that is indicative of a sinking motion. This inference of sinking air over the enhanced ozone region (point of interest location is 63N, 162W) is also supported by the cross-section analysis. Cross-sections of potential and absolute vorticity (Figure 3.52a) constructed across the ozone enhanced region (from 68N, 167W to 58N, 157W) reveal that for a constant pressure level values of potential vorticity decrease in the center of the high pressure region (i.e., equal-potential vorticity surfaces increase in altitude at the center, e.g., values of 1 PVU at 300 mb). This area of depressed potential vorticity corresponded with a minimum of absolute vorticity of less than 10 AVU above the point 63N, 162W. The position of these areas are indicative of high pressure and subsidence influencing the

air at this point. The cross-sections of winds and relative humidity (Figure 3.52b) over the same area also support the assertion of sinking air. Winds along the northwest-southeast slice of the atmosphere indicate anticyclonic turning. Dry air with relative humidity of less than 30 percent existed over the point 61.3N, 162W at the 303K potential temperature level. A relative humidity minimum of less than 10 percent also existed at 59.5N, 159.3W at an altitude of 3.5 km (i.e. on the 303K potential temperature surface). The isentropic back trajectories (Figure 3.53) also show a gradual sinking of air. The air parcel located at point 61.3N, 162W on the 303K potential temperature surface followed a 73 mb (1 km) descending path of during the previous 60 hours. An adjacent air parcel located at point 59.5N, 159.3W on the 303K surface also followed a descending path of 54 mb (0.7 km) over the previous 48 hours. This analysis indicates that the Mission 13 ozone enhancement is an example of subsidence associated with a high pressure system. Both the meteorological analysis and the trajectories give strong evidence to support descending air in this area.

The Mission 15 lidar sounding (Figure 3.54) depicts an area of enhanced ozone at 3 km to the west of 159W and an area with less ozone to the east. Ozone values for these regions were 70 ppbv at 3km for the enhanced area near the location 61N, 162W and a depressed ozone value of 40 ppbv at 4 km near the location 63.58N, 158.5W. The normal altitudes corresponding to background ozone values of 10 and 40 ppbv are 6 km and 2 km, respectively. In order to explain these

differences by simple transport, descent of air should have occurred near 61N, 162W at 3 km with an ascent of air occurrences near 63.58N, 158.5W at 4 km. Meteorological conditions support this assertion of vertical air movement near these points. The 500 mb chart (Figure 3.55) for 28/00Z indicates a high pressure ridge with its axis crossing near the location of interest, 61N, 162W. The other location of interest (63.58N, 158.5W) was to the rear of the high pressure ridge axis, a position that is conducive to ascending air. Cross-sections constructed from 52.5N, 170.5W to 72.5N, 150.5W further support this. The potential and absolute vorticity cross-sections (Figure 3.56a) indicate that the high pressure ridge was dominating flow. This is also seen in the elevated values of potential vorticity and the center of minimum of absolute vorticity over the location 61N, 162W. In contrast, the location 63.58N, 158.5W, was in an area of increasing absolute vorticity. Cross-sections of relative humidity and winds (Figure 3.56b) show a dry slot at 5 km of less than 20 percent relative humidity near 61N, 162W, whereas values of larger relative humidity of greater than 90 percent existed near 63.58N, 158.5W. For the location 61N, 162W isentropic back trajectories on the 298K potential temperature surface (Figure 3.57a) indicate that the parcel followed a 94 mb (~1 km) ascending motion of during the previous 96 hours. For the 63.58N, 158.5W point (Figure 3.57b) on the 303K surface, the parcel followed a path with generally neutral vertical motion during the previous 48 hours. Thus, the meteorological analysis supports descending air while the trajectory analysis result is somewhat uncertain. Terrain features along the trajectory

paths, such as the southern Alaskan range where tops reach 5 km at Mt. Feaker, may be introducing uncertainties into the trajectories at the subgrid level. *Sandholm et al.*'s (1992) study of Mission 13 found mixing ratios of CO, C_2H_2, C_2H_6, and C_3H_8 were all near background values while the NO_y/O_3 ratio were close to, but not equal to stratospheric values. Their conclusion was that the air was modified if it originated from the stratosphere. The meteorological analysis carried out here suggests that simple ascending and descending atmospheric motion may be responsible for the apparent altitude displacement of these ozone features and generally agrees with the earlier chemical analysis.

The Mission 18 lidar sounding (Figure 3.58) shows an area enhanced ozone above 4 km. This enhanced ozone region appears as a lowered tropopause with ozone values of 100 ppbv at 4.8 km. The nominal altitude for a background ozone value of 100 ppbv is 7 km. Meteorological conditions did favor descending air near this enhanced ozone region. The 700 mb chart for 31/12Z (Figure 3.59) indicates that a persistent ridge dominated western central Alaska in conjunction with a polar vortex located to the south. The cross-section constructed from 55.9N, 157.6W to 65.9N, 167.6W further supports the sinking motion of air in this area. The potential and absolute vorticity cross-sections (Figures 3.60a and 3.60c) depict values of potential and absolute vorticity increasing along a constant altitude when moving southwest (from right to left), which signifies the transition between the region of high pressure and the polar vortex. The relative humidity and winds cross-section

plot (Figure 3.60b) indicates that dry air persisted northeast of the location 60.9N, 162.6W at 5 km, whereas southwest of this location a maximum in relative humidity occurred. On July 31 at 12Z, the enhanced ozone region (60.9N, 162.6W at 4.8 km) was in an area of minimum relative humidity (25 percent, Figure 3.60b). The humidity increased in this region to 60 percent by August 1 at 00Z. Other dry regions occurred over the points 62.4N, 164.1W at 3.5 km (less than 10 percent, Figure 3.60b), and 63.4N, 165W at 3.5 km (less than 30 percent Figure 3.60d). Isentropic back trajectories were run beginning at these three points to evaluate the role of vertical transport. These trajectories (Figure 3.61a-b) indicate that all the air parcels followed descending paths during the previous 90 hours. The parcel located at 60.9N, 162.6W on the 306K potential temperature surface descended 80 mb (~1 km) during the previous 90 hours. Similarly, the parcels on the same 306K surface located at 62.4N, 164.1W descended by 90mb (~1.2 km) in 42 hours, and 63.4N, 165W descended by an even greater 140 mb (~1.8 km) during the previous 84 hours, respectively. Potential vorticity values along all the trajectory paths remained rather constant with values ranging from 0.70 PVU to 1.0 PVU. Two of these trajectory paths crossed over the Kilbruck mountains (tops at 2 km) and the southern Alaskan range (tops at 3 km). Even though the 3.5 to 4.8 km trajectories indicate the descent of these parcels, some uncertainty may be introduced by the terrain features whose heights (tops at 3 km) are near the height of the trajectories. *Sandholm et al.*'s (1992) study of Mission 18 found that, based on measurements of NO_y/NO_3ratio, the

enhanced ozone parcel may have originated from sources other than the stratosphere, unless significant aging occurred. Their conclusion was that the origin of the ozone enhanced air was uncertain. The meteorological and trajectory analysis presented here indicate that the origin of the area of enhanced ozone located at 60.9N, 162.6W can be explained by the transport of subsiding air into the region.

The Mission 21 lidar sounding (Figure 3.62) depicts a region of ozone enriched air near values of 70 ppbv with altitude 2.5 km. The nominal background altitude for this level of ozone is 4.4 km. Meteorological conditions favored the descent of air near this region of enhanced ozone. The 500 mb chart (Figure 3.63) for 04/00Z indicates that southwest Alaska was dominated by a strong high pressure ridge. Cross-sections constructed from 56.9N, 165.9W to 66.9N, 155.9W further supported the descent of air in this region. The cross-sections of potential and absolute vorticity (Figure 3.64a) reveal an increase in altitude for a given level of potential vorticity and a depressed area of absolute vorticity values to the northeast of the enhanced ozone region (61.9N, 161.9W). The cross-section of relative humidity (Figure 3.64b) indicates a minimum of less than 10 percent occurred above the point 61.9N, 160.4W at 3.5 km and a value of 20 percent occurred at 2.5 km. An isentropic back trajectory (Figure 3.65) of the ozone enhanced parcel indicates a gradual sinking motion. The air parcel at point 61.9N, 161.9W on the 307K potential temperature surface had followed a 81 mb (~1.2 km) descending path. This analysis indicates that the seemingly anomalous low altitudes area of enhanced ozone can be

explained by simple mechanisms of subsidence along the parcel's path.

The Mission 33 lidar sounding (Figure 3.66) depicts a region where ozone was most likely enhanced by pollution from the surface to 2 km. The corresponding aerosol distribution (not shown) depicts enhanced aerosol concentrations below 2km. *Blake et al.* (1992) also found enhanced levels of non-methane hydrocarbons and *Sandholm et al.* (1992) found levels of NO_x that were sufficient for substantial ozone production. Above 2 km ozone levels were also enhanced over nominal background values for a given altitude. Ozone values over location 39.5N, 73.5W were 75 ppbv at 1 km and 70 ppbv at 3 km. In order to explain these enhancements by simple transport, descent of air should have occurred. Meteorological conditions favored descending air near the region of enhance ozone. The 500 mb chart for 17/00Z (Figure 3.67) indicates that the flight path occurred on the backside of a rather strong wave, in an area that was favorable for the descent of air. Cross-sections constructed from 38N, 75W to 43N, 70W further support this assertion. Comparing the potential and absolute vorticity cross-sections at 17/00Z and 17/12Z (Figures 3.68a and 3.68c), potential vorticity increased with altitude and absolute vorticity values decreased. These changes indicate the sinking of air on the rearward side of an exiting wave. Relative humidity and wind cross-sections (Figures 3.68b and 3.68d) were constructed for 17/00Z and 17/12Z. These cross-sections indicate relatively dry humidity values of less than 10 percent existed from 3 to 7 km at 39.5N, 73.5W. By 17/12Z (Figure 3.68b), the dry slot still persisted with values of less than 30 percent.

The isentropic back trajectory analysis for their parcel (Figure 3.69) indicates a gradual sinking motion of the air with the parcel located at point 39.5N, 73.5W, on the 314K potential temperature surface, following a 73 mb (~1 km) descending path over the previous 60 hours. Potential vorticity values slowly decreased along the path of the parcel, ranging from 0.86 PVU to 0.45 PVU. The meteorological analysis and trajectory results suggest that the transport of subsiding air is responsible for the ozone enhancement located at 3 km. At lower altitudes, near 1 km, some combination of transport of subsiding air with strong chemical production was responsible for enhancing the ozone values.

(5) Minor Ozone Enhanced Regions based on Ozone Profiles. Areas of enhanced ozone from the ozone profiles were identified and investigated in order to ascertain if the enhancements could be explained by a simple vertical transport mechanism. Areas of enhanced ozone were identified by determining a delta ozone value from nearby levels above and below the altitude where the enhancement was found. The meteorological analysis of these case studies include the use of constant level charts to determine the general circulation and cross-sections to further define the local environment around the enhancement. In addition, isentropic back trajectories are used to evaluate the role of vertical transport along a given parcels' path. If a sinking motion occurred, a subsidence layer and a corresponding dry slot were found.

The Mission 10 ozone profile (Figure 3.70) indicates a region of enhanced

ozone between 4.4 and 5.6 km with an apparent excess level of ozone of 18 ppbv at 5 km. Meteorological conditions favored sinking air near the area of enhanced ozone. The 500 mb chart for 19/00Z (Figure 3.71) indicates that northern Alaska was dominated by the influence of the eastern edge of a area of high pressure. This situation is usually indicative of sinking air. The influence of this high pressure influence showed up on the Barrow, AK (station 70026) meteorological sounding for 19/00Z. The sounding (Figure 3.72) indicates the presence of multiple subsidence layers between 3.5 and 5.6 km. Cross-sections over the region of enhanced ozone from 71N, 180W to 71N, 150W also indicate that conditions were conducive for the sinking of air. The potential and absolute vorticity cross-section (Figure 3.73a) indicate depressed values of potential vorticity and absolute vorticity at a given altitude. The cross-section of relative humidity and winds over this same area (Figure 3.73b) show less than 40 percent at 5 km above the point of interest at 70.4N, 157W. This area of low relative humidity is also represented in the Barrow (station 70026) station time-series plot of relative humidity (Figure 3.74) where 0 percent relative humidity dry slot existed from 550 mb to 680 mb at 18/00Z and values increased to 20 to 30 percent by 19/00Z. The isentropic back trajectory analysis (Figures 3.75) also indicates a gradual sinking of the air. The air parcel located at point 70.4N, 157W on the 308K potential temperature surface (5 km) followed a 70 mb (~0.9 km) descending path during the last 36 hours. Potential vorticity values along this trajectory path varied little ranging from 0.76 to 0.85 PVU.

Isentropic back trajectories computed at the same location on the 308K and 311K surfaces produced similar results. Both the meteorological and trajectory analyses suggest that the simple mechanism of subsidence along the parcel's path was responsible for the ozone enhancement.

The Mission 11 ozone profile (Figure 3.76a) shows a region of enhanced ozone between 3.2 and 4.6 km with an apparent excess of 10 ppbv at 4.2 km. A second region of ozone enhancement (Figure 3.76b) existed between 7.5 and 8 km with an apparent excess of 20 ppbv at 7.6 km. Meteorological conditions favored sinking air near these areas of enhanced ozone. The 500 mb chart for 20/00Z (Figure 3.77) indicates that northern Alaska was dominated by the eastern edge of an area of high pressure. This situation is usually indicative of sinking air. This influence of the high pressure also showed up on the Barrow, AK (station 70026) 20/00Z sounding. This sounding (Figure 3.78) indicates that multiple subsidence layers resided above 3 km and included the altitudes of the ozone-enhanced regions. Cross-sections over the ozone-enhanced region, from 71N, 170W to 71N, 150W, marginally support conditions conducive to the sinking of air. The cross-sections of potential and absolute vorticity (Figure 3.79a) indicate little change in either potential and absolute vorticity values at a given altitude. The relative humidity and wind cross-section (Figure 3.79b) indicates that a dry slot, with relative humidity of 45 percent, existed at 3.2 km and extended to 6.5 km 35 percent over the point 70.9N, 158W. These low values of relative humidity are also found in the Barrow

(station 70026) station time-series plot from 19/00Z to 20/12Z (Figure 3.80),which also indicates relatively dry air at both altitudes. In this cross-section, relative humidity values were near 0 percent at 6.2 km. The isentropic back trajectory analysis (Figure 3.81) indicated a gradual sinking of air. A parcel (Figure 3.81a) at point 70.9N, 158W on the 306K potential temperature surface (4.2 km) followed a 50 mb (~0.7 km) descending path of during the previous 72 hours. Another parcel (Figure 3.81b) at point 70.9N, 158W on the 316K surface (7.6 km) followed a 52 mb (~0.8 km) descending path of during the previous 72 hours. Potential vorticity along both these paths varied little during the 72 hour travel period. The meteorological and trajectory analysis carried out here suggest that simple descending atmospheric motion may be responsible for the apparent displacement of this ozone feature.

The Mission 20 ozone profile (Figure 3.82) exhibited a region of enhanced ozone from 10.2-10.8 km with a ozone value enhanced by 16 ppbv at 10.8 km and by 12 ppbv at 7.6 km. Meteorological conditions favored a sinking air motion near the area of enhanced ozone. The 500 mb chart for 03/12Z (Figure 3.83) depicts high pressure influencing southwest Alaska near Bethel, AK. The high pressure's influence is also evident on the meteorological cross-sections from 62N, 170W to 62N, 150W. Cross-sections of potential and absolute vorticity (Figure 3.84a) depict decreasing values of absolute vorticity from east (right) to west (left) and enhanced values of potential vorticity to the west. These tendencies signify an area conducive to a sinking air motion. Relative humidity and winds cross-sections over this same

area (Figure 3.84b) also indicate a dry slot was over the point 62N, 161W between 6.8 km to 8.2 km (relative humidity was less than 20 percent). This dry slot also appears on the nearby Bethel, AK (station 70029) at 60.8N, 161.8W meteorological sounding located. A comparison of the Bethel soundings at 03/12Z (Figure 3.85a) and 04/00Z (Figure 3.85b), indicates a region of subsidence above 2 km. this feature is more pronounced in the 04/00Z sounding. A station time series for Bethel (Figure 3.86), from 02/12Z to 04/12Z, also depicts a dry slot above 480 mb (6 km). The isentropic back trajectory analysis(Figure 3.87a) also indicates a sinking of the air around the areas of enhanced ozone. The air parcel located at the point 62N, 167W on the 318K potential temperature surface (6 km) followed a 25 mb (~0.5 km) descending path during the previous 36 hours. The potential vorticity decreased along the descending path going from 1.67 PVU to 0.83 PVU. This trend and magnitude indicates that stratospheric air may have been encountered. These analyses indicate that a tropopause fold has possibly been identified here. Extensions of the isentropic back trajectory to 96 hours indicates that the parcel followed a 133 mb descending path during the 66-84 hour period prior to the point. This is also supported by a cross-section near the parcel's location at 67.7N, 148E, which indicates a dry slot developing at the altitude just to the west of the parcel's location. An isentropic back trajectory (Figure 3.87b) for the region of enhanced ozone located at point 61N, 162W at 10.8 km (329K) indicates the parcel followed a path with little vertical movement during the previous 72 hours. However, potential vorticity along

the path ranged from 1.8 PVU at the initial point to 8.54 PVU 48 hours back. These analyses indicate that the region of enhanced ozone was associated with high enough potential vorticity values to indicate a vigorous stratospheric-tropospheric air exchange.

The Mission 22 ozone profile (Figure 3.88) indicates a region of enhanced ozone between 6.8 to 8.6 km having an excess ozone of 31 ppbv at 7.4 km. Meteorological conditions favored a descending air motion near the region. The 500 mb chart (Figure 3.89) for 8/00Z indicates that the area of southwest Alaska was under the influence of a high pressure ridge in association with a polar vortex that was off to the east. The effects of the high pressure ridge and the polar vortex can be seen in the cross-sections (from 68.5N, 170.4N to 48.5N, 150.4N). The potential and absolute vorticity cross-sections (Figure 3.90a) depict a sharp high pressure ridge to the west of the points of interest (58.5N, 160.4W) with enhanced values of potential vorticity and depressed values of absolute vorticity. These features are suggestive of a favorable area for descending air. Relative humidity and wind's cross-sections (Figure 3.90b) depict a dry slot with relative humidity near 30 percent near the region of enhanced ozone (6.8 to 8.6 km) at 58.5N, 160.4W. A nearby Cold Bay, AK sounding station 70316, located 55.3N, 162.7W Figure 3.91 for 08/00Z depicts a dry slot from 5 to 7.4 km. This dry slot is more easily seen in the station time series of Cold Bay (Figure 3.92). This time series depicts a dry air slot from 550-420 mb (5-7 km) at 08/00Z that further develops down to near 800 mb by 08/12Z. The

isentropic back trajectory for this parcel (Figure 3.93) also indicates a gradual sinking of the air of 50 mb over the previous 12 hours. The air parcel located at 58.5N, 160.4W on the 320K potential temperature surface (7.4 km) followed a slight 26 mb (0.4 km) ascending path during the previous 72 hours. Potential vorticity values along this path ranged from 0.99 to 1.28 PVU. The meteorological analysis supports the descending atmospheric motion needed for the displacement of this ozone feature. The trajectory analysis is less clear and suggests descending motion only during the previous 12 hours, but an overall slight ascending motion over the 72 hour period. This may be due to the spatial grid not properly representing the feature.

Summary of case studies. During ABLE 3A, a variety phenomologically different of ozone enhancements were encountered. Table 3.4 summarizes this investigation of these enhancements. This summary includes the significant identifiers for each case found in the analyses in each section. Each column header is defined at the bottom of Table 3.4. Summary information includes each mission investigated, the altitudes that each ozone enhancement was encountered, the ozone value, plus several summary identifiers indicating the analysis' conclusions about the origin of each ozone enhancement. These identifiers describe the following conclusions: (1) Whether the meteorological analyses agree with the simple transport based on expected vertical movement; (2) Whether the isentropic back trajectory analysis also agrees with the expected vertical movement; (3) Whether the parcel's

ozone enhancement appears to be of stratospheric origin; (4) Whether the parcel's origin appears to be from an expected higher altitude; (5) The highest value of potential vorticity found; and (6) Which physical mechanism was most likely responsible for the feature found. The summary Table also includes an estimate of spatial size and scale of the enhancements based on the observations. Since the grid scale of the meteorological data used is 2.5 degrees, values of potential vorticity and other parameters may not be representative of sub-grid ozone enhancements. A total of five major ozone enhancements were found; two in Missions 8, 19, and the other three in Mission 3. Mission 8 represents the best documented case of a tropopause fold. A nearly perfect set of conditions for stratospheric-tropospheric exchange existed. In this case, a wave interacted with a polar vortex and increased the depth of the ozone with the tropopause sinking to near 4.5 km. This wave then moved out of the polar vortex and transported enriched values of ozone long distances, from central Russia to near Barrow, AK.. Another example of a fold was found in Mission 3. Though the parcel-time series and the trajectories provided solid support for this fold's occurrence, the path of the parcels of interest went over the data-sparse area above the Arctic circle. Thus this case study could not be completely developed. The major ozone enhancement in Mission 19 did not indicate evidence for a recent stratospheric origin. The trajectory for the parcel even indicates a slow ascent of air, and the meteorological analysis indicated that a weakened polar vortex was moving away. No real evidence for strong vertical transport was present. The region of

enhanced ozone was quite small and may represent an intact subgrid filament of air that originated either outside of or on much smaller scales of this analysis.

A total of 15 minor ozone enhancements were also investigated. In 9 of the cases, the various analyses methods agreed on the possible origin of the parcel of interest. High pressure, or a gradual sinking of air was the primary mechanism identified for most of the minor enhancements. In these cases, potential vorticity usually varied little along the parcel's path, and values remained rather small-about 0.9 PVU. It is believed that all of these cases should eventually lead to a stratospheric origin for the ozone enhancement. Light winds and stagnant conditions can lead to the slow mixing and dissipation of an ozone enhancement over a period of weeks. However, two cases, both on Mission 20, yielded higher values of potential vorticity. The ozone enhancement identified at 10.8 km, had a corresponding potential vorticity of 8.54 PVU and was associated with the polar vortex. The other enhanced parcel was the result of a tropopause fold. The other ozone features investigated have been classified as ozone intrusions with little associated vertical motion. These features occurred in Missions 19, 4, and 30. All of these cases have helped to build an overall hypothesis on the structure of the atmosphere and the primary mechanisms responsible for the source of ozone in the Arctic summertime. These characteristics will be brought together in the next section.

Table 3.1 The 309K potential temperature isentropic back-trajectory indicating the pressure (mb), location (lat/lon), and potential vorticity values (PVU).

Date	Time(Z)	Pressure(mb)	Lat/Lon (deg)	PV(PVU)
Jul 14	00Z	490	67.2N/115.6E	1.06
Jul 14	06Z	493	67.5N/123.3E	
Jul 14	12Z	498	69.7N/138.0E	1.47
Jul 14	18Z	536	71.5N/155.7E	
Jul 15	00Z	542	71.9N/165.5E	1.01
Jul 15	06Z	558	72.3N/173.4E	
Jul 15	12Z	566	72.5N/172.9W	.84
Jul 15	18Z	548	72.8N/161.3W	
Jul 16	00Z	526	73.2N/150.0W	.84

Table 3.2 Parcel Time-Series Stations representing the isentropic back-trajectories of the 309K and 322K potential temperature levels.

ICAO	LOCATION	Lat/Lon	TIME	TROP HEIGHT
For 309K				
20891	Khatanga, RS	72.0N 102.5E	13/12Z	330/287mb
24125	Olenek-In-Yakut, RS	68.5N 112.4E	14/00Z	295mb
24266	Verhojansk, R	71.6N 128.85E	14/12Z	223/250mb
21965	Chetyrekhstolbo, RS	70.6N 162.4E	15/00Z	265mb
21982	Vrangelys Isl, RS	71.0N 178.5W	15/12Z	250mb
70026	Barrow, Ak	71.3N 156.8W	16/00Z	278mb
For 322K				
20292	CelKuskin, RS	77.7N 104.3E	13/12Z	401mb
20891	Khatanga, RS	72.0N 102.5E	14/00Z	383mb
21824	Tiksi, RS	71.6N 128.8E	14/12Z	376mb
21647	Salaurova	73.2N 143.5E	15/00Z	255/300mb
21982	Vrangelys Isl, RS	71.0N 178.5W	15/12Z	250mb
70026	Barrow, Ak	71.3N 156.8W	16/00Z	278mb

Table 3.3 Parcel-Time series stations for Mission 3 representing the isentropic back-trajectory at the 313K potential temperature level.

ICAO	LOCATION	LAT/LON	TIME	TROP HEIGHT
71924	Resolute, CN	74.7N 95.0W	6Jul88/00Z	300mb
71925	Cambridge Bay, CN	69.1N 105.1W	7Jul88/00Z	277mb
71926	Baker Lake, CN	64.3N 96W	7Jul88/12Z	N/A
		8Jul88/00Z	200mb	
71913	Churchill, CN	58.8N 94.1W	8Jul88/12Z	289mb

TABLE 3.4 Summary of ozone enhancements describing conclusions of the investigation. Each column header is explained below the table.

MAJOR OZONE ENHANCEMENTS

Mission	ALT (km)	Ozone Value (ppbv)	Met Anal.	Traj.	Strat. Orgin	High PVU	Phy. Mech	Ozone Spatial Size (deg)	Ozone Spatial Scale
8	4.5	255	YES	YES	YES	1.47	FOLD	.6	subgrid
19	4.0	180	NO	NO	UNK	1.03	UNK	.4	subgrid
3	5.3	170	YES	YES	YES	1.32	FOLD	.4	subgrid
3	5.3	150	YES	YES	YES	2.03	FOLD	1.6	subgrid
3	5.3	168	YES	YES	YES	2.19	FOLD	.6	subgrid

MINOR OZONE ENHANCEMENTS

Mission	ALT (km)	Ozone Value (ppbv)	Met Anal.	Traj.	HI/LO Orgin	High PVU	Likely Phy. Mech	Ozone Spatial Size (deg)	Ozone Spatial Scale
6	.5	70(+40)	YES	Weak	Weak HI	.60	UNK	<.1	subgrid
7	8.0	30(-70)	YES	NO	NO	.83	UNK	4.1	grid
13	2.0	60(+18)	YES	YES	HI	.78	HIGH PRESS	3.0	grid
13	2.5	70(+25)	YES	YES	HI	.74	HIGH PRESS	3.0	grid
15	3.0	70(+17)	YES	NO	NO	1.03	UNK	3.4	grid
15	4.0	40(-21)	YES	NO	NO	.91	UNK	1.8	subgrid
18	4.8	100(+32)	YES	YES	HIGH	.91	HIGH PRESS	2.5	grid
21	2.5	70(+25)	YES	YES	HIGH	.91	HIGH PRESS	.9	subgrid
33	3.0	70(+17)	YES	YES	HIGH	.86	WAVE	6.0	grid
10	5.0	(+18)	YES	YES	HIGH	.85	HIGH PRESS	3.5	grid
11	3.9	(+10)	YES	YES	HIGH	.89	HIGH PRESS	4.3	grid
11	7.6	(+20)	YES	YES	HIGH	.82	HIGH PRESS	4.3	grid
20	10.8	(+16)	YES	YES	HIGH	8.54	POLAR VORTEX	2.0	near-grid
20	7.6	(+12)	YES	YES	HIGH	1.67	FOLD	2.0	near-grid
22	7.4	(+31)	YES	NO	NO	1.28	UNK	1.0	subgrid

ALT ---------- altitude of enhancement
Ozone Value -- measured or delta amount in parenthesis
Met. Anal ---- Does analysis agree with expected vertical movement (higher values expected to descend where lower value to ascend)?
Traj.--------- Does the isentropic back-trajectory agree with expected vertical movement
Strat. Orgin-- Is parcel of stratospheric origin
HI/LO Orgin--- HI - origin of higher altitude as expected, NO - does not agree with expected vertical movement
High PVU------ The highest value of potential vorticity
Phy. Mech----- Which physical mechanism is likely
Spatial Size-- Size of ozone enhancement region in degrees
Spatial Scale- Scale of ozone enhancment based on grid scale of 2.5 degrees. Subgrid is < 2.0 degrees, grid is > 2.5 degrees and near-grid is 2.0 - 2.5 degrees.

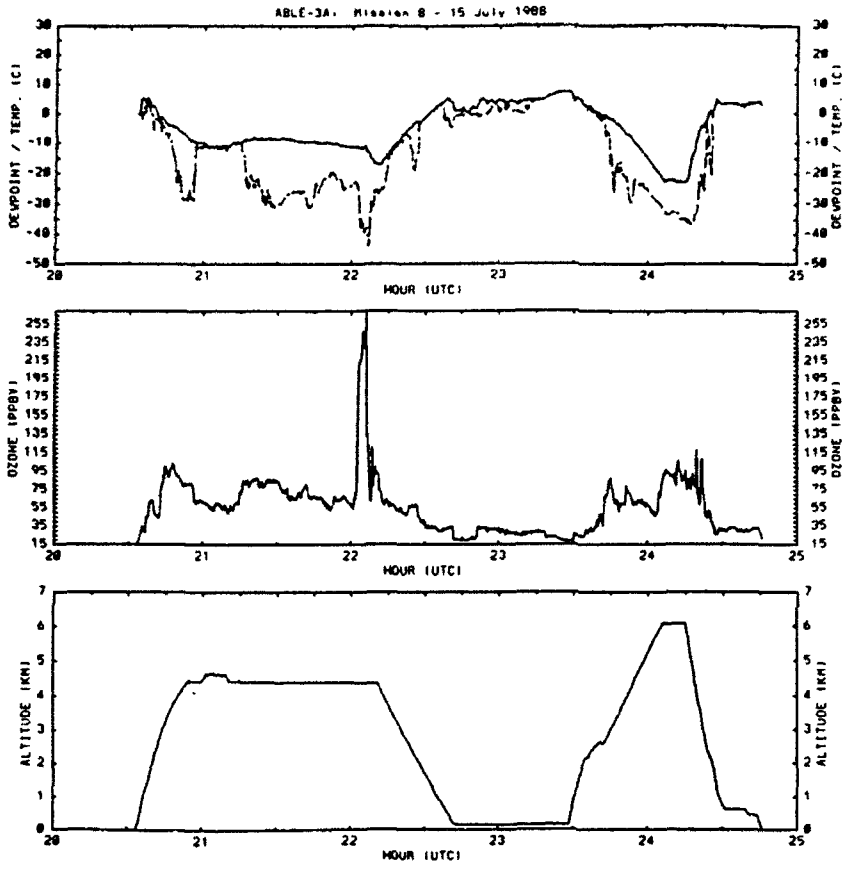

Figure 3.1 ABLE 3A Mission 8 inflight measurements of (a) temperature, (b) dewpoint, (c) ozone and (d) altitude.

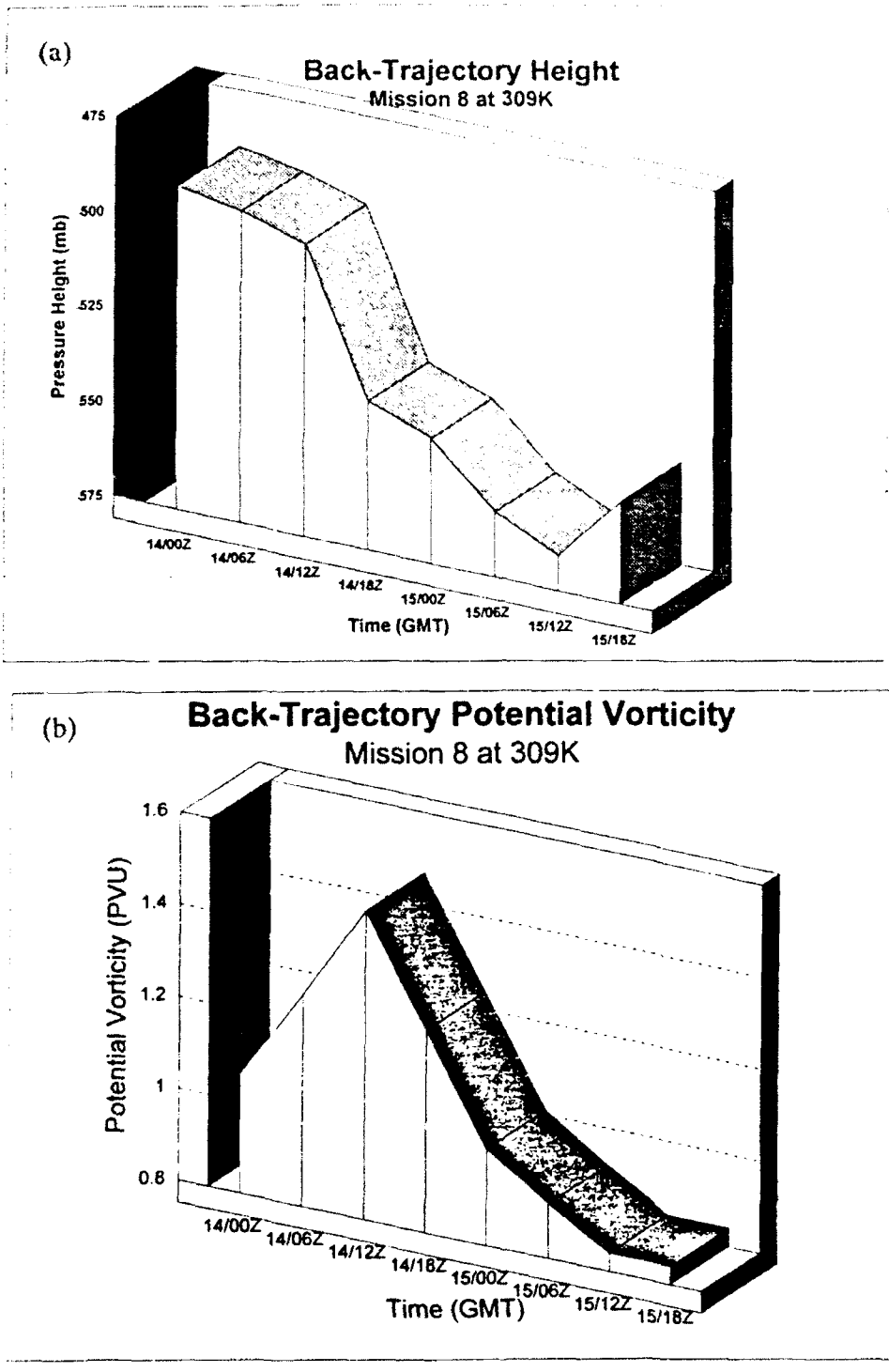

Figure 3.2 Isentropic back-trajectory (a) pressure heights and (b) potential vorticity for Mission 8 at the 309K potential temperature level.

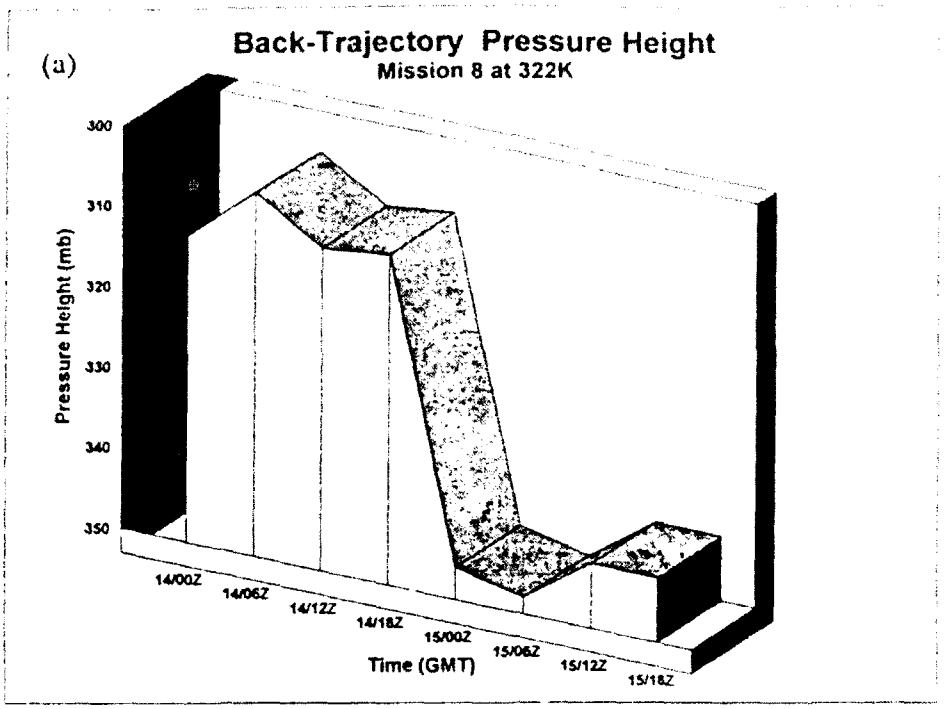

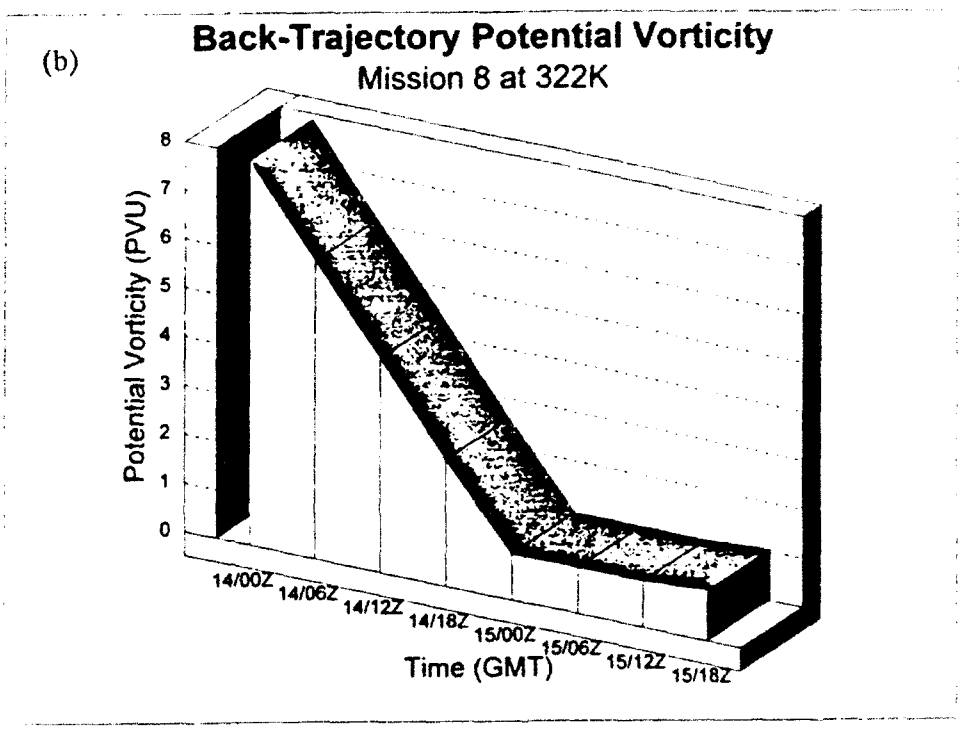

Figure 3.3 Isentropic back-trajectory (a) pressure heights and (b) potential vorticity for Mission 8 at the 322K potential temperature level.

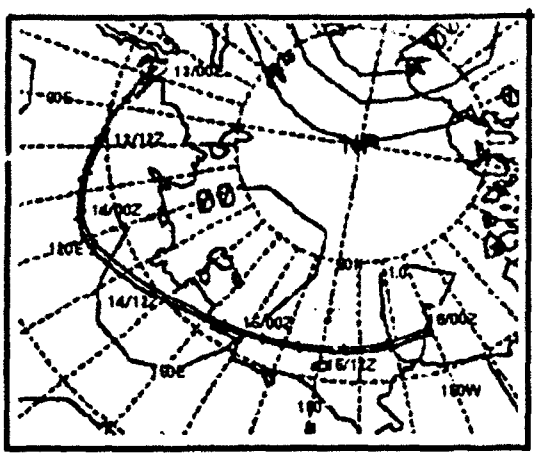

a 15/12Z

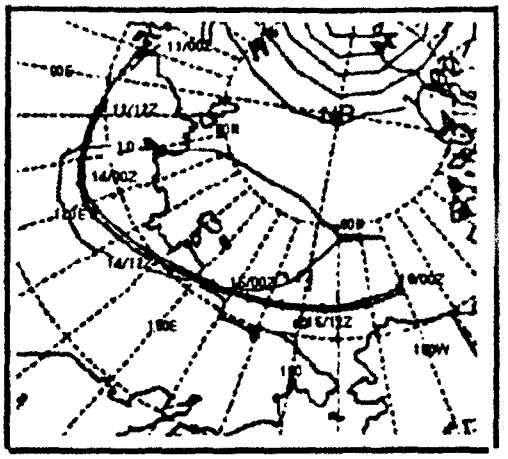

b 15/00Z

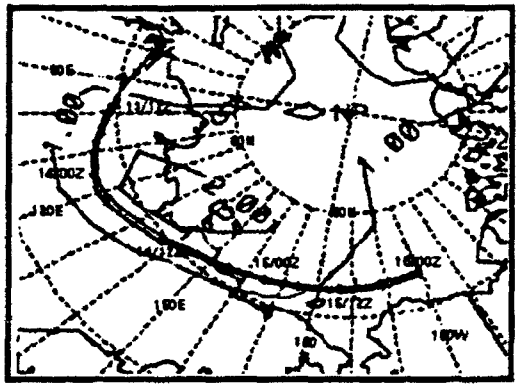

c 14/12Z

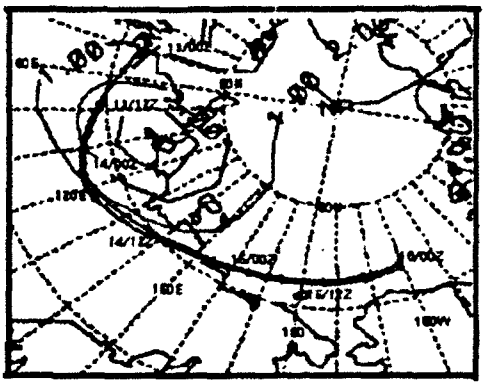

d 14/00Z

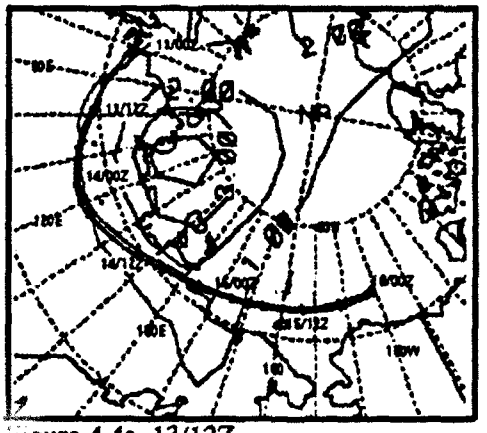

Figure 4.4e 13/12Z

Figure 3.4 Potential vorticity plots (solid lines) in PVU units, and the back trajectory path (thick line) at the 309K potential temperature level at times: (a) -12 hr (15/12Z), (b) -24 hr (15/00Z), (c) -36 hr (14/12Z), (d) -48 hr (14/00Z), and (e) -48 hr.

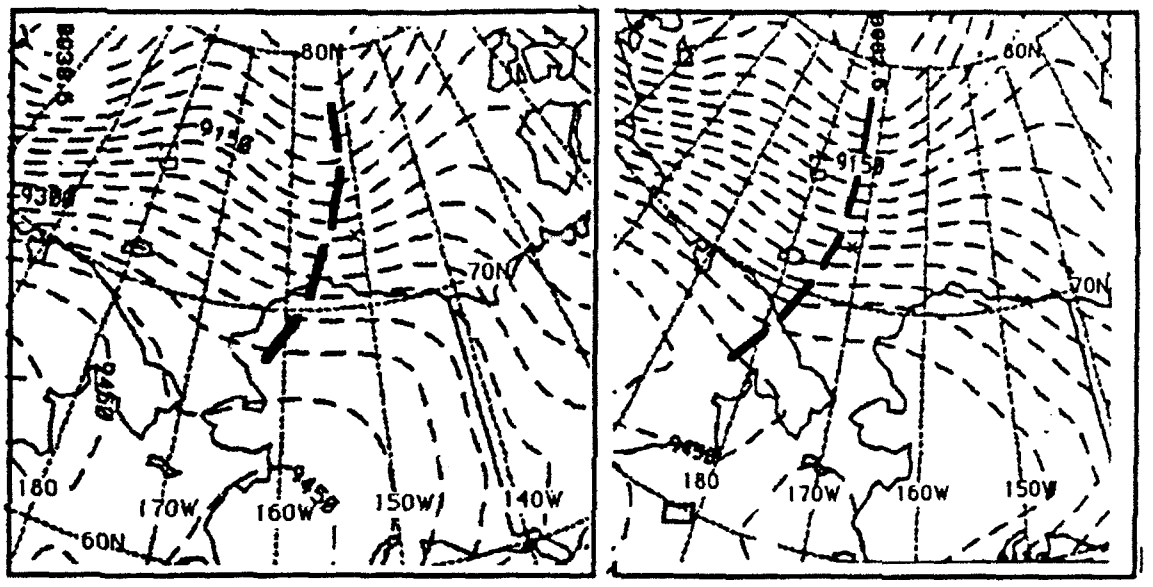

a 300mb at 16/00Z

b 300mb at 15/12Z

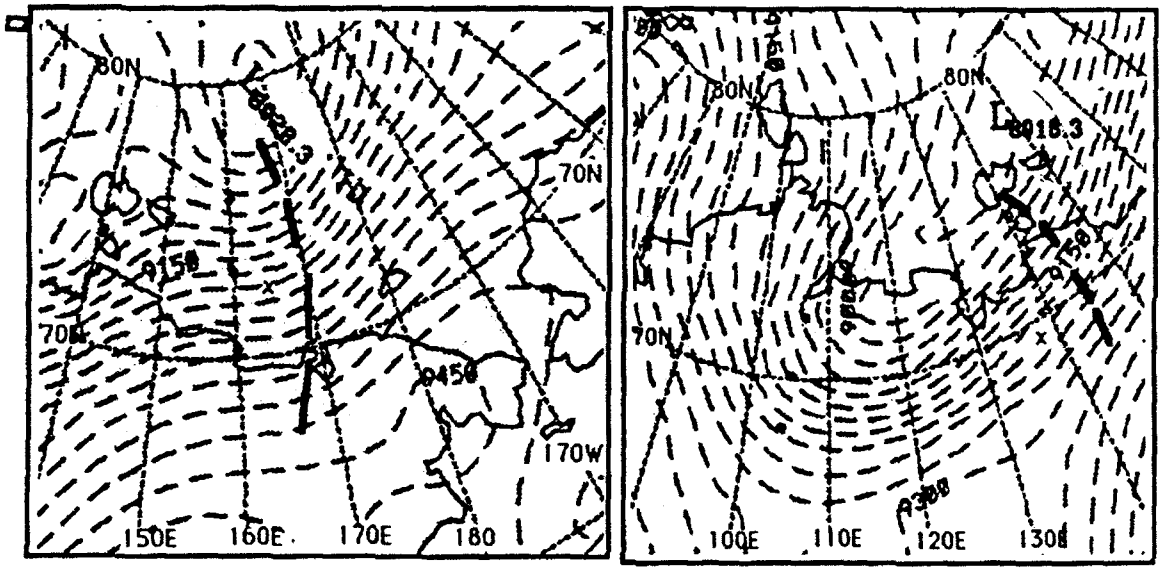

c 300mb at 15/00Z

d 300mb at 14/12Z

Figure 3.5 300mb pressure heights in m (dashed) showing wave of interest (thick dashed line) during July 1988 at times: (a) 16/00Z, (b) 15/12Z, (c) 15/00Z, (d) 14/12Z, (e) 14/00Z, (f) 13/12Z, and (g) 13/00Z.

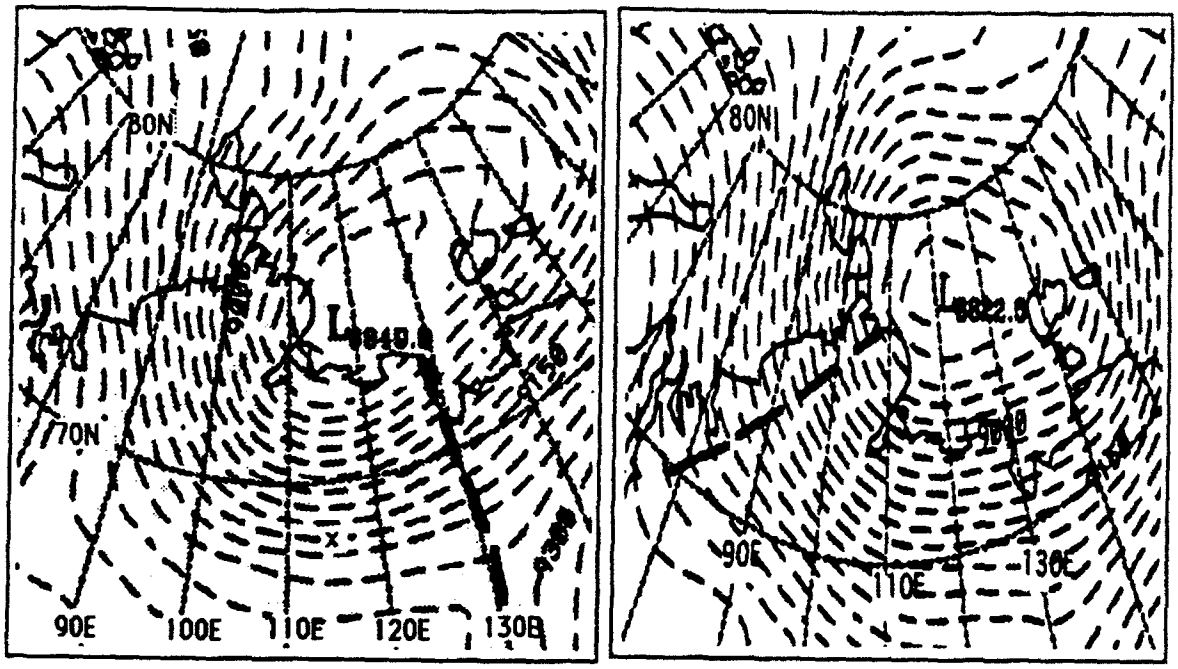

e. 300mb at 14/00Z

f. 300mb at 13/12Z

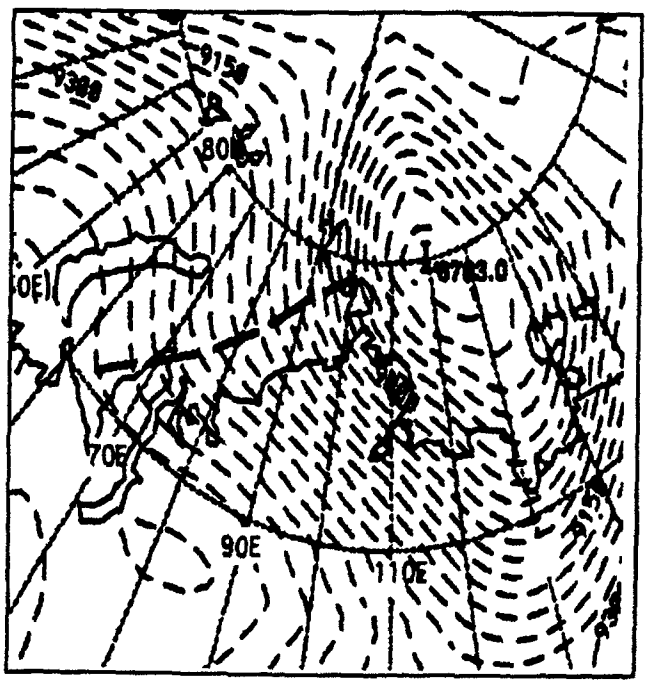

g. 300mb at 13/00Z

Figure 3.5 300mb pressure heights in m (dashed) showing wave of interest (thick dashed line) during July 1988 at times: (a) 16/00Z, (b) 15/12Z, (c) 15/00Z, (d) 14/12Z, (e) 14/00Z, (f) 13/12Z, and (g) 13/00Z.

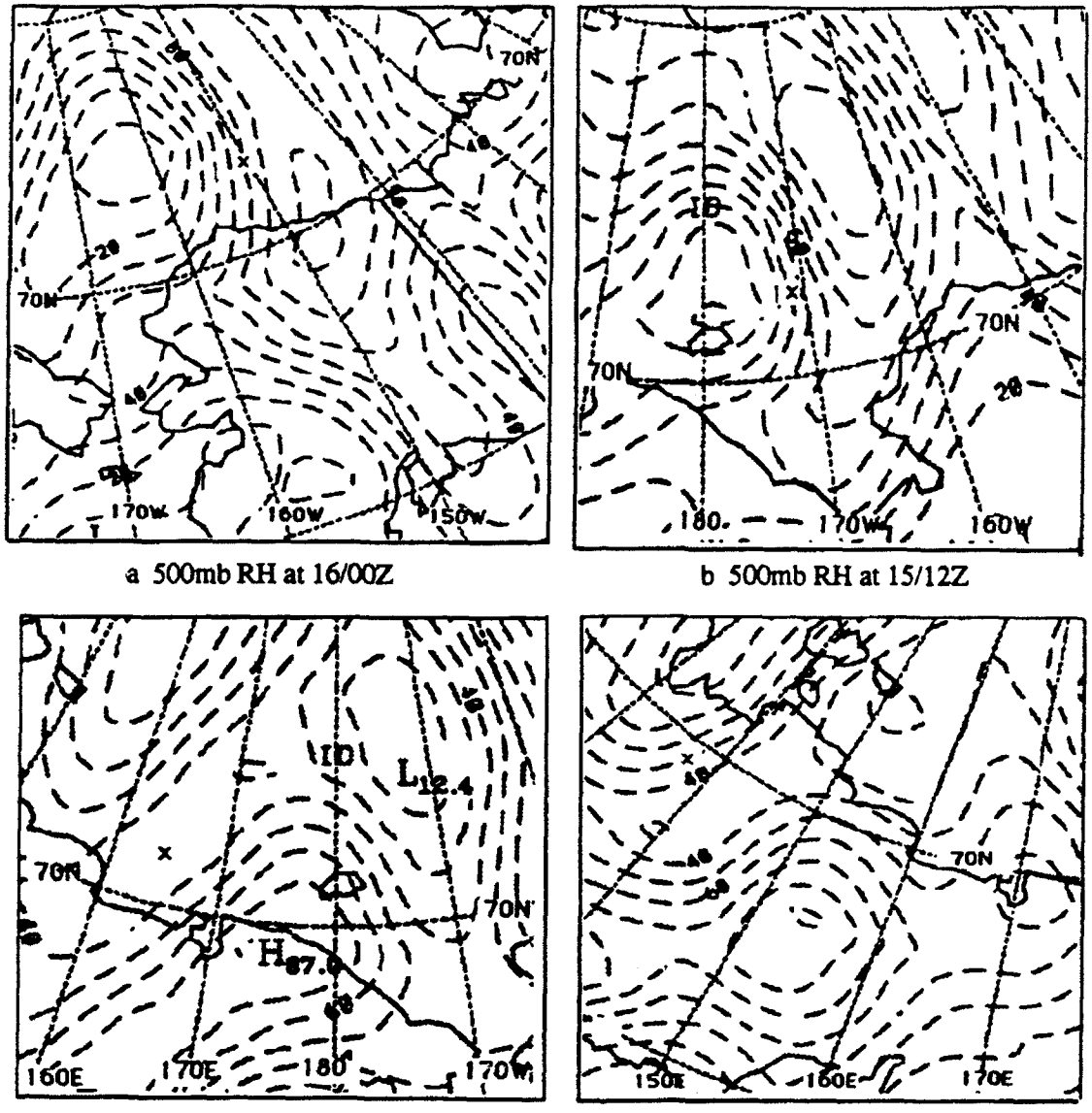

a 500mb RH at 16/00Z

b 500mb RH at 15/12Z

c 500mb RH at 15/00Z

d 500mb RH at 14/12Z

Figure 3.6 500mb relative humidity in percent (dashed) during July 1988 for times: (a) 16/00Z, (b) 15/12Z, (c) 15/00Z, (d) 14/12Z, and (e) 14/00Z.

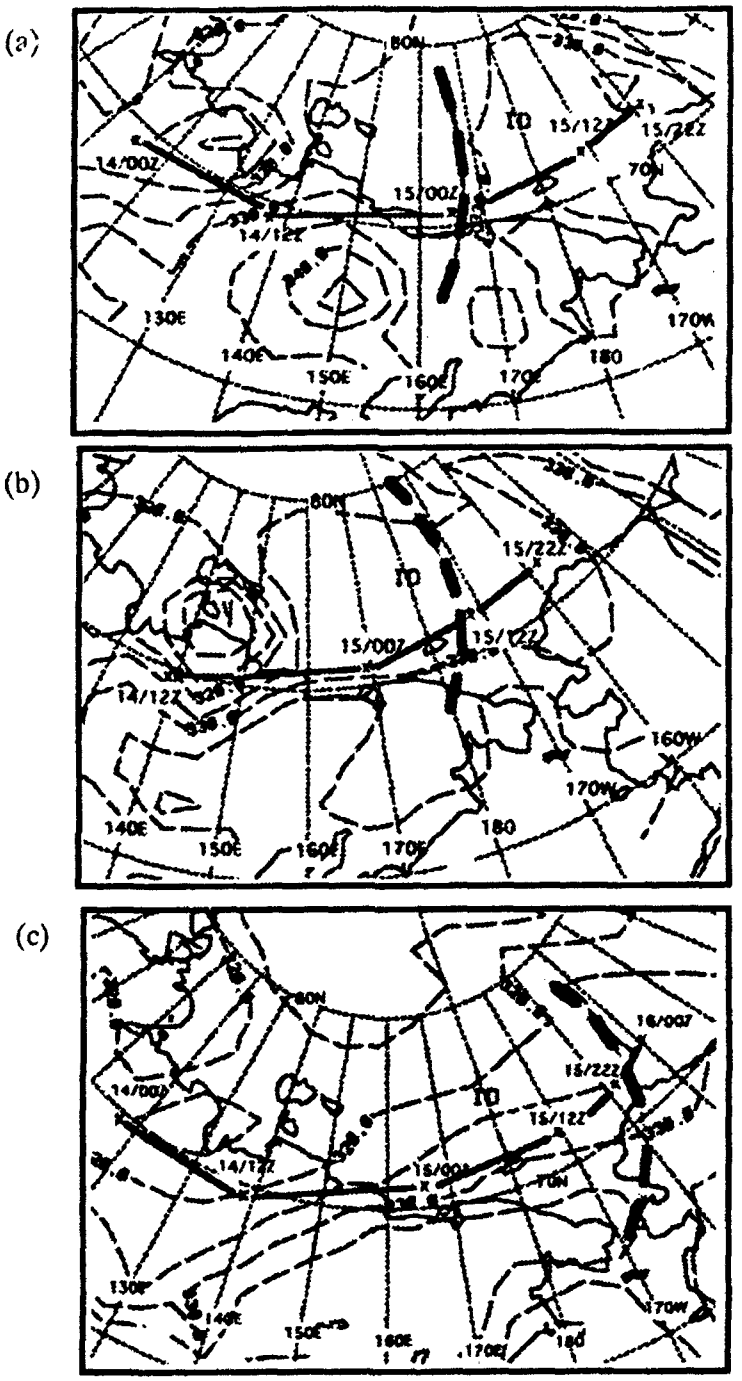

Figure 3.7 Tropopause heights in K (potential temperature level) and wave location (dashed line) in July 1988 for times (a) 15/00Z, (b) 15/12Z, and (c) 16/00Z.

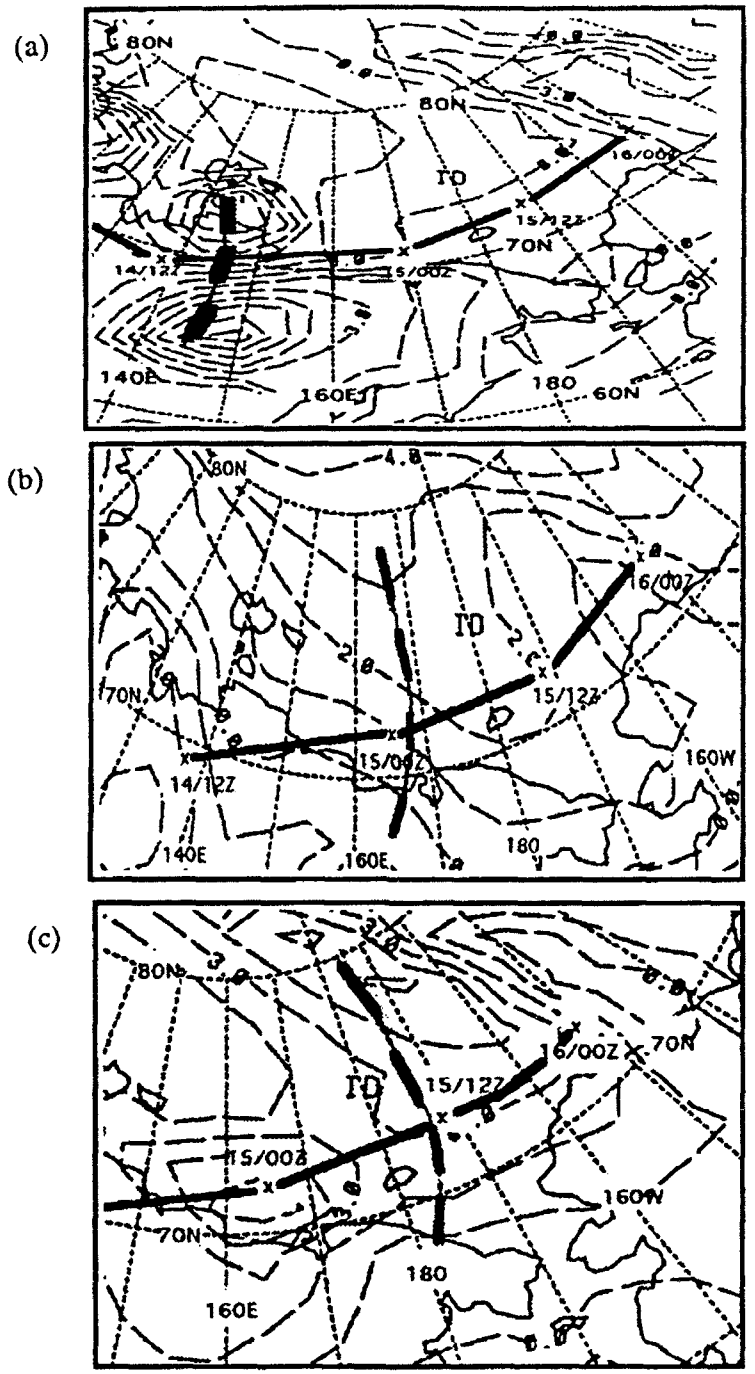

Figure 3.8 Tropopause vertical velocity (dashed) in mb/hr for times (a) 14/12Z, (b) 15/00Z, and (c) 15/12Z. The 309K back trajectory path (times indicated on path) is noted by a thick, solid line and wave position by a dashed line.

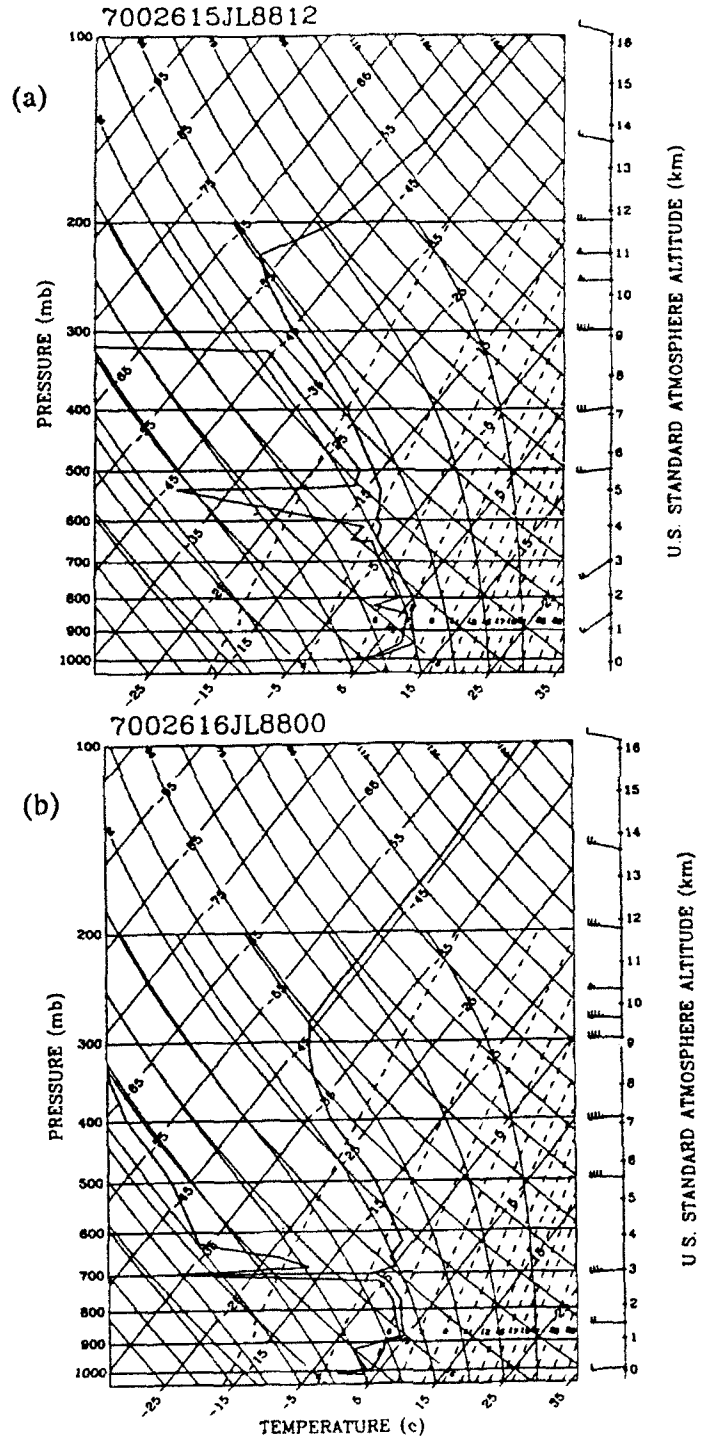

Figure 3.9 Point Barrow (70026) Skew-t LogP plot of temperature and dewpoint (solid lines) and wind in July 1988 for times (a) 15/12Z and (b) 16/00Z.

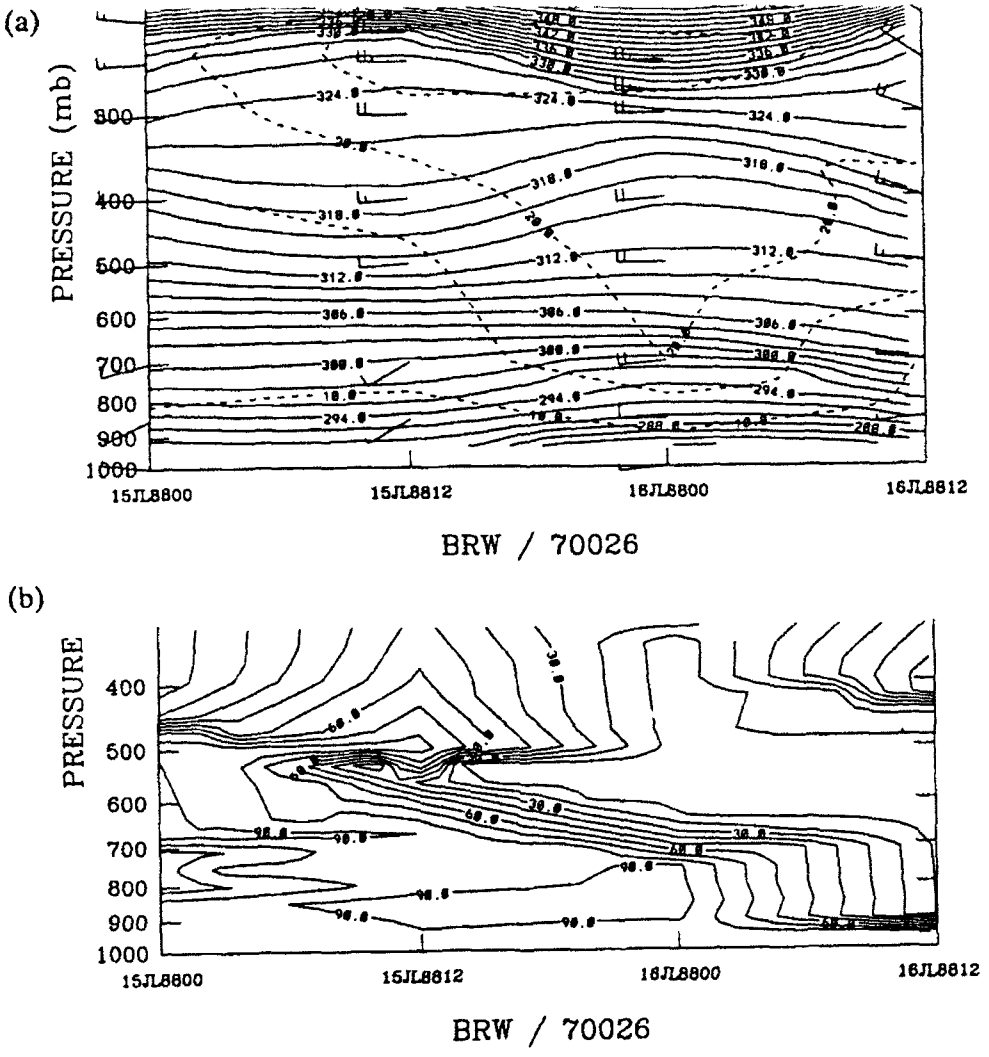

Figure 3.10 Station time-series plot of Barrow, AK (station 70026) for (a) potential temperature (solid), windspeed (dashed), and windbarbs and (b) relative humidity (dashed). Times are DD/MM/YY/HH for day/month/year/hour.

(a)

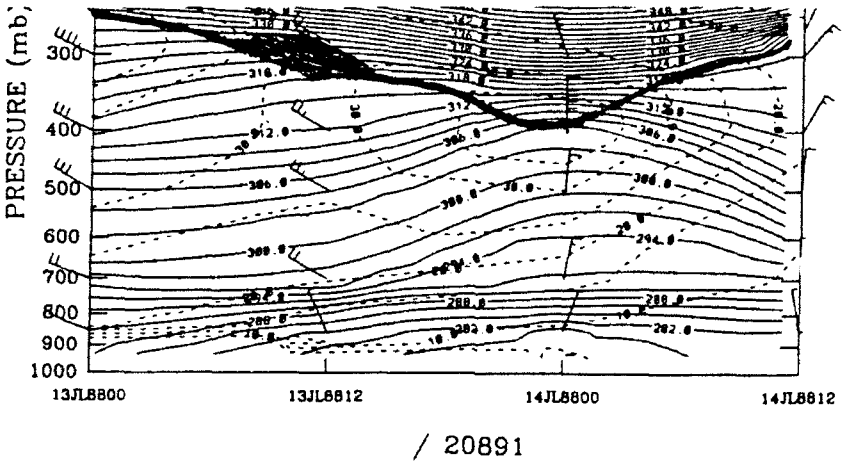

(b)

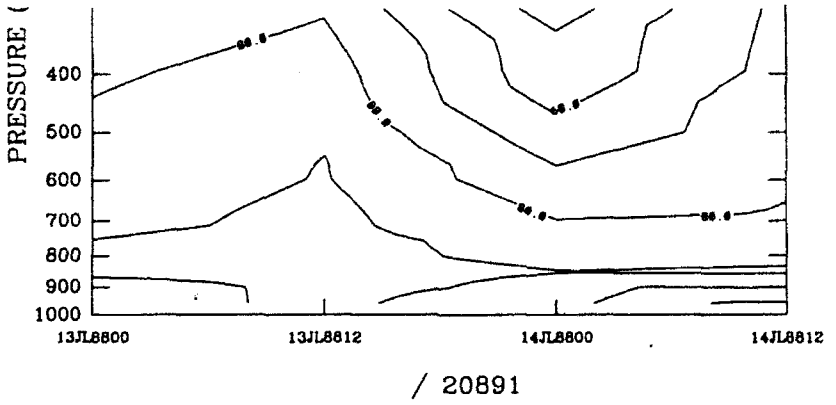

Figure 3.11 Station time-series plot of station 20891 (a) potential temperature in K (solid line), windspeed in m/s (dashed), and winbarbs and (b) relative humidity (dashed). Tropopause height noted by thick line.

(a)

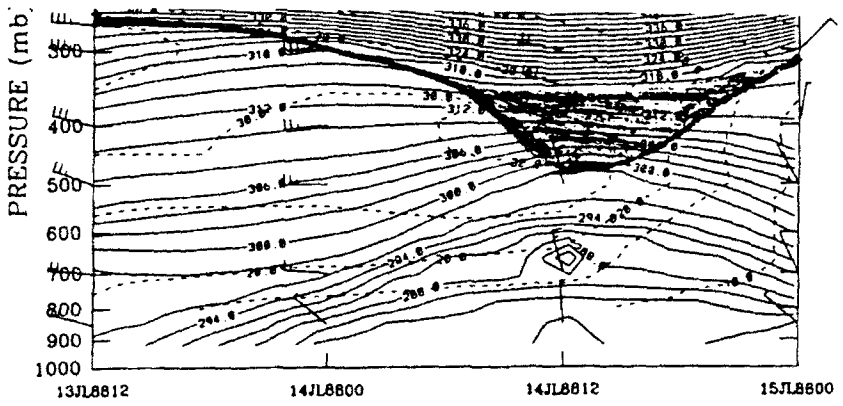

/ 24125

(b)

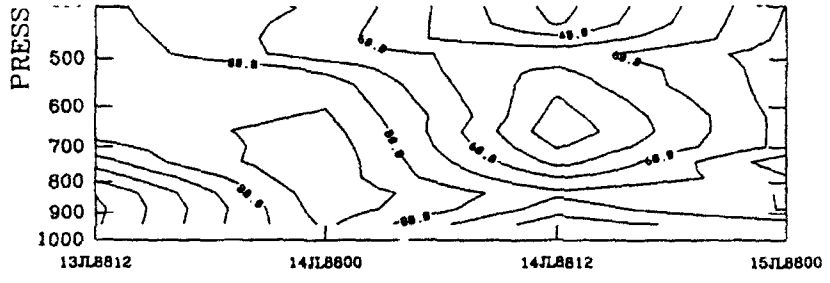

/ 24125

Figure 3.12 Station time-series plot of station 24125 (a) potential temperature in K (solid line), windspeed in m/s (dashed), and windbarbs and (b) relative humidity (dashed). Tropopause height noted by thick line.

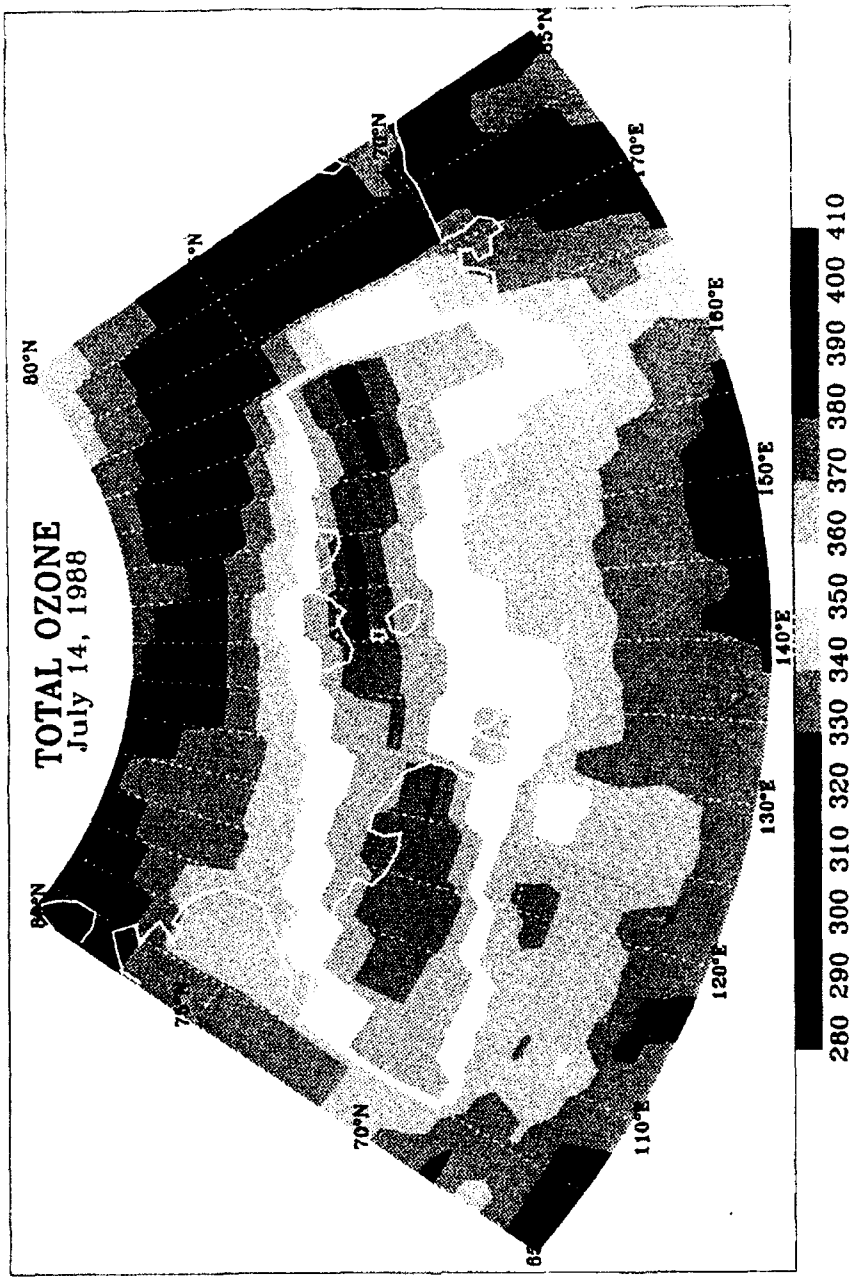

Figure 3.13a TOMS total ozone (DU). Maximum values appear over northern Russia due a west-east jet. TOMs here compares with meteorological data taken at 14/00Z.

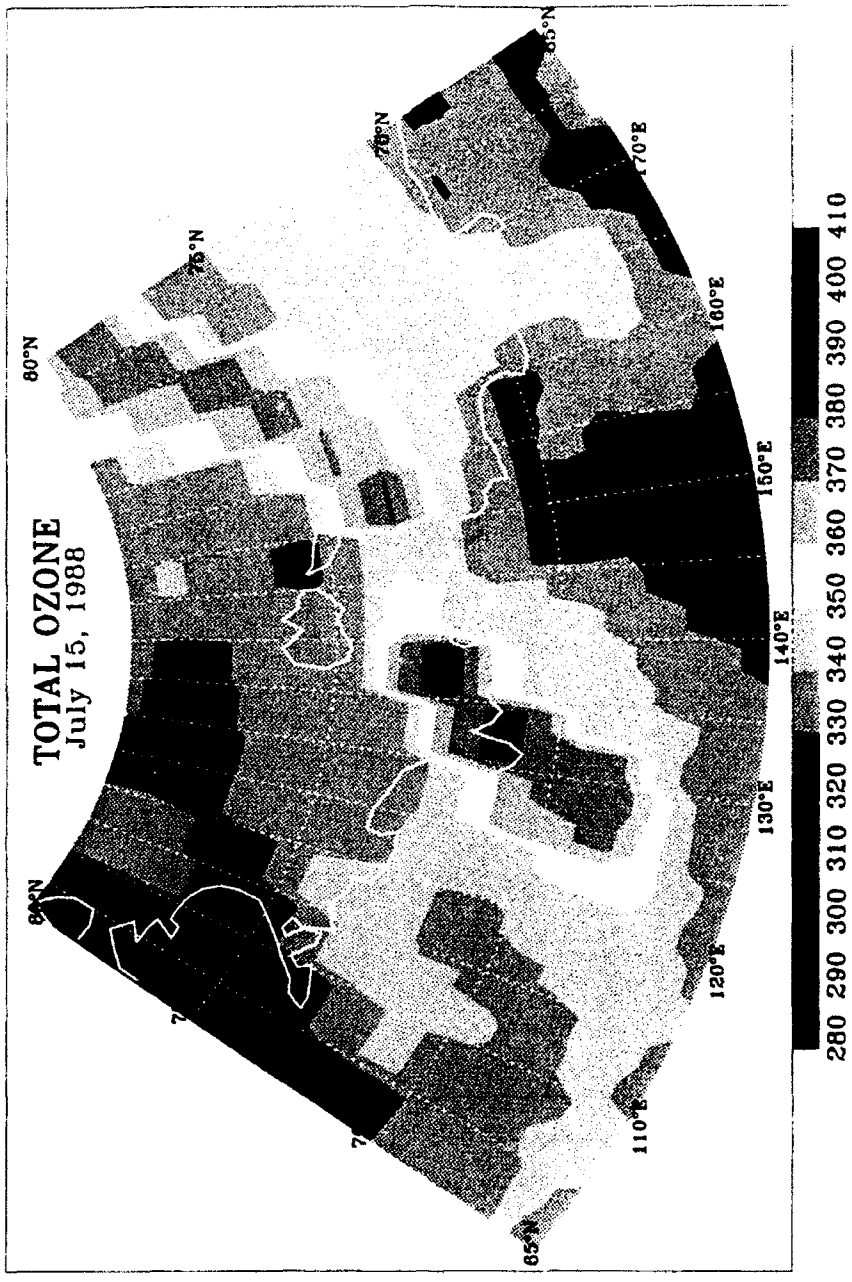

Figure 3.13b TOMS total ozone in DU. Maximum band at 165E corresponds with wave of interest in Mission 8. TOMs here compares with meteorological data at 15/00Z.

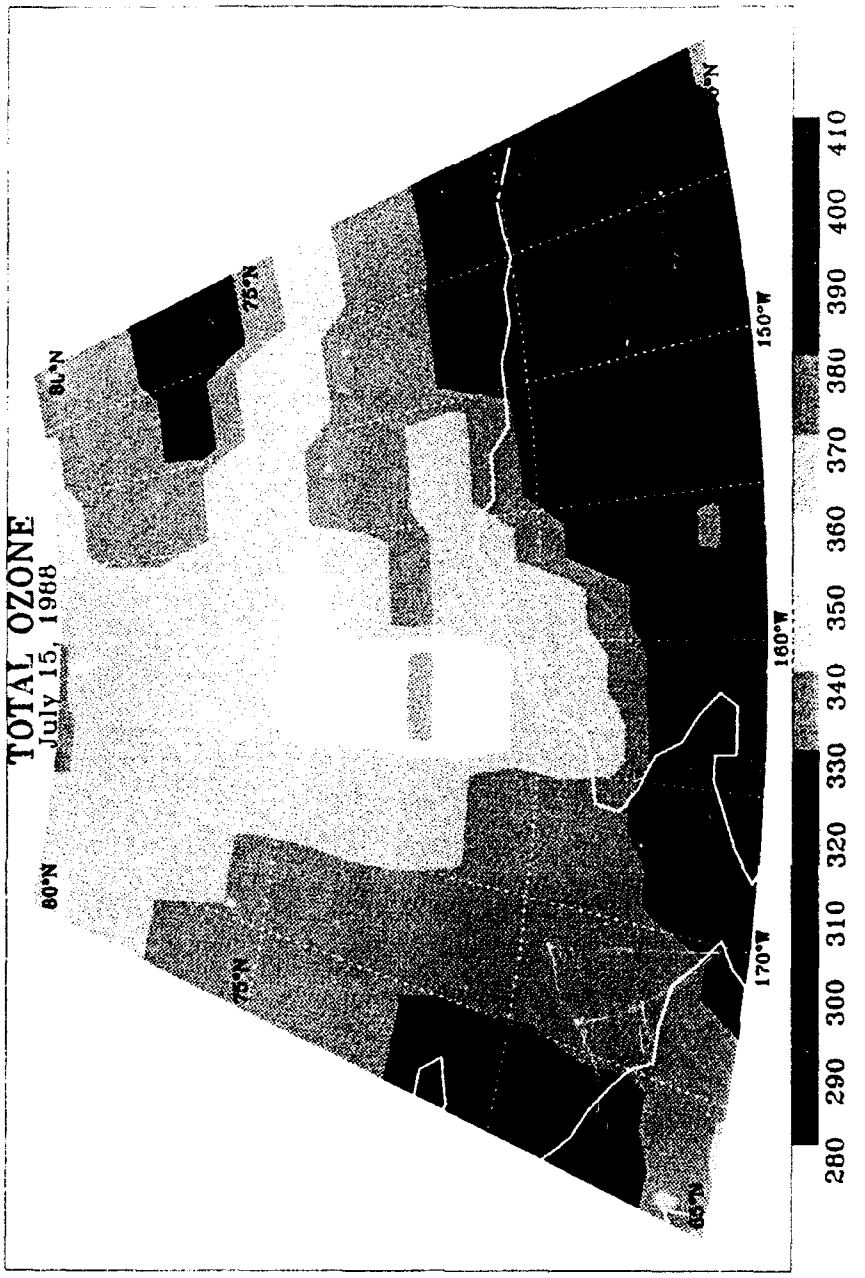

Figure 3.13c TOMS total ozone in DU. Maximum values appear ove: northern Alaska due the wave in interest. TOMs here compares with meteorological data at 16/00Z.

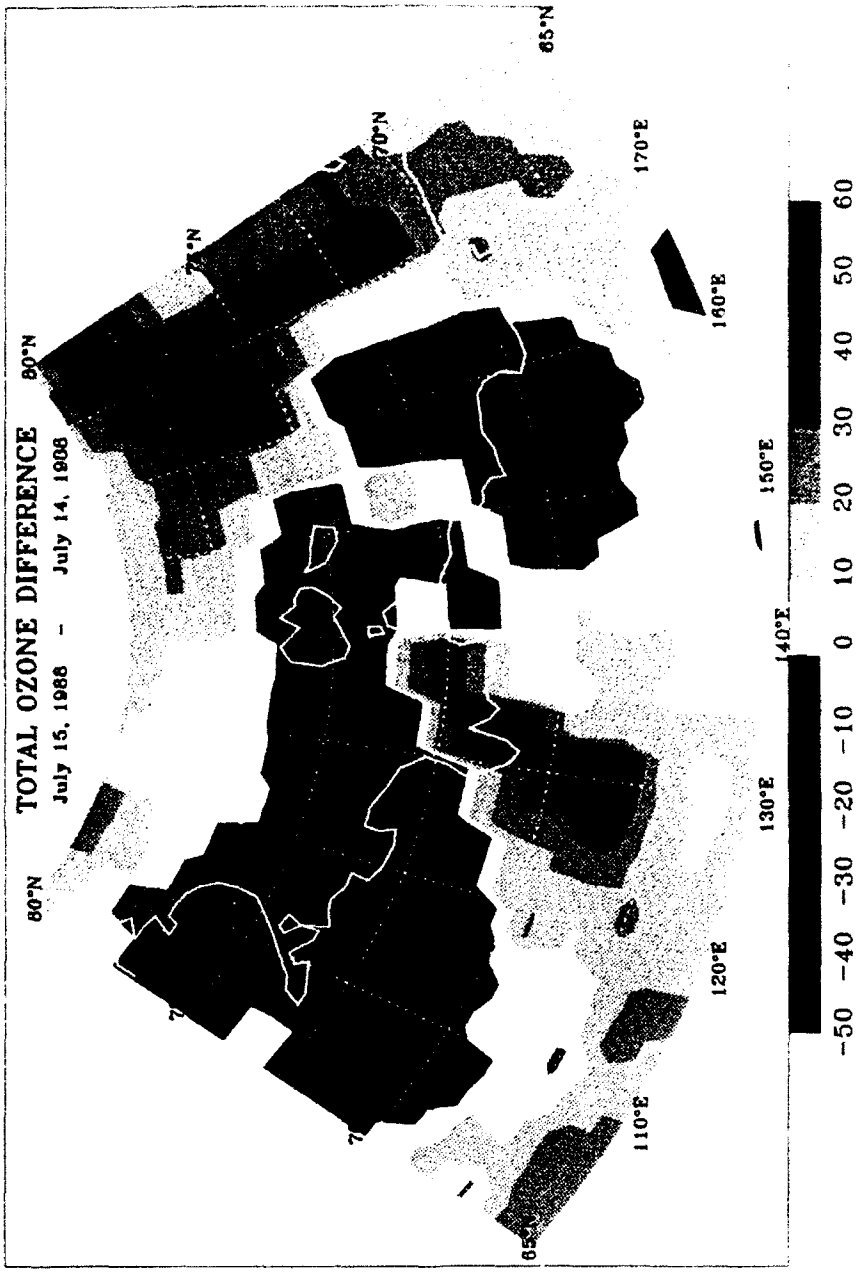

Figure 3.14a TOMS Ozone Difference in DU. Timeperiod compares with meteorological data at 14/00Z and 13/00Z. An increase in ozone near 110E and extending NE corresponds with the increase in intensity of jet and upper low.

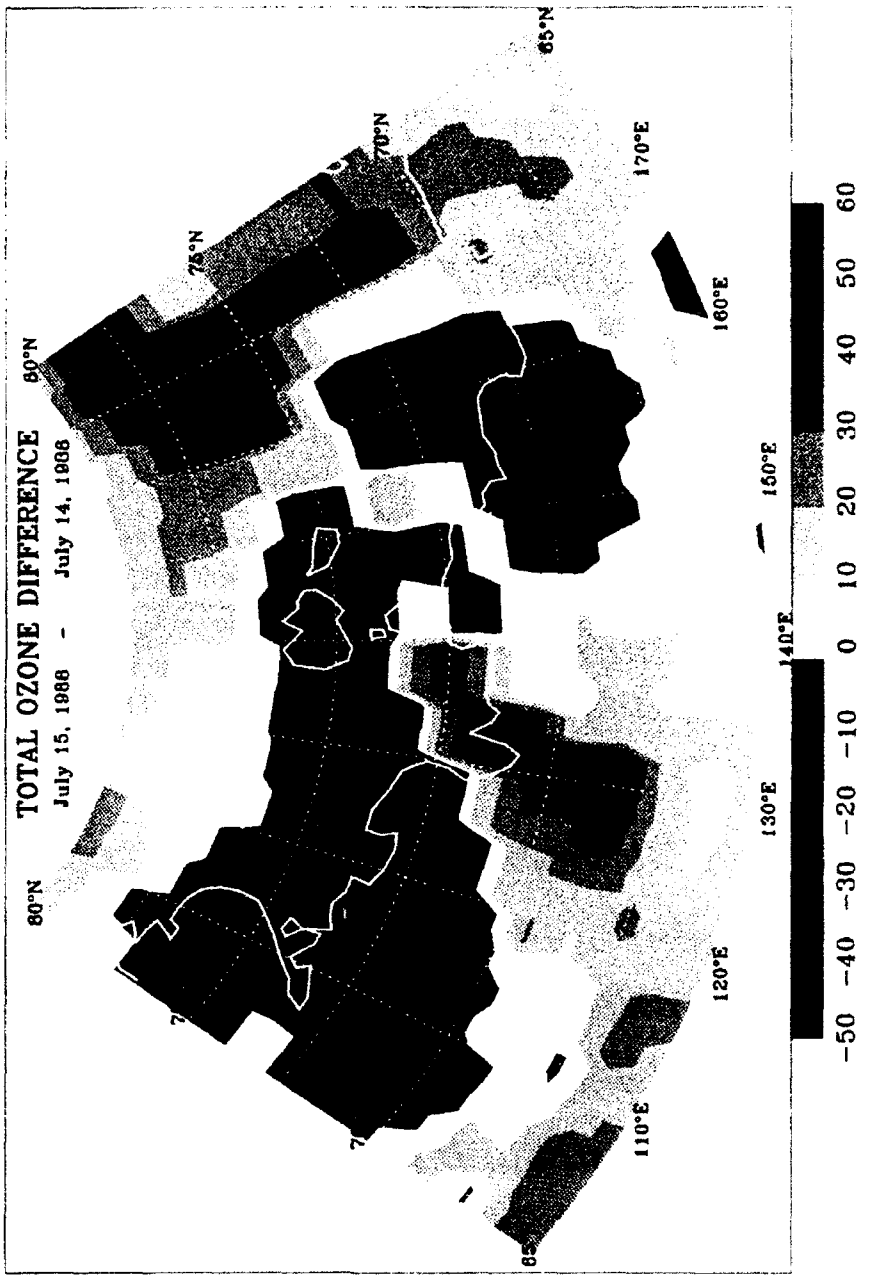

Figure 3.14b TOMS Ozone Difference in DU. Timeperiod compares with meteorological data of 15/00 and 14/00Z. An increase in ozone near 130E corresponds with the wave of interest in Mission 8.

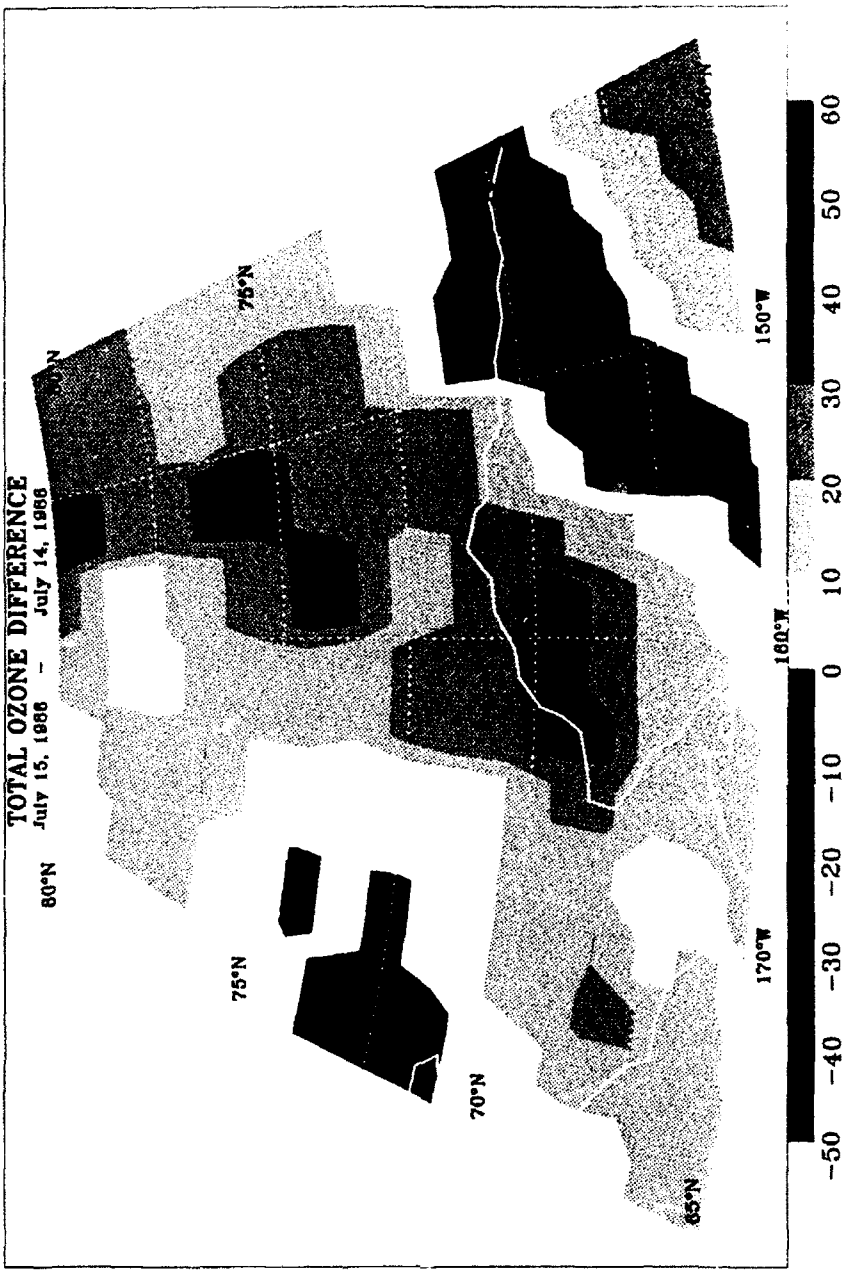

Figure 3.14c TOMS Ozone Difference in DU. Timeperiod compares with meteorological data of 16/00 and 15/00Z. An increase in ozone near 160W corresponds with the wave of interest in Mission 8.

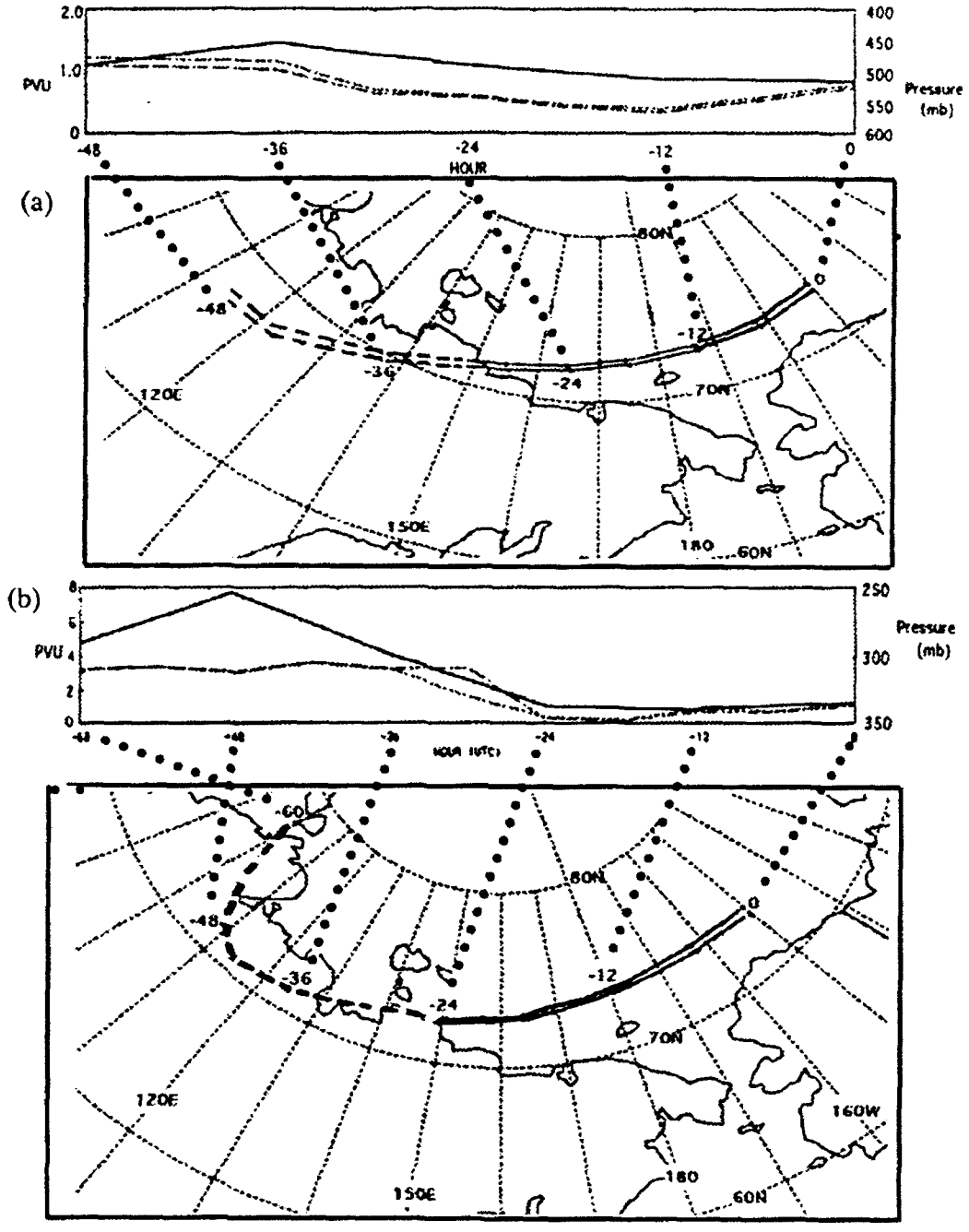

Figure 3.15 Isentropic back-trajectory at starting points 73.2N, 150W and 73.7N, 150W for graph of potential vorticity (solid line) and pressure heights (dashed) with corresponding trajectory path for (a) the 309K potential temperature level and (b) the 322K potential temperature level. The dashed portion of the trajectory paths represent questionable positions due to the parcel being influenced by the tropopause fold.

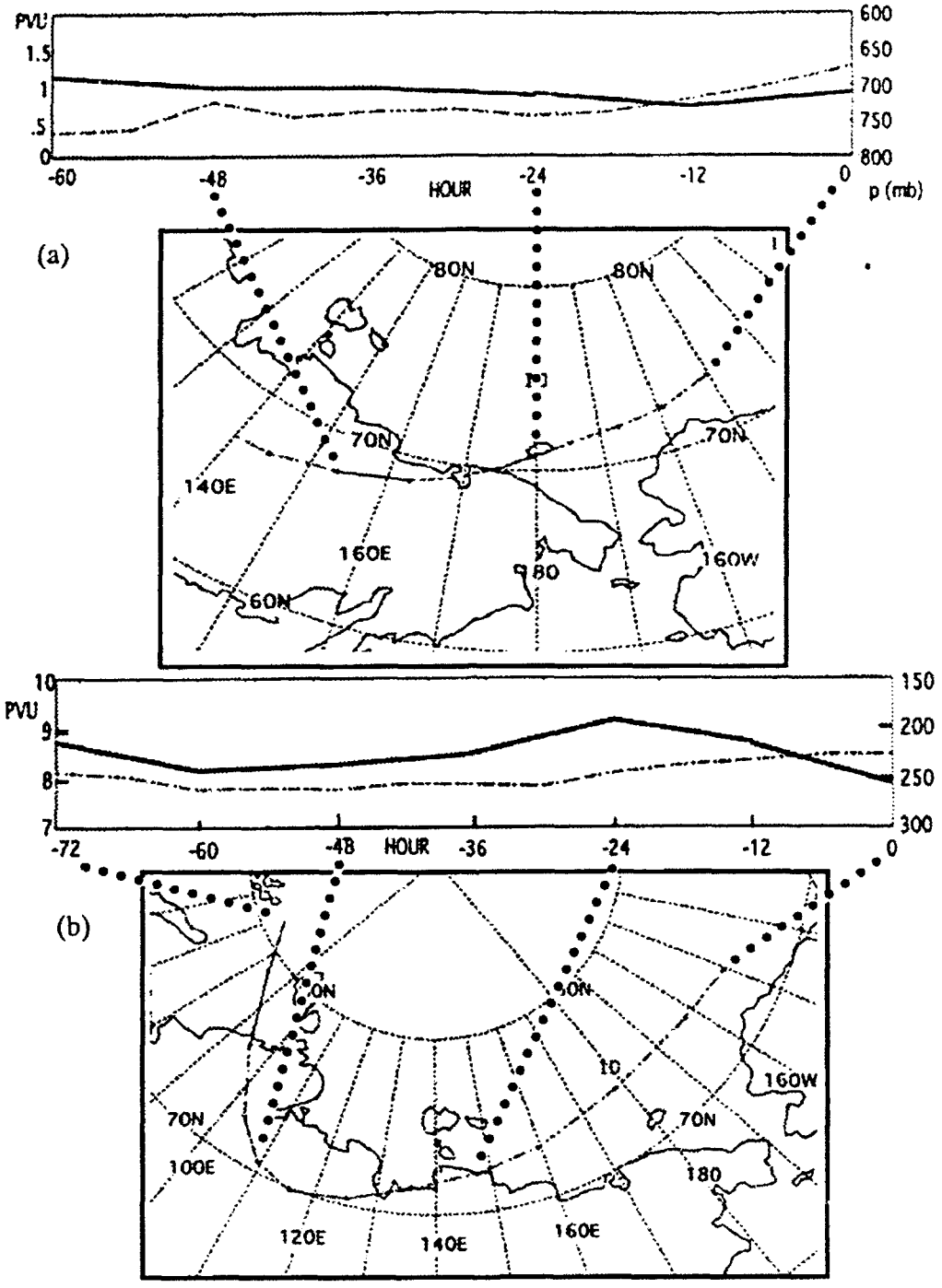

Figure 3.16 Isentropic back trajectory at starting point 73.2N, 150W for graph of potential vorticity (solid line) and pressure heights (dashed) with corresponding trajectory path for (a) the 300K potential temperature level and (b) the the 340K potential temperature level.

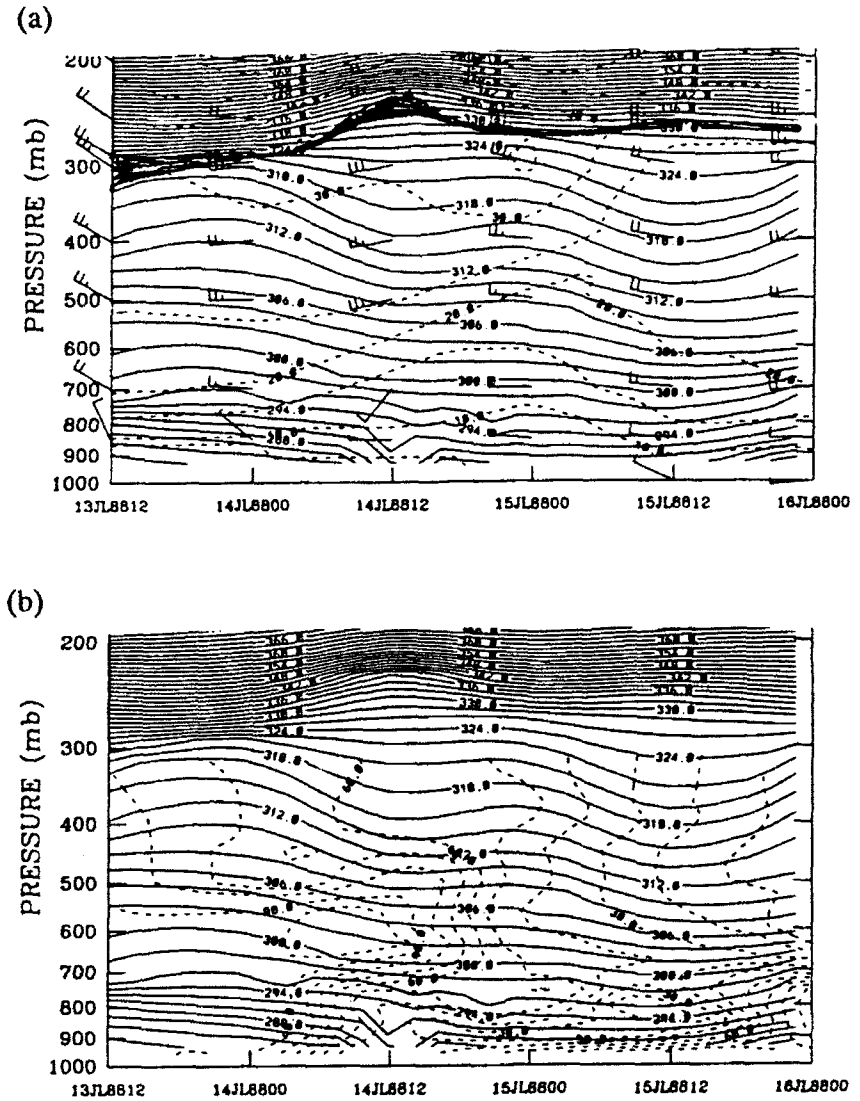

Figure 3.17 Parcel-Time Series for points in Table 4.2 at the 309K potential temperature level for (a) potential temperature in K (solid lines), windspeed in m/s (dashed) and windbarbs and (b) potential temperature in K and relative humidity in percent (dashed). Thick line represents tropopause.

(c)

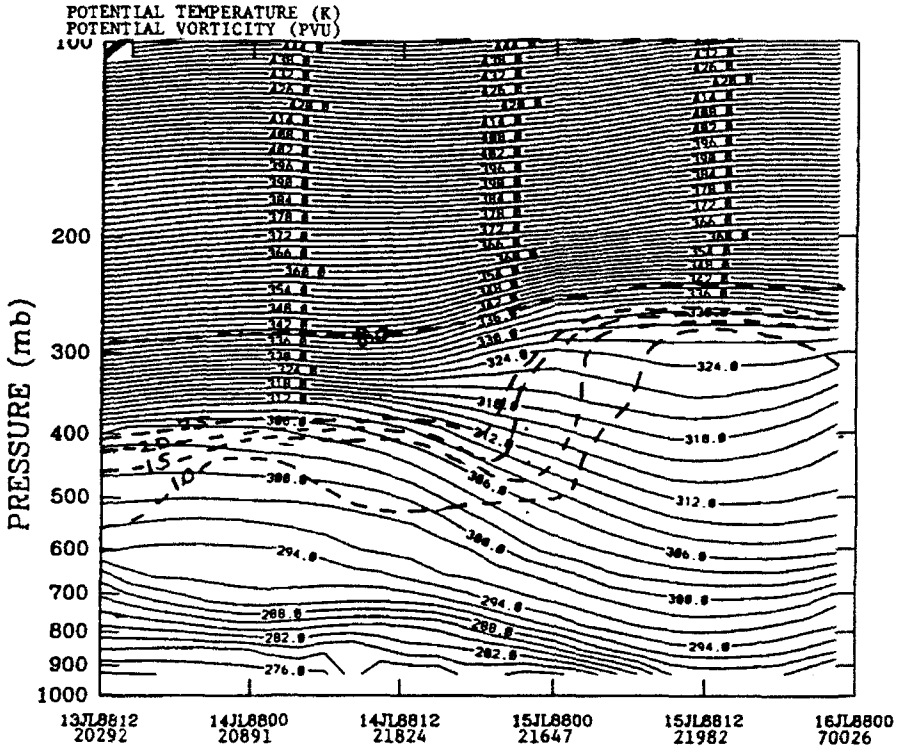

Figure 3.17 Parcel-Time Series for points in Table 4.2 at the 309K potential temperature level for (a) potential temperature in K (solid lines), windspeed in m/s (dashed) and windbarbs and (b) potential temperature in K and relative humidity in percent (dashed). Thick line represents tropopause and (c) potential temperature in K and potential vorticity (dashed) in PVU.

(a)

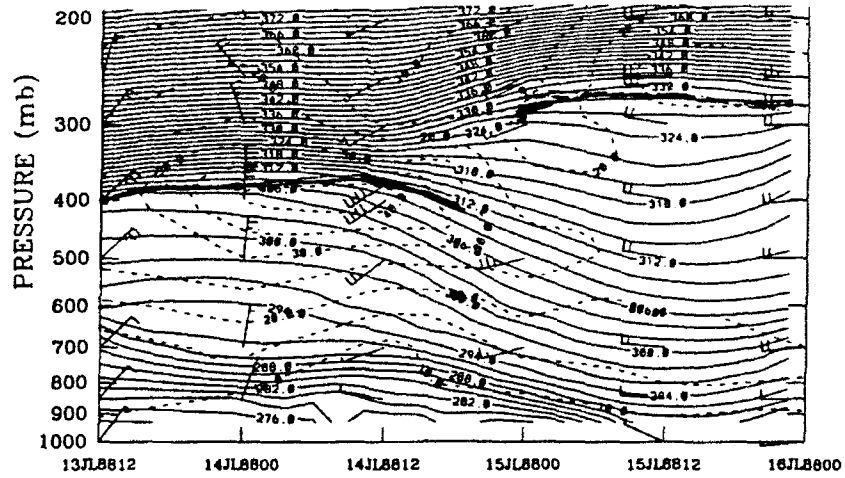

(b)

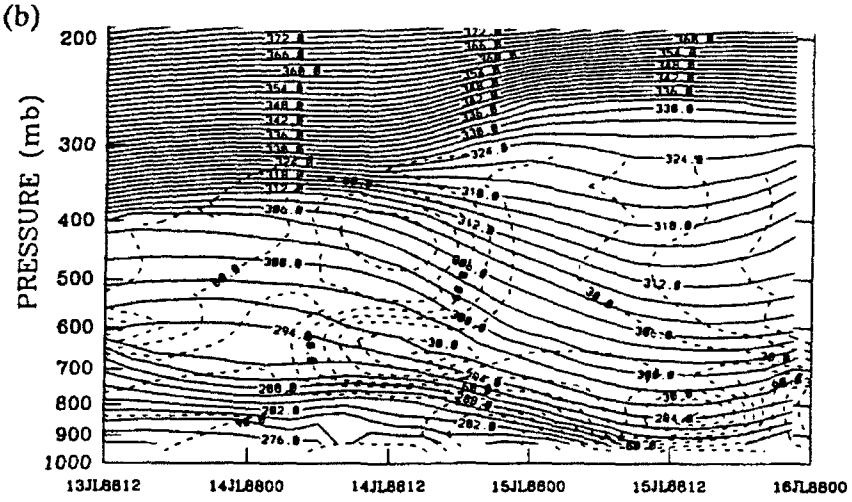

Figure 3.18 Parcel-Time Series for points in Table 4.2 at the 322K potential temperature level for (a) potential temperature in K (solid lines), windspeed in m/s (dashed) and windbarbs and (b) potential temperature in K and relative humidity in percent (dashed). Thick line represents tropopause and (c) potential temperature in K and potential vorticity (dashed) in PVU.

(c)

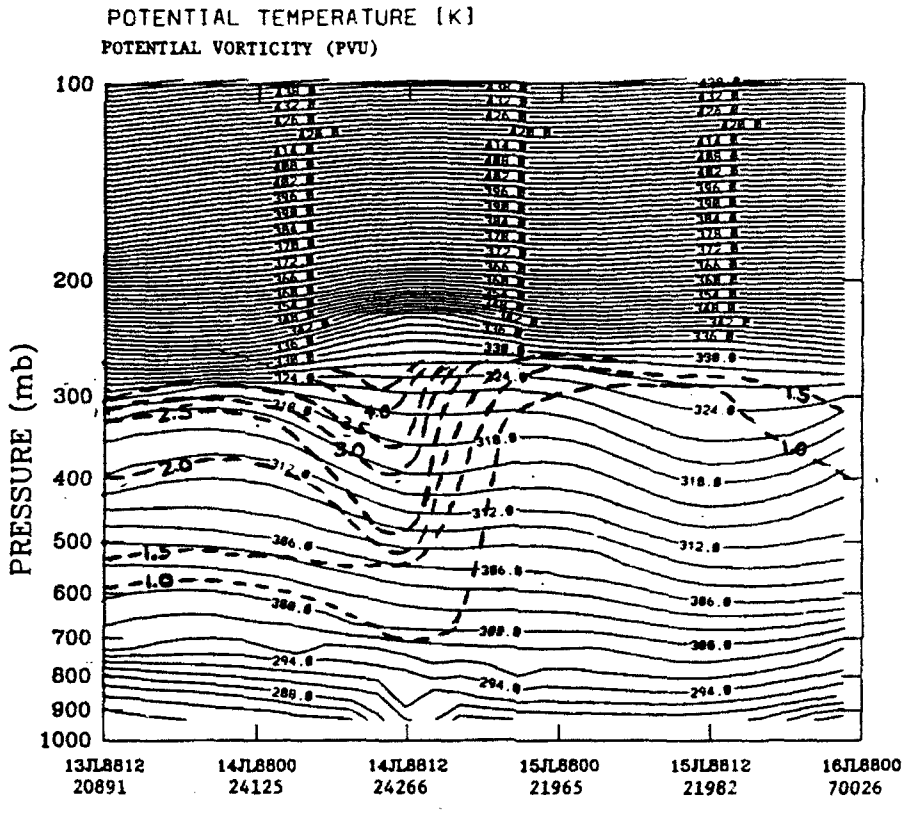

Figure 3.18 Parcel-Time Series for points in Table 4.2 at the 322K potential temperature level for (a) potential temperature in K (solid lines), windspeed in m/s (dashed) and windbarbs and (b) potential temperature in K and relative humidity in percent (dashed). Thick line represents tropopause and (c) potential temperature in K and potential vorticity (dashed) in PVU.

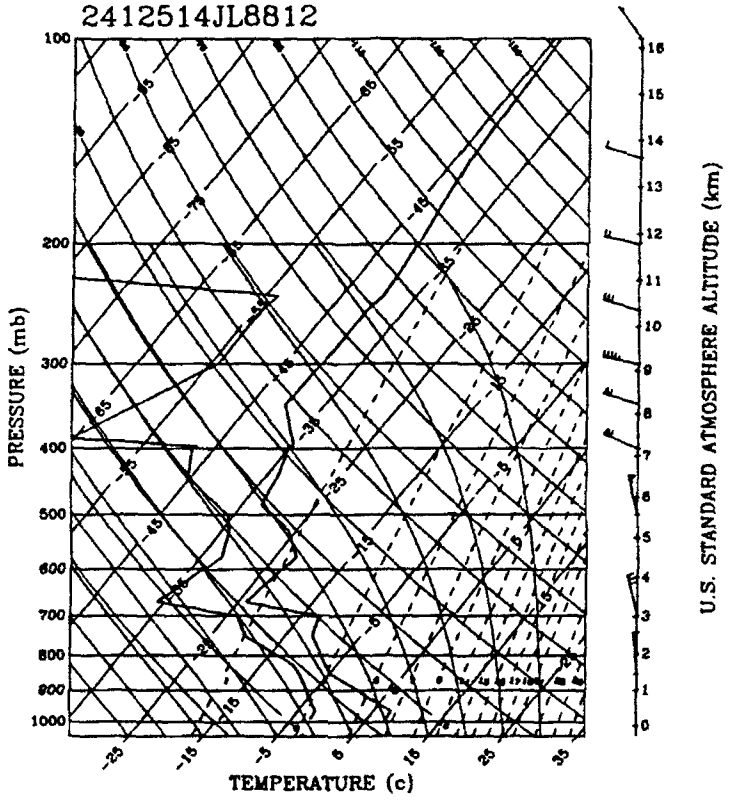

Figure 3.19 Station 24125 Skew-t LogP plot of temperature and dewpoint (solid lines) and wind in July 1988 at 14/12Z. Plot shows a low tropopause of 490 and 340mb.

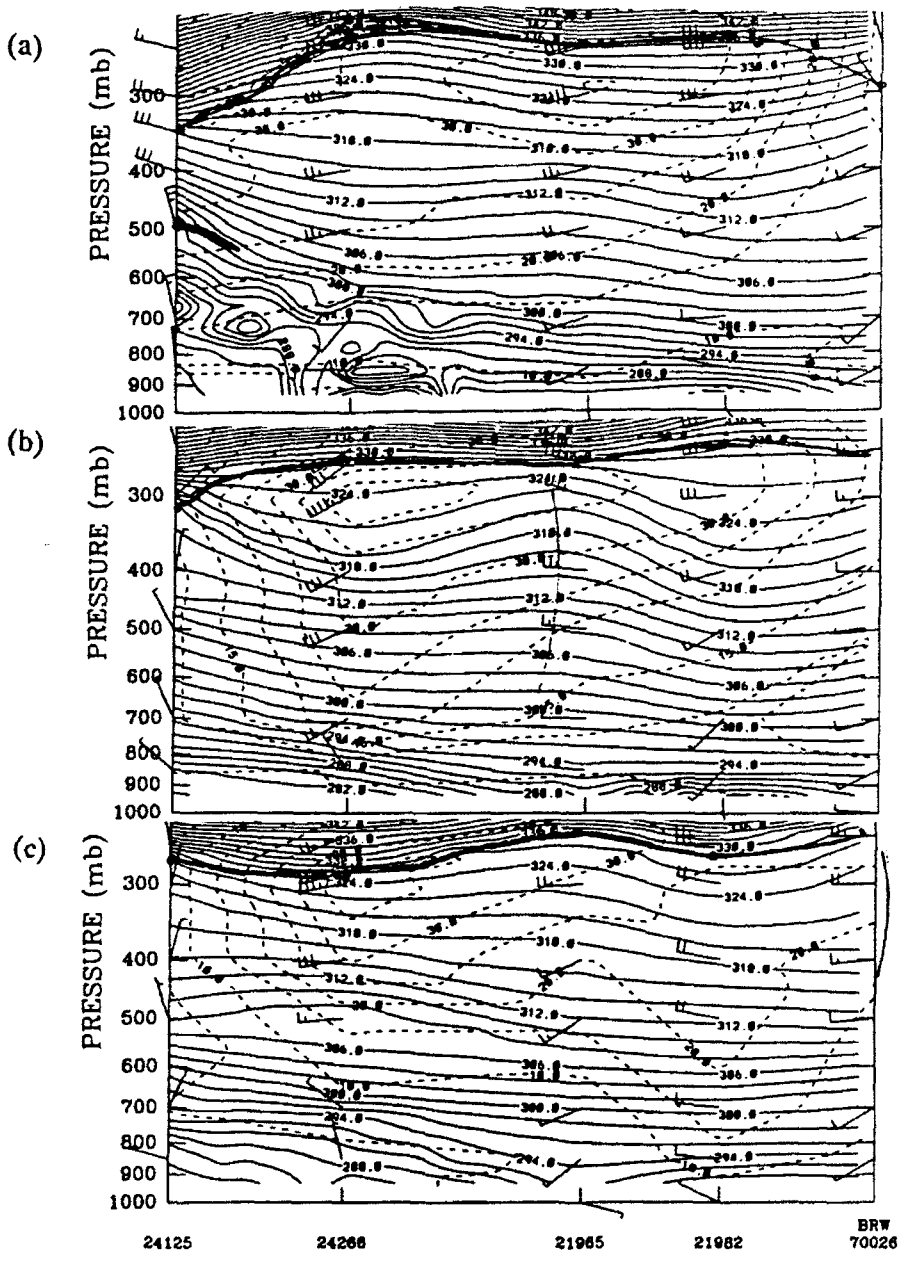

Figure 3.20 Cross-Section of potential temperature in K (solid), windspeed in m/s, and windbarbs for stations:

24125-24266-21965-21982-70026 for times: (a) 14/12Z, (b) 15/00Z, and (c) 15/12Z. In (a), a zonal west-east flow exists with jet maximum of over 40 m/s. In (b), a wave forms over station 21965 embedded in jet centered over 24266. This is wave responsible for ozone maximum measured near Barrow. In (c), wave exiting to right of picture.

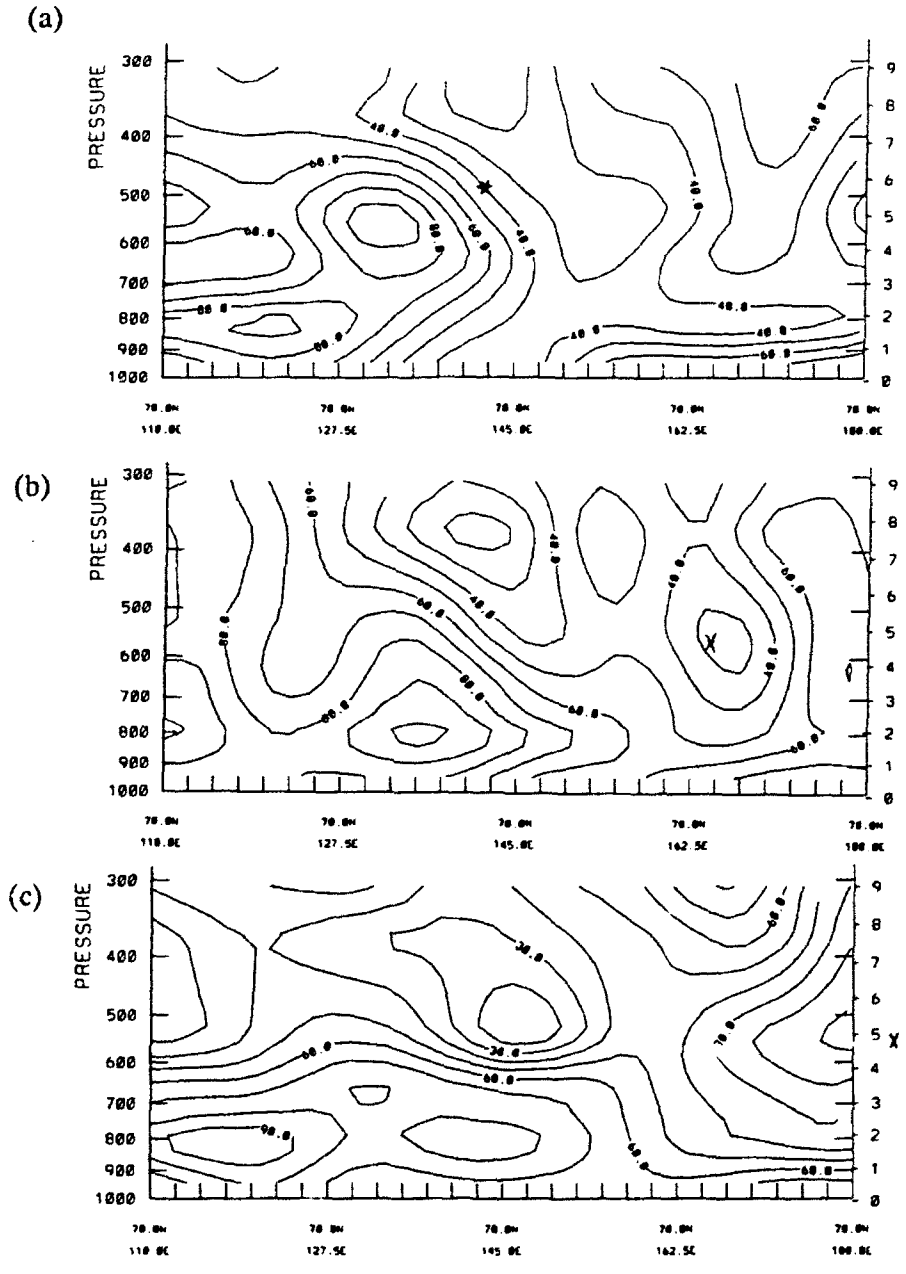

Figure 3.21 Cross-section of relative humidity from 70N, 110E to 70N, 180E for parcel (marked by x) moving in a developing dry slot for (a) 14/12Z shows parcel on edge of dry slot while (b) 15/00Z (middle), centered in a dry slot less than 30 percent, and (c) 15/12Z (bottom) in an area of less than 10 percent.

(a)

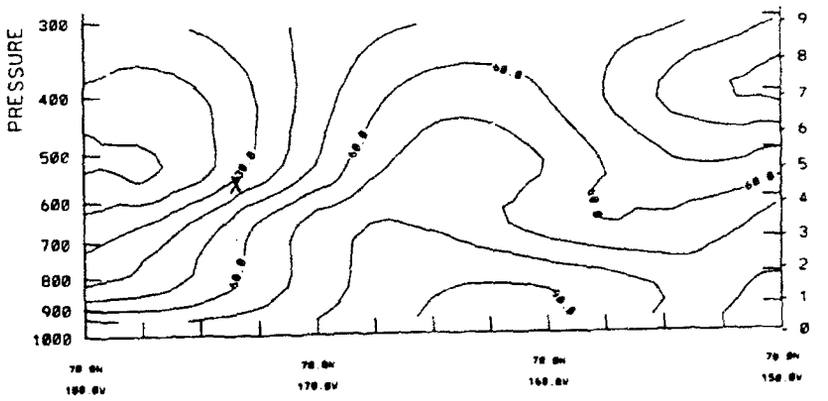

88 07 15 12 UT

(b)

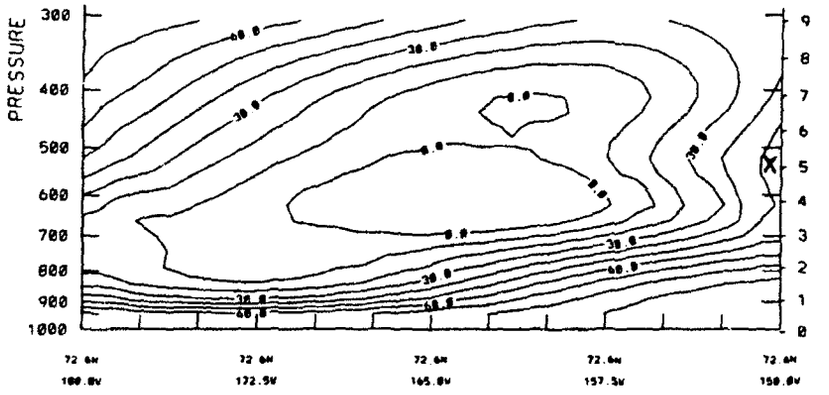

88 07 16 00 UT

Figure 3.22 Cross-section of relative humidity from (a) top from 70N, 180W-140W at 15/12Z and (b) bottom from 72.6N, 180W-140W at 16/00Z. Parcel position marked by an x. Top indicates parcel in dry slot at less than 10% and bottom shows parcel on front side of dry slot. Winds here are from left to right.

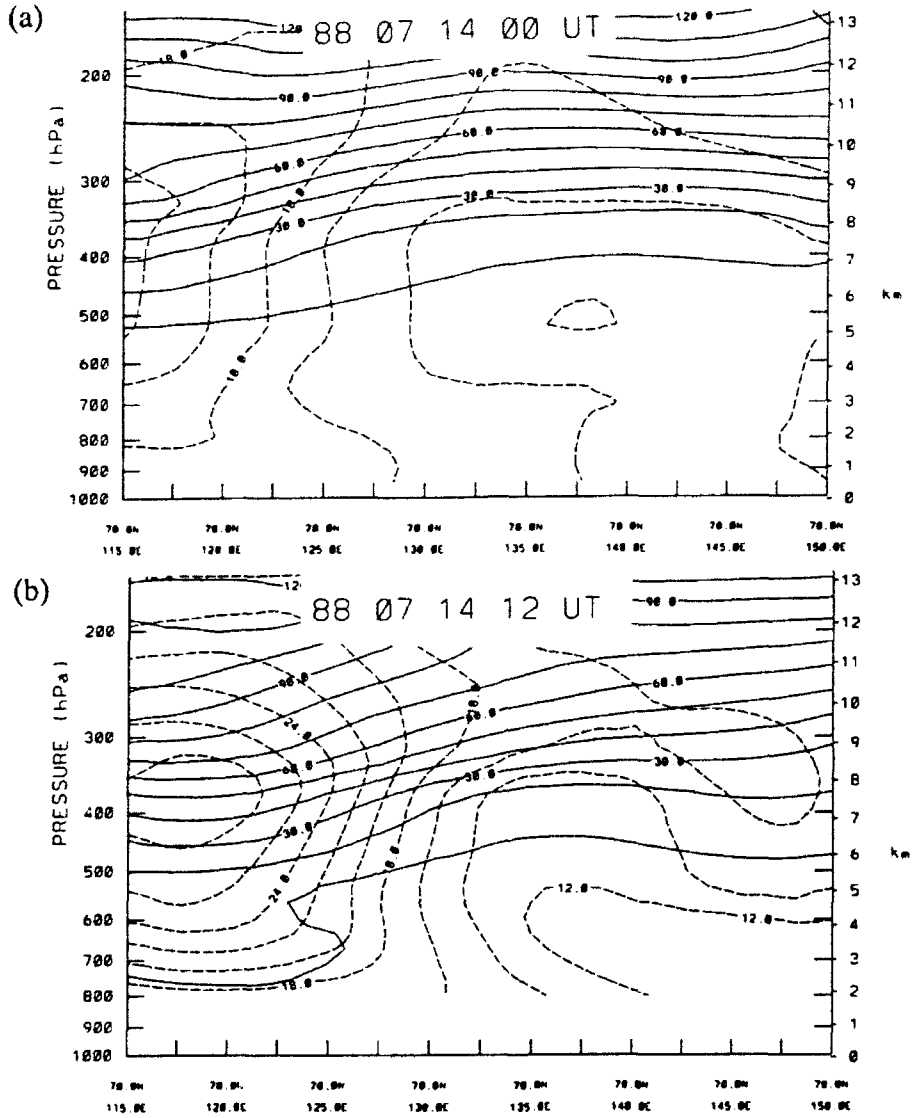

Figure 3.23 Cross-section of potential vorticity in deca-PVU (solid) and absolute vorticity in AVU (dashed) indicating strength of wave from:

(a) 70N, 115E-150E at 14/00Z
(b) 70N, 115E-150E at 14/12Z
(c) 72.6N, 130E-175E at 15/00Z
(d) 72.6N, 180W-145W at 15/12Z

(c)

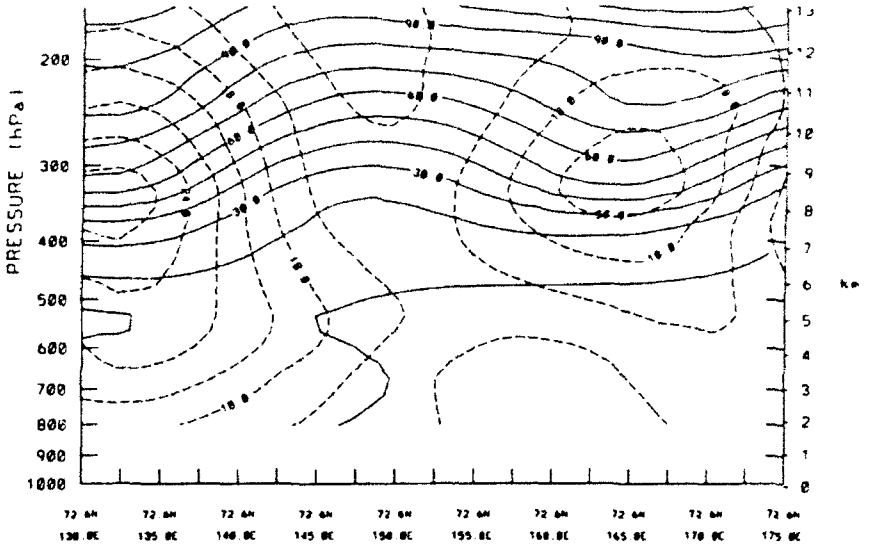

(d)

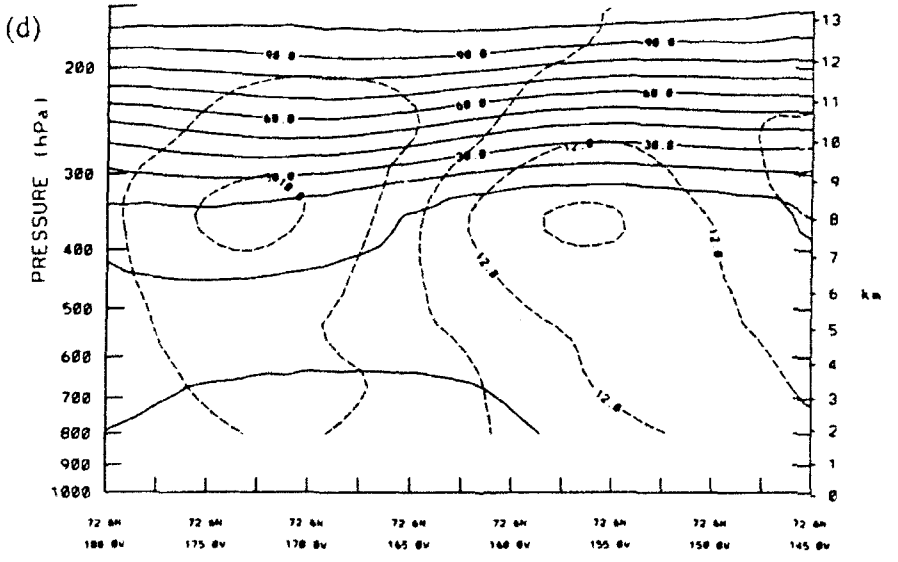

Figure 3.23 Cross-section of potential vorticity in deca-PVU (solid) and absolute vorticity in AVU (dashed) indicating strength of wave from:

(a) 70N, 115E-150E at 14/00Z
(b) 70N, 115E-150E at 14/12Z
(c) 72.6N, 130E-175E at 15/00Z
(d) 72.6N, 180W-145W at 15/12Z

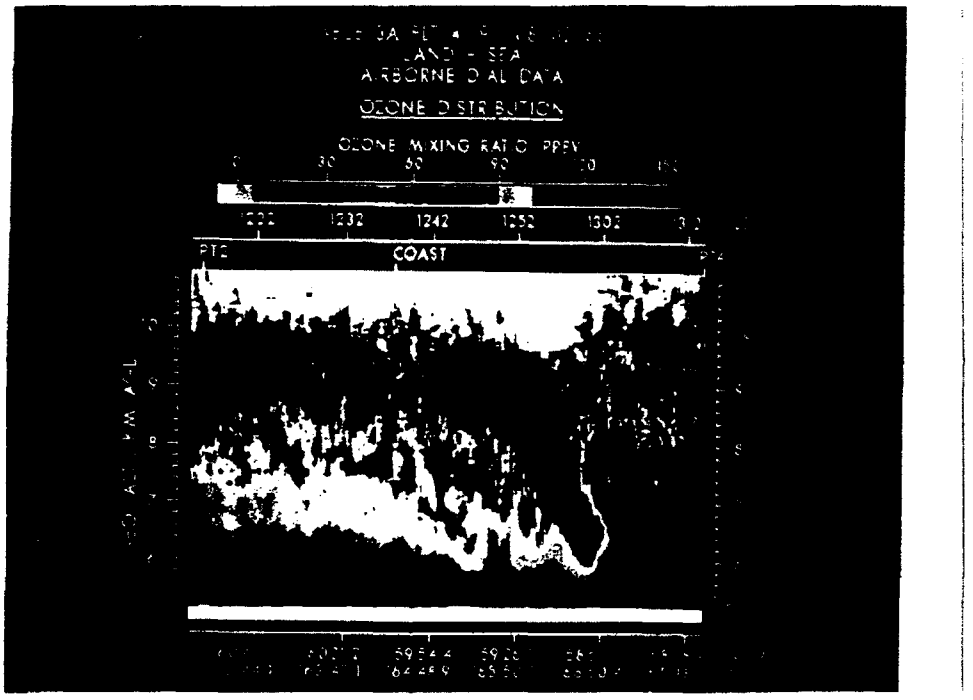

Figure 3.24 Lidar for Mission 19 depicting intrusion of ozone. Picture shows lower tropopause of 6.5-7km in left 2/3 of frame rising quickly to 8.5 km in right.

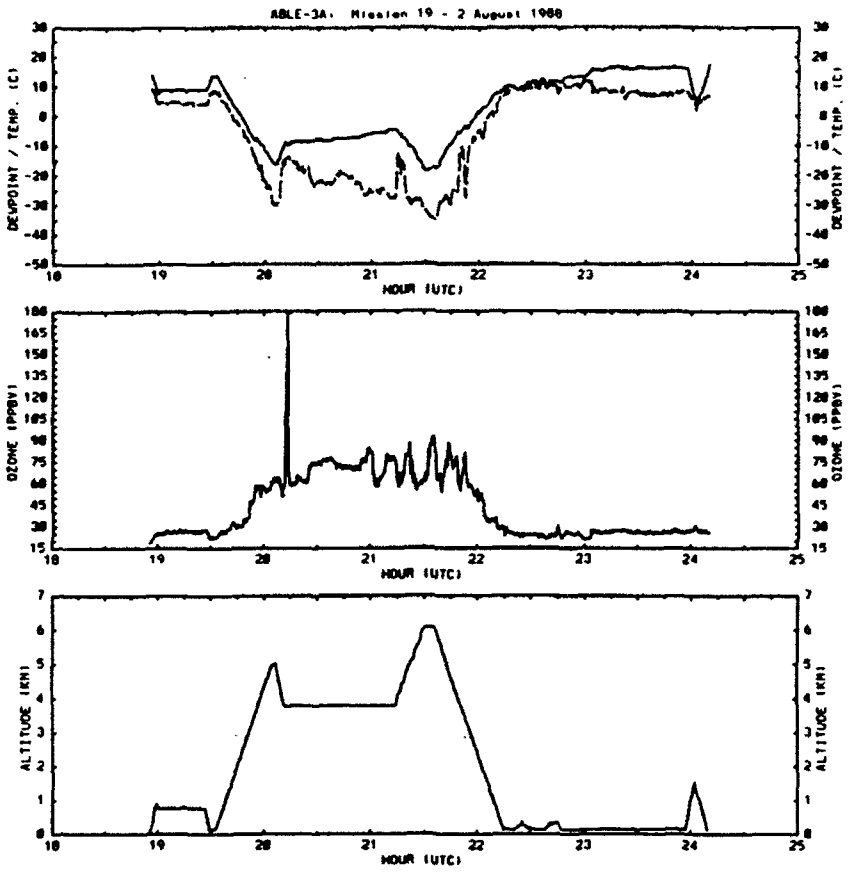

Figure 3.25 ABLE 3A Mission 19 inflight measurements of temperature, dewpoint, ozone and altitude. Note spike of ozone just after 20Z.

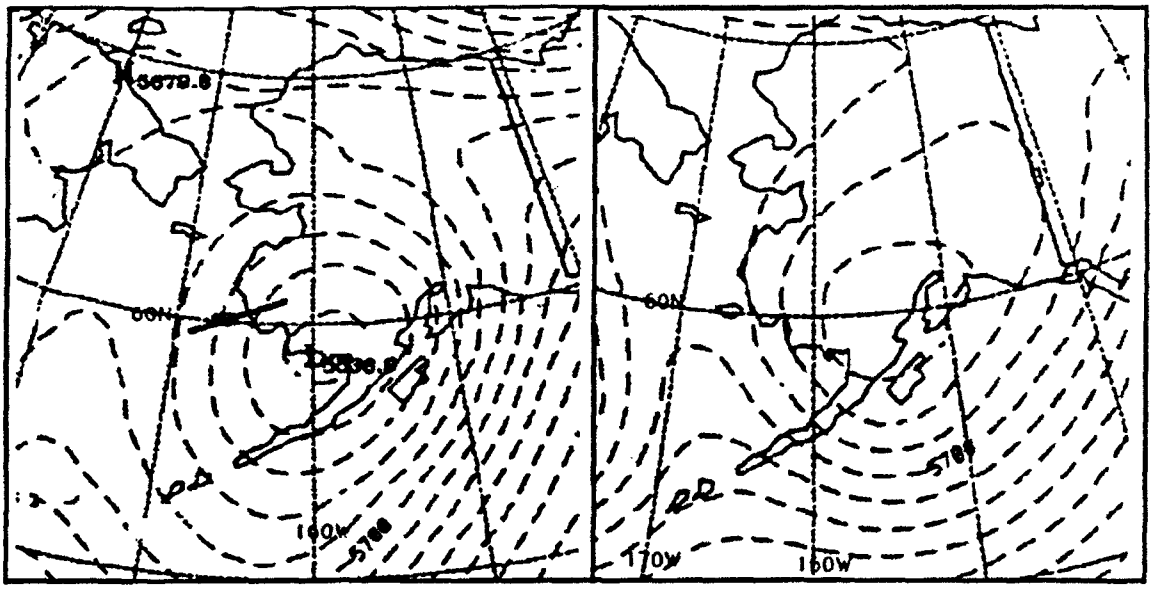

(a) 500mb heights at 2/00Z

(b) 500mb heights at 2/12Z

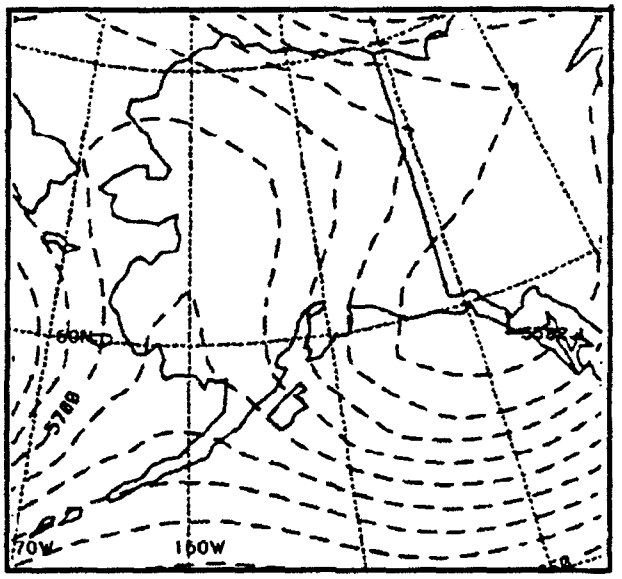

(c) 500mb heights at 4/00Z

Figure 3.26 500mb pressure heights in m (dashed) at (a) 2/00Z, (b) 3/00Z, and (c) 4/00Z. Mission 3 flight path noted by thick solid line in (a).

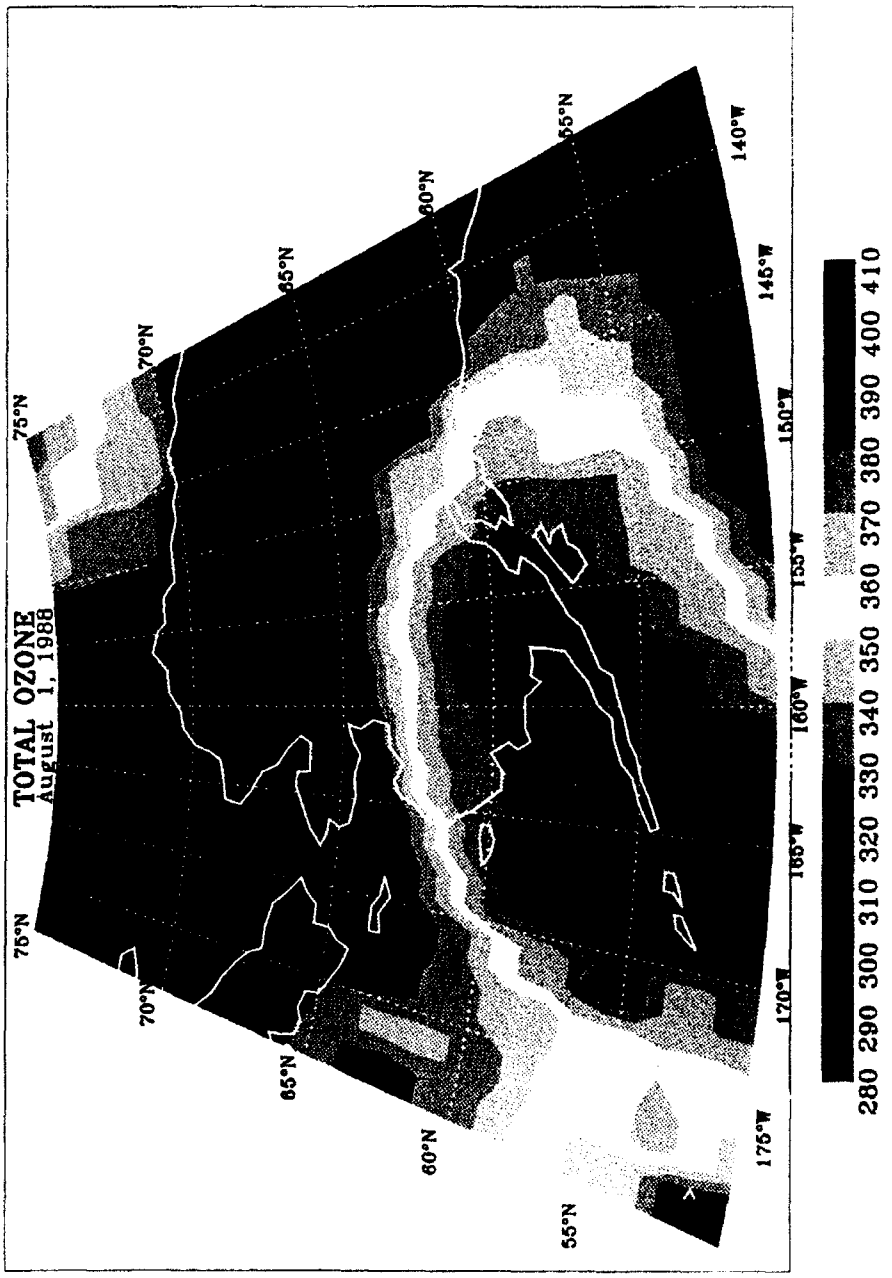

Figure 3.27a TOMS total ozone in DU. Maximum values appear over southwest Alaska due to polar vortex. TOMS here compares with meteorological data taken at 2/00Z.

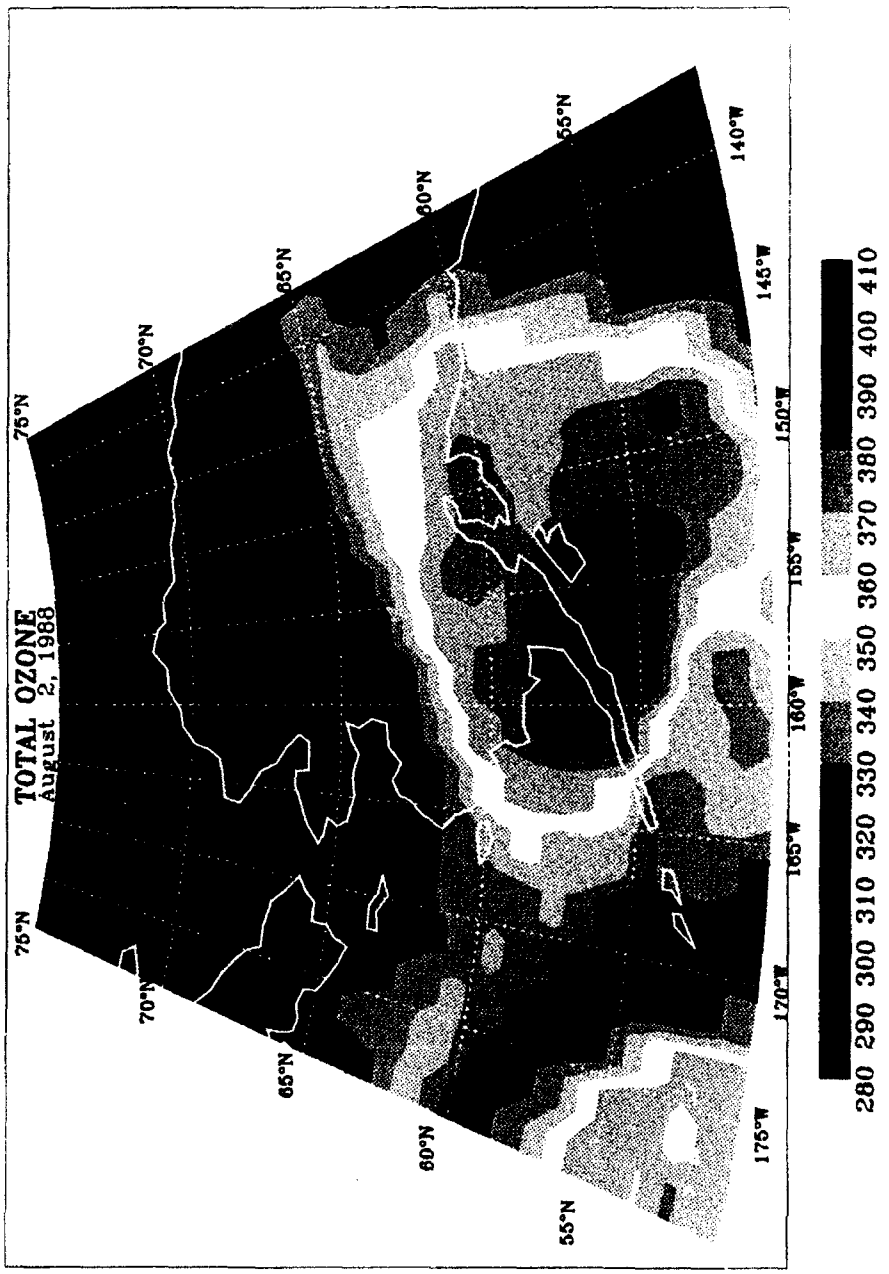

Figure 3.27b TOMS total ozone in DU. Maximum values appear over SW Alaska due to upper low. TOMs here compares with meteorological data taken at 3/00Z.

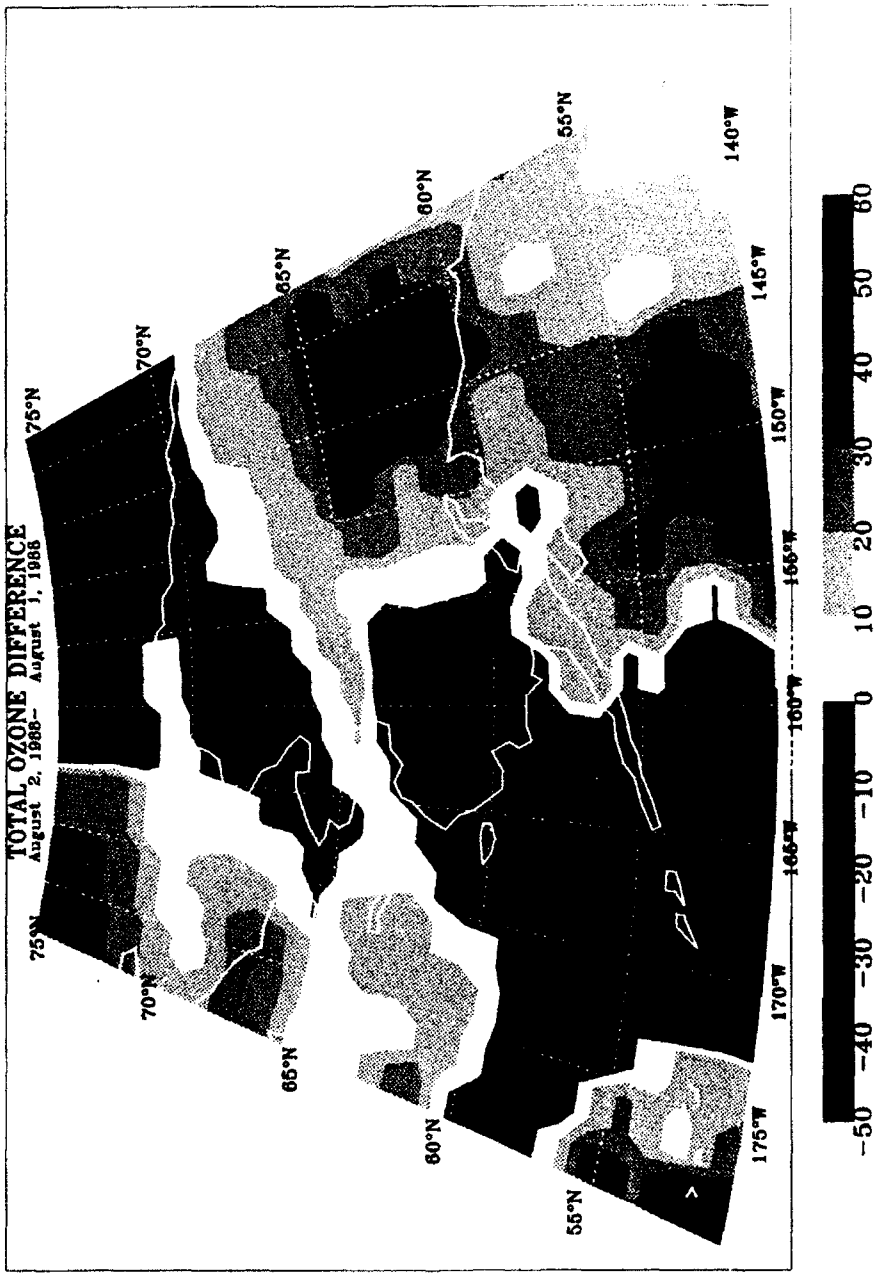

Figure 3.27c TOMS total ozone in DU. Maximum values have weakened and moved to the east. TOMs here compares with meteorological data taken at 4/00Z.

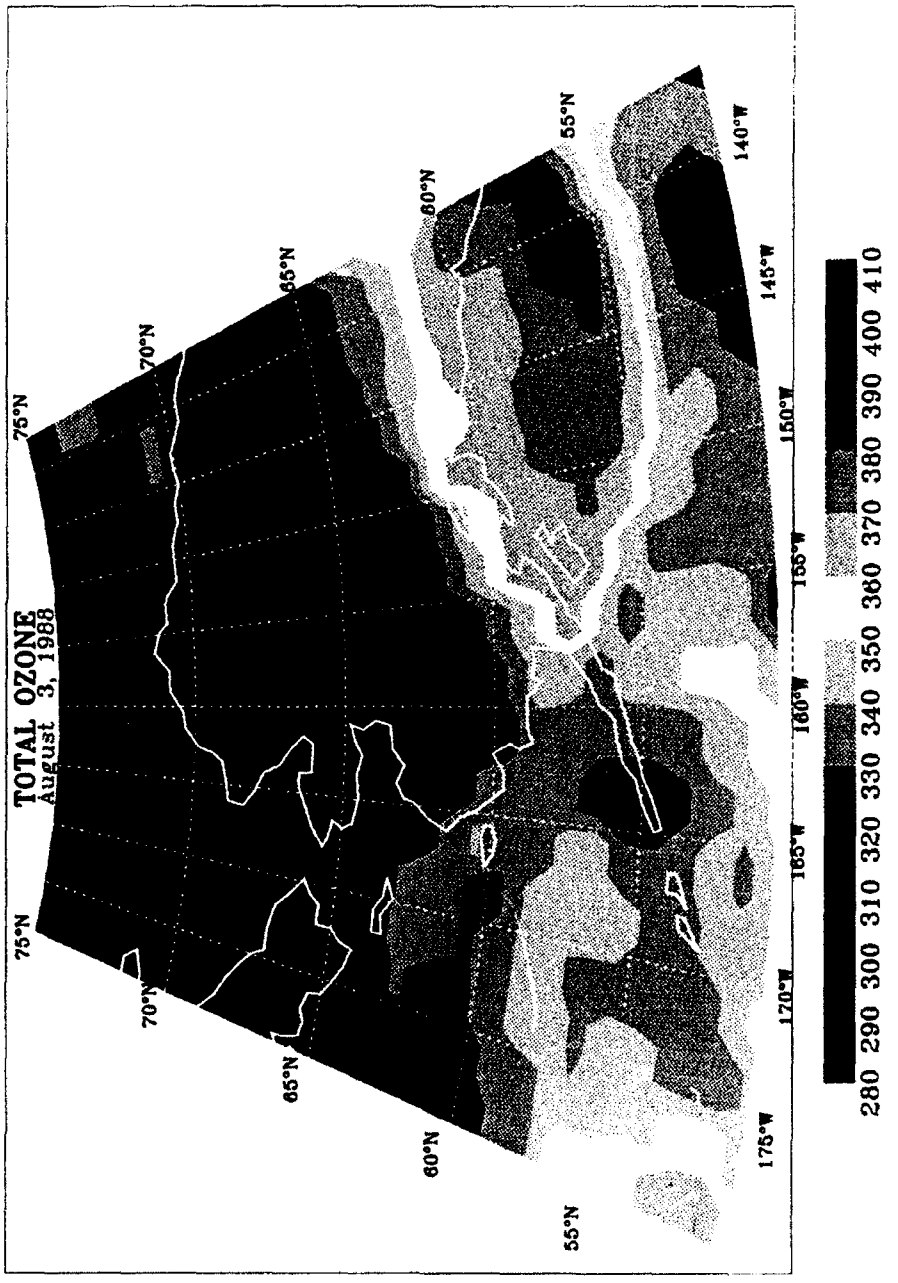

Figure 3.28 TOMS Ozone Difference in DU. Timeperiod compares with meteorological data at 3/00Z and 2/00Z. An increase in ozone over eastern Alaska corresponds with the movement of the low. Over the Mission 19 area near 61N, 162W, ozone values are decreasing.

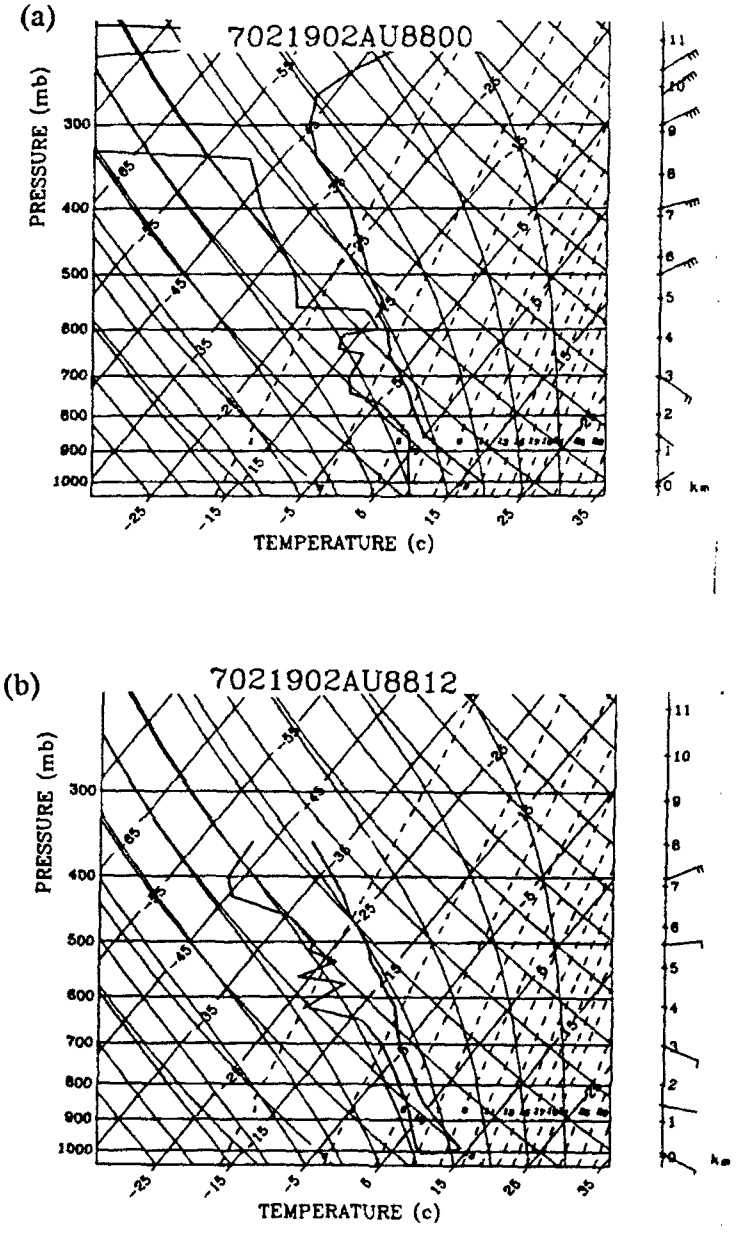

Figure 3.29 Skew-t LogP plot for Bethel, AK (station 70219) at (a) 2/00Z; (b) 2/12Z; and (c) 3/00Z showing development of subsidence layers between 400-600mb. In (a) and (b), subsidence not very strong even though drying above 550mb. By (c), stronger subsidence layer formed 600-460mb indicating the polar vortex exiting the area.

(c)

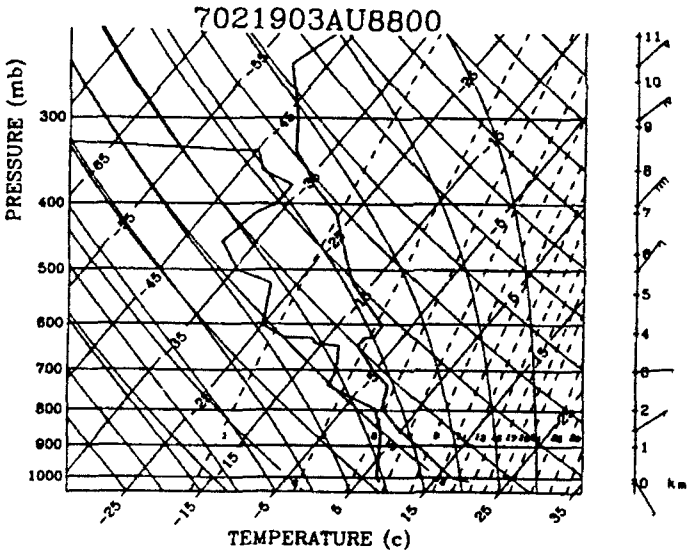

Figure 3.29 Skew-t LogP plot for Bethel, AK (station 70219) at (a) 2/00Z; (b) 2/12Z; and (c) 3/00Z showing development of subsidence layers between 400-600mb. In (a) and (b), subsidence not very strong even though drying above 550mb. By (c), stronger subsidence layer formed 600-460mb indicating the polar vortex exiting the area.

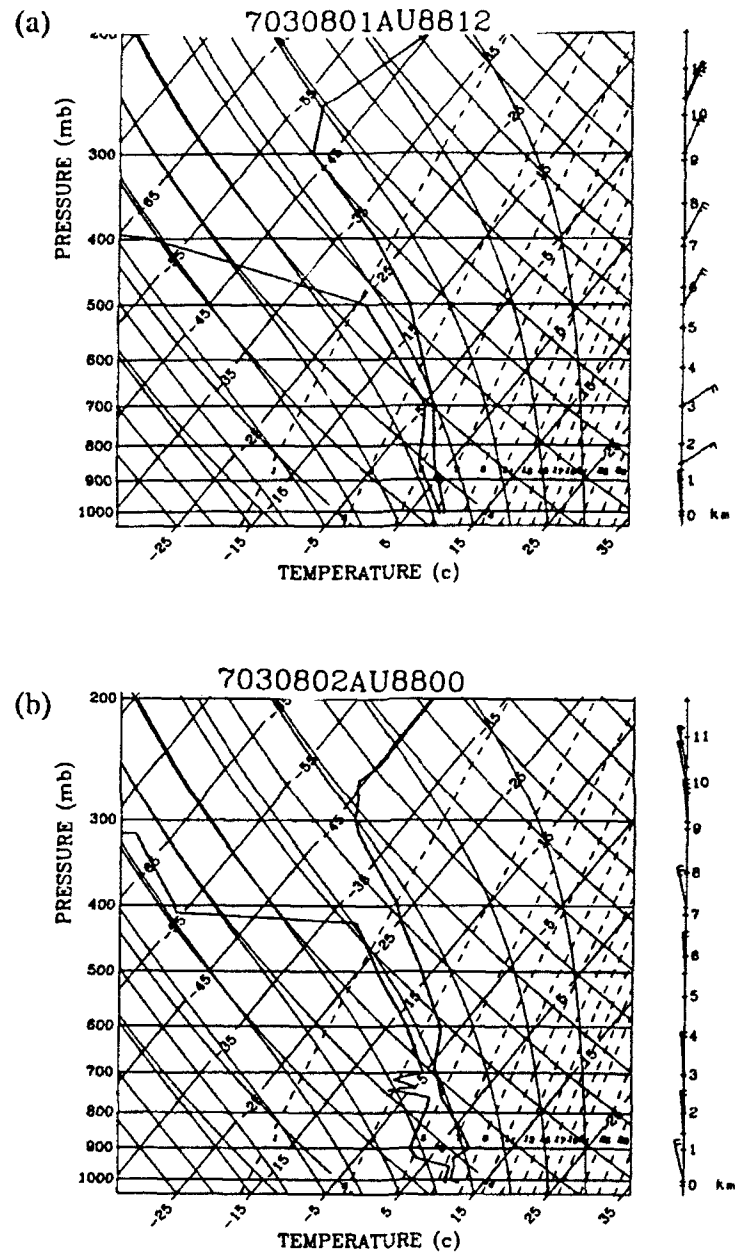

Figure 3.30 Skew-t Plot at St. Paul, AK (station 70308) at (a) 1/12Z, (b) 2/00Z, (c) 2/12Z, and (d) 3/00Z. Moist sounding in (a) gives way to drying above 420mb in (b), (c), and (d). Tropopause rises from 200mb in (a) to 200mb in (d).

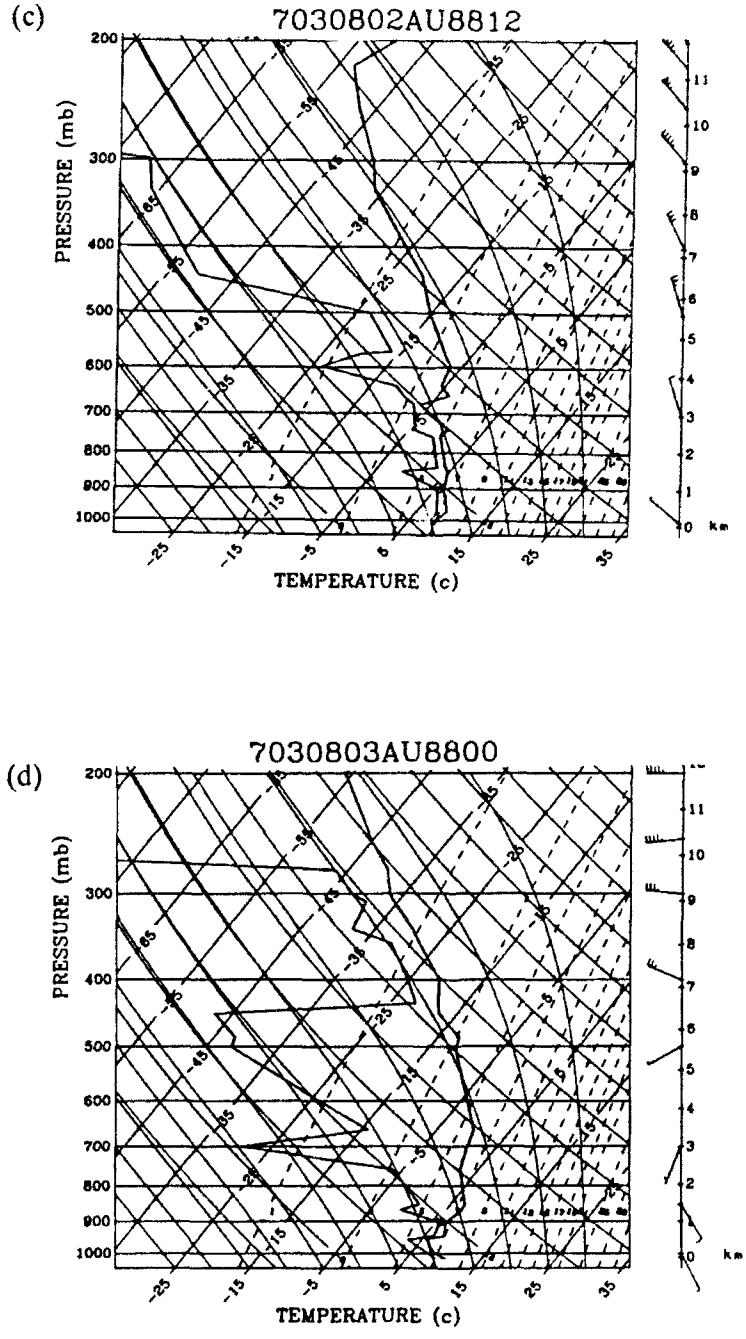

Figure 3.30 Skew-t Plot at St. Paul, AK (station 70308) at (a) 1/12Z, (b) 2/00Z, (c) 2/12Z, and (d) 3/00Z. Moist sounding in (a) gives way to drying above 420mb in (b), (c), and (d). Tropopause rises from 200mb in (a) to 200mb in (d).

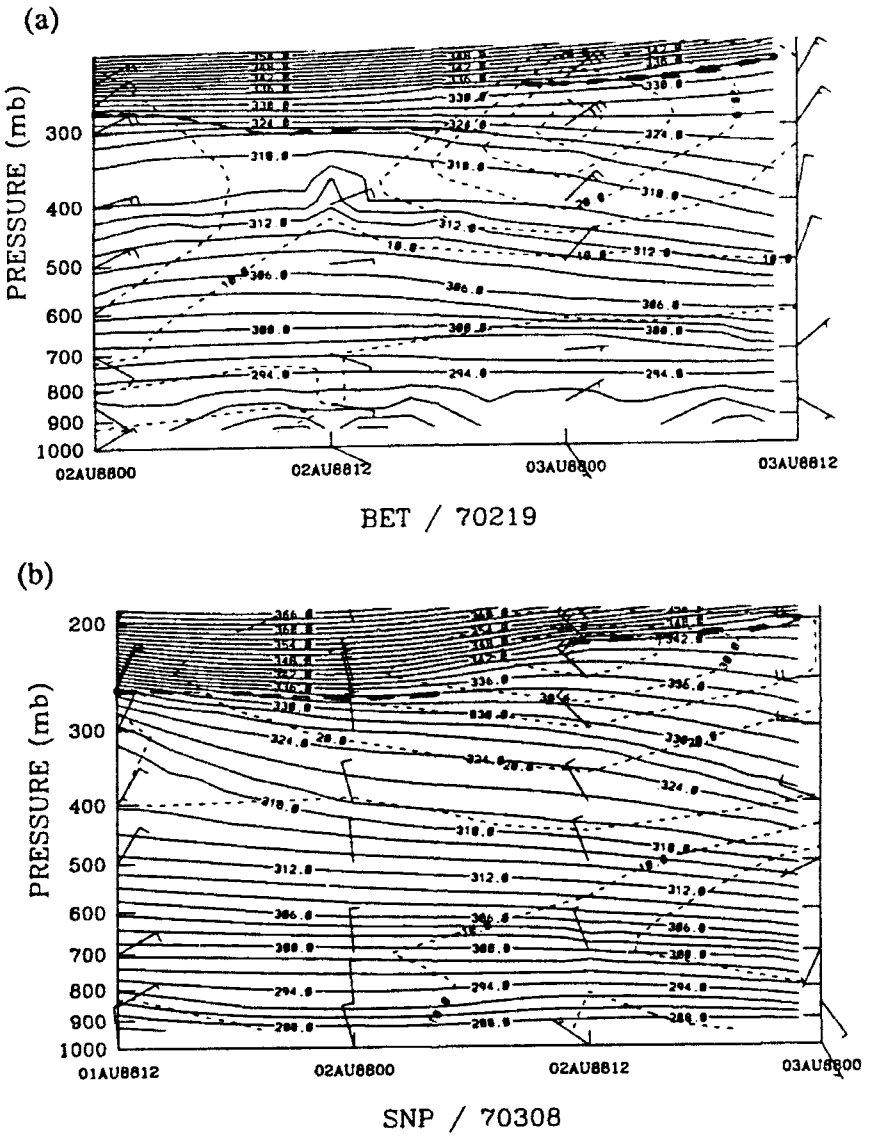

Figure 3.31 Station Time-Series for PT (solid) K and WS (dashed) m/s for (a) Bethel (70219) from 2/00Z to 03/12Z and (b) St. Paul (70308) from 1/12Z to 03/00Z

Tropopause indicated by heavy dashed line. Both figures indicate jet maximum moves through point with the tropopause rising.

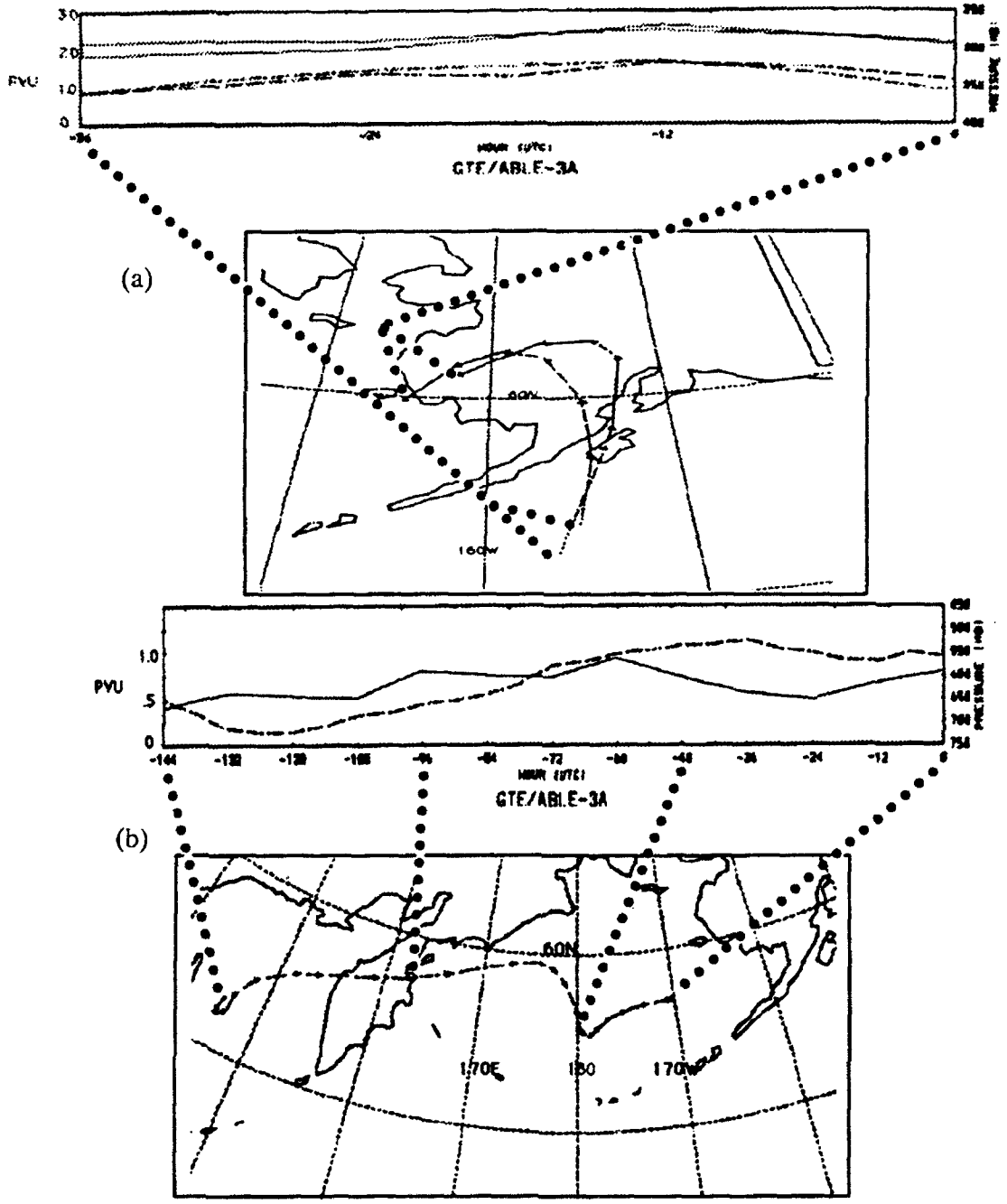

Figure 3.32 Isentropic back trajectory for graph of potential vorticity in PVU (solid line) and pressure heights in mb (dashed) with corresponding trajectory path for (a) 321K potential temperature level for point 61.1N, 162W, (b) the 311K potential temperature level for point 57.2N, 170.2W and (c) same as in "a", except for the 303K potential temperature level without potential vorticity.

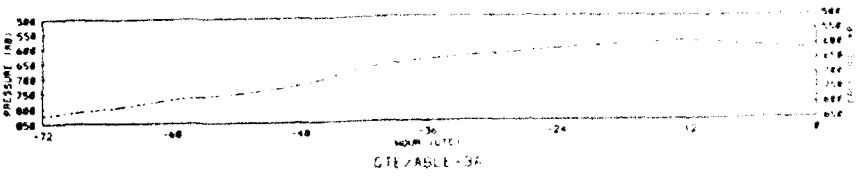

(c)

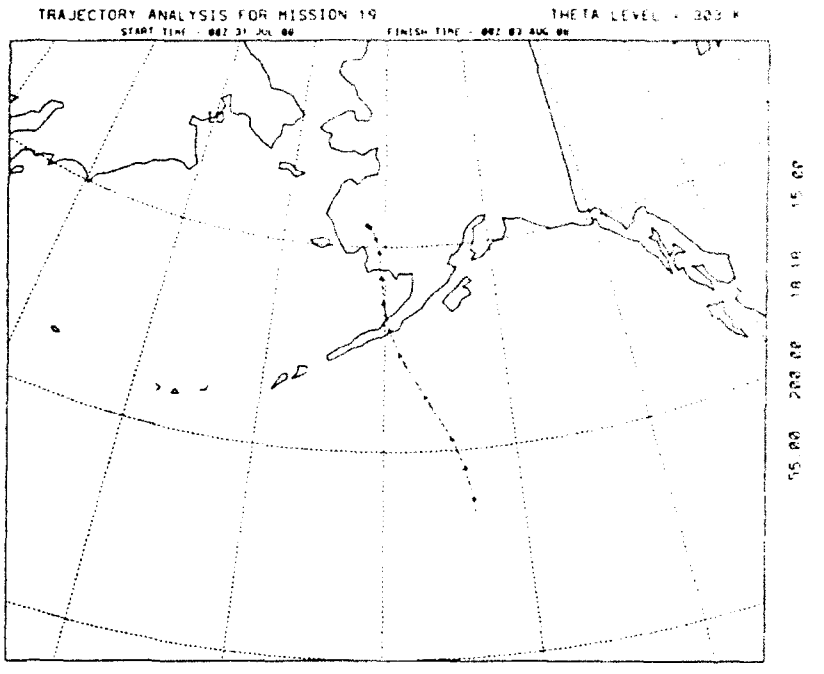

Figure 3.32 Isentropic back trajectory for graph of potential vorticity in PVU (solid line) and pressure heights in mb (dashed) with corresponding trajectory path for (a) 321K potential temperature level for point 61.1N, 162W, (b) the 311K potential temperature level for point 57.2N, 170.2W and (c) same as in "a", except for the 303K potential temperature level without potential vorticity.

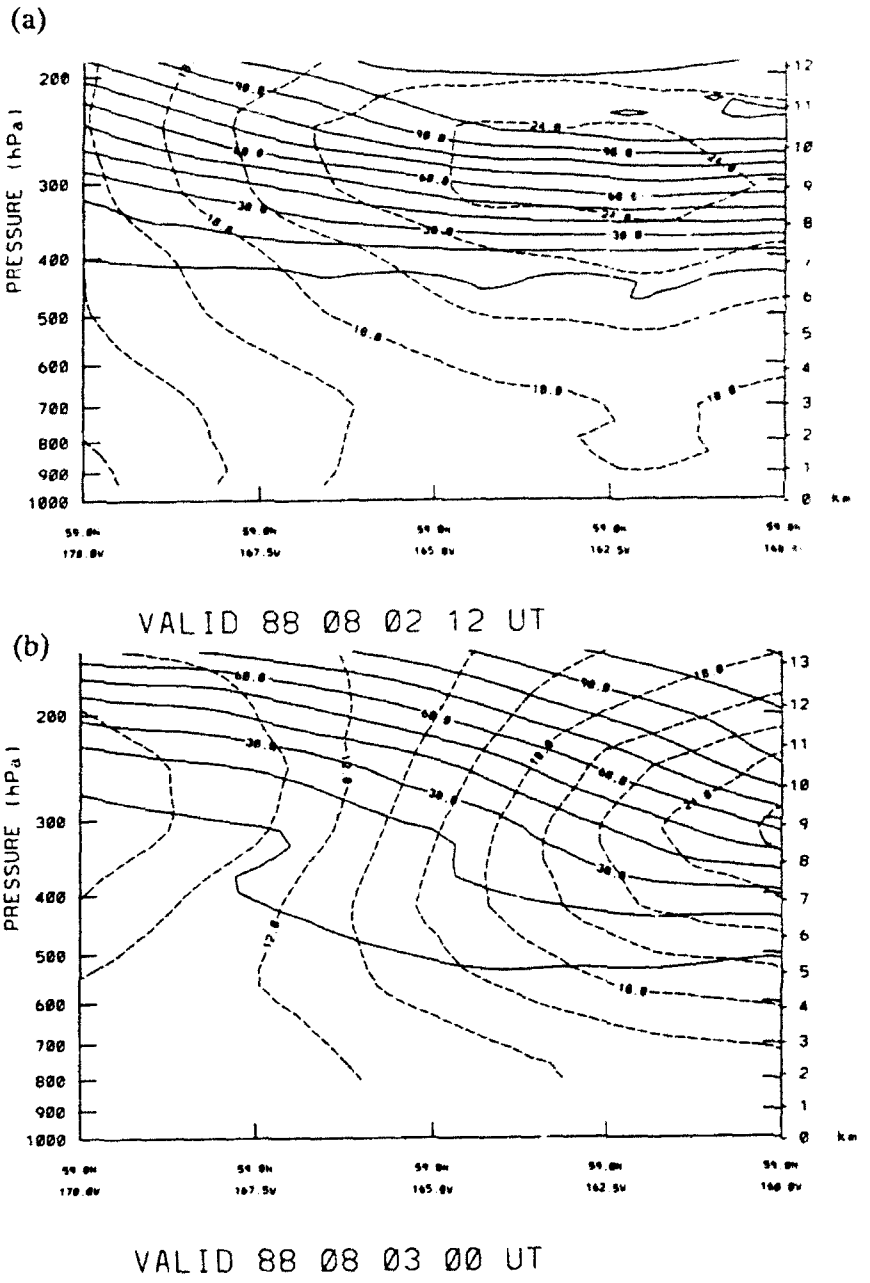

Figure 3.33 Cross-Section of potential vorticity in deca-PVU (solid) and absolute vorticity in AVU (dashed) at (a) 02/12Z; (b) 03/00Z; and (c) 03/12Z for 59N, 170W-160W. In (a), polar vortex influences cross-section with a maximum absolute vorticity and large potential vorticity values at low altitudes. In (b), vortex begins to move off, and in (c) has exited to the right.

(c)

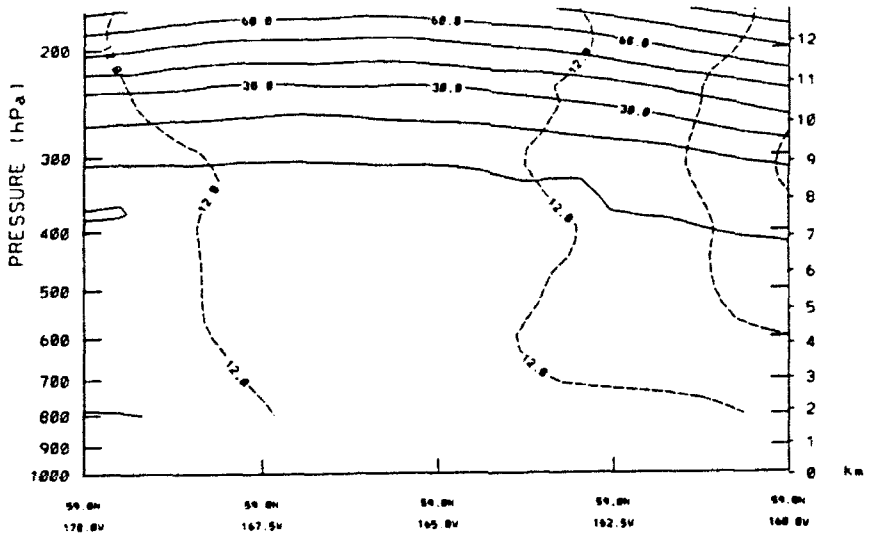

Figure 3.33 Cross-Section of potential vorticity in deca-PVU (solid) and absolute vorticity in AVU (dashed) at (a) 02/12Z; (b) 03/00Z; and (c) 03/12Z for 59N, 170W-160W. In (a), polar vortex influences cross-section with a maximum absolute vorticity and large potential vorticity values at low altitudes. In (b), vortex begins to move off, and in (c) has exited to the right.

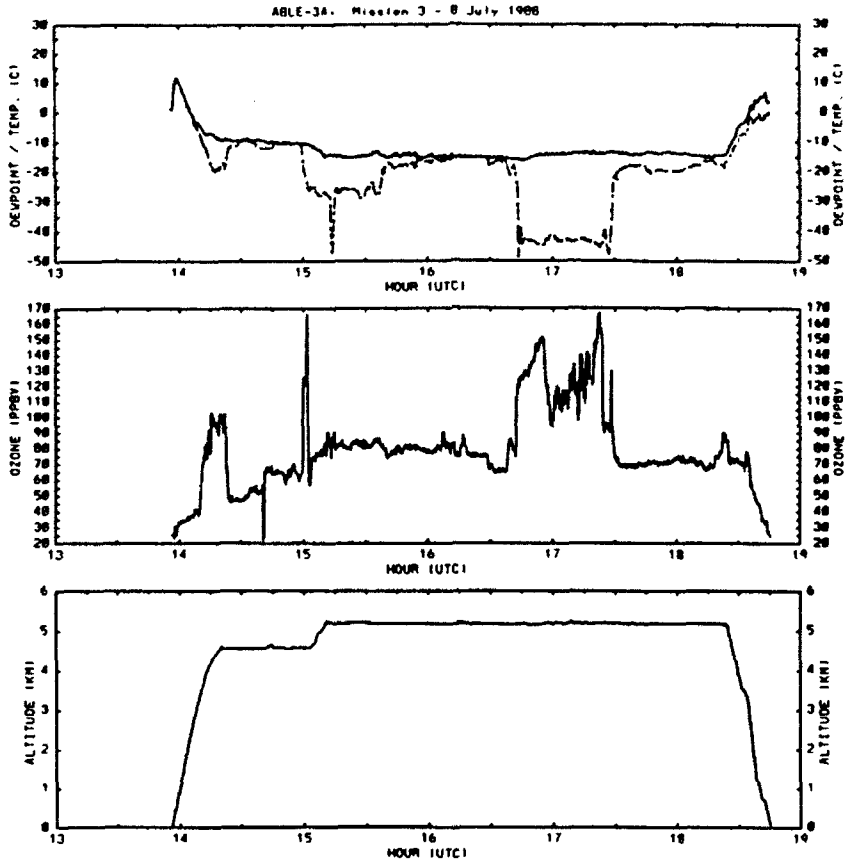

Figure 3.34 ABLE 3A Mission 3 inflight measurements of temperature, dewpoint, ozone and altitude. Note spike of high ozone values around 15 and 17Z.

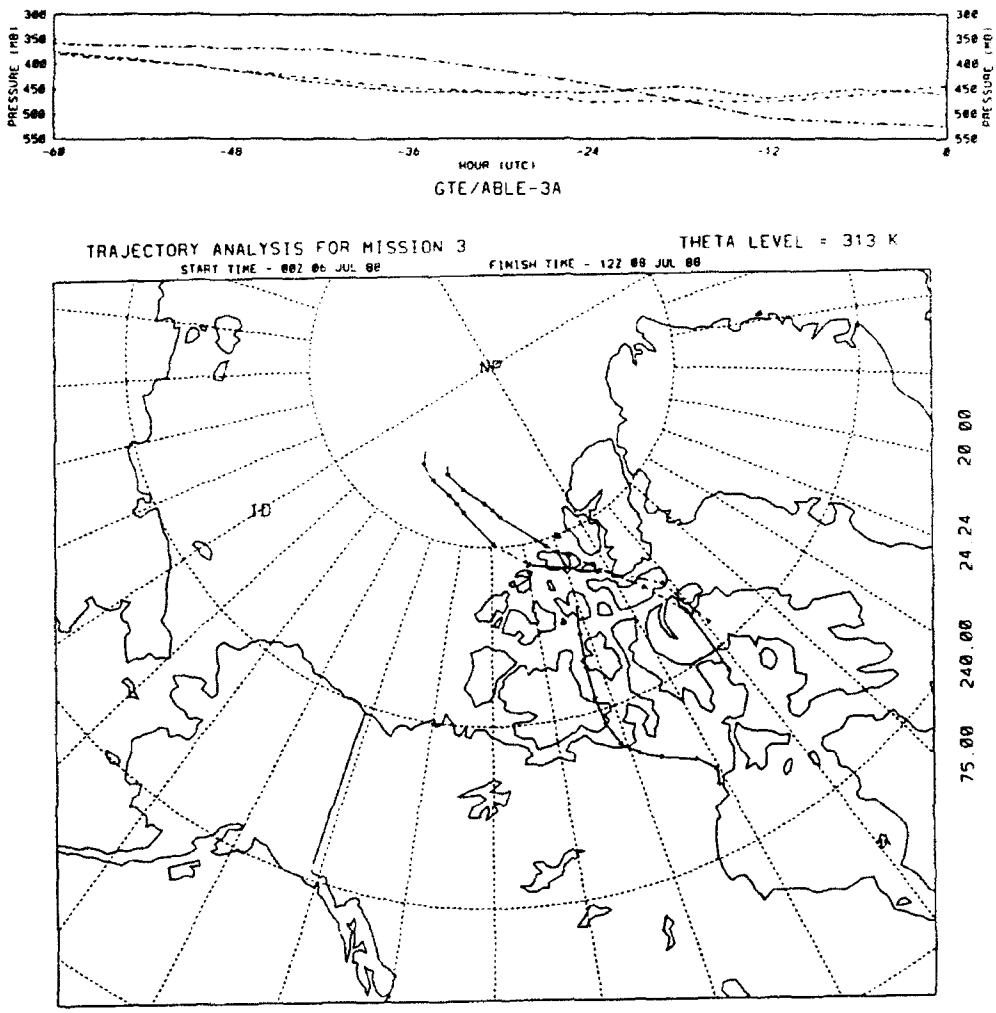

Figure 3.35 Isentropic back trajectory at the 313K potential temperature level for enhanced ozone areas at points 63.6N, 91W; 61.6N, 81.5W; 71.3N, 79.2W. Top graph shows pressure heights (dashed) with the corresponding path on map.

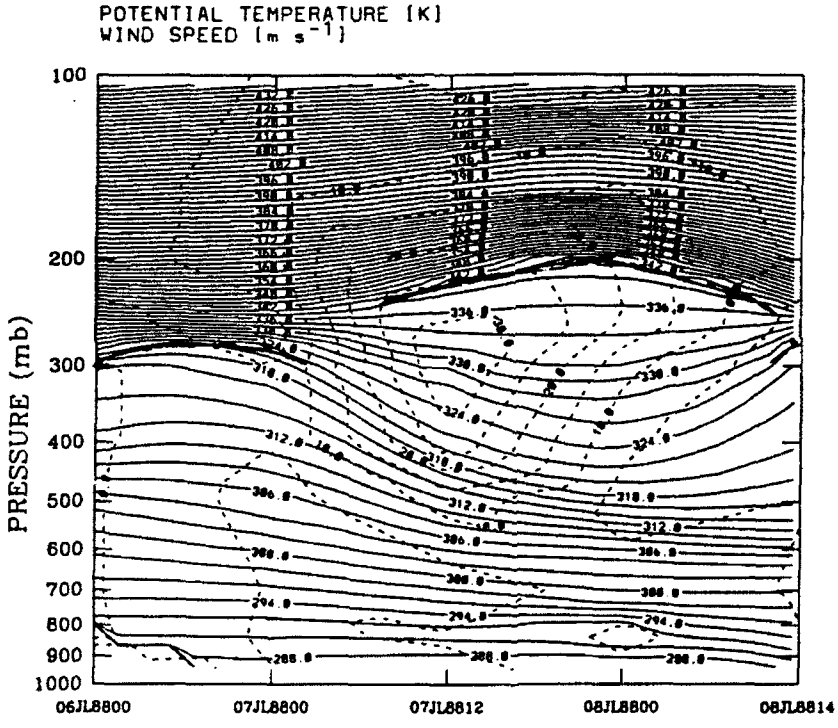

Figure 3.36 Parcel-Time Series for points in Table 3.3 at 313K potential temperature level for potential temperature in K (solid lines), and windspeed in m/s (dashed). Heavy line represents tropopause.

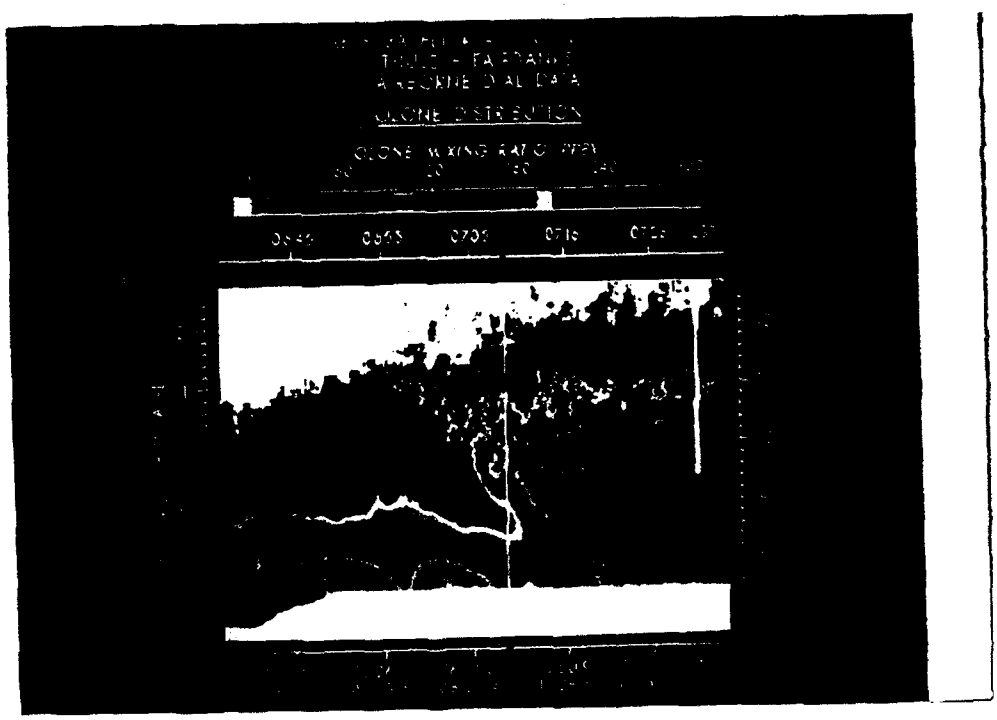

Figure 3.37 Airborne Lidar measurements of ozone mixing ratio during Mission 4 showing an intrusion due to a polar vortex.

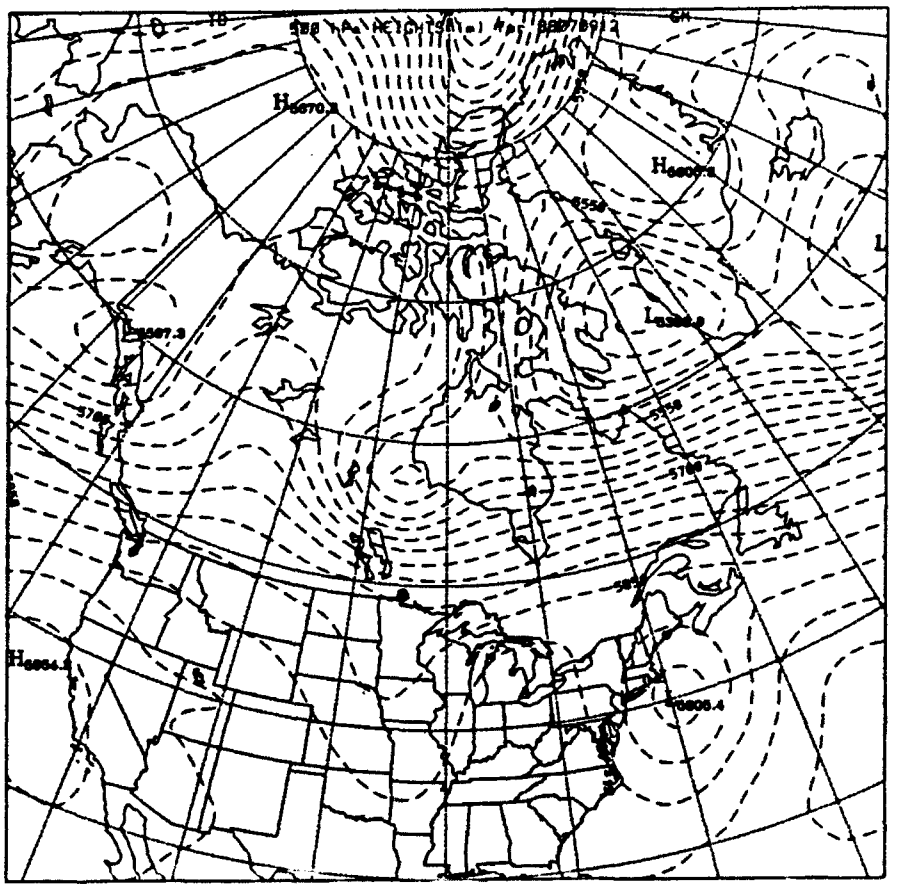

Figure 3.38 500mb pressure heights in m (dashed) for Jul 1988 at 9/12Z. Mission 4 flight path noted by thick solid line.

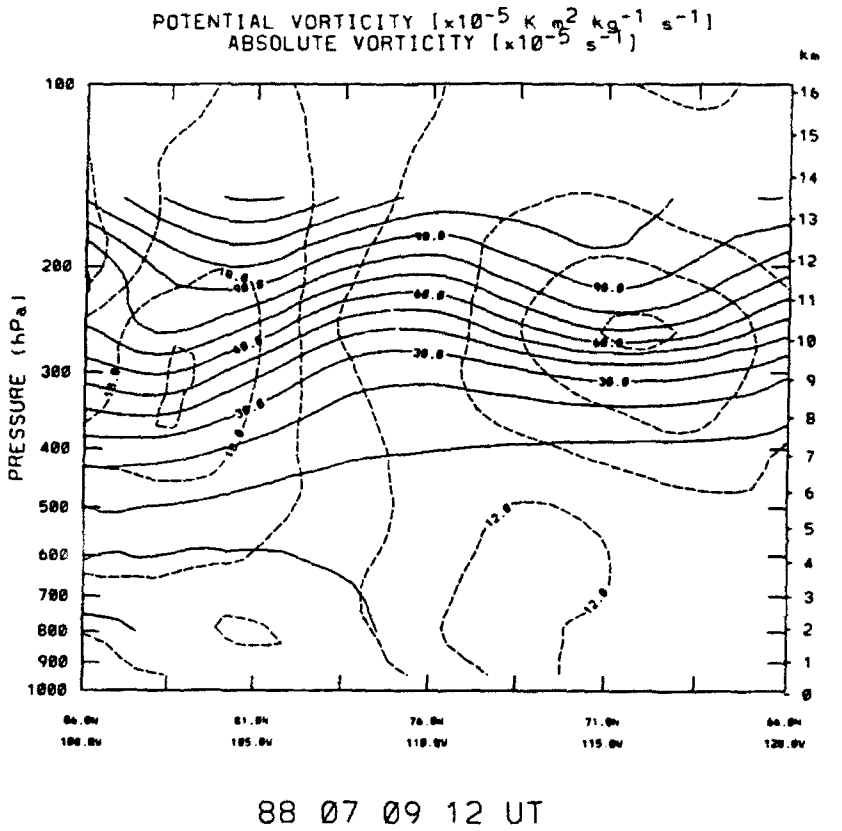

Figure 3.39 Cross-section from 86N, 100W to 66N, 120W at 9/12Z of potential vorticity (solid line) and absolute vorticity (dashed). Point of interest 76N, 110W on the edge of absolute vorticity maximum and in the area of changing potential vorticity at altitude 8-10 km.

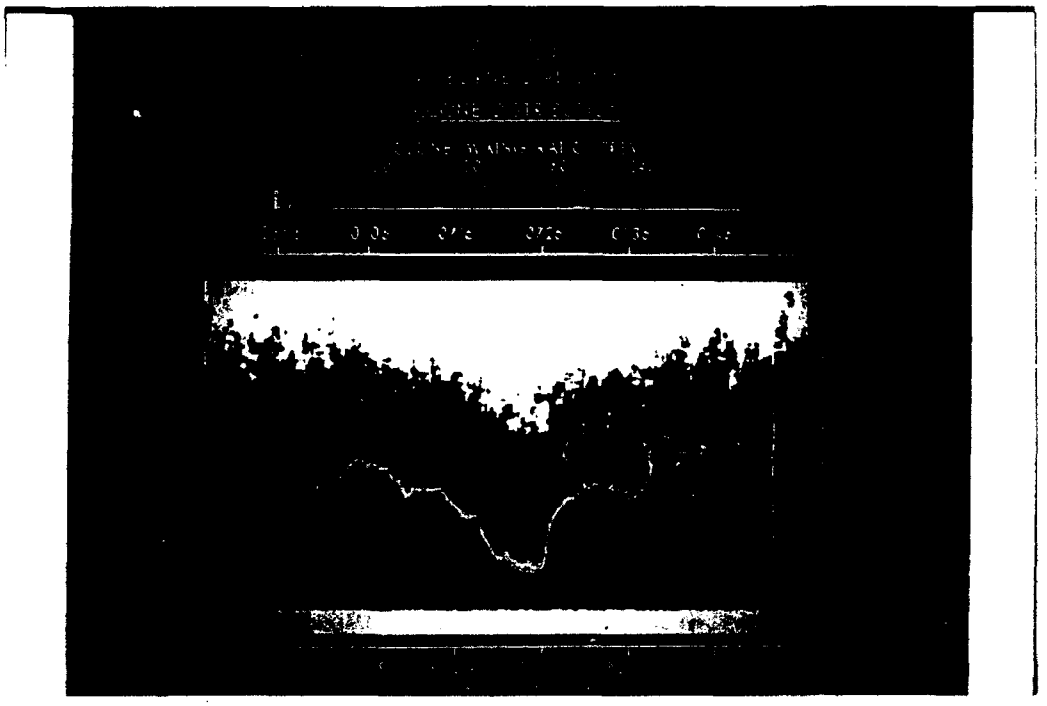

Figure 3.40 Airborne Lidar measurements of ozone mixing ratio during Mission 30 showing an intrusion due to a polar vortex.

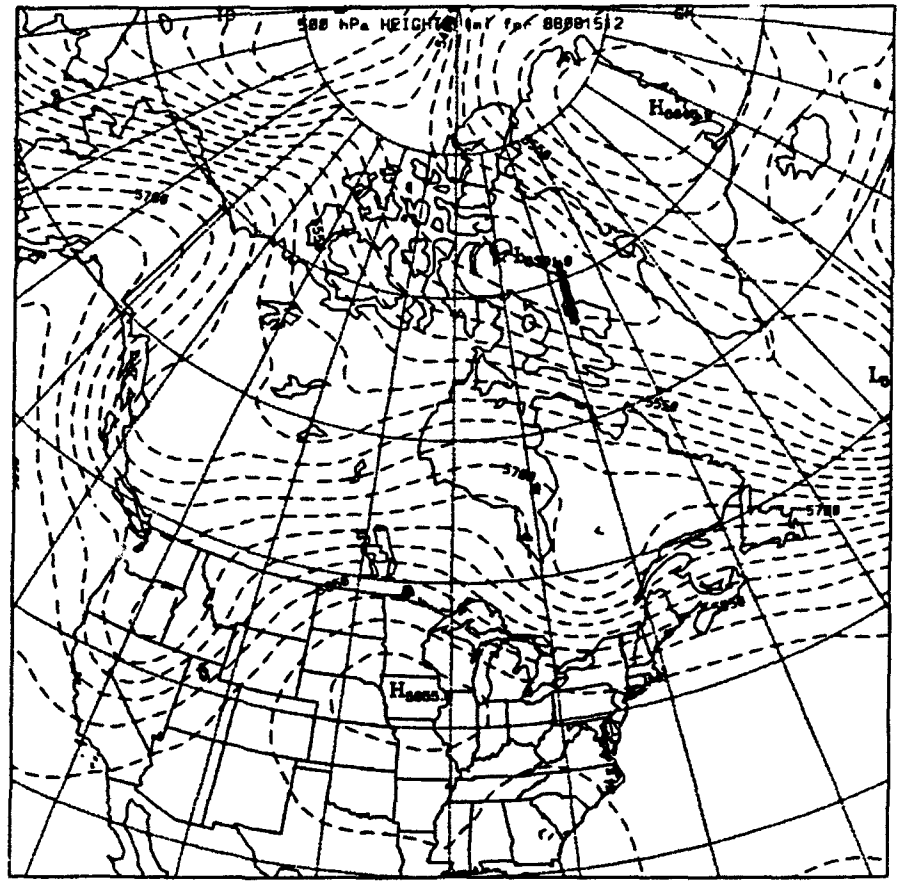

Figure 3.41 500mb pressure heights in m (dashed) for August 1988 at 15/12Z. Mission 30 flight path noted by thick solid line.

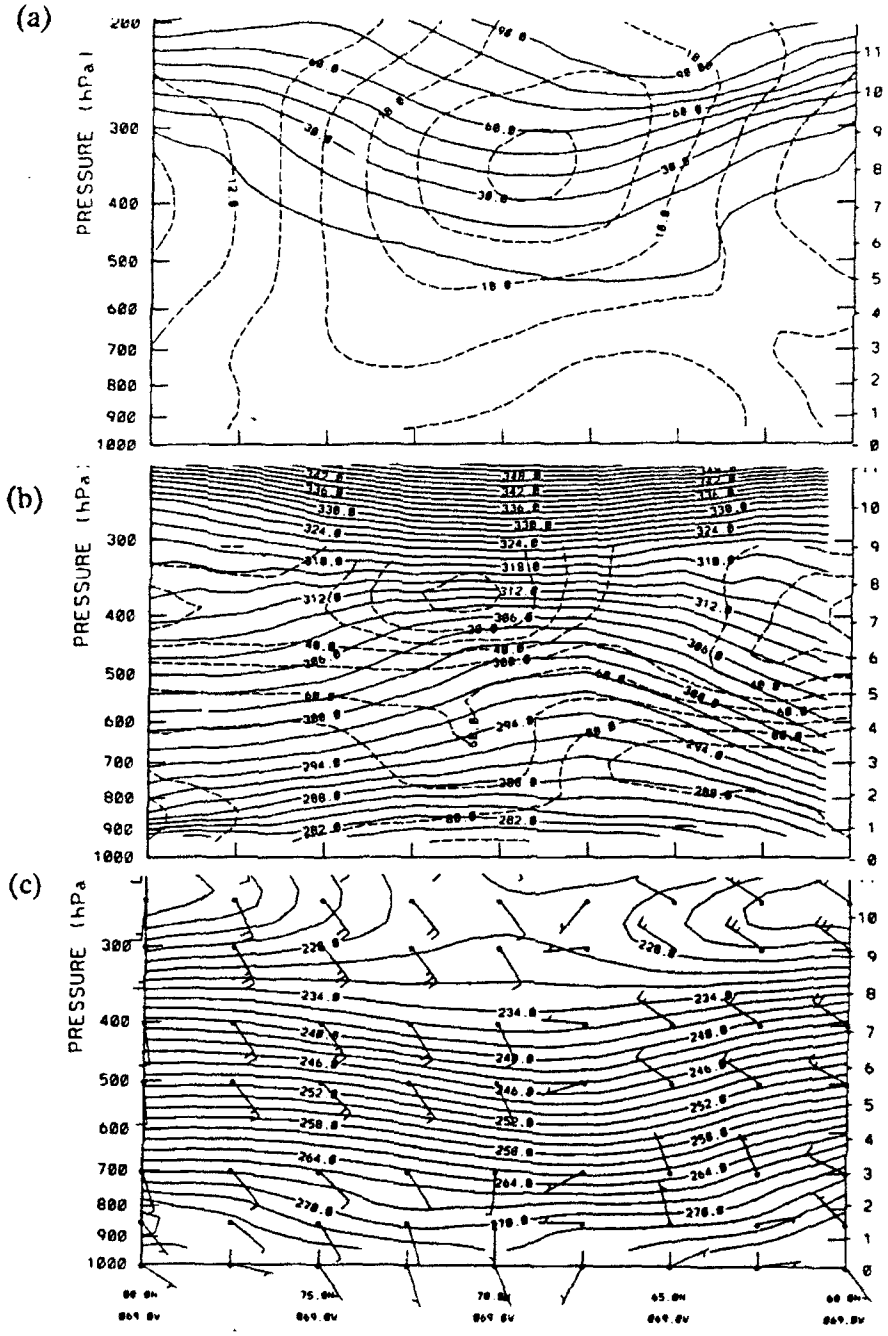

Figure 3.42 Cross-section from 80N, 69W to 60N, 69W for August 1988 at 15/12Z. (a) potential vorticity in deca PVU (solid) and absolute in AVU (dashed), (b) potential temperature in K (solid)/relative humidity in percent (dashed); (c) temperature in K (solid) and windbarbs.

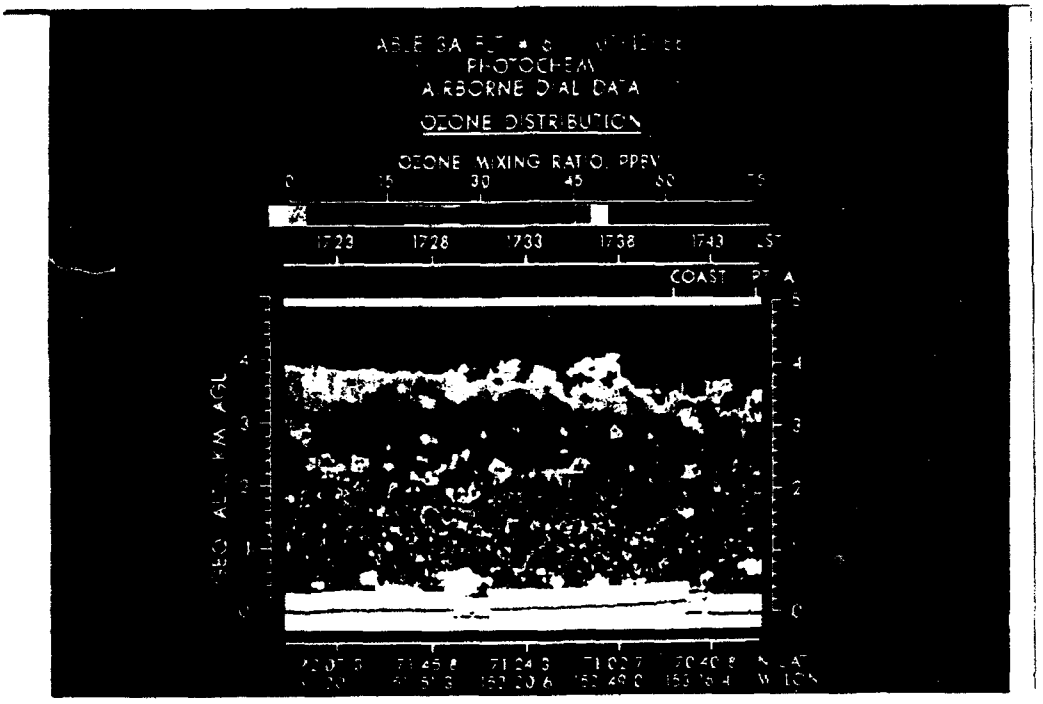

Figure 3.43 Airborne Lidar measurements of ozone mixing ratio during Mission 6 showing patches of ozone maximums at lower levels.

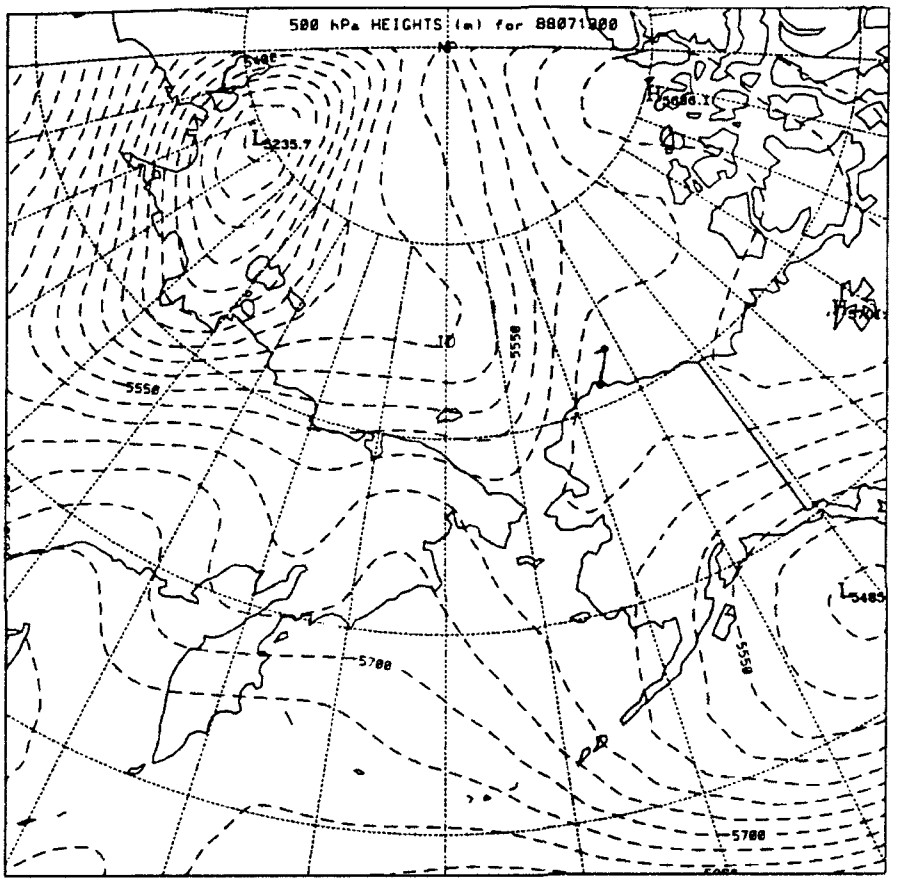

Figure 3.44 500mb pressure heights in m (dashed) for July 1988 at 13/00Z. Mission 6 flight path noted by thick solid line.

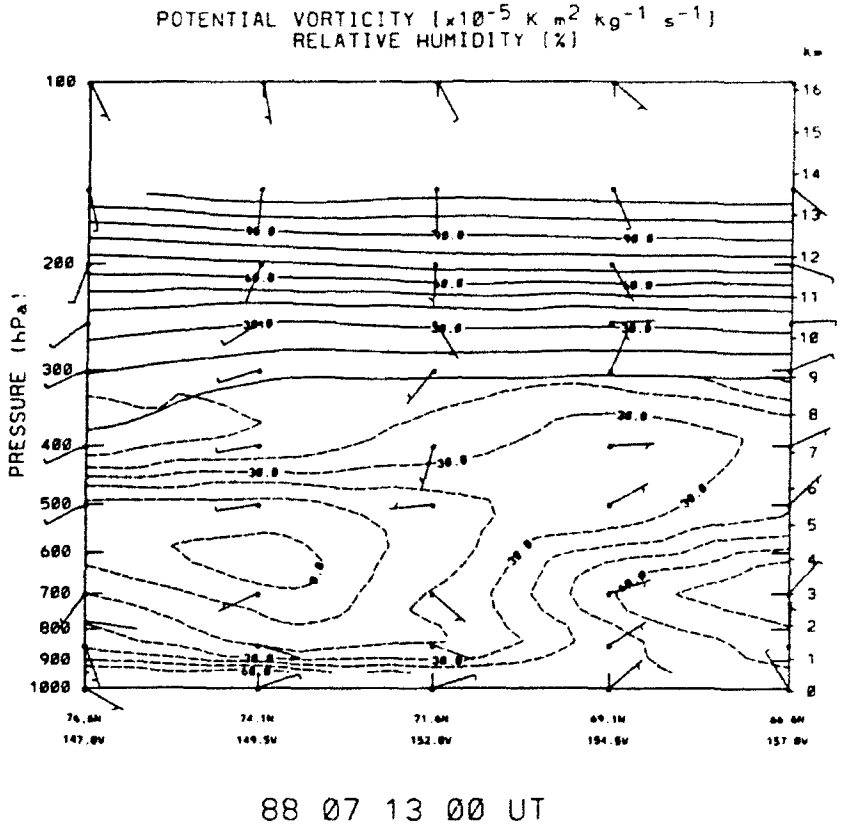

Figure 3.45 Cross-section from 76.6N, 147W to 66.6N, 157W for July 1988 at 15/12Z of potential vorticity in deca PVU (solid), relative humidity (dashed) and windbarbs. The relative humidity indicates dry air at altitudes 1-7km to right of 153W.

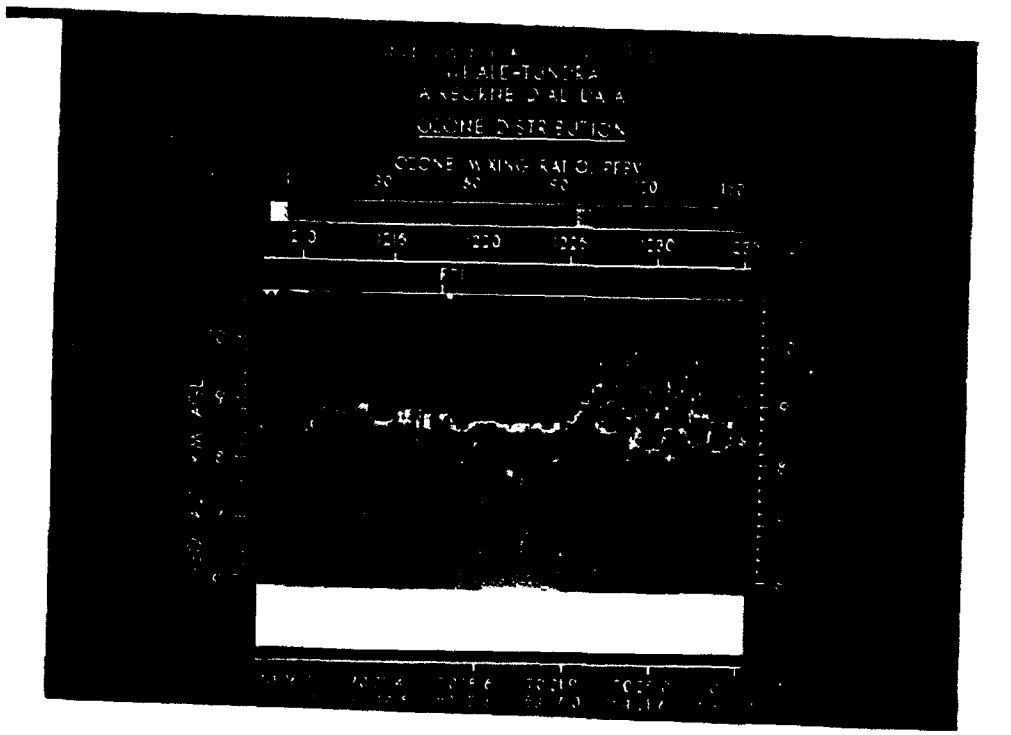

Figure 3.46 Airborne Lidar measurements of ozone mixing ratio during Mission 7 showing patches of ozone minimums at lower levels.

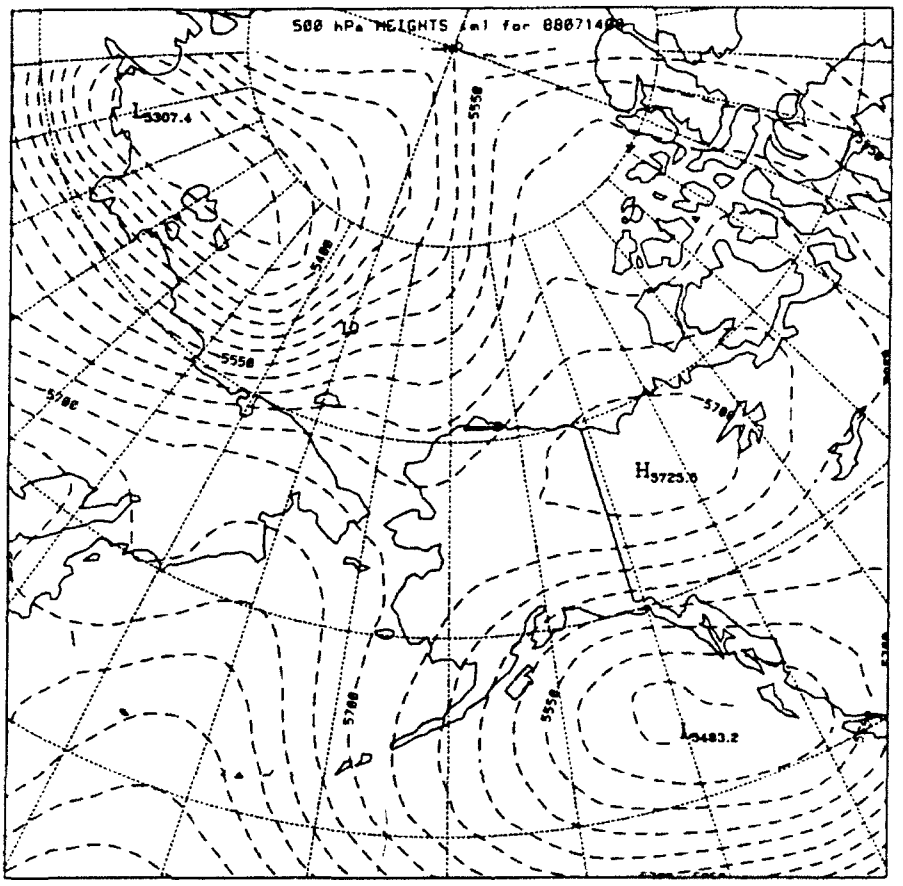

Figure 3.47 500mb pressure heights in m (dashed) for July 1988 at 14/00Z. Mission 7 flight path noted by thick solid line.

(a)

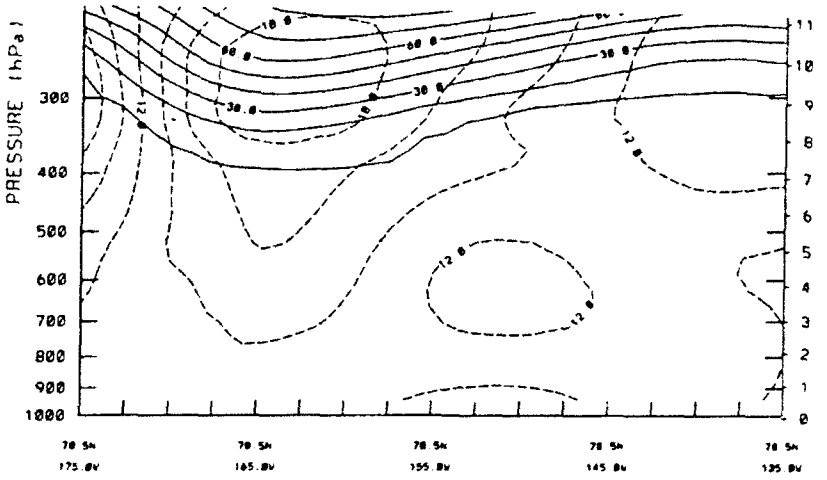

88 07 14 00 UT

(b)

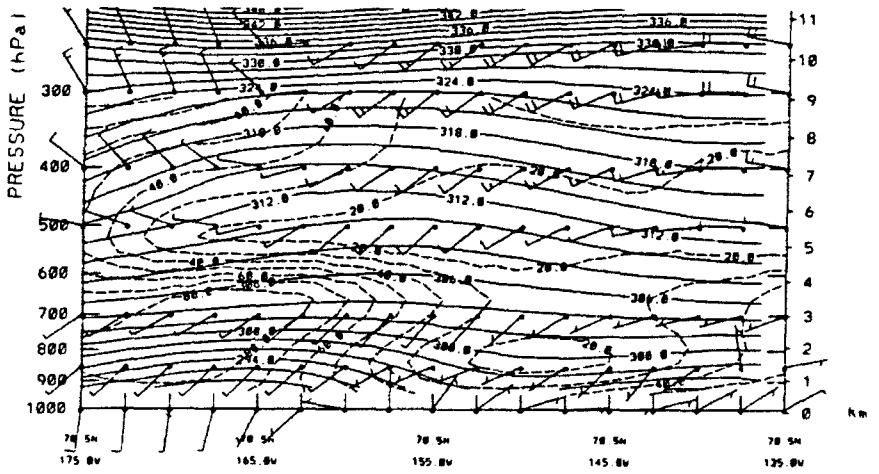

88 07 14 00 UT

Figure 3.48 Cross-section from 70.5N, 175W-135W for July 88 at 14/00Z. (a) potential vorticity in deca PVU (solid) and absolute vorticity in AVU (dashed) and (b) potential temperature in K (solid) and relative humidity in percent (dashed) and windbarbs.

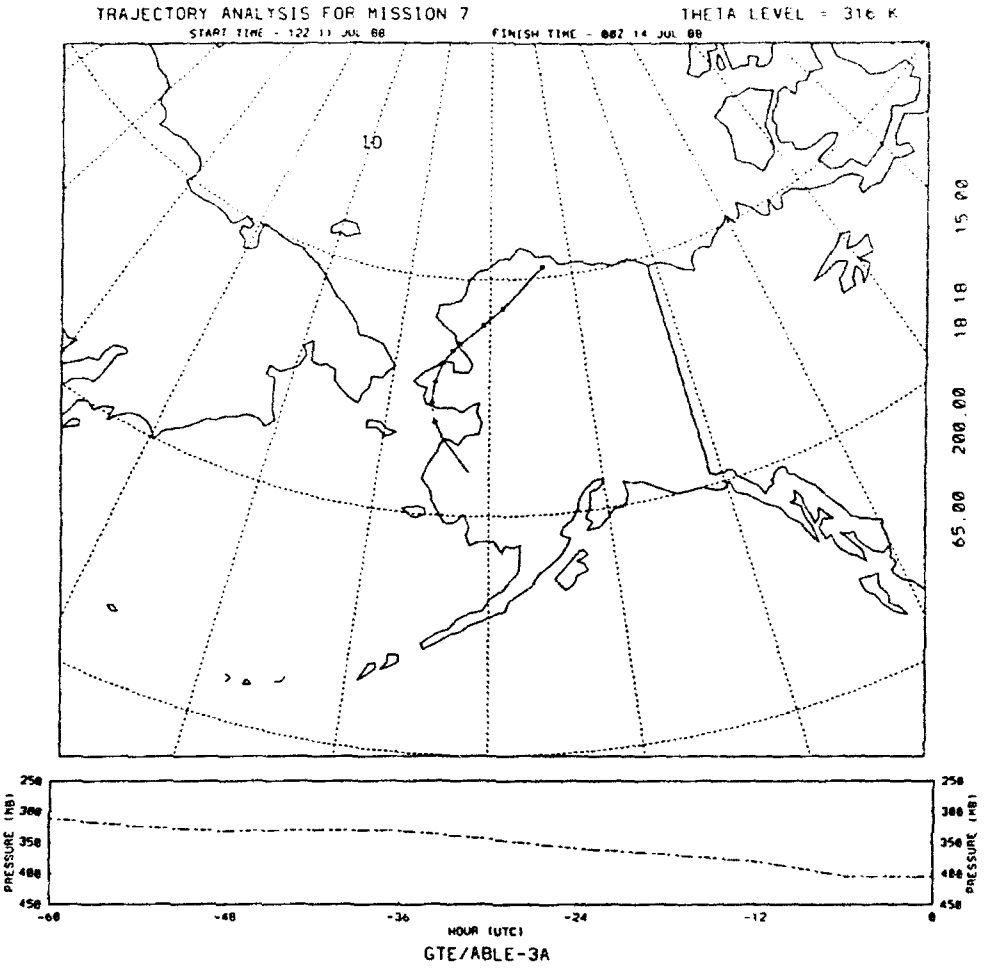

Figure 3.49 Isentropic back trajectory at the 316K potential temperature level for enhanced ozone areas at point 70.5N, 153.3W. Top graph shows pressure heights (dashed) with the corresponding path on map.

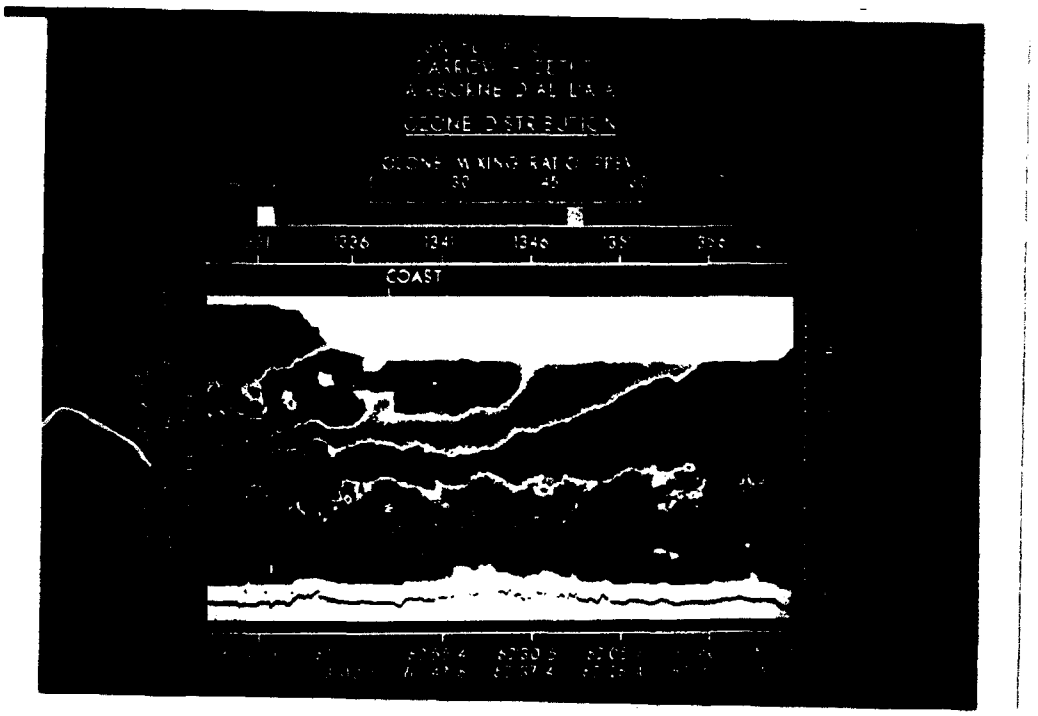

Figure 3.50 Airborne Lidar measurements of ozone mixing ratio during Mission 13 showing a tongue of enhanced ozone at 2.5km.

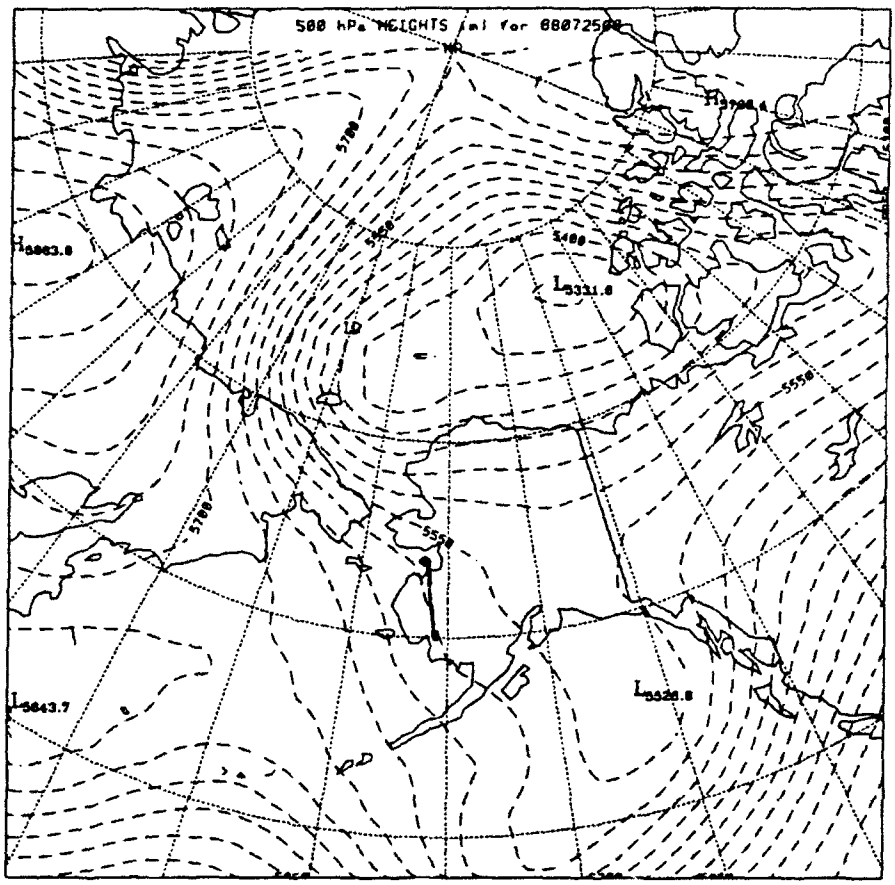

Figure 3.51 500mb pressure heights in m (dashed) for July 1988 at 25/00Z. Mission 13 flight path noted by thick solid line.

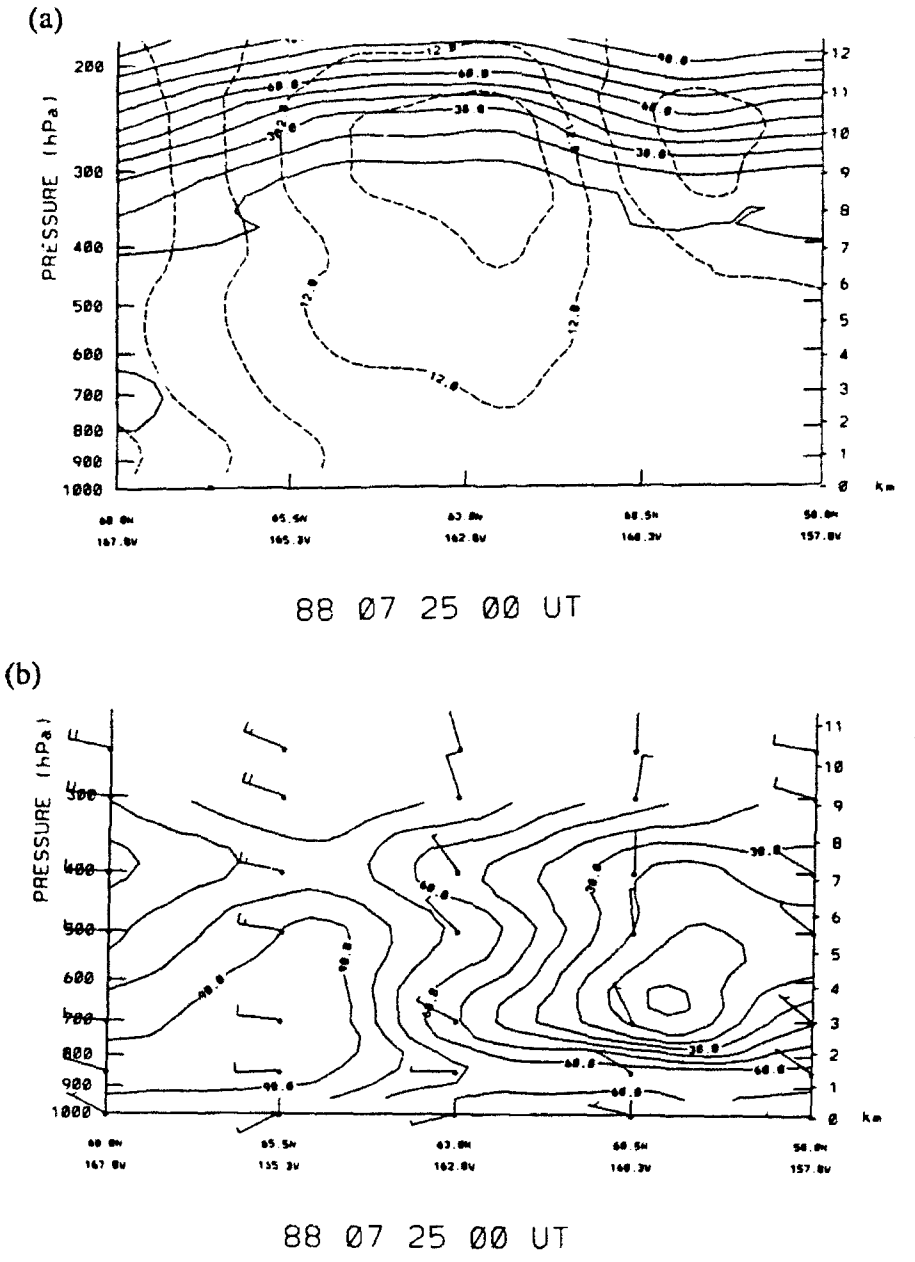

Figure 3.52 Cross-section from 68N 167.8W to 58N 157.8N for July 88 at 25/00Z for (a) potential vorticity in deca PVU (solid) and absolute vorticity AVU (dashed) and (b) relative humidity in percent (solid) and windbarbs. In (a), absolute vorticity minimum over area covered by figure 3.50 indicating high pressure (sinking air). In (b), low relative humidity also over N 162.8W and to east.

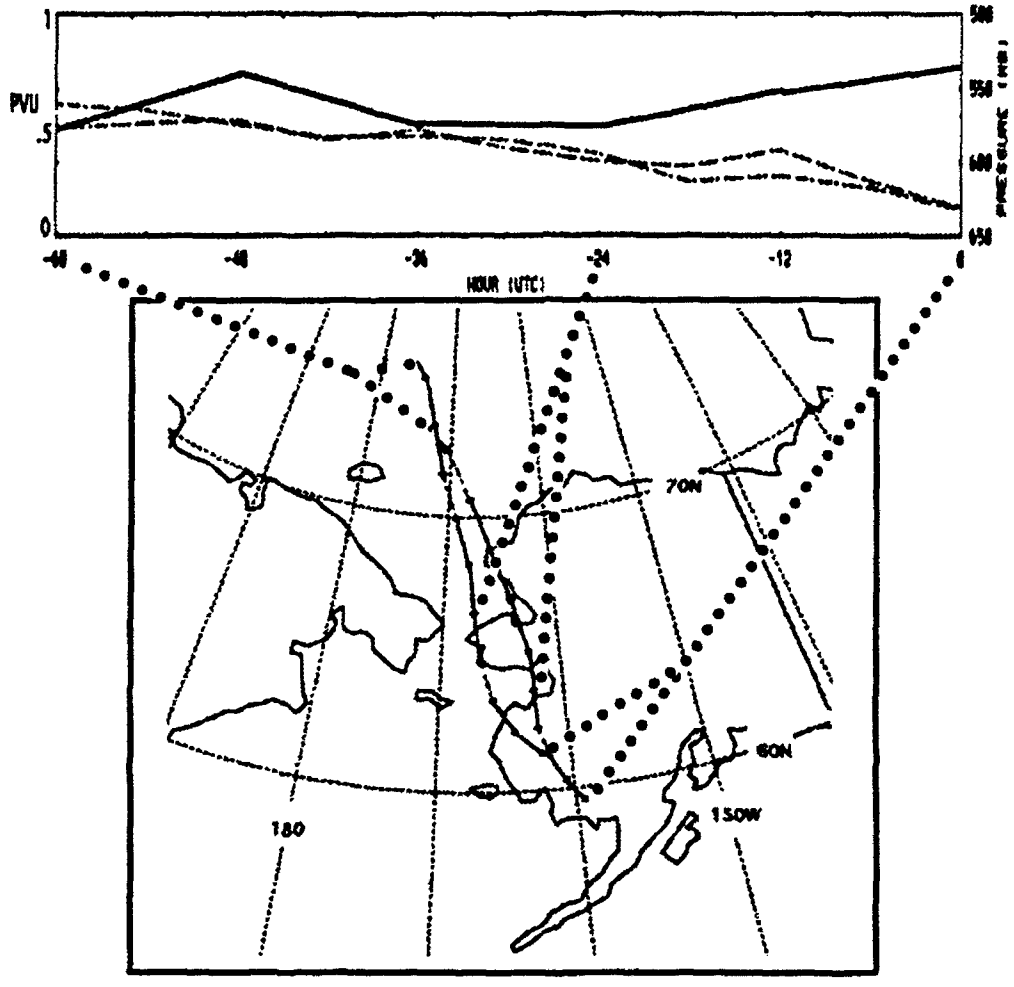

Figure 3.53 Isentropic back trajectory for graph of potential vorticity in PVU (solid line) and pressure heights in mb (dashed) with corresponding trajectory path for 303K potential temperature level for point 59.5N, 159.3W and 61.3N, 162W.

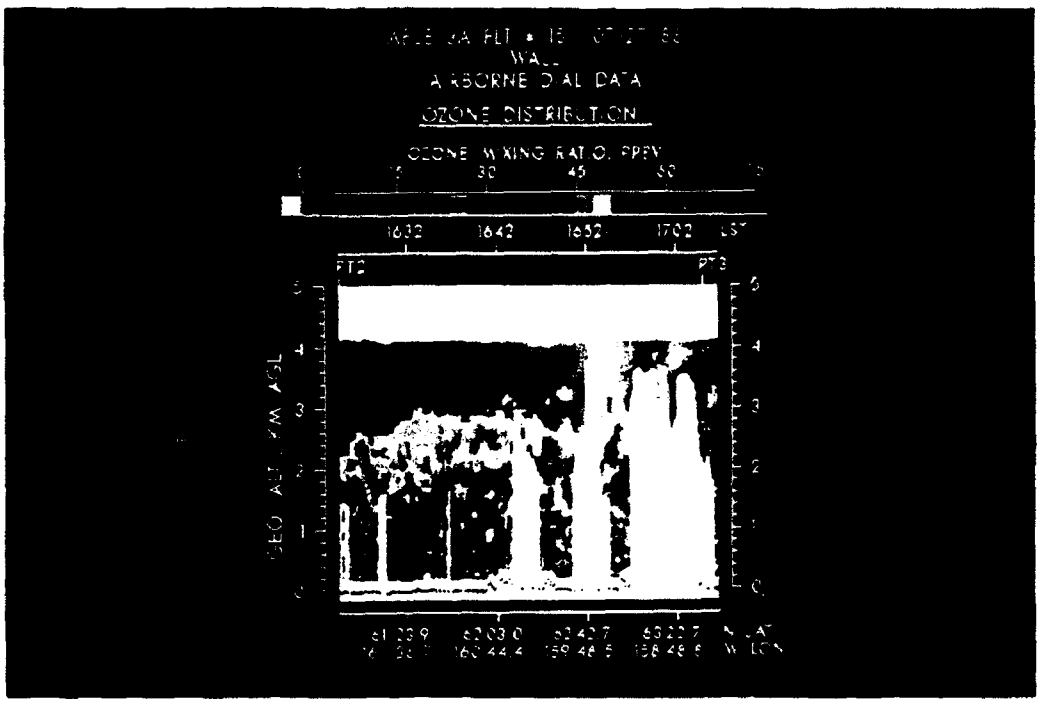

Figure 3.54 Airborne Lidar measurements of ozone mixing ratio during Mission 15 showing a tongue of maximum ozone at 2.5km.

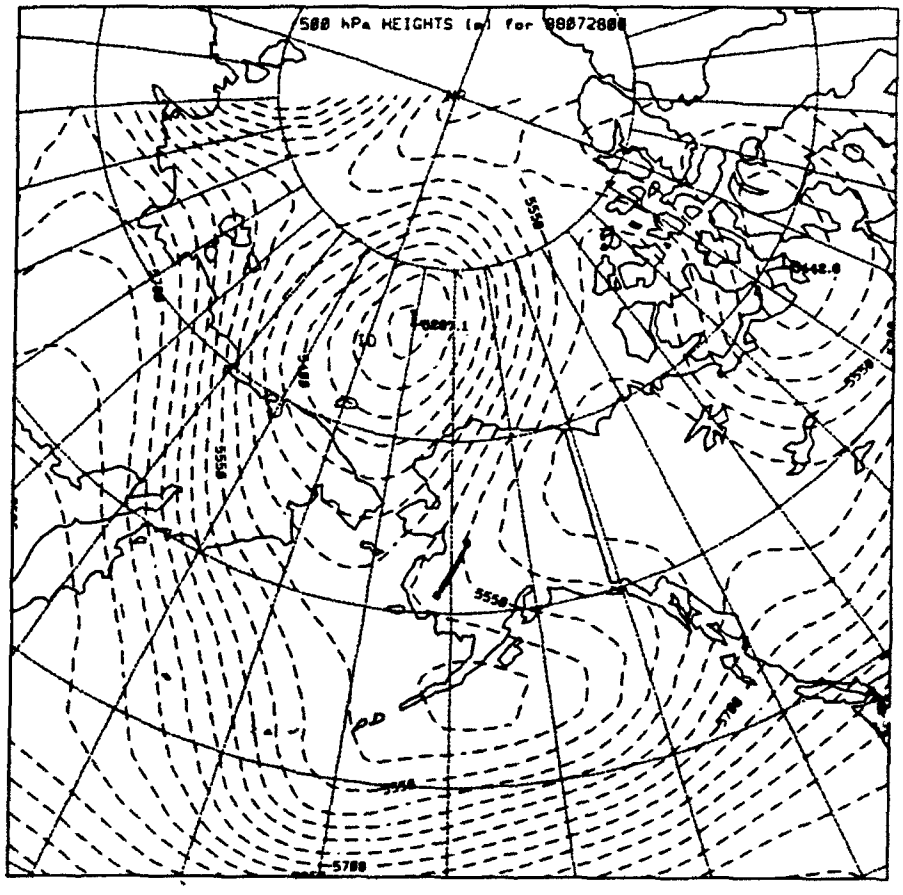

Figure 3.55 500mb pressure heights in m (dashed) for July 1988 at 28/00Z. Mission 15 flight path noted by thick solid line.

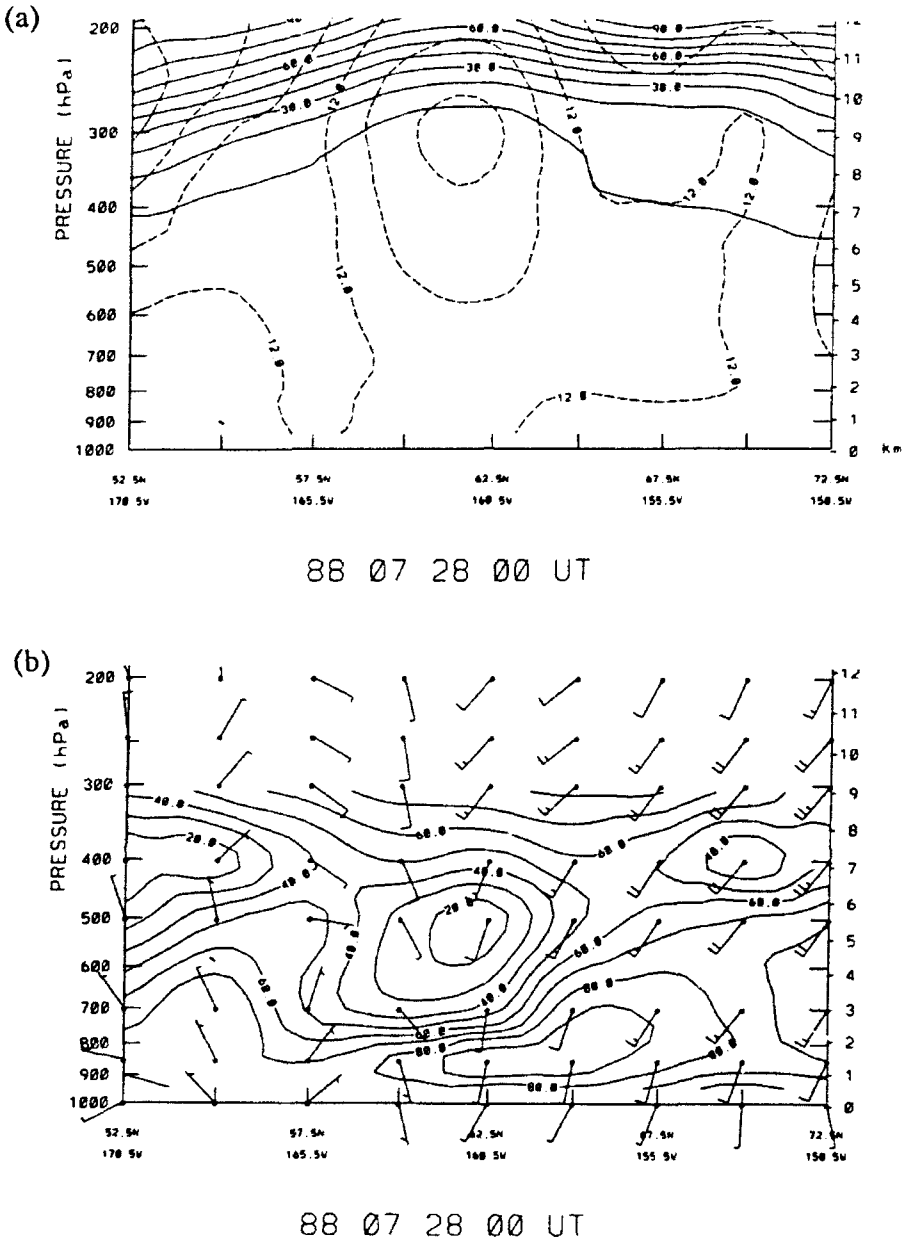

Figure 3.56 Cross-section from 52.5N, 170.5W to 72.5N, 150.5N for July 88 at 28/00Z for (a) potential vorticity in deca PVU (solid) and absolute vorticity in AVU (dashed) and (b) relative humidity in percent (solid) and windbarbs. An area absolute vorticity and relative humidity minimum at altitude over area in Figure 3.54 indicated high pressure (sinking air).

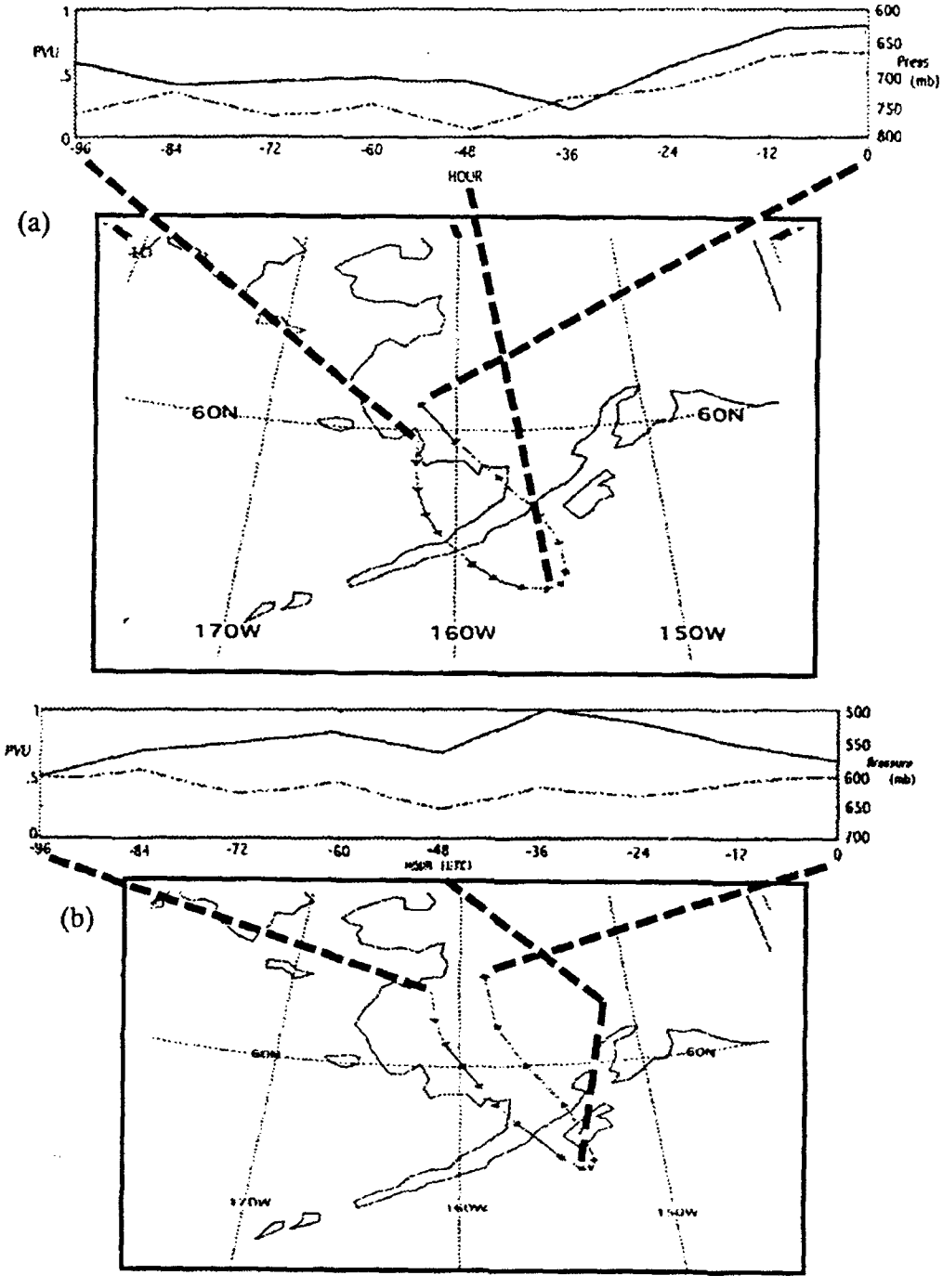

Figure 3.57 Isentropic back-trajectory for graph of potential vorticity in PVU (solid line) and pressure heights in mb (dashed) with corresponding trajectory path for (a) 298K potential temperature level for point 61N, 162W and (b) 303K potential temperature level for point 63.58N, 158.5W.

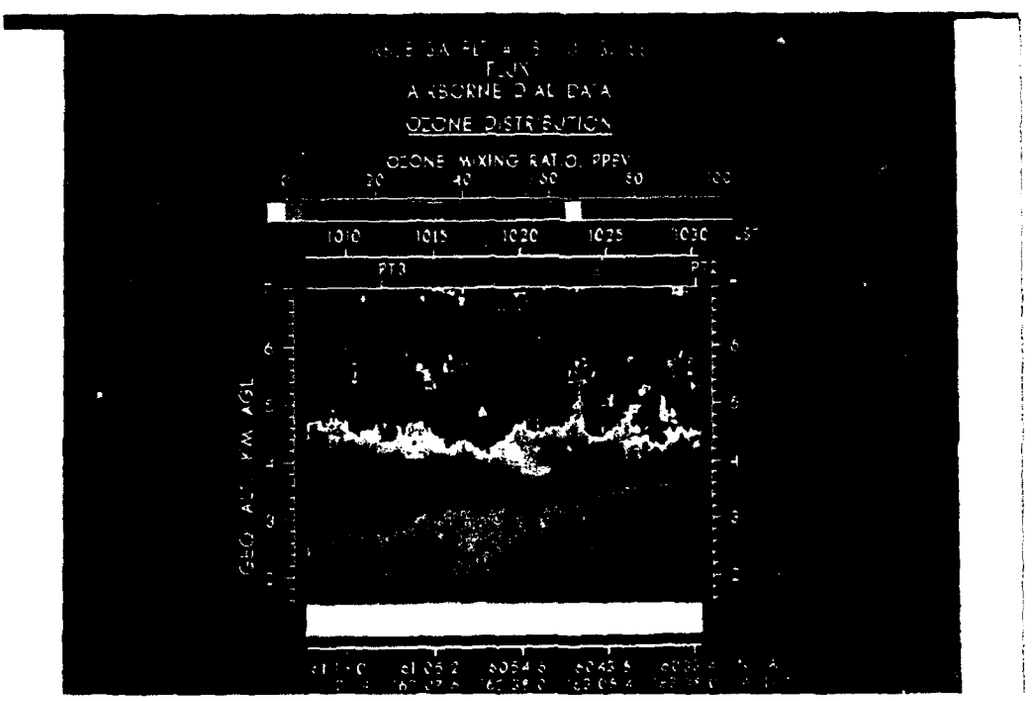

Figure 3.58 Airborne Lidar measurements of ozone mixing ratio during Mission 18 showing larger than normal ozone values above 5km.

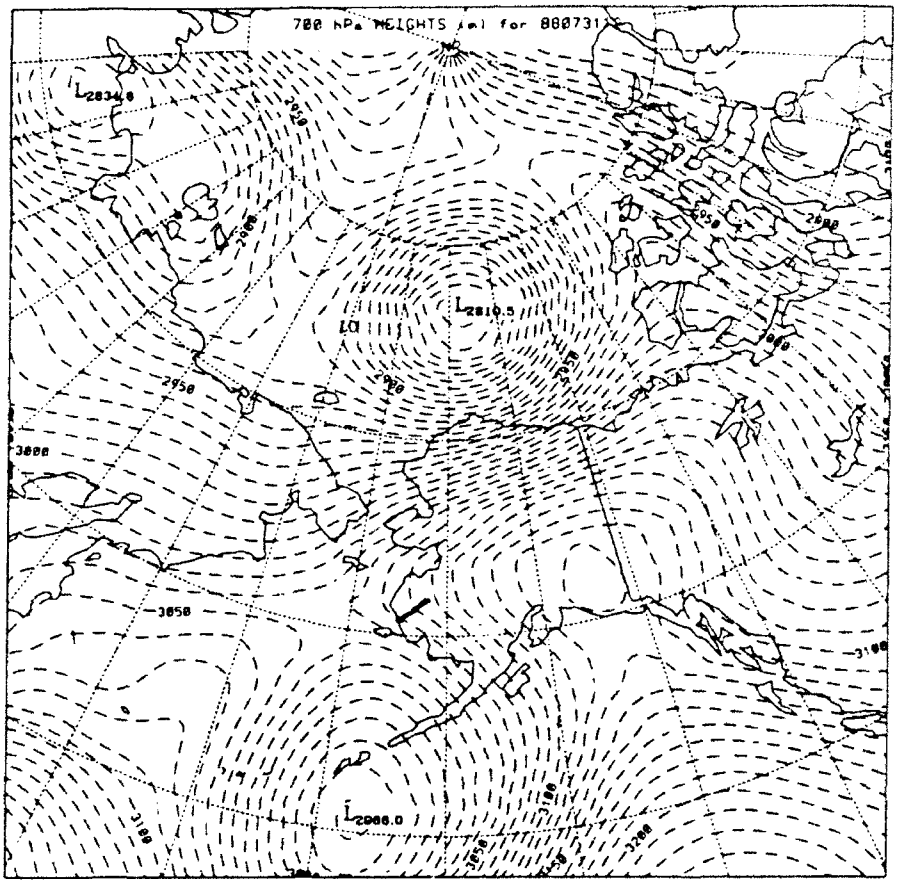

Figure 3.59 700:nb pressure heights in m (dashed) for July 88 at 31/12Z. Mission 18 flight path noted by thick solid line.

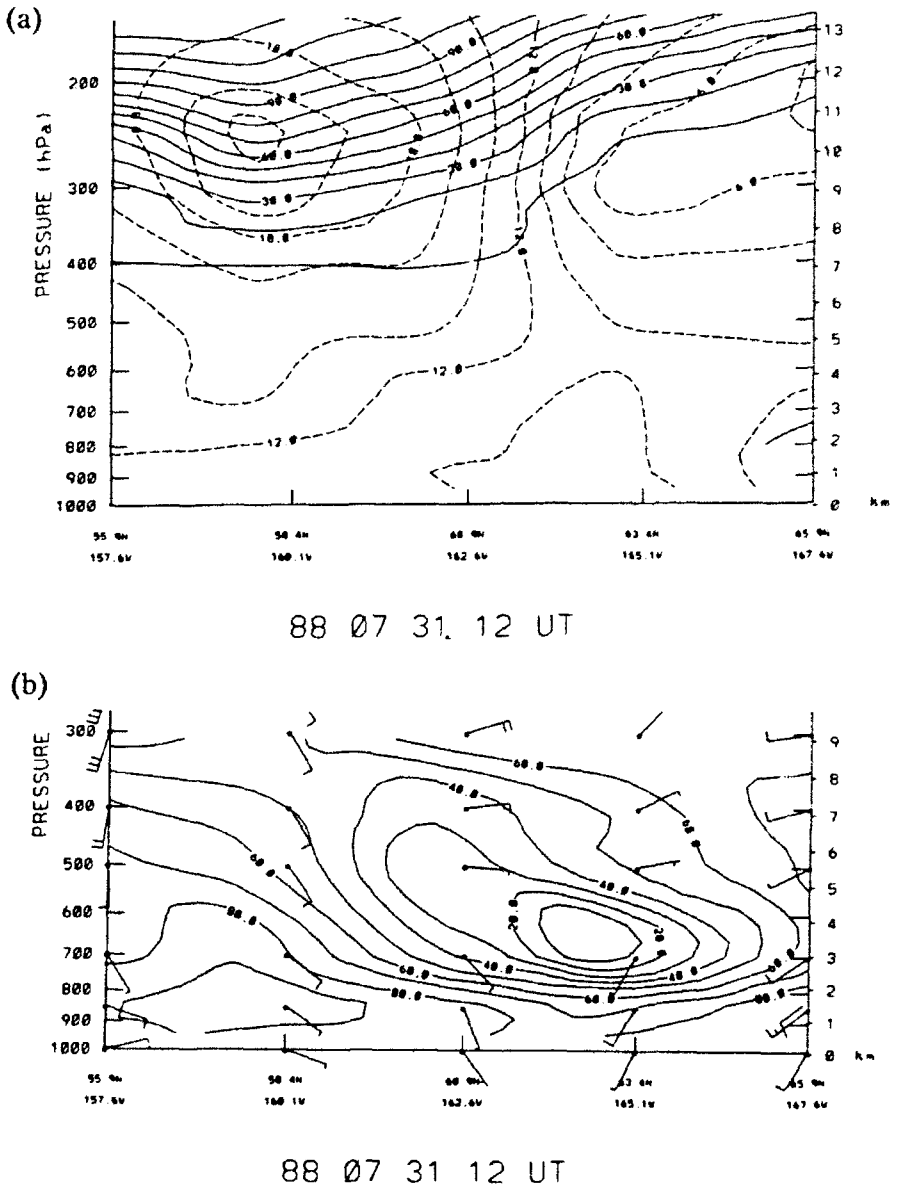

Figure 3.60 Cross-section from 55.9N, 157.6W to 65.9N, 167.6W (a) potential vorticity in deca PVU (solid) and absolute vorticity in AVU (dashed) at 31/12Z July 1988, (b) relative humidity in percent (solid) and inbarbs at 31/12Z July 1988, (c) same as (a) except at 01/00Z August 1988, and (d) same as (b) except at 01/00Z August 1988.

(c)

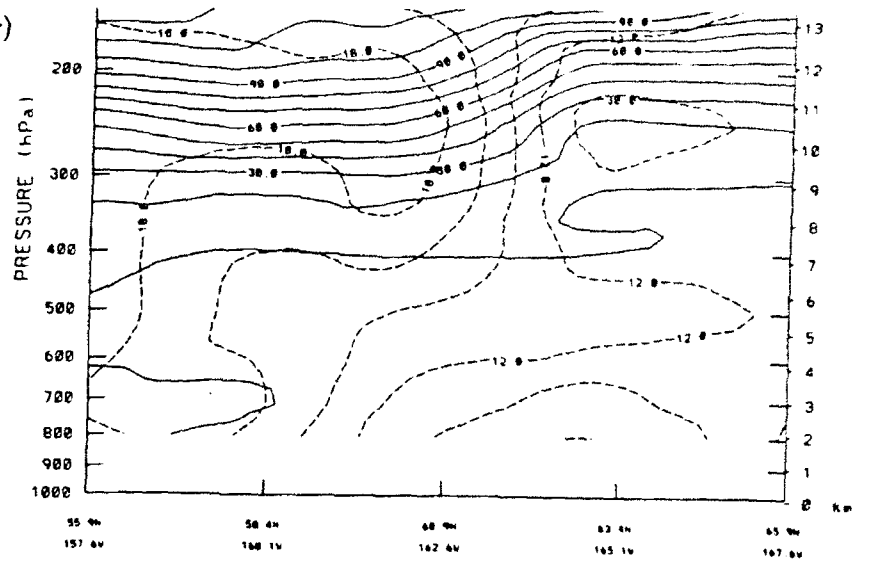

88 08 01 00 UT

(d)

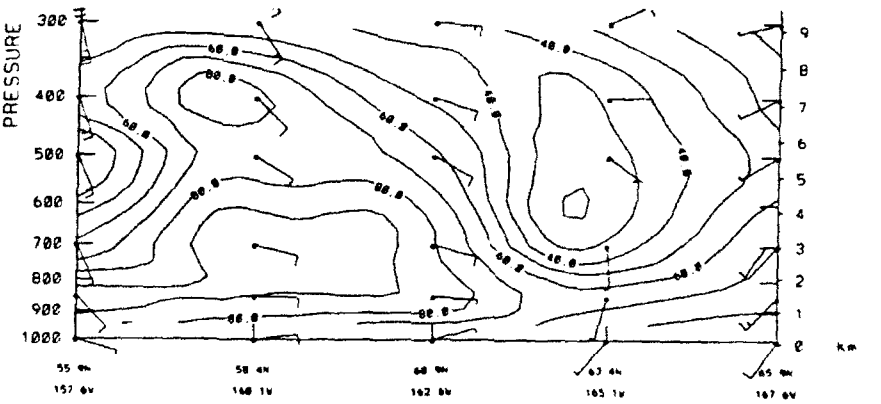

88 08 01 00 UT

Figure 3.60 Cross-section from 55.9N, 157.6W to 65.9N, 167.6W (a) potential vorticity in deca PVU (solid) and absolute vorticity in AVU (dashed) at 31/12Z July 1988, (b) relative humidity in percent (solid) and inbarbs at 31/12Z July 1988,
(c) same as (a) except at 01/00Z August 1988, and (d) same as (b) except at 01/00Z August 1988.

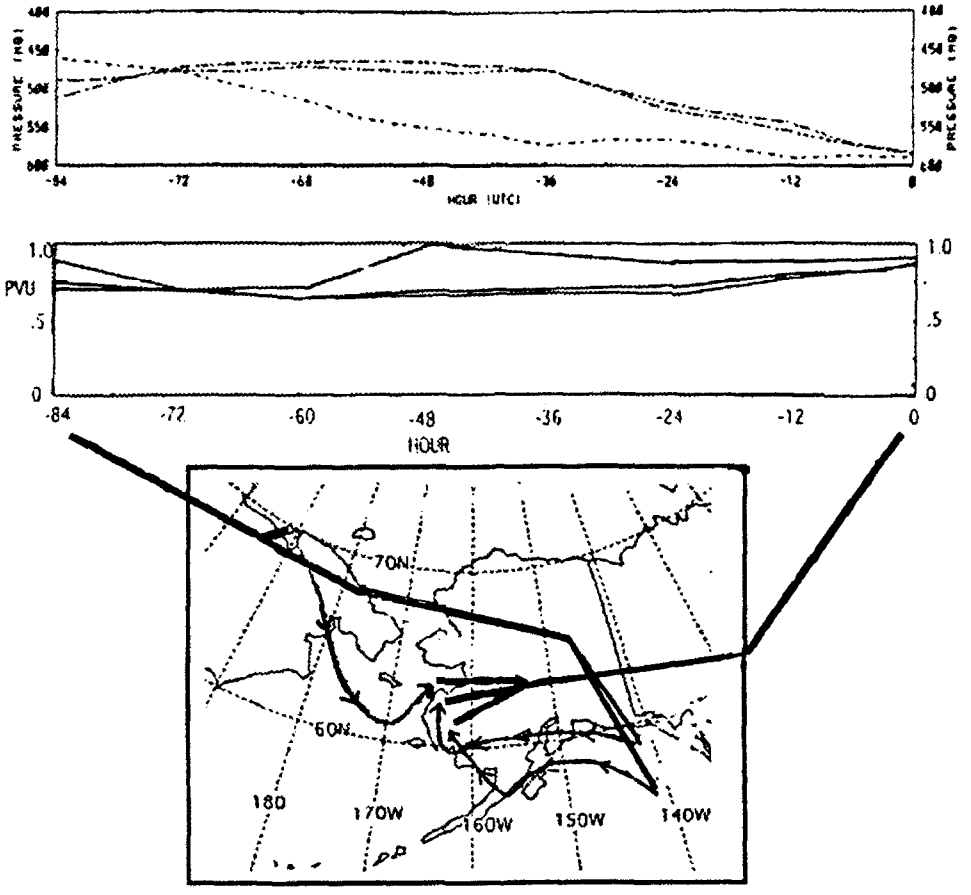

Figure 3.61 Isentropic back trajectory for graph of potential vorticity in PVU (solid line) and pressure heights in mb (dashed) with corresponding trajectory path at the 306K potential temperature level for points (a) 60.9N, 162.6W, (b) 62.4N, 164.1W and (c) 63.4N, 165W.

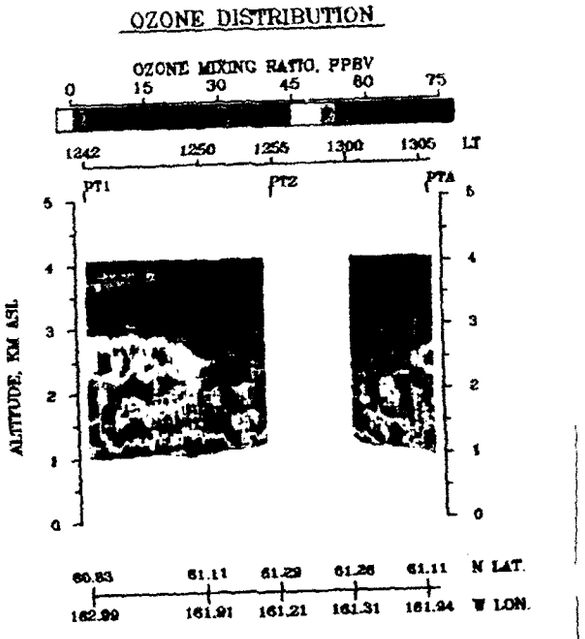

Figure 3.62 Airborne Lidar measurements of ozone mixing ratio during Mission 21 showing larger than normal ozone values at 2.5km.

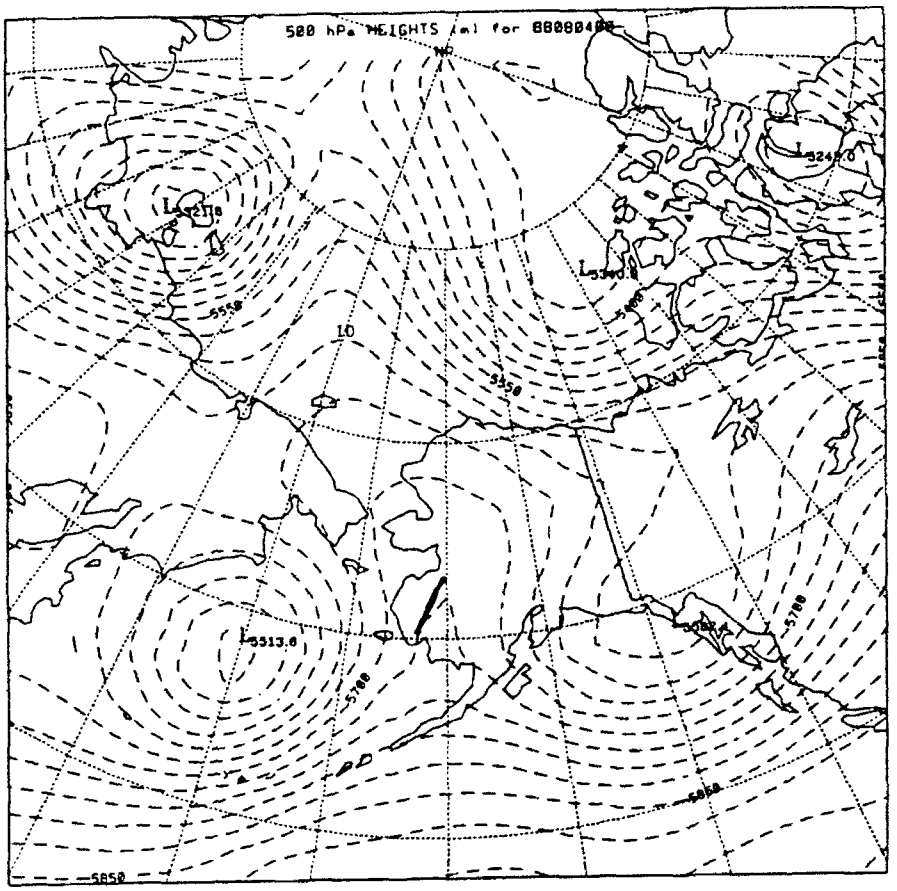

Figure 3.63 500mb pressure heights in m (dashed) for August 88 at 4/00Z. Mission 21 flight path noted by thick solid line.

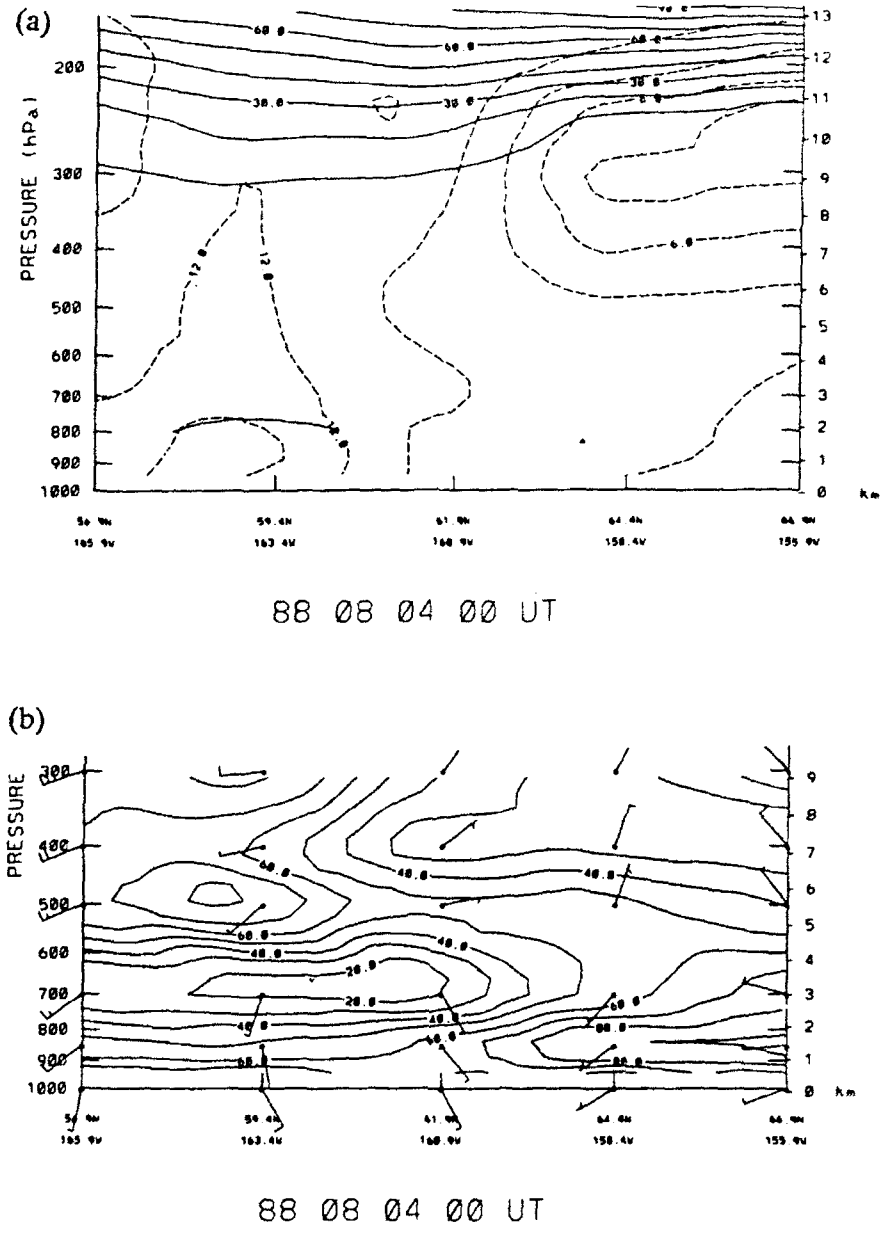

Figure 3.64 Cross-section from 56.9N, 165.9W to 66.9N, 155.9W at 4/00Z August, 1988 for (a) potential vorticity in deca PVU (solid) and absolute vorticity in AVU (dashed) and (b) relative humidity in percent (solid) and windbarbs. In (a), potential and absolute vorticity indicate point 61N, 161W under edge of ridge. In (b) dry air exists at points between 3-4km.

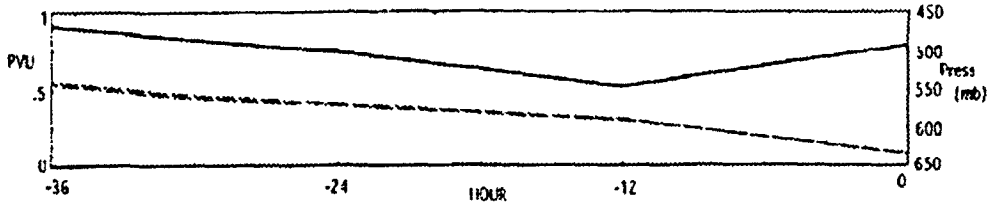

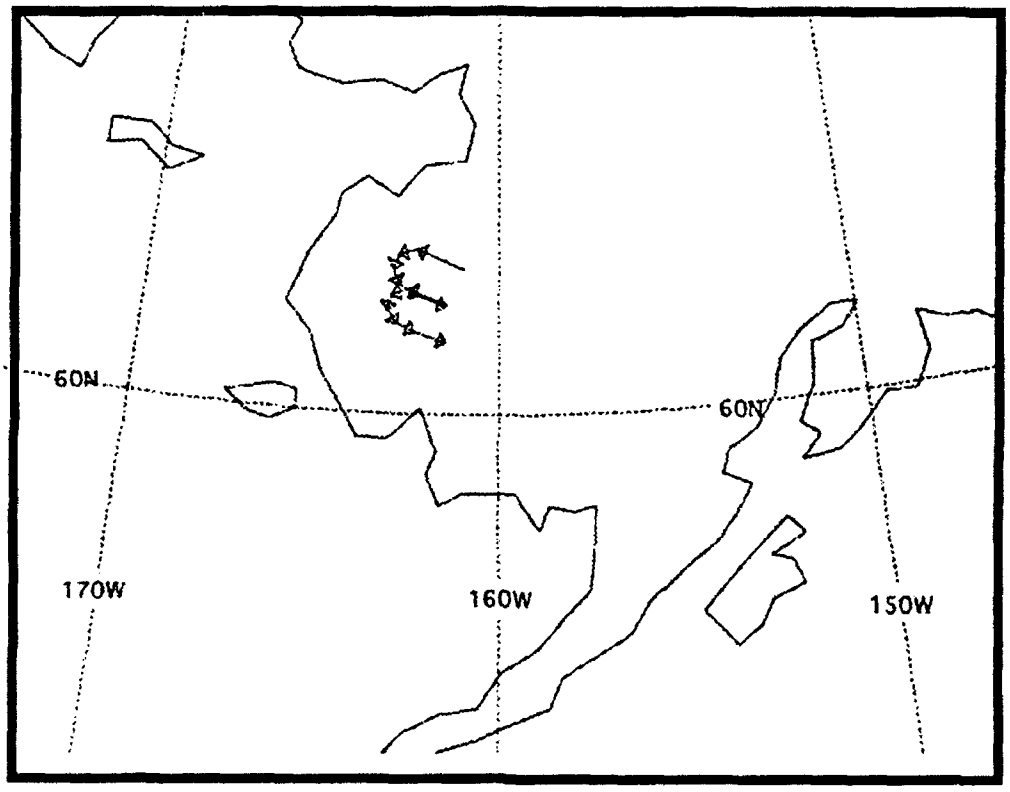

Figure 3.65 Isentropic back trajectory for graph of potential vorticity in PVU (solid line) and pressure heights in mb (dashed) with corresponding trajectory path at the 307K potential temperature level for point 61.9N, 161.9W.

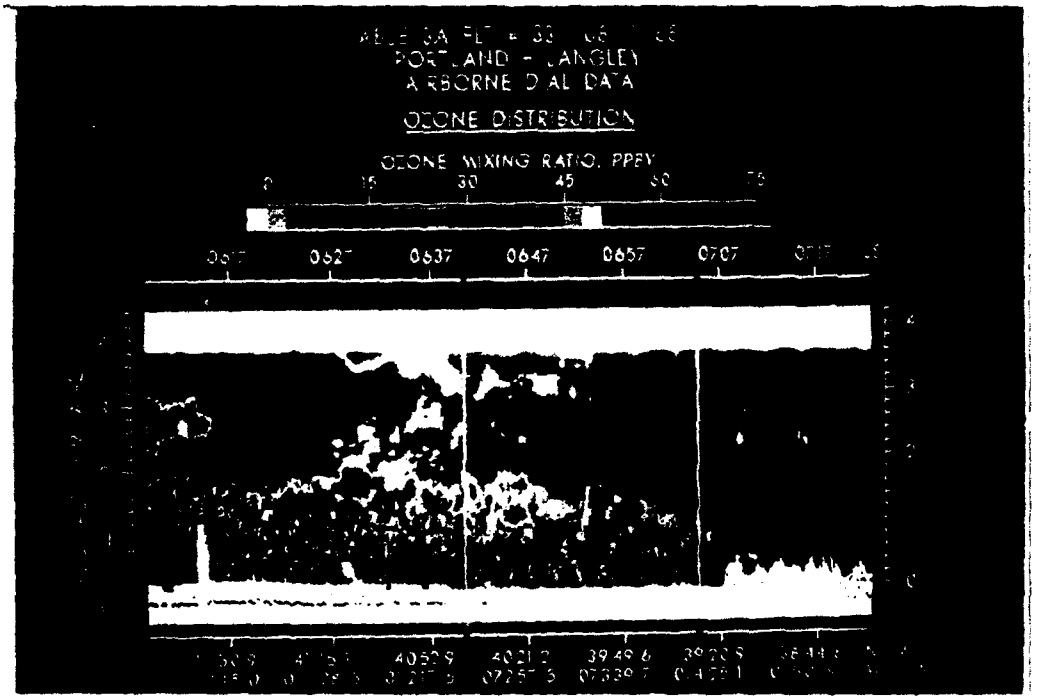

Figure 3.66 Airborne Lidar measurements of ozone mixing ratio during mission 33 showing larger than normal ozone values at 2-4 km.

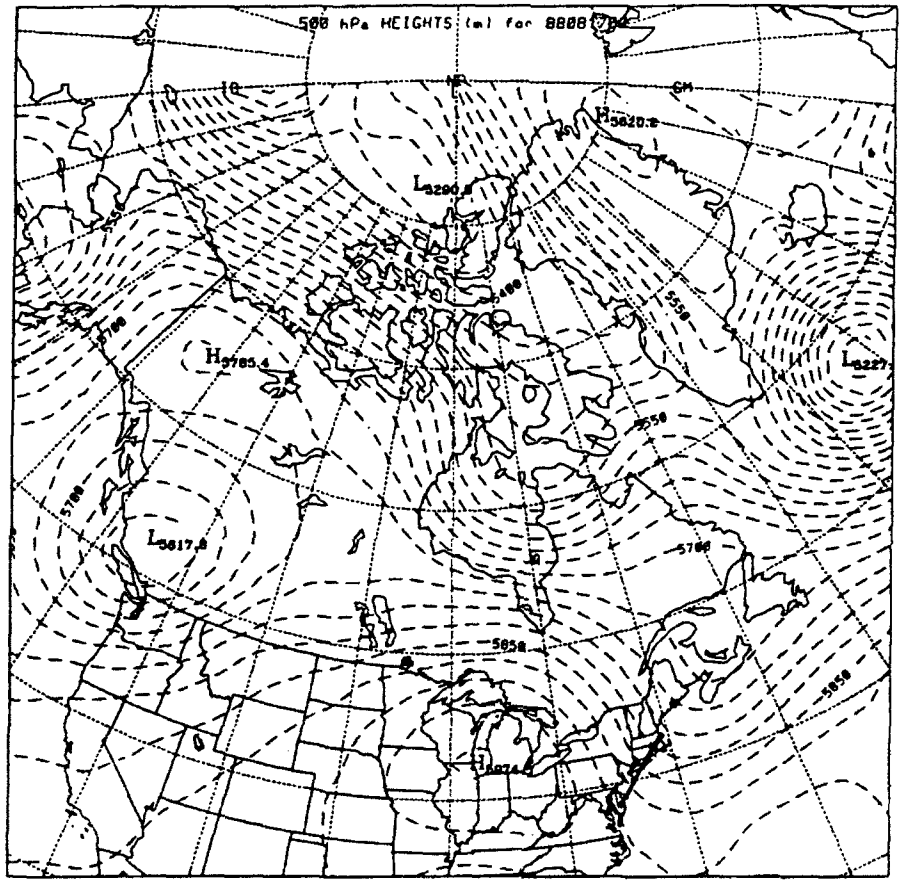

Figure 3.67 500mb pressure heights in m (dashed) for August 1988 at 17/00Z. Mission 33 flight path noted by thick solid line.

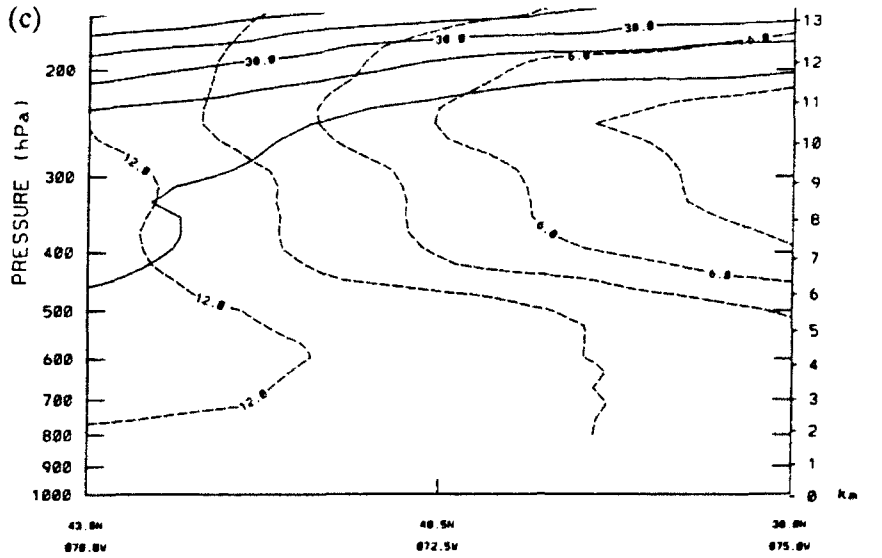

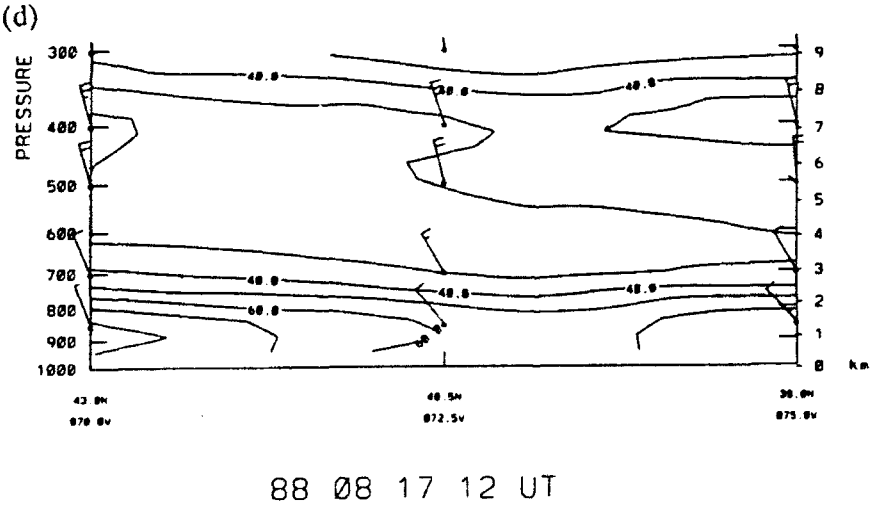

Figure 3.68 Cross-section from 43N, 70W to 38N, 75W for August 1988
(a) potential vorticity in deca PVU (solid) and absolute vorticity in AVU (dashed) at 17/00Z, (b) relative humidity in percent (solid) and windbarbs at 17/00Z, (c) same as (a) at 17/12Z and (d) same as (b) at 17/12Z.

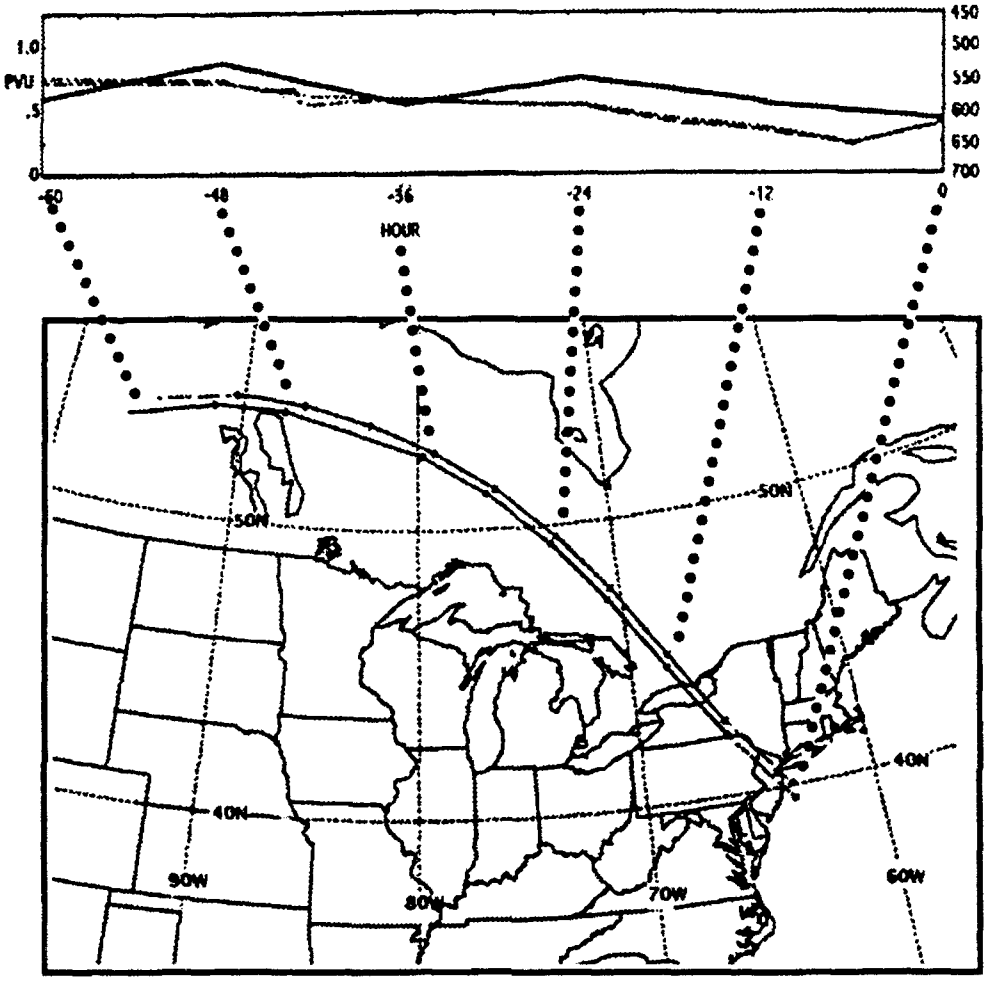

Figure 3.69 Isentropic back trajectory for graph of potential vorticity in PVU (solid line) and pressure heights in mb (dashed) with corresponding trajectory path at the 314K potential temperature level for point 39.5N, 73.5W.

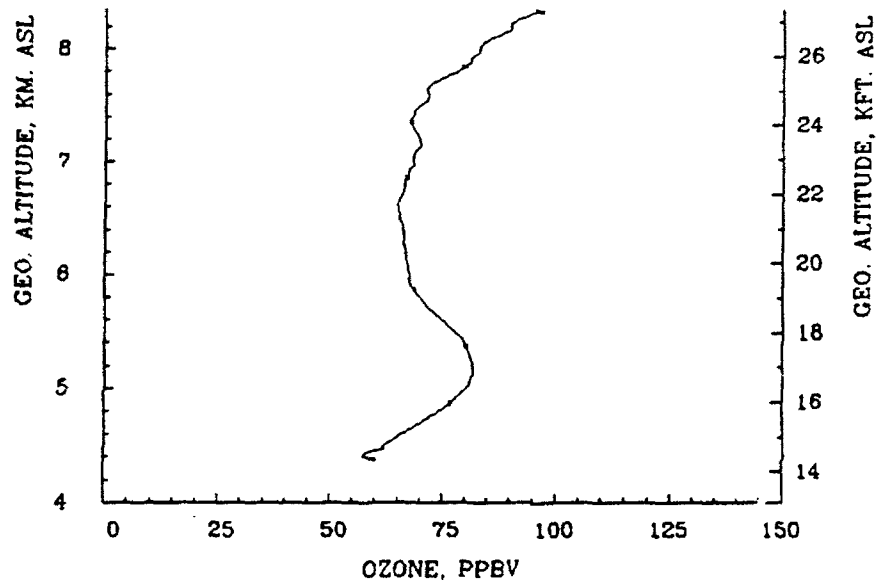

Figure 3.70 Average ozone profile for Mission 10 from 1939-2004Z on July 18, 1988. Note region of larger ozone values between 4.5 and 5.5 km.

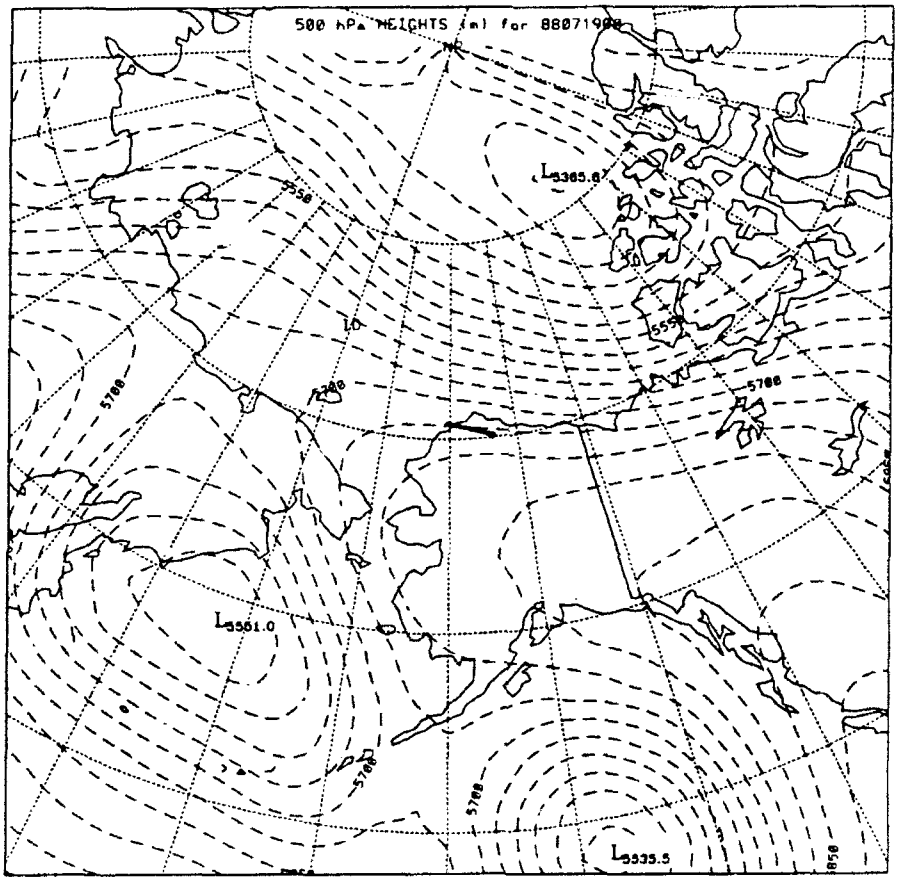

Figure 3.71 500mb pressure heights in m (dashed) for July 88 at 19/00Z. Mission 10 flight path noted by thick solid line.

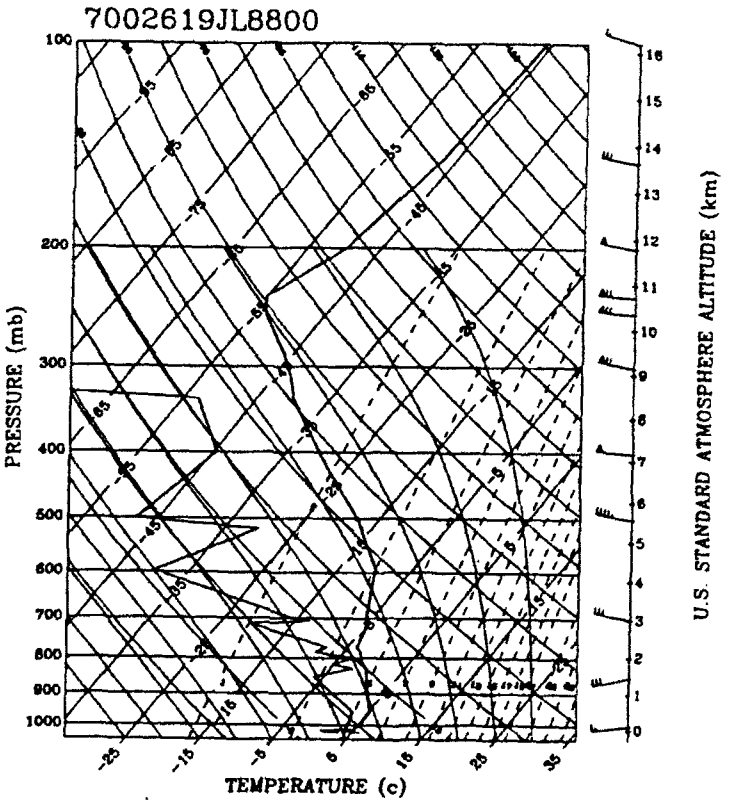

Figure 3.72 Skew-t Plot at Barrow, AK (70026) for July 1988 at 19/00Z showing dry slot at 3.5-5.6km.

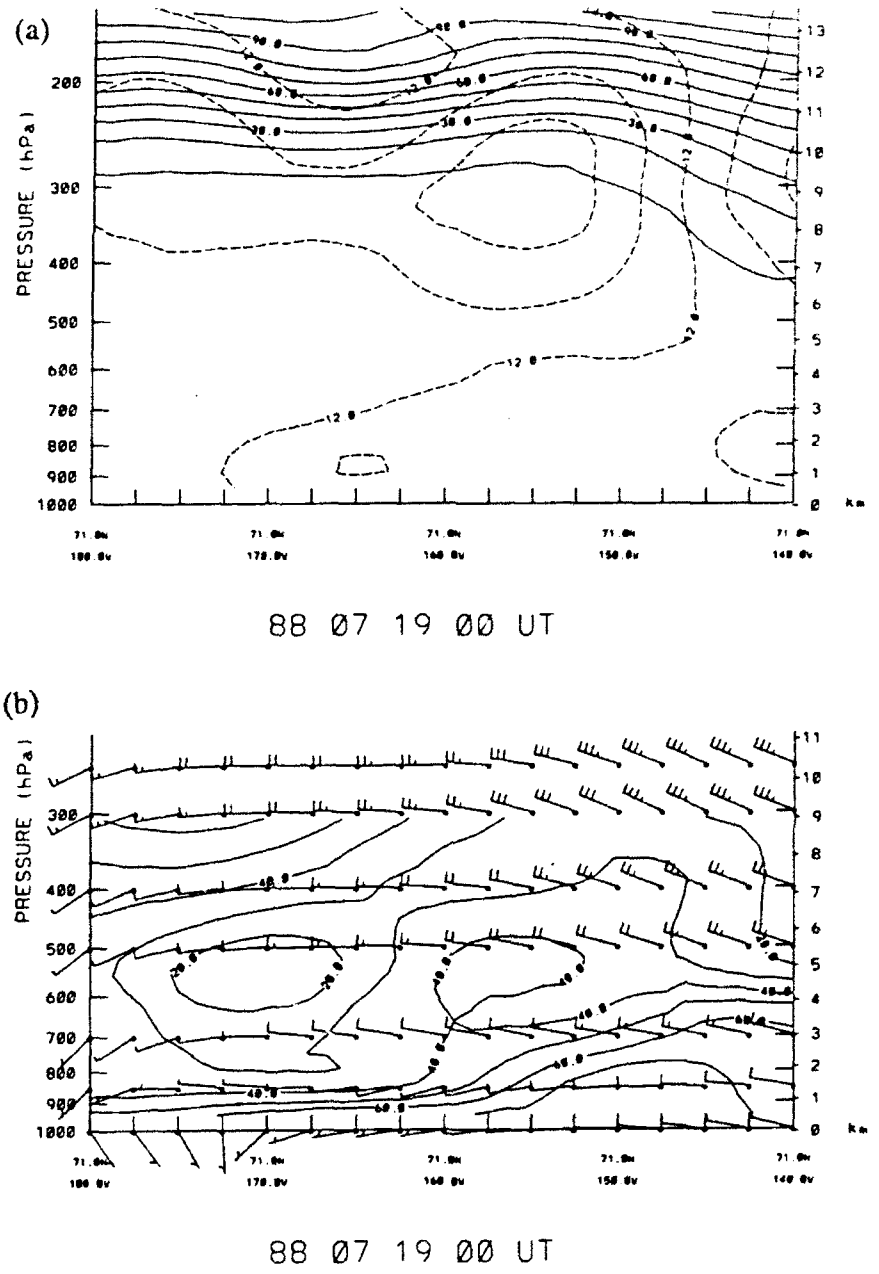

Figure 3.73 Cross-section from 71N 180-140W for 19/00Z July 1988 for (a) potential vorticity in deca-PVU (solid) and absolute vorticity in AVU (dashed) and (b) relative humidity in percent (dashed) and windbarbs.

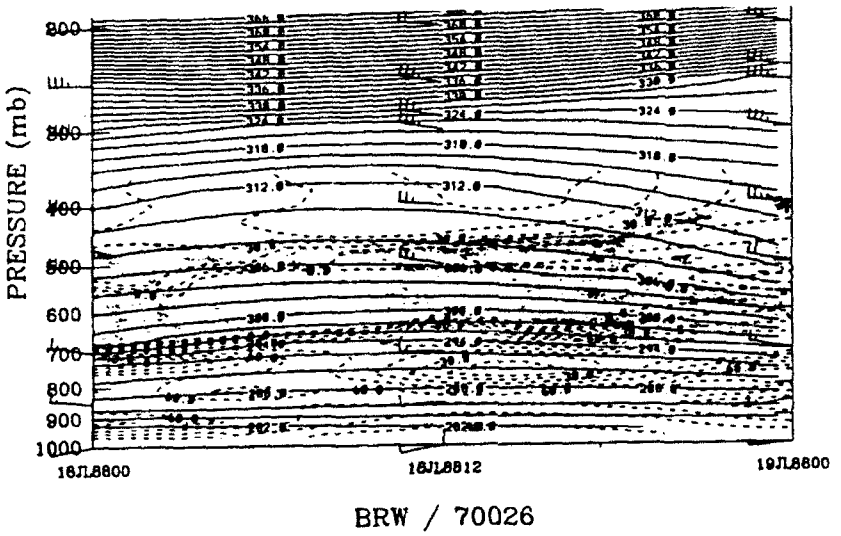

Figure 3.74 Station Time-Series at Barrow, AK (70026) for July 1988 from 18/00Z to 19/00Z of potential temperature in K (solid)/relative humidity in percent (dashed) and windbarbs.

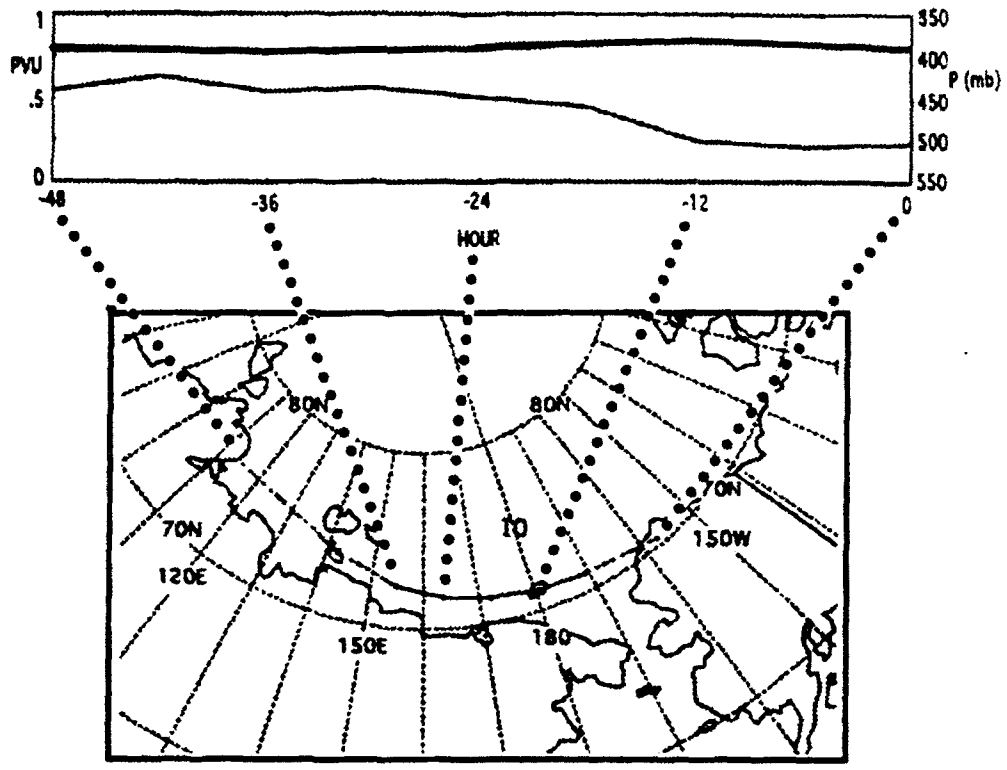

Figure 3.75 Isentropic back trajectory for graph of potential vorticity in PVU (solid line) and pressure heights in mb (dashed) with corresponding trajectory path at the 311K potential temperature level for point 70.4N, 157W.

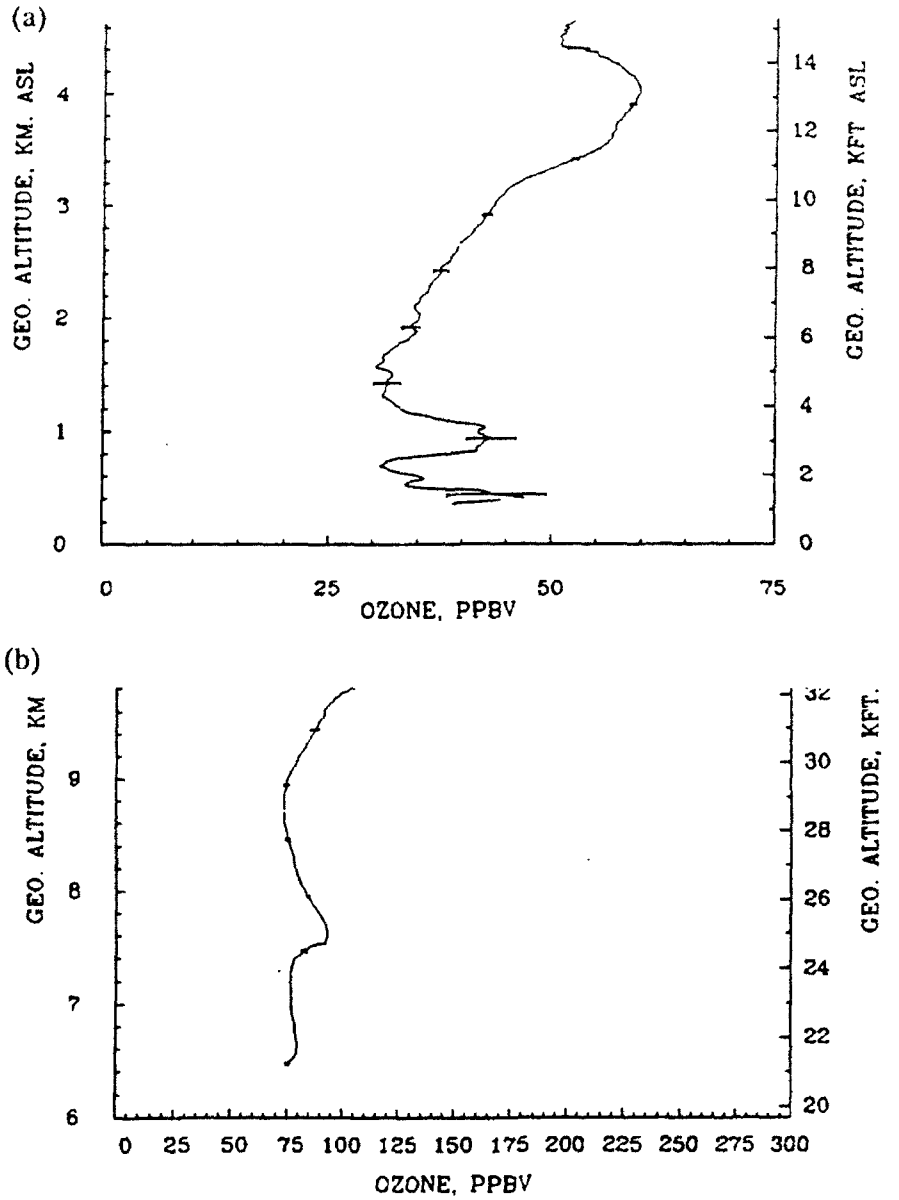

Figure 3.76 Average ozone profile for Mission 11 from 2139-2235Z on July 19, 1988. Note region of larger ozone values between (a) 3.2-4.4km and (b) 7.6 km.

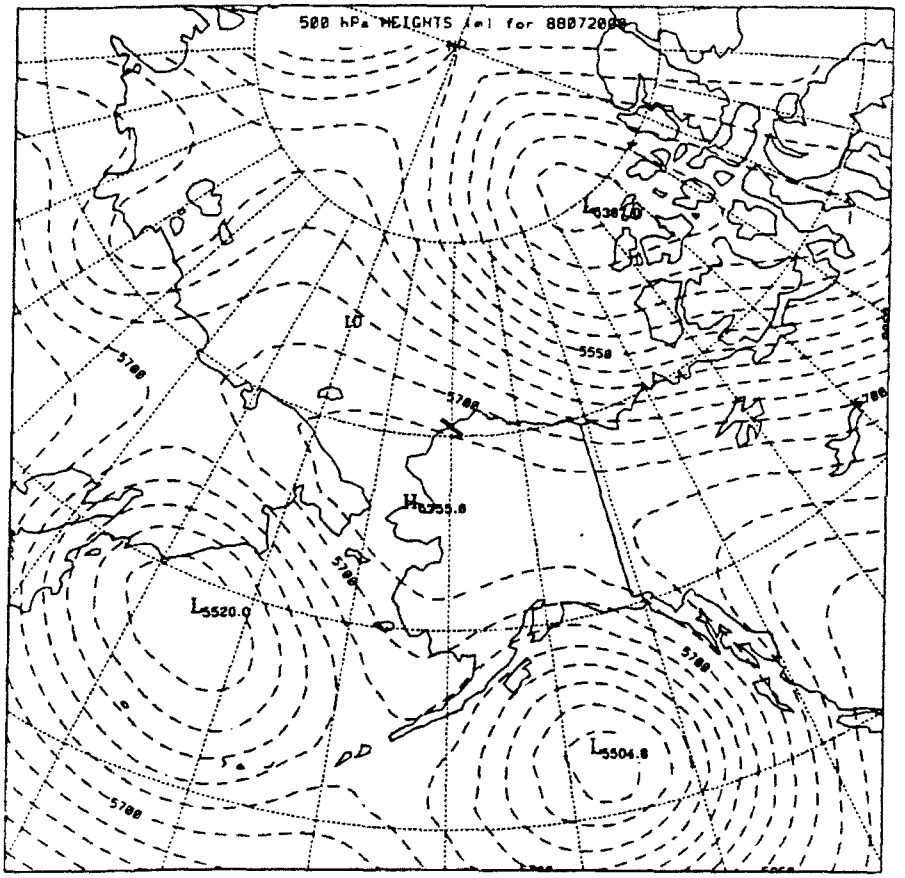

Figure 3.77 500mb pressure heights in m (dashed) for July 1988 at 20/00Z. Mission 11 flight path noted by thick solid line.

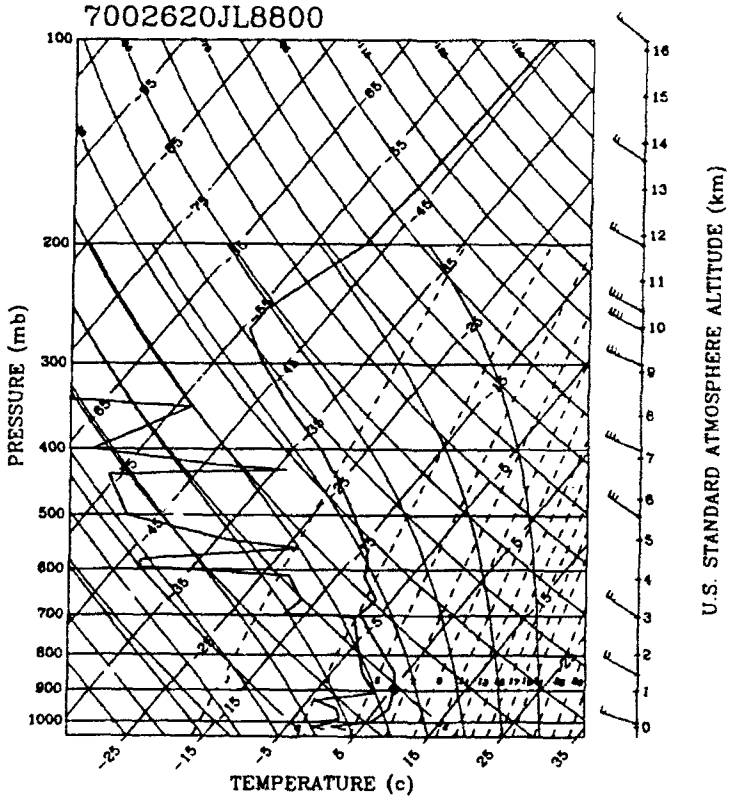

Figure 3.78 Skew-t LogP plot at Barrow, AK (70026) for July 1988 at 20/00Z showing dry slots at 4km and 7.6km.

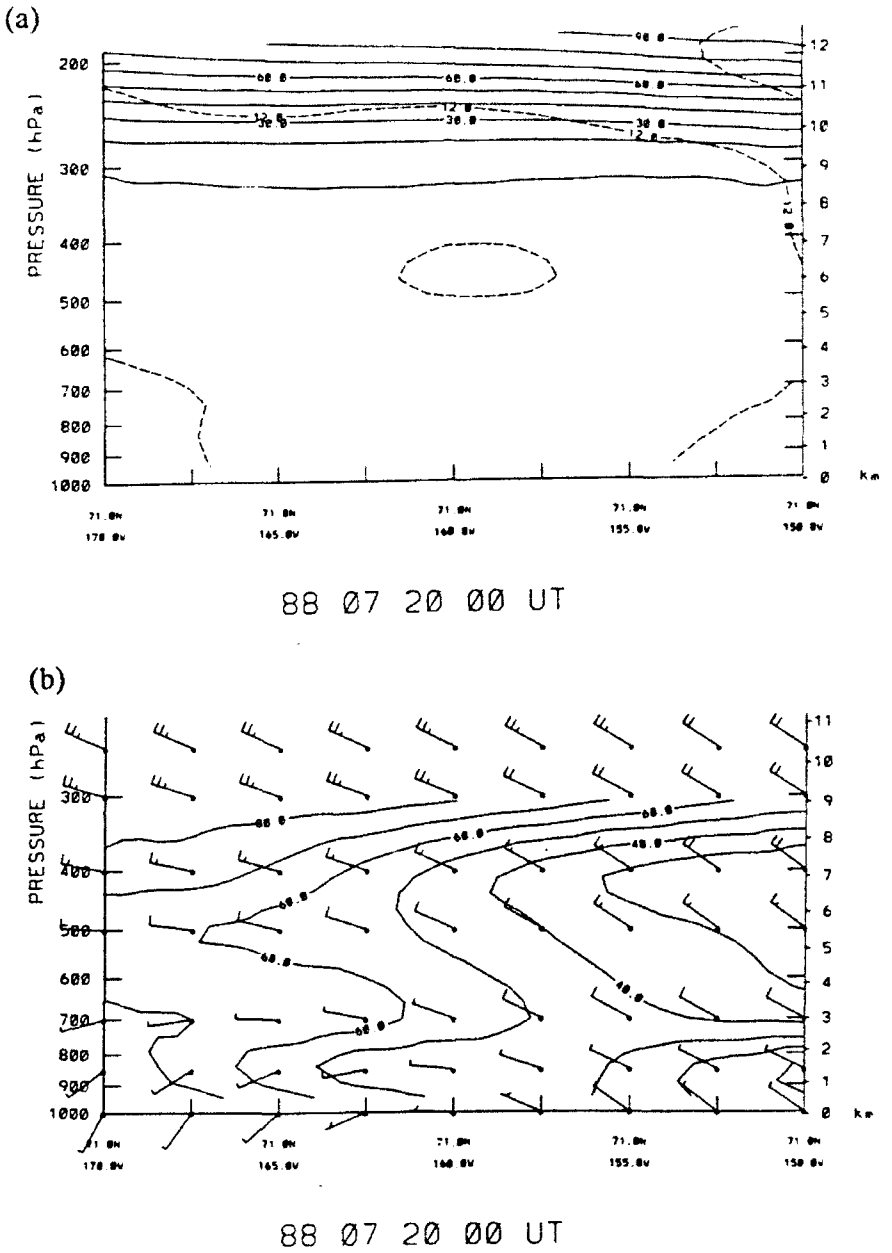

Figure 3.79 Cross-section from 71N, 170-150W for July 1988 20/00Z for (a) potential vorticity in deca PVU (solid) and absolute vorticity in AVU (dashed) and (b) relative humidity in percent (dashed) and windbarbs.

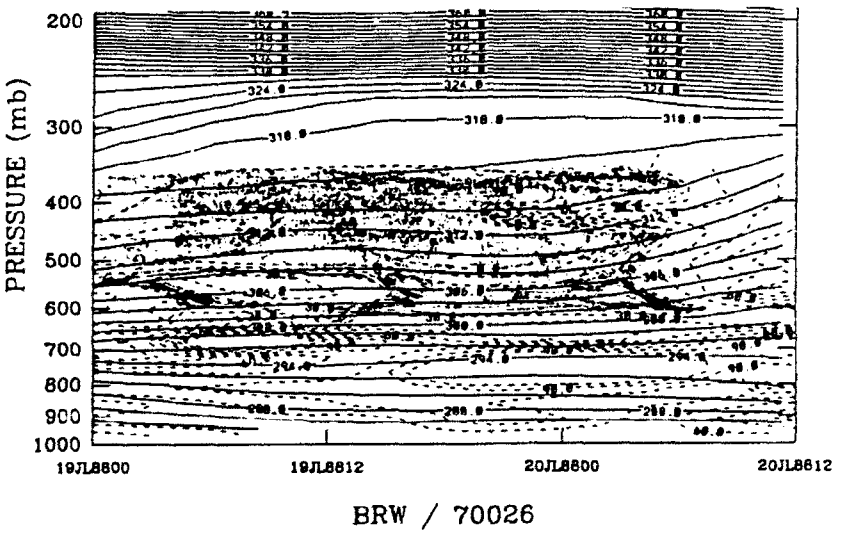

Figure 3.80 Station Time-Series at Barrow, AK (70026) for July 88 from 19/00Z to 20/12Z for potential temperature in K (solid), relative humidity in percent (dashed) and windbarbs.

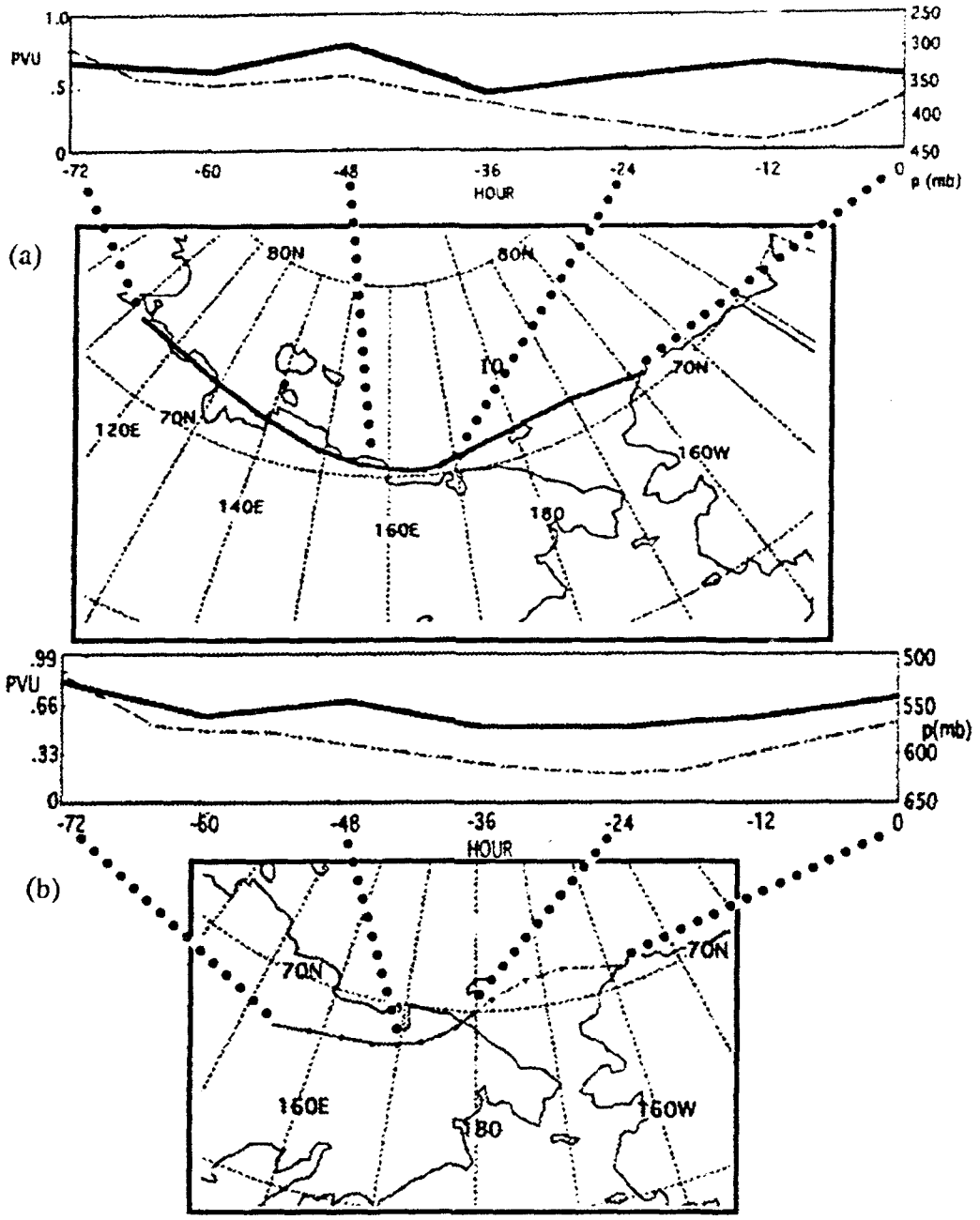

Figure 3.81 Isentropic back trajectory for graph of potential vorticity in PVU (solid line) and pressure heights in mb (dashed) with corresponding trajectory path at the point 70.9N, 158W for the (a) 316K potential temperature level and (b) 306K potential temperature level.

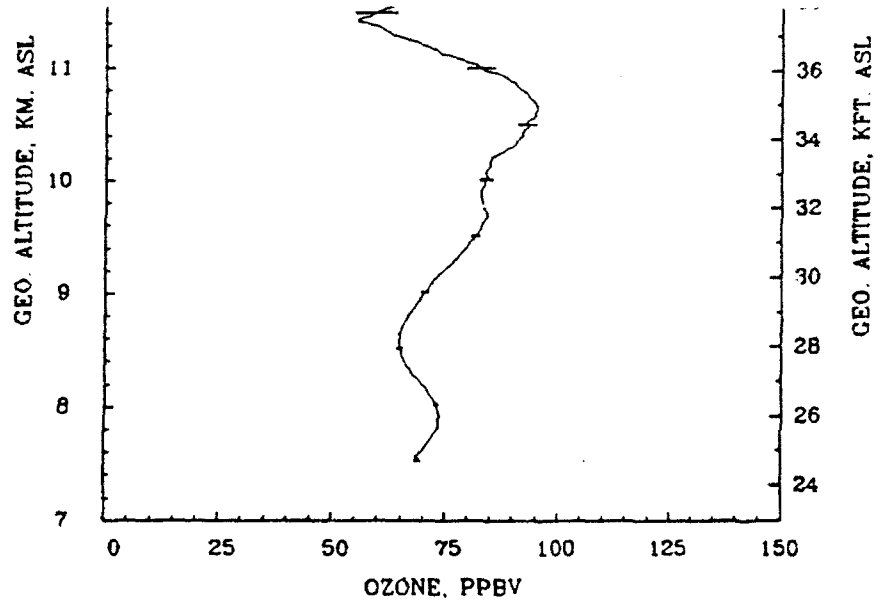

Figure 3.82 Average ozone profile for Mission 20 from 1834-1854Z on August 3, 1988. Note region of larger ozone values between 10.2-10.8km and 7.6 km.

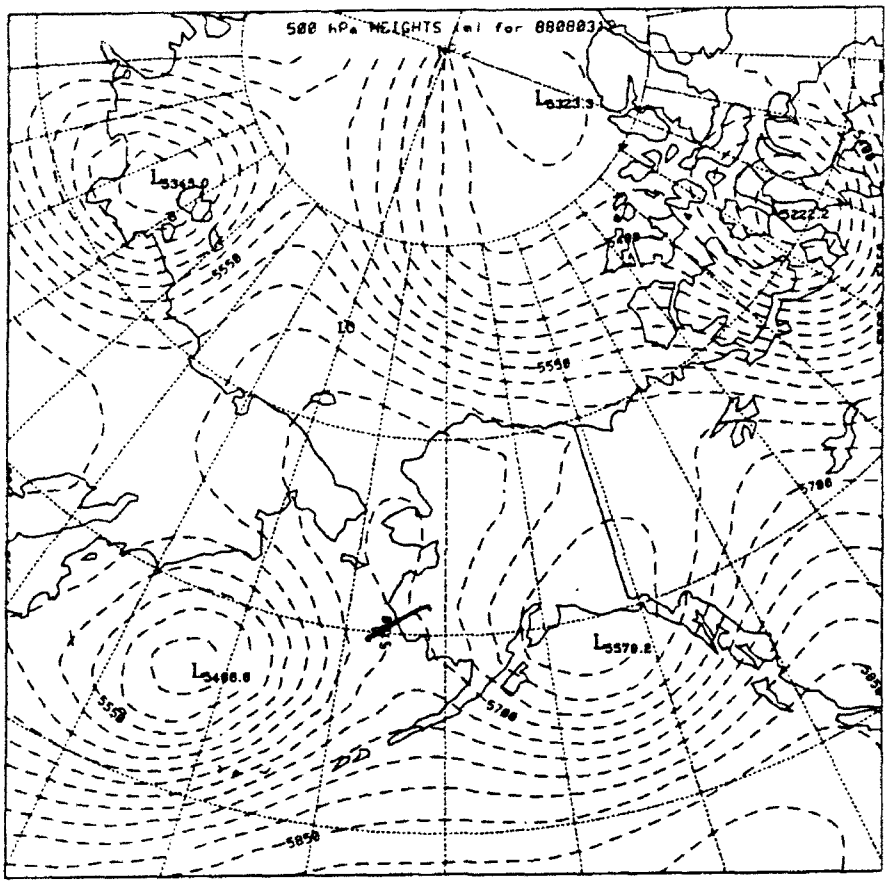

Figure 3.83 500mb pressure heights in m (dashed) for August 88 at 03/12Z. Mission 20 flight path noted by thick solid line.

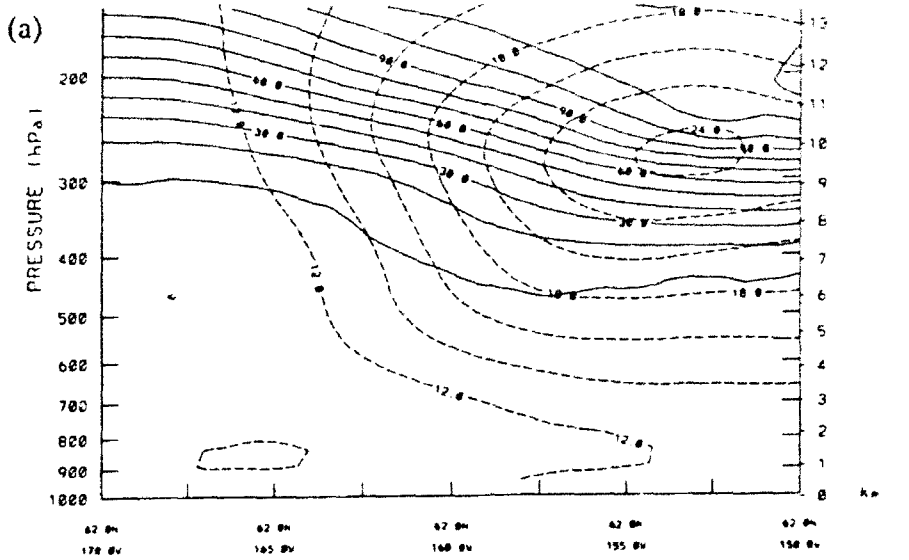

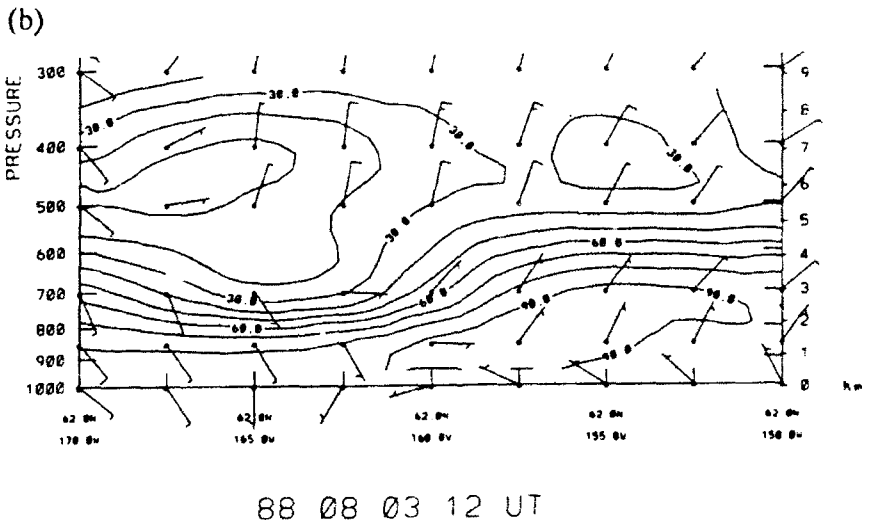

Figure 3.84 Cross-section from 62N, 170-150W for 03/12Z August, 1988 for (a) potential vorticity in deca PVU (solid) and absolute vorticity in AVU (dashed) and (b) relative humidity in percent (dashed) and windbarbs.

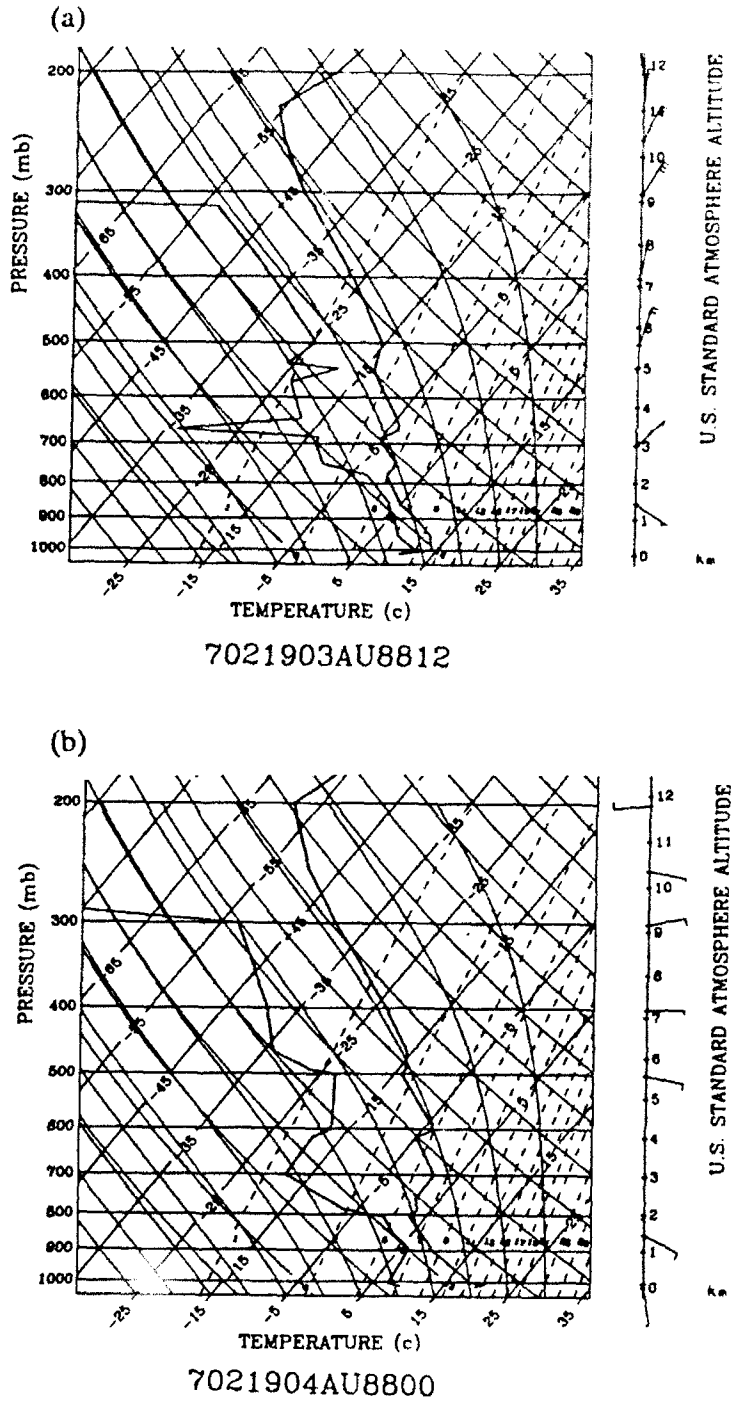

Figure 3.85 Skew-t LogP plot at Bethel, AK (70219) for August 1988 at (a) 3/12Z; (b) 4/00Z showing drying above 500mb.

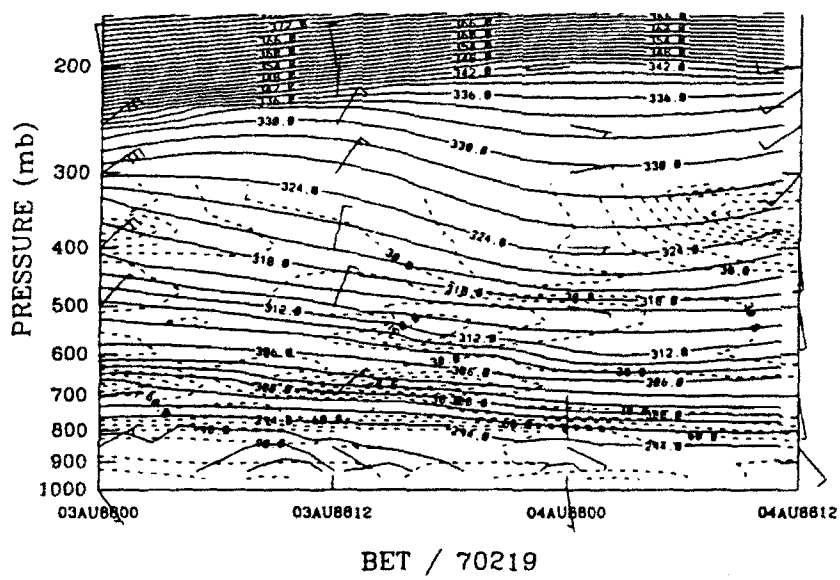

Figure 3.86 Station Time-Series at Bethel, AK (70219) for August 1988 from 3/00Z to 4/12Z for potential temperature in K (solid), relative humidity in percent (dashed) and windbarbs.

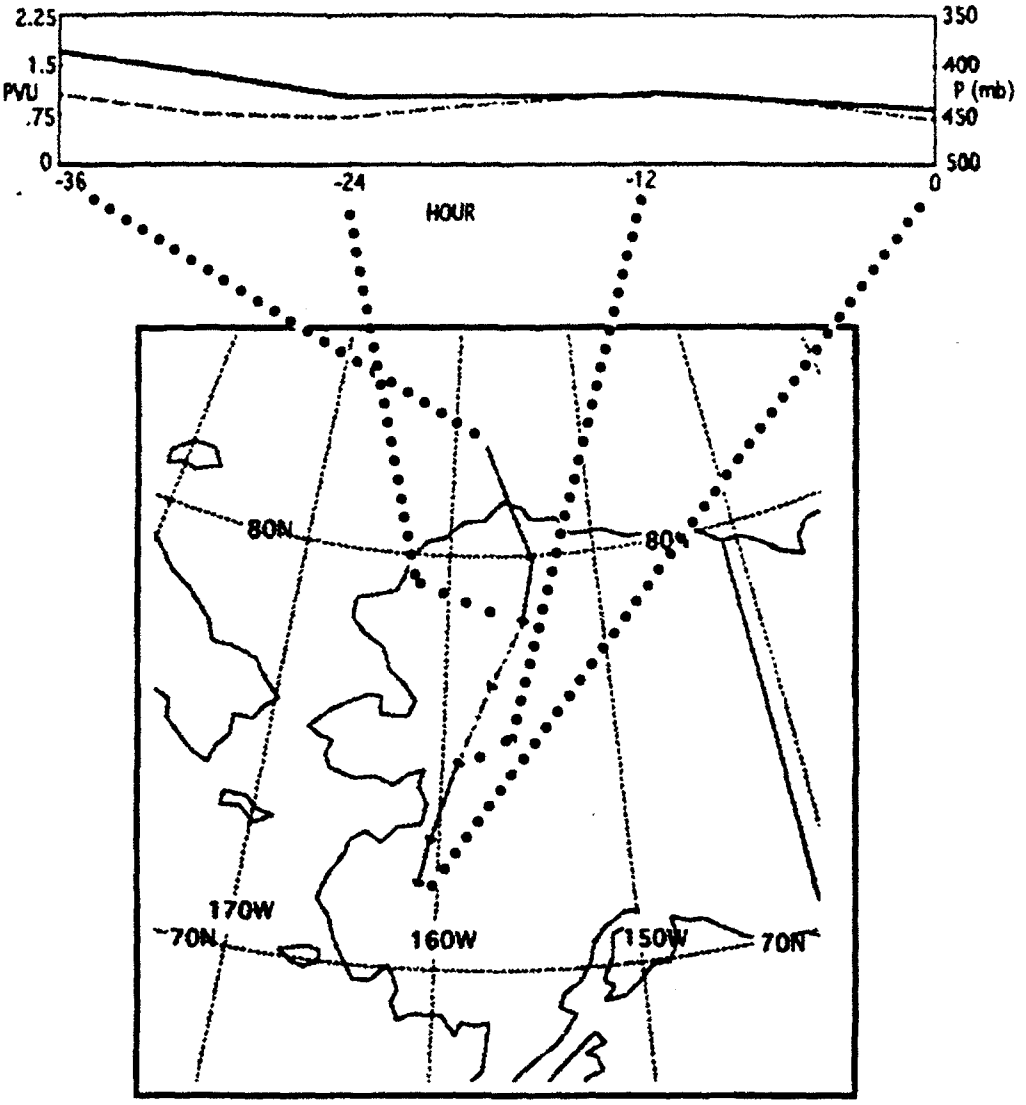

Figure 3.87 Isentropic back trajectory with pressure heights in mb (dashed) and corresponding trajectory path for (a) point 62N, 162W for the 318K potential temperature level with graph of potential vorticity in PVU (solid line) and (b) point 61.1N, 162W at the 329K potential temperature level.

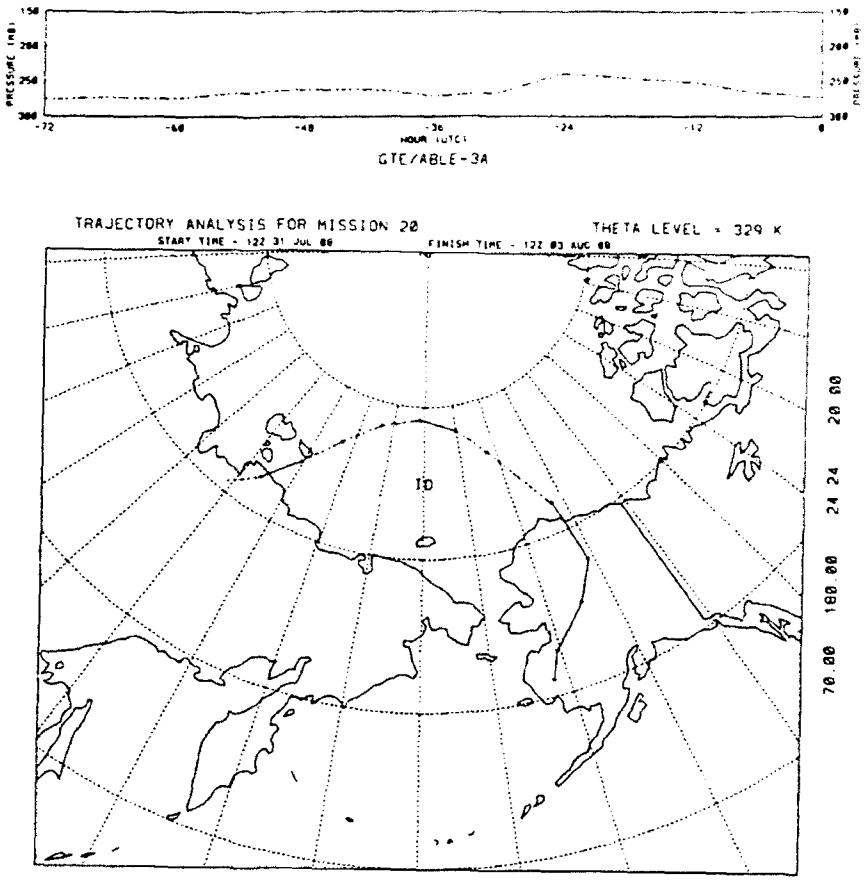

Figure 3.87 Isentropic back trajectory with pressure heights in mb (dashed) and corresponding trajectory path for (a) point 62N, 162W for the 318K potential temperature level with graph of potential vorticity in PVU (solid line) and (b) point 61.1N, 162W at the 329K potential temperature level.

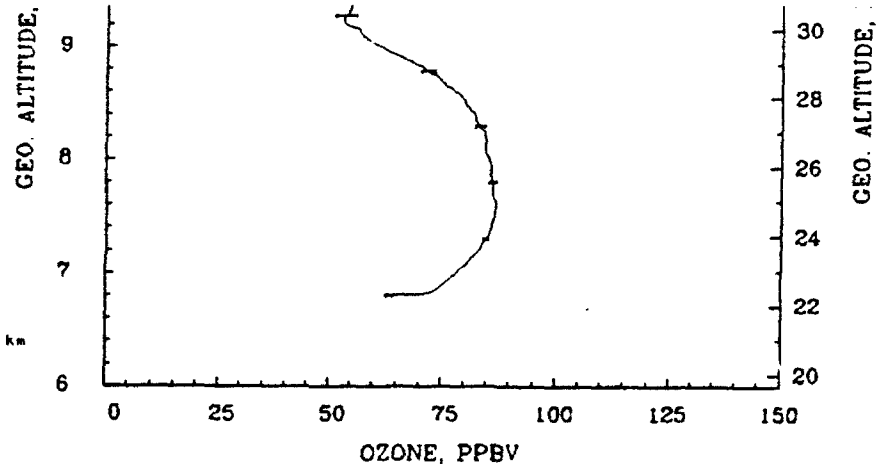

Figure 3.88 Average ozone profile for Mission 22 from 1934-1954Z on August 7, 1988. Note area of higher ozone values between 6.8-8.6 km.

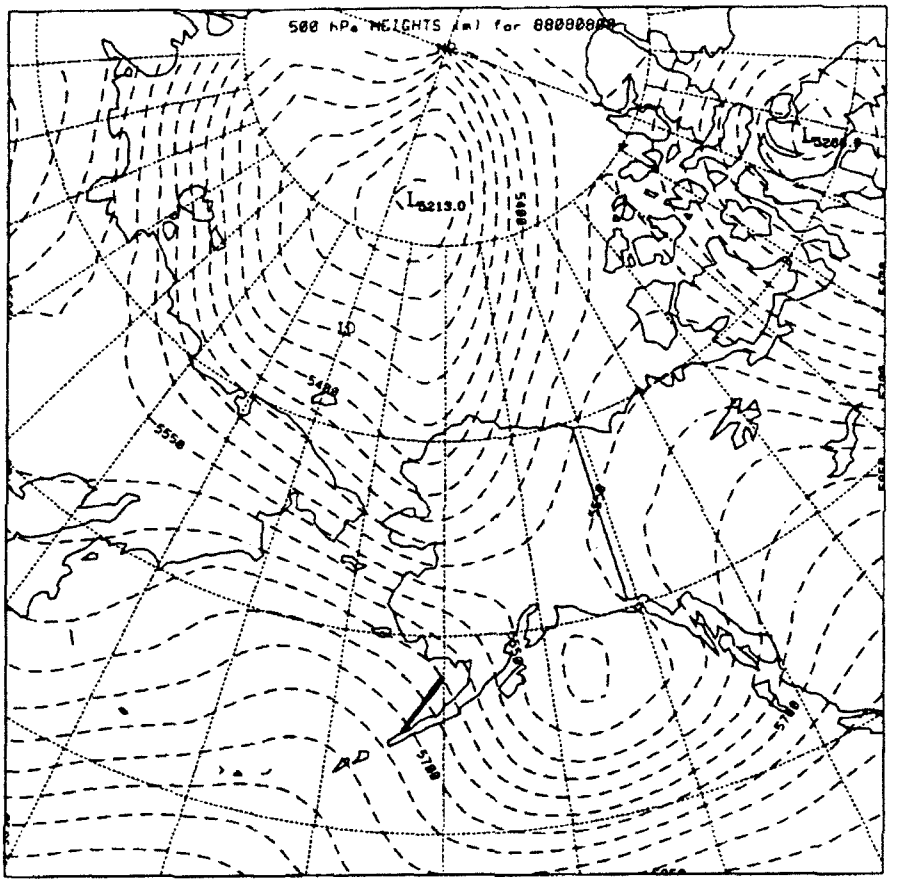

Figure 3.89 500mb pressure heights in m (dashed) for August 1988 at 8/00Z. Mission 22 flight path noted by thick solid line.

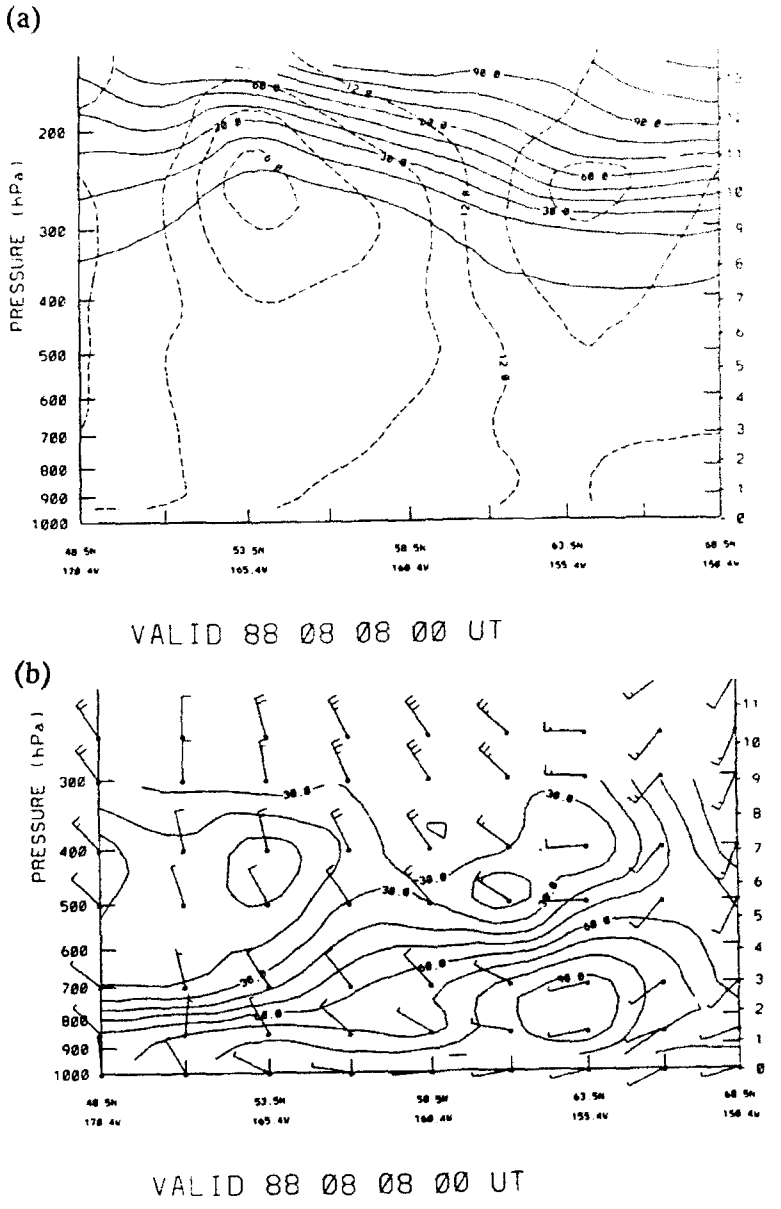

Figure 3.90 Cross-section from 48.5N, 170.4W to 68.5N, 150.4W at 8/00Z August 1988 for (a) potential vorticity in deca PVU (solid) and absolute vorticity in AVU (dashed) and (b) relative humidity in percent (dashed) and windbarbs.

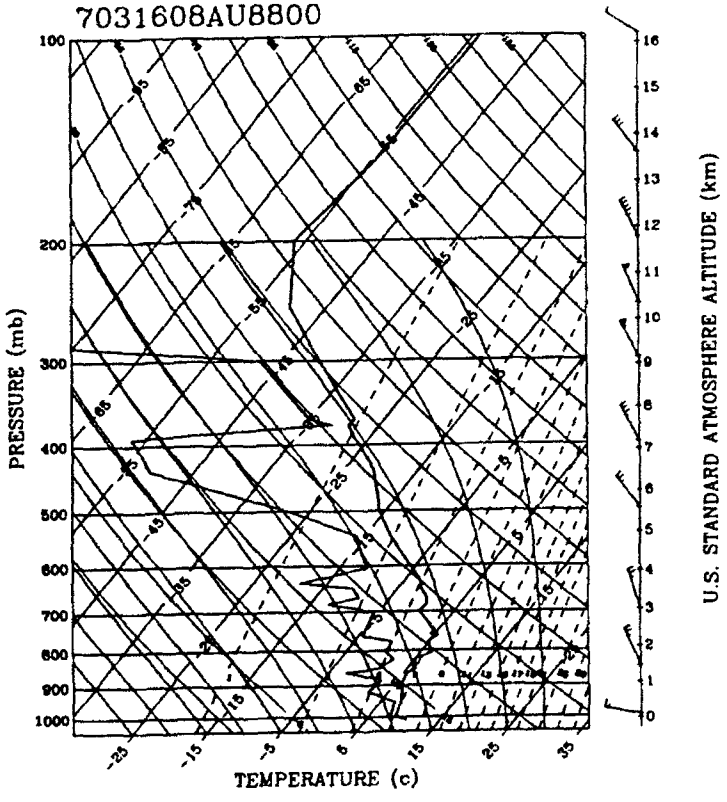

Figure 3.91 Skew-t LogP plot at Cold Bay, AK (70316) for August 1988 at 8/00Z showing a dry slot at 550-420mb (5-7 km).

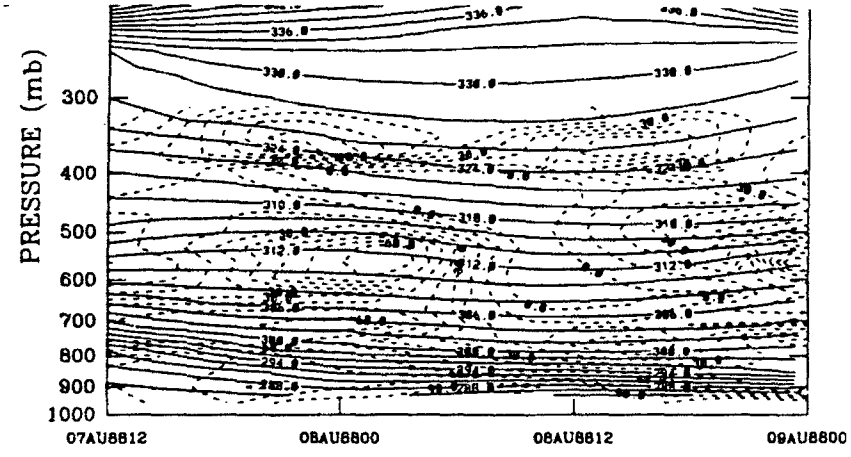

Figure 3.92 Station Time-Series for Aug 88 at Cold Bay, AK (70316) from 7/12Z to 9/00Z for potential temperature in K (solid), relative humidity in percent (dashed) and windbarbs.

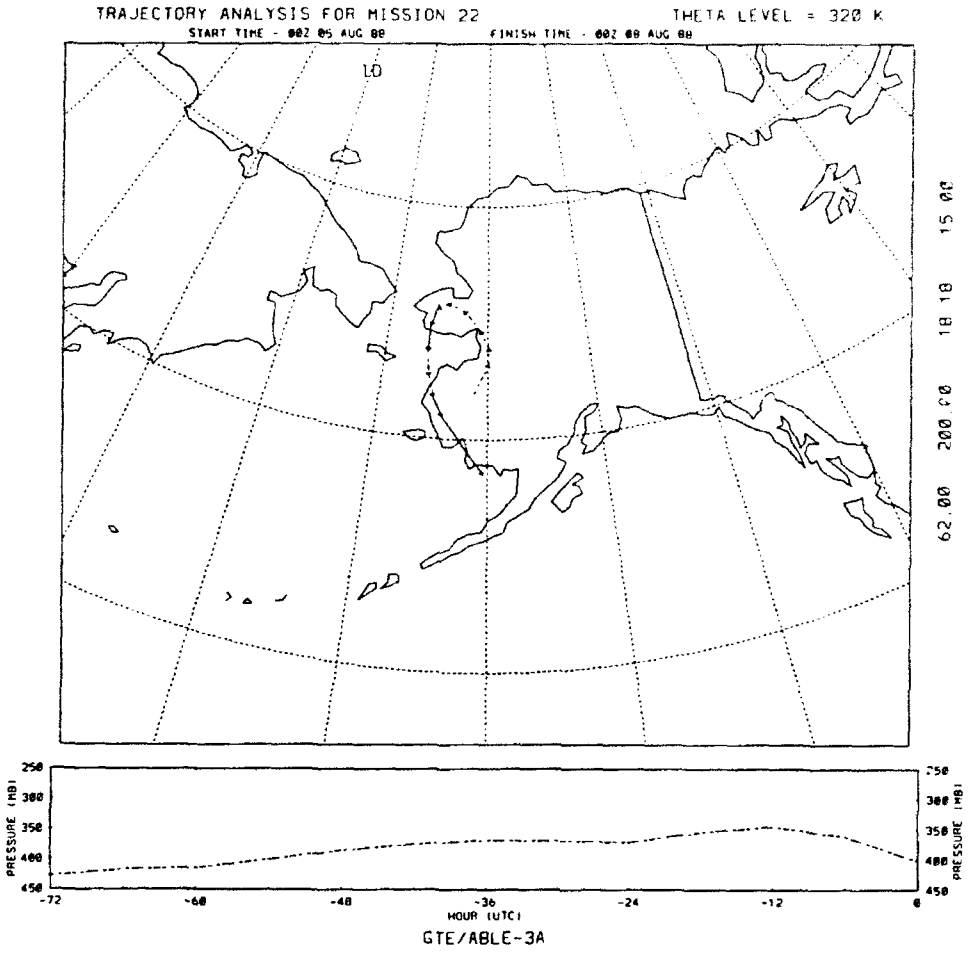

Figure 3.93 Isentropic back trajectory for graph of potential vorticity in PVU (solid line) and pressure heights in mb (dashed) with corresponding trajectory path at the point 58.5N, 160.4W for the 320K potential temperature level.

CHAPTER IV

COMPARISONS AND CONTRASTS BETWEEN MISSION ANALYSES

(1) Development of Exchange Theory. *Gregory et al.* [1992], and *Jacob et al.* [1992] found that summertime tropospheric air over a large region of the Arctic exhibited a low potential for the photochemical production of ozone. The low mixing ratios of NO_x (10-50 ppt) that were measured accounted for this low photochemical production of ozone, even in a number of smoldering biomass burning plumes. With these low, but existent, mixing ratios of NO_x, *Jacob et al.* [1992] calculated the lifetime of ozone to be 46 days compared to 26 days if NO_x were not present. Further, computations by *Jacob et al.* [1992] for ozone deposition to the surface and for photochemical production in the 0-6 km column revealed a loss of 8.2 and 8.9 x 10^{10} molecules $cm^{-2}s^{-1}$, respectively. These values for ozone production and deposition were estimated for locations above 60 degrees N. Assuming a negligible transport of ozone from the mid latitudes (below 60 degrees N), then for steady state conditions an additional source of 16.2 x 10^{10} molecules $cm^{-2}s^{-1}$, such as from the stratosphere, would be needed.

Ozone enhancements investigated in this thesis can be categorized by mechanisms responsible for the transport of air from the stratosphere. These mechanisms include high-pressure-induced subsidence, tropopause relocation in a polar vortex, and tropopause folding. From the case study results in this thesis, an estimation of stratospheric/tropospheric exchange can be calculated for each of the mechanisms affecting the polar regions above 60°N. This estimation can be calculated by determining an average spatial scale, ozone enhancement value, and vertical thickness from the case studies. Constant pressure heights can then be analyzed for July and August 1988 to determine the frequency of each mechanism above 60°N. The exchange rates obtained for these sources of ozone can then be compared to the earlier results obtained for assessments of the chemical sources and sinks affecting the ABLE 3A study.

For subsidence associated with high pressure systems, a total of 146 events were noted over a 57 day period during the summer of 1988. Based on case studies, the average spatial scale for high-pressure-induced subsidence was three degrees with an average vertical thickness of 1.6 km. Combining these yields an estimate of the flux of ozone, due to subsidence, of approximately 4.4×10^9 molecules/cm^{2}s. For tropopause folding events, a total of 25 events were noted over the same 57 day period. From the case studies, the average spatial scale for tropopause folding was 1.9 degrees with an average vertical thickness of 1.3 km. Combining these yields an ozone flux, due to tropopause folding, of approximately 2.1×10^9 molecules/cm^{2}s.

For the mechanism of tropopause relocation in a polar vortex, a total of 16 events were noted over the same 57 day period. From the case studies, the average spatial scale for a polar vortex was 20 degrees with an average thickness of 2 km. Comparing these values for the mechanisms, the amount of ozone exchanged above 60°N may be dominated by the tropopause relocation in polar vortices. The magnitude of ozone exchange from this mechanism is comparable to the ozone sink values estimated by *Jacob et al.* [1992] in which the summertime high latitude ozone depositional loss was estimated at 8.2×10^{10} molecules/cm^{2}s and the photochemical loss was estimated at 8×10^{10} molecules/cm^{2}s. This gives an overall ozone sink of 1.6×10^{11} molecules/cm^{2}s in the troposphere over these regions. This ozone sink is comparable to the magnitude of the stratospheric source characterized in this thesis. From the estimates made above, the major source of ozone to the Arctic summertime is most likely from tropopause relocations in polar vortices. This mechanism, rather than tropopause folds, could be the dominant summertime source of ozone contributing to the background abundance of ozone over this region and to the large fraction of stratospherically influenced air described by *Browell et al.*, (1993).

As a consistency check, the above estimated ozone flux can be compared to recent results on a global scale. The estimated 1.2×10^{11} molecules/cm^{2}s ozone flux, for high latitude tropopause relocation, would yield an exchange rate of 4×10^{28} molecules/s for the region above 60°N. This can be compared to *Murphy and*

Fahey's (in print) recent total global ozone flux estimate of 3.5 x 10^{10} molecules/cm^2s, which is well within the range of 2.5-7.8 x 10^{10} molecules/cm^2s from previous studies (*WMO*, 1985). This global value yields in a total global exchange rate of 1.8 x 10^{29} molecules/cm^2s. Comparing these values suggests that summertime tropopause relocation in high latitudes can account for approximately 25% of the average global flux of ozone from the stratosphere.

Tropopause folds, which have been attributed as an important stratospheric/tropospheric exchange mechanism, occur here primarily as a result of the interaction of short waves and polar vortices. This interaction requires a short wave plus a long wave in phase (ideal case #1) as depicted in Figure 4.1a, or a short wave and a polar vortex that is already in place as depicted in Figure 4.1b (ideal case #2). As the process leading to exchange develops, the short wave increases in amplitude (as the two waves come into phase). Exchange begins as the amplitude becomes strong enough to reach the tropopause. If the interaction is strong enough, a polar vortex will develop and part of the short wave will move out as the polar vortex begins spinning. The second method of exchange (Figure 4.1b) requires the vortex to already be in place. In this case, a short wave rotates around the flow into the polar vortex and air is easily exchanged with the stratosphere since the polar vortex already has a lowered tropopause.

Shapiro et al. (1987) proposed a model for the atmosphere that identified tropopause folds due to the subtropical, polar, and arctic jets. Some research has

been conducted on the jet-related arctic and polar tropopause folds, but little is known about how significant the exchange process is for the subtropical jet. In the arctic summer, only the polar jet is active. Figure 4.2a is proposed to represent the atmosphere for the Arctic summer under ideal conditions in the entrance region of a jet maximum. Figure 4.2b gives the positioning of the cross-section in relation to the polar vortex. The ideal situation for stratospheric/tropospheric exchange consists of a polar jet with a depressed tropopause, which is identified by the stratospheric threshold potential vorticity value (dark line). In this case, a polar front can protrude from the point of the depressed tropopause. This polar front would be the strongest near the tropopause with a broadening of the transition zone as the front approaches the surface. In this case, the polar front would separate polar air from mid-latitude air. This would enable tropopause folds to form along the polar front under these ideal interacting conditions.

Ideal conditions include:

1. An existing strong long wave interacting with a strong short wave, which can lead to formation of a polar vortex and a tropopause fold.

2. A polar vortex or cut-off low existing with an interacting short wave producing a tropopause fold.

However, not all waves can cause a fold to occur. Waves in the atmosphere are classified according to their wavelength. Lengths are determined by considering the distance between troughs. Long waves are major troughs with wavelengths on

the order of 1000 km. Amplitude of long waves are usually large and increase with altitude in the troposphere. Movement of long waves can be as much as 200 km per day, be stationary, or actually retrogress as interaction takes place with other waves. The number of long waves present at any one time in the northern hemisphere is 3 to 7.

Short waves are progressive waves that move within the contours of the long waves. Wavelengths of short waves are on the order of 100 km and move as much as 1000 km per day. Amplitude of shortwaves can range from easily detectable to virtually undetectable. As a short wave moves through the flow, interaction with long waves can occur. As the short wave approaches a long wave, its vorticity increases. The number of active short waves in a hemisphere at any one time usually vary from 5 to 10. Their interaction with long waves allows energy to be transferred and in some cases, can cause full blown cyclogenesis.[18] Note that ridges (i.e., cut-off highs) can be treated in the same manner.

In the ideal case 2 discussed earlier, the tropopause folds' exchange of ozone occurs when a strong short wave interacts with the long-wave pattern (see Figure 4.1a). It takes this interaction to overcome the strong inversion at the tropopause and to initiate the vertical motions needed to cause the ozone to be drawn down into the troposphere. As the polar vortex is formed, the tropopause level decreases in altitude and high concentrations of ozone move into the cold pool of air. Looking

[18]Cyclogenesis refers to a developing wave of low pressure

in a three dimensional view, the high ozone area looks like a "bowl" as indicated in Figure 4.3a. The same picture appears in two dimensions when viewed as a constant level chart as in Figure 9.3b. Short waves move along the contours (see Figure 4.3a-b) of the long wave and exchange air with the polar vortex thus bringing high values of ozone from the vortex while entraining tropospheric air into the stratosphere.

(2) Case Studies of Exchange Theory. Examples of each of the ideal cases are now presented. Examples of ideal case 1 can easily be found because polar vortices interacting with short waves occur frequently. But for ideal case 2, a short wave forming a vortex is harder to find.

(a) Example of ideal case 1 - An existing polar vortex interacting with a short wave. The July 13-15, 1988 or Mission 8 the meteorology exhibits ideal case 1 behavior. First looking at the 300 mb chart for 13/00Z July 1988 (Figure 3.5g of Mission 8), a strong short wave was centered at 75N, 80E. Over the next couple of time periods, this short wave rotated around (see Figure 3.5 a-f) and emerged out of the southern part of the polar vortex at 15/12Z (Figure 4.5b) and 16/00Z (Figure 3.5a). During this time, and especially around 14/00Z, these two features interact to produce a tropopause fold. The tropopause fold occurred at around 14 July at 00Z (71.5N, 102.3E) as the short wave interacted with the polar vortex.

The cross-section analysis of meteorological parameters showed how the fold developed. Starting at 12/12Z, the short wave showed up well on the 300 mb chart. The cross-section of absolute vorticity (Figure 4.4a) also depicted the short-wave well.

This north-south cross section showed a well defined center of cyclonic absolute vorticity at 75N, 60E and 350 mb with values greater than 18 AVU. Twelve hours later at 13/00Z, the short wave had now moved to a position near 78N, 88E to 70N, 65E (see Figure 3.5g). The wave had moved 20 degrees in latitude in 12 hours. Note how the wave began to enter the vicinity of the polar vortex. The cross-section of absolute vorticity (Figure 4.4b) showed persistent cyclonic turning and a maximum absolute vorticity value of greater than 18 AVU occurred at 72.5N, 77.5E at 350 mb. Twelve hours later at 13/12Z, the short wave had moved to a position defined by 76N, 108E to 68N, 78E (see Figure 3.5f) with its movement slowing to about 10 degrees longitude during the previous 12 hour period. The cross-section of absolute vorticity (Figure 4.4c) still identifies this persistent short-wave well as a cyclonic turning and an absolute vorticity maximum of greater than 18 AVU are indicated at 75N, 95E at 350 mb. By 14/00Z, the short wave had moved to position 74N, 115E to 66N, 82E (see Figure 3.5e). The cross-section of absolute vorticity (Figure 4.4d) showed a maximum of 24 AVU at 70E 110E at 350 mb. During this time, the wave had increased in intensity as it rotated around the polar vortex with a 12 hour movement of 15 degrees longitude. Twelve hours later on 14/12Z, the short wave was moving around the southern edge of the polar vortex. At this point, the short wave was difficult to detect because it was embedded in a strong wind flow (30-35 m/s, see Figure 3.5d). Here the wave accelerated, moving to the 148E meridian. The cross-sections of absolute vorticity (Figure 4.4e and 4.4f) also showed that the short

wave had moved through the strongest part of the long wave. The absolute vorticity value of the short wave was now just greater than 16 AVU at 70N, 148E and 350 mb. Higher values of absolute vorticity, greater than 28 AVU were also found nearby at 70N, 120E at 400 mb. This higher value signifies that the short wave had moved through the long wave and increased the intensity of the long wave. As the short wave moved away, the value should also drop with time. During this period, the movement of the wave had picked up speed travelling 38 degrees longitude during the preceding 12 hours. Following the wave to 15/00Z, the 300 mb position (see Figure 3.5c) is near the 170E longitude. At this time the polar vortex appeared somewhat split, having two centers, one located at 73N, 130E and the other residing with the wave at 80N, 170E. The cross-section of absolute vorticity (Figure 4.4g) was greater than 16 AVU at 70N, 168E and 300 mb. At this point, the wave had slowed its movement to a 12 hour movement of 20 degrees longitude. Further positions of the wave indicated that it continued to the east, being centered at 75N, 172W on 15/12Z (Figure 3.5b) and at 75N, 152W at 16/00Z (Figure 3.5a). During this time, the wave continued to have nearly the same magnitude of absolute vorticity at the 300 mb level.

Since the analysis documents the path of the wave through the polar vortex, let us see how the potential vorticity field agrees with the proposed ideal case 1. Assuming that the tropopause fold started when the short wave entered the polar vortex, then the parcel-time series for Mission 8 (see Figure 3.17 and 3.18 of the

Mission 8 case study) should indicate the fold starting to occur between 14/00Z and 15/00Z, at the time the parcel passed over the point at 69N, 120E. The north-south cross-section of potential vorticity (Figure 4.5a) does resemble the features in the meteorological chart (Figure 4.2). The potential vorticity protruded to lower levels, as low as 800 mb, near 70N, precisely at the location of the fold. Figure 4.5b depicts the same feature in the cross-sections of winds and potential vorticity. The wind maximum also shows up nicely, indicating where the tropopause break occurs. The potential temperature surfaces along with the maximum wind band can be used in this case to indicate the location of the polar front. The tropopause was at 304K potential temperature at 70N and at 324K potential temperature at 66N. In this case, the polar front extended from the tropopause at the 324K potential temperature level (at 70N) and down to the surface by the time it reached 55N.

(2) An example of ideal case 2 is now presented. Ideal case 2 describes an existing short wave that interacts with a long-wave pattern that leads to the formation of a polar vortex. The July 7-10, 1990[19] meteorological data over Canada demonstrates ideal case 2. This event will be demonstrated by a series of 300 mb charts and cross-section that will show how this system formed during a period when the short wave moved into an area favorable for intensification.

Starting at 7/00Z, a wave (called hereafter wave#1) was easily identifiable

[19]All clear examples for ideal case 2 in the ABLE 3A time period were located in data-sparse areas where cross-section could not be plotted. The next data available to the author was 1990.

on the 500 mb chart (Figure 4.6a) 65N, 104W to 40N, 118W. Previous charts indicated the short wave migrated around an upper level ridge. Movement of wave #1 was approximately 8 degrees longitude during the previous 12 hours. A west-east cross-section of absolute vorticity for 7/00Z (Figure 4.7a) at 60N identified the center of wave#1 by the position of a center of absolute vorticity with greater than 20 AVU at 60N, 110W and 500 mb. Twelve hours later at 7/12Z, wave #1 had moved to location 68N, 90W to 50N, 115W (Figure 4.6b). At his point, movement of the wave #1 had slowed to 5 degrees longitude. At this time, the west-east cross-section of the atmosphere at 62N also showed a center of absolute vorticity with greater than 20 AVU at 62N, 108W and 500 mb (Figure 4.7b). By 8/00Z, wave #1 continued to move east and slowly intensify. At this time wave #1 was positioned at 68N, 85W to 50N, 110W (Figure 4.6c), having followed a steady movement of 5 degrees longitude. At this time, a second wave (wave #2) is also evident in Figure 4.6c at 64N, 100W to 64N, 115W. Wave #2 will help maintain the vortex after formation. The initial indication of this are seen in the curving of the isobars which continues to increase in the vicinity of 62N, 95W when compared to previous 500 mb charts (compare Figures 4.6a and 4.6b). The west-east cross-section at 55N (Figure 4.7c) depicted a center of absolute vorticity with greater than 14 AVU located at 55N, 103W at the 250 mb level. By 8/12Z, the wave#1 had nearly completed the formation of the polar vortex (Figure 4.6d). Wave#1 was now located at 60N, 90W to 50N, 97W and continued a five degrees longitude movement during the time

period. During this time, wave #2 had moved 2 degrees to the south (now at 62N) and was located at 90W to 110W. The west-east cross-section at 55N (Figure 4.7d) showed a center of absolute vorticity greater than 18 AVU at 55N, 95W at the 250 mb level. By 9/00Z, wave #1 had closed off contours on the 500 mb chart with its center located at 60N, 82W (Figure 4.6e) and with the center's 500 mb pressure height at 5508 m. At this time, wave #1 had moved to position 60N, 82W to 50N, 82W following a past 12 hour movement of 8 degrees longitude. Wave #2 was now at position 60N from 85W to 105W and had moved south 2 degrees. The west-east cross-section for 55N (Figure 4.7e) showed an center of absolute vorticity of greater than 22 AVU at 55N, 82W at the 500 mb level. By 9/12Z, the center of the low had fallen to 5410 m and was located at 58N, 75W (Figure 4.6f). At this same time, wave #1 was located at 58N, 75W to 48N, 72W following a continued movement of 8 degrees longitude in the past 12 hours. Wave#2 had moved to location 58N to 85W-105W having rotated around the western edge of the polar vortex. A third wave (hereafter called wave #3) can now be seen at location 67N from 70W to 92W. Wave #3 also helped the polar vortex to maintain its intensity. The west-east cross-section for 55N (Figure 4.7f) showed a center of absolute vorticity of greater than 22 AVU extending from 280 mb down to 900 mb. By 10 Jul 90 at 00Z, the center of the low had lifted to 5435 m (Figure 4.6f) an was located at 58N, 72W. The 25 m rise can be attributed to wave #1 starting to move out of the vortex. At this point, wave#1 was located at 58N, 68W to 50N, 60W following the movement of about 14

degrees longitude. Wave #2 was rounding the western edge with its location 58N from 75W to 90W, and wave #3 was located at 67N, 70W to 70N, 90W. The analysis carried out here describes two ideal cases that account for most of the stratospheric/tropospheric exchange of ozone in the Arctic summertime. The ideal case (#1 and #2) mechanisms describe the situations found in the Mission 8 case study and the 1990 event. A general atmospheric structure is suggested by noting similarities between the cases studied. In both these ideal cases, the ozone is exchanged through a tropopause fold as a polar vortex forms or intensifies through the interaction of waves. Exchange happens again during the dissipation of the polar vortex as the tropopause relocates. Calculations from case studies reveal that the exchange associated dissipation of the polar vortex mat represent a significant source of ozone to the Arctic summertime.

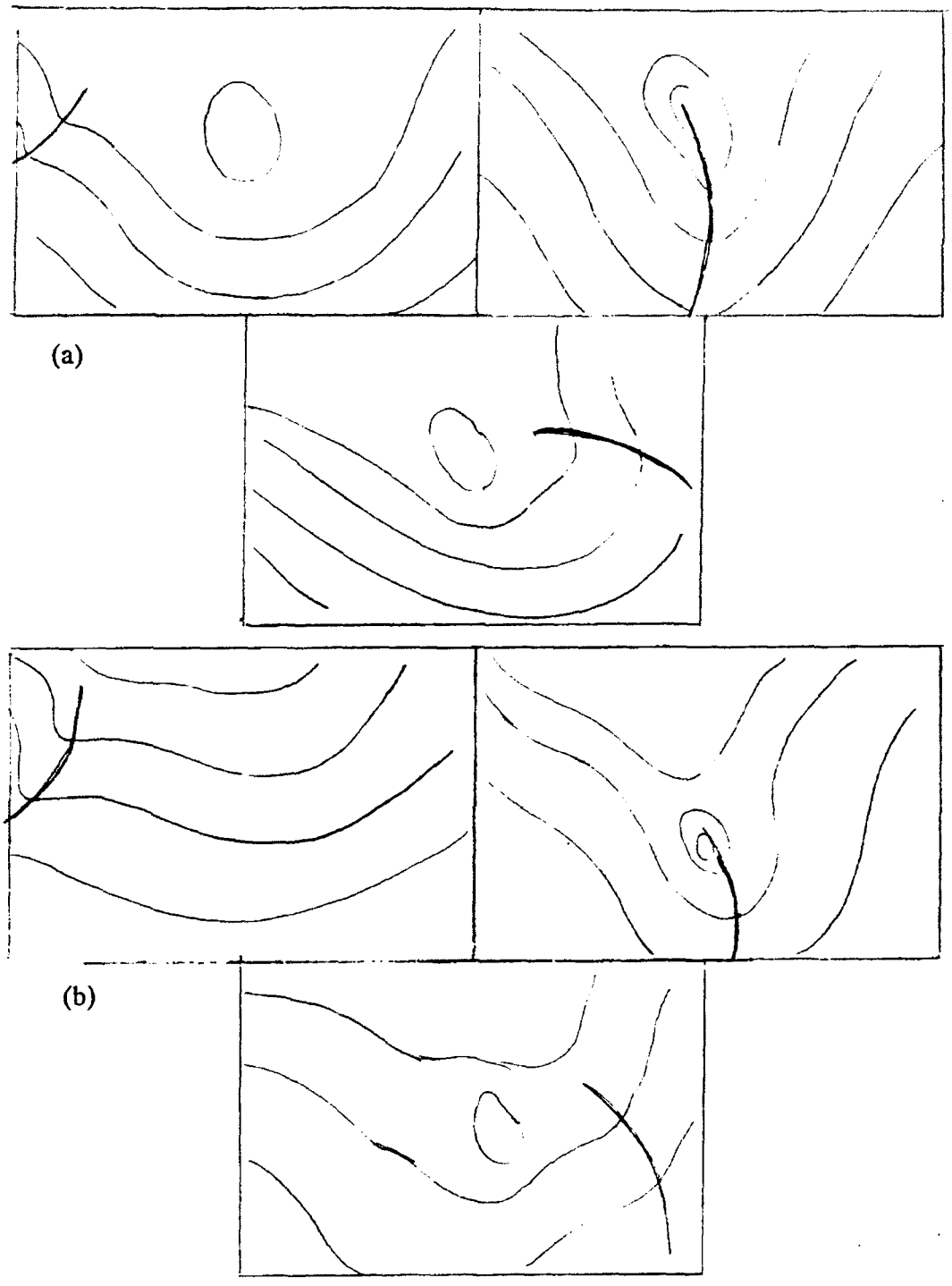

Figure 4.1 Cartoon describing ideal conditions for a tropopause fold to occur. (a) A strong wave comes in phase with a longwave; (b) A wave interacts with an existing polar vortex.

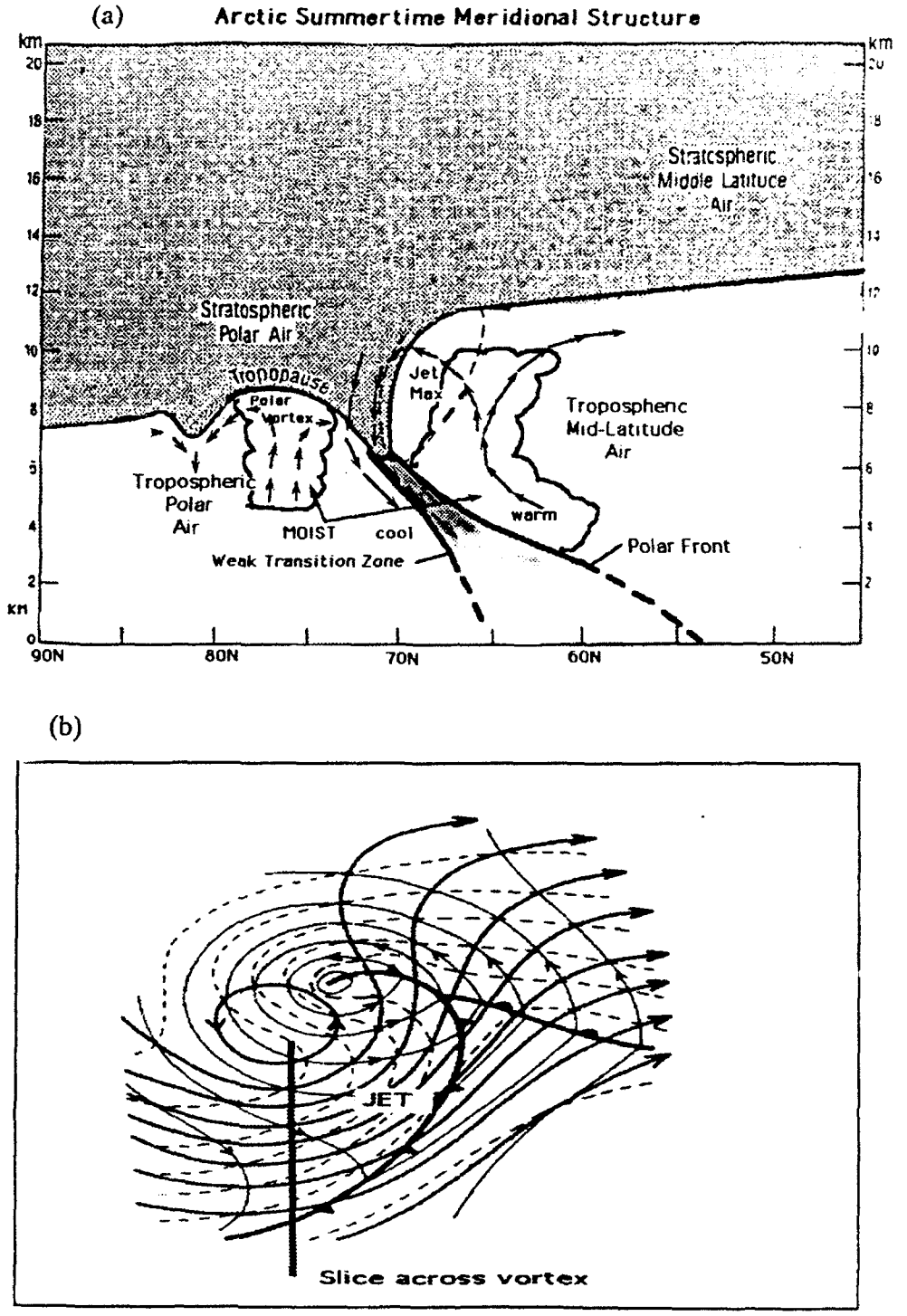

Figure 4.2 Cartoon. (a) Meridional Structure of the atmosphere in the Arctic summer along slice indicated in (b). Tropopause depicted by thick, solid line. The weak polar front is in the shaded area below the jet maximum. The tropopause fold can be found below the jet. (b) Depicts slice of the atmosphere across vortex (thick line) with solid lines the 500mb height contours, 1000-500mb thickness (dashed), 1000mb contours (thin).

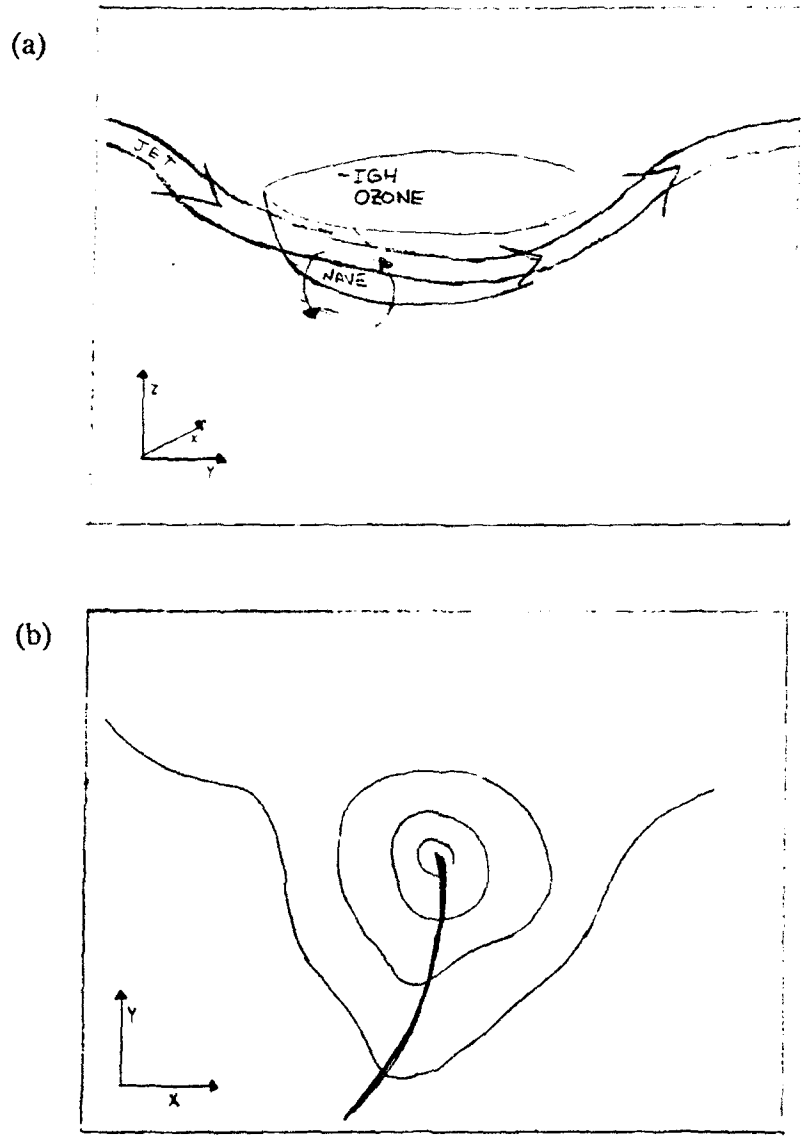

Figure 4.3 Cartoon describes interaction of a short wave with a polar vortex (a) A three-dimensional look at a wave interacting with a bowl of ozone (polar vortex); (b) same as in "a",except pictured as would be seen on a constant level chart (two dimensional).

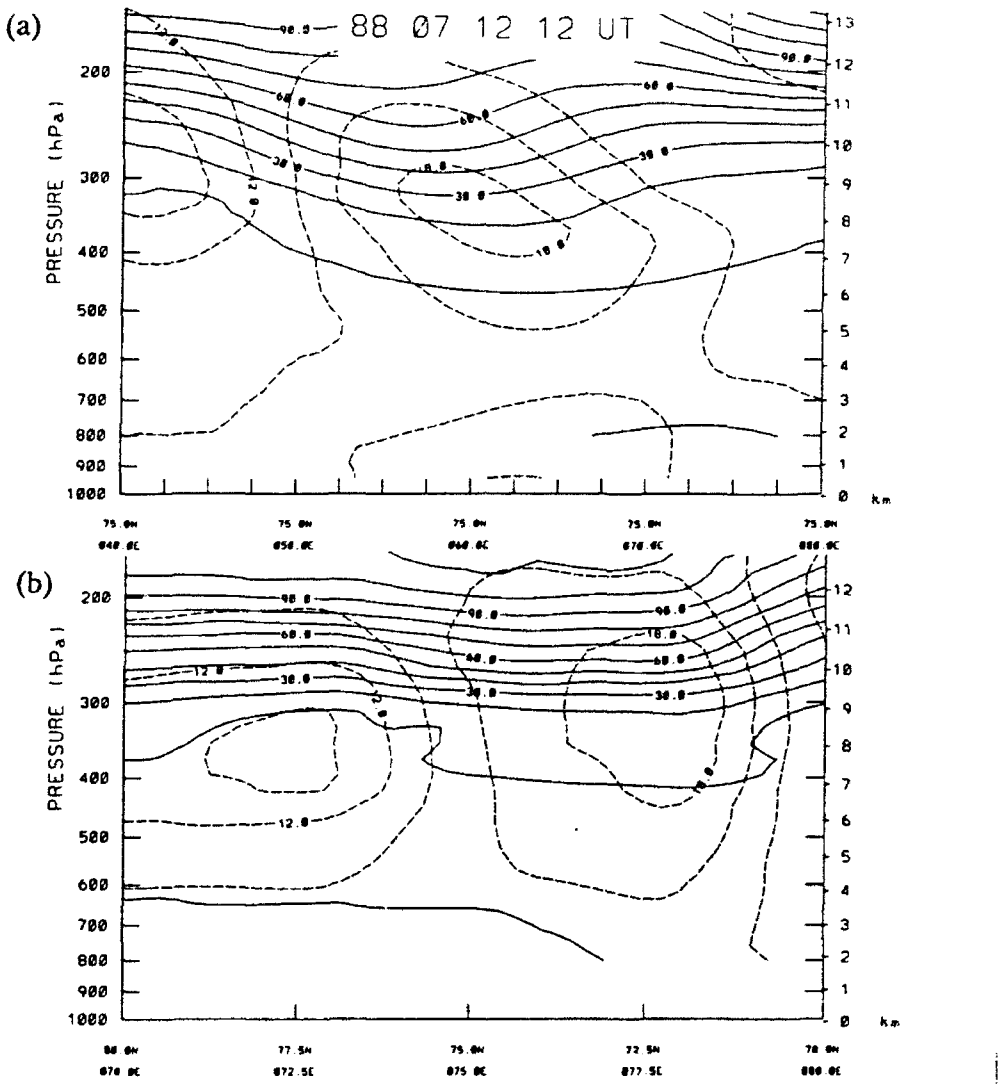

Figure 4.4 Cross-section in July 1988 for potential vorticity in deca PVU (solid) and absolute vorticity AVU (dashed) at:(a) 75N, 40E to 75N, 80E at 12/12Z;(b) 80N, 70E to 70N, 80E at 13/00Z;(c) 80N, 90E to 70N, 100E at 13/12Z;(d) 70N, 90E to 70N, 130E at 14/00Z;(e) 70N, 100E-140E at 14/12Z;(f) 70N, 140E-180E at 14/12Z;(g) 70N, 140E-180E at 15/00Z

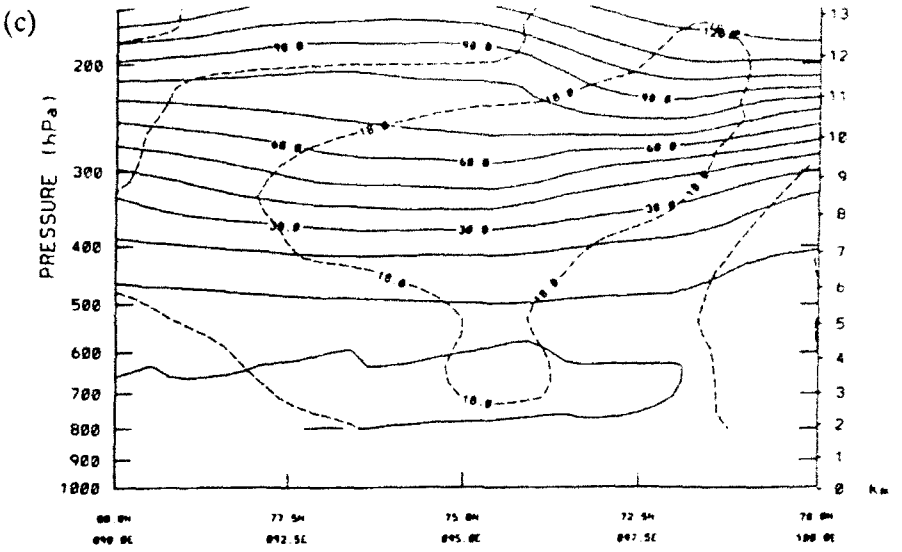

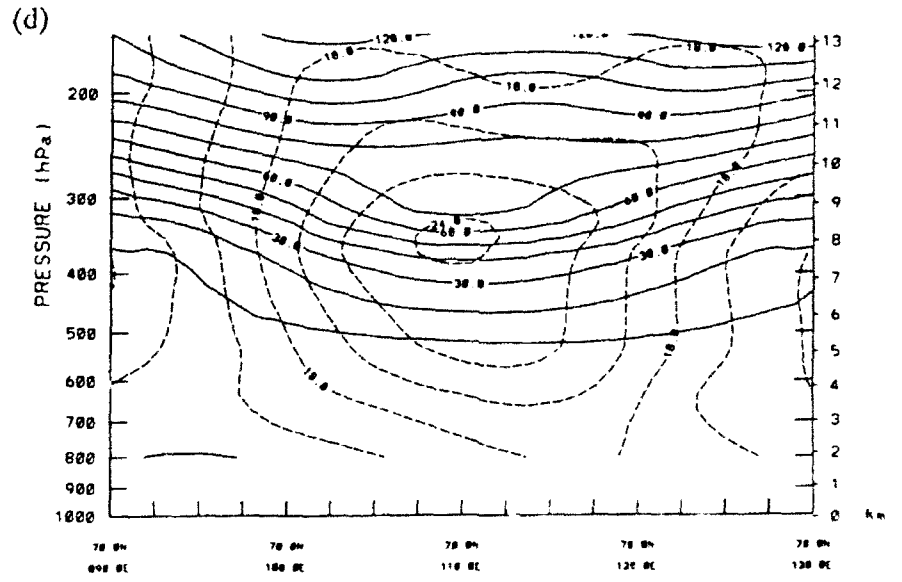

Figure 4.4 Cross-section July 1988 for potential vorticity in deca PVU (solid) and absolute vorticity AVU (dashed) at:(a) 75N, 40E to 75N, 80E at 12/12Z;(b) 80N, 70E to 70N, 80E at 13/00Z;(c) 80N, 90E to 70N, 100E at 13/12Z;(d) 70N, 90E to 70N, 130E at 14/00Z;(e) 70N, 100E-140E at 14/12Z;(f) 70N, 140E-180E at 14/12Z;(g) 70N, 140E-180E at 15/00Z

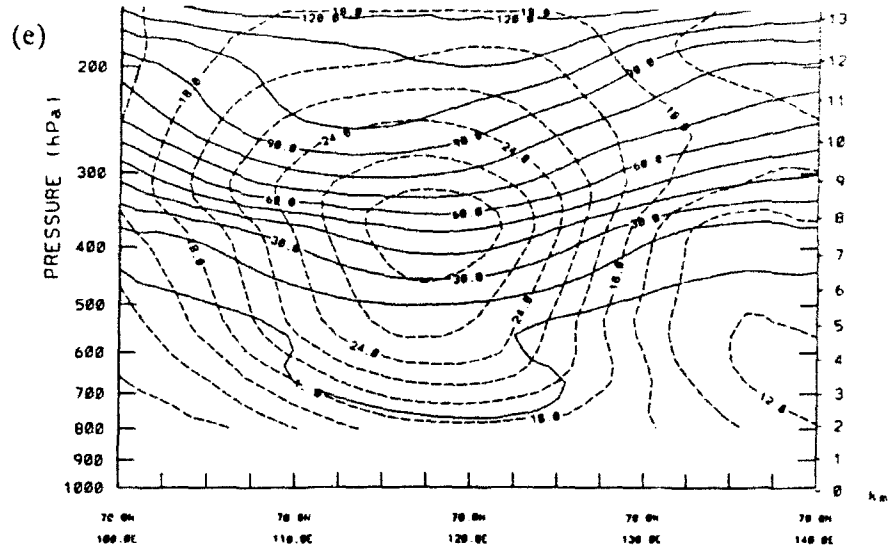

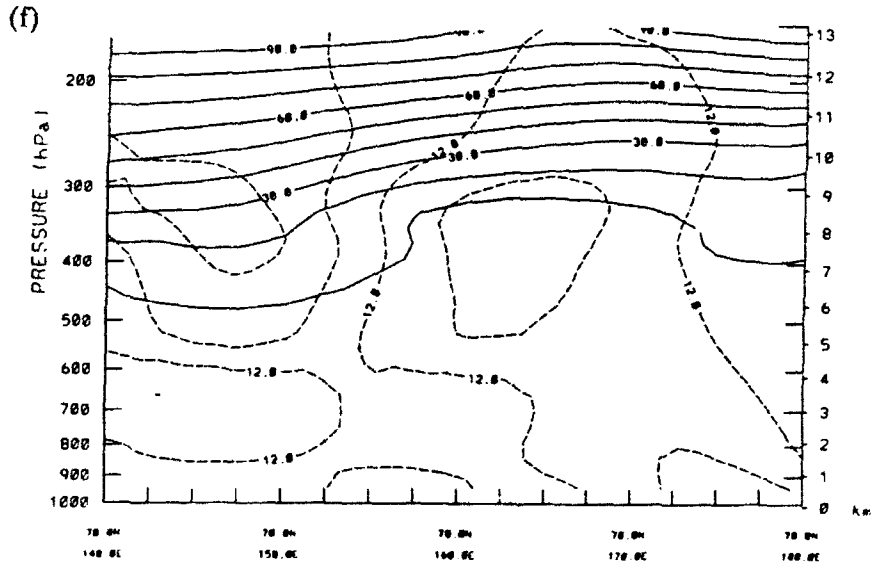

Figure 4.4 Cross-section July 1988 for potential vorticity in deca PVU (solid) and absolute vorticity AVU (dashed) at:(a) 75N, 40E to 75N, 80E at 12/12Z;(b) 80N, 70E to 70N, 80E at 13/00Z;(c) 80N, 90E to 70N, 100E at 13/12Z;(d) 70N, 90E to 70N, 130E at 14/00Z;(e) 70N, 100E-140E at 14/12Z;(f) 70N, 140E-180E at 14/12Z;(g) 70N, 140E-180E at 15/00Z

(g)

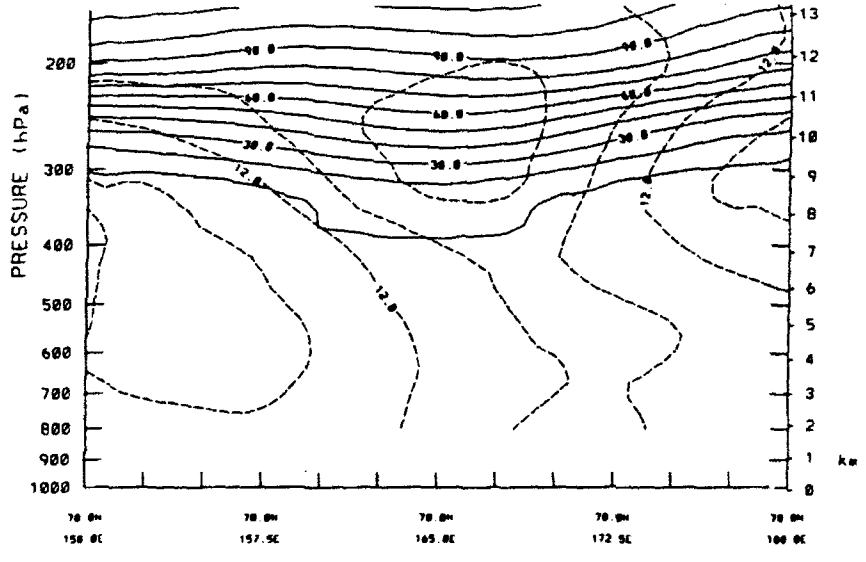

Figure 4.4 Cross-section in July 1988 for potential vorticity in deca PVU (solid) and absolute vorticity AVU (dashed) at:(a) 75N, 40E to 75N, 80E at 12/12Z;(b) 80N, 70E to 70N, 80E at 13/00Z;(c) 80N, 90E to 70N, 100E at 13/12Z;(d) 70N, 90E to 70N, 130E at 14/00Z;(e) 70N, 100E-140E at 14/12Z;(f) 70N, 140E-180E at 14/12Z;(g) 70N, 140E-180E at 15/00Z

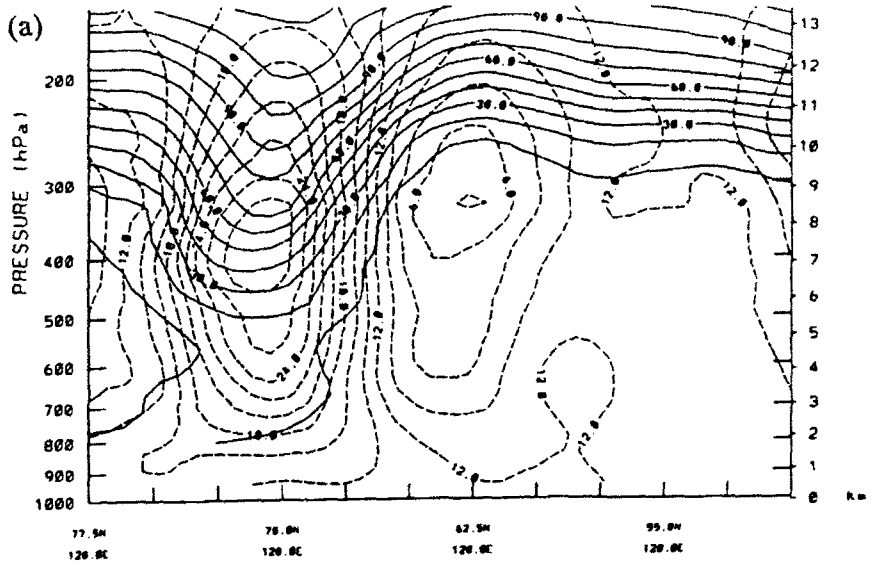

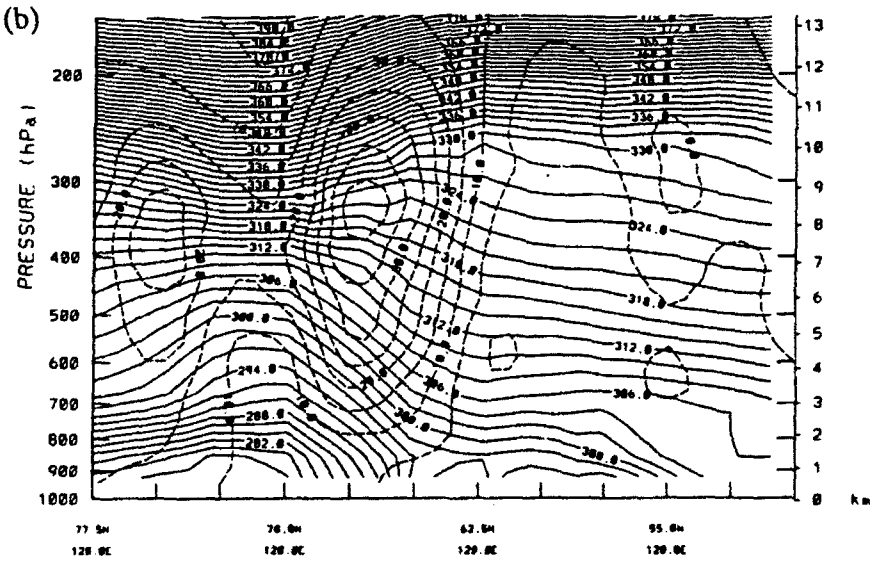

Figure 4.5 Cross-section from 90N, 120E to 48N, 120E at 14/12Z Jul 1988 for (a) potential vorticity in deca PVU (solid) and absolute vorticity in AVU (dashed), (b) potential temperature in K (solid) and windspeed in m/s (dashed).

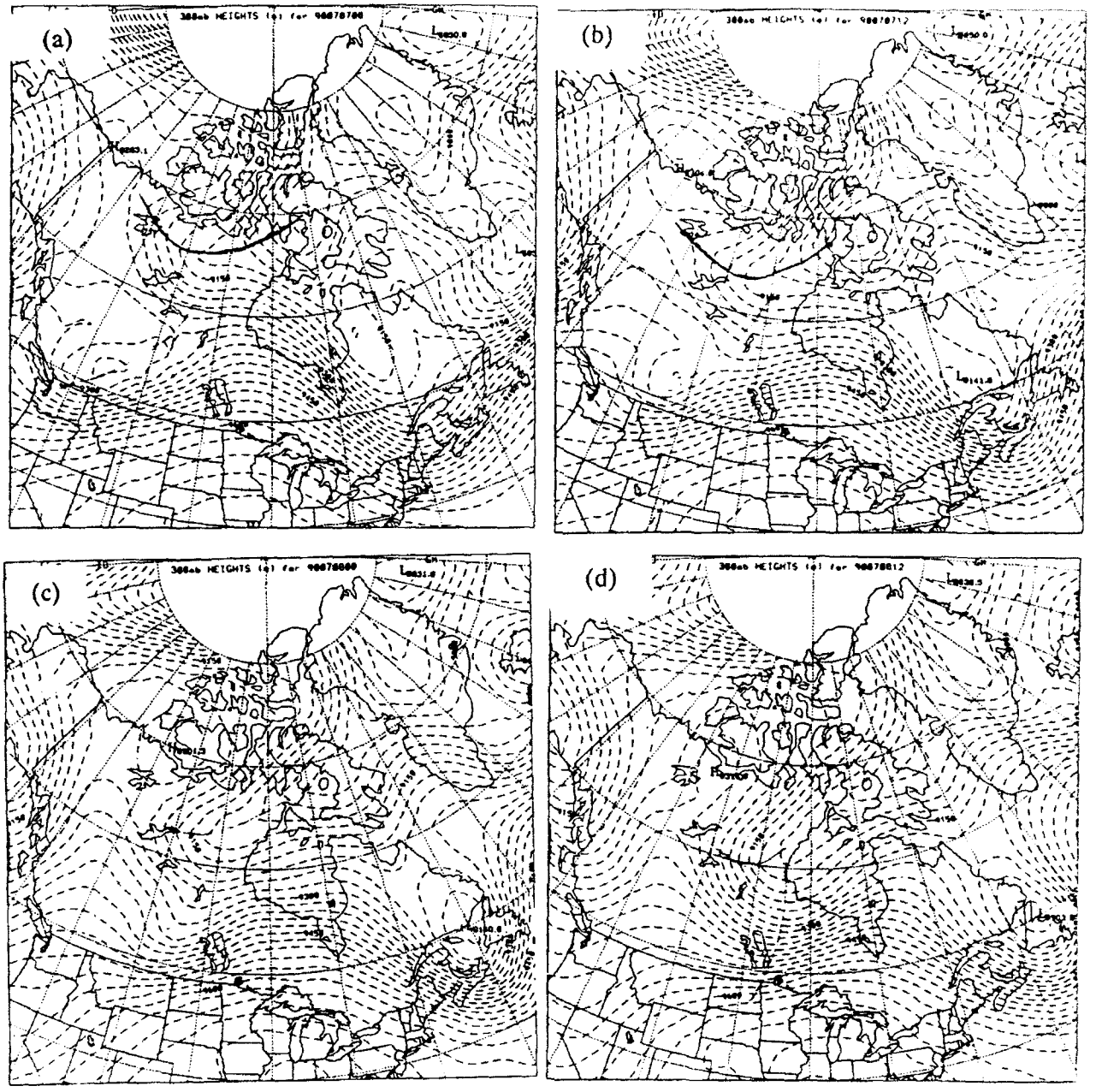

Figure 4.6 300mb pressure heights in m (dashed). Waves interacting to produce a polar vortex. Waves of interest noted by solid line for July 1990 at (a) 7/00Z, (b) 7/12Z, (c) 8/00Z, (d) 8/12Z, (e) 9/00Z, (f) 9/12Z, and (g) 10/00Z.

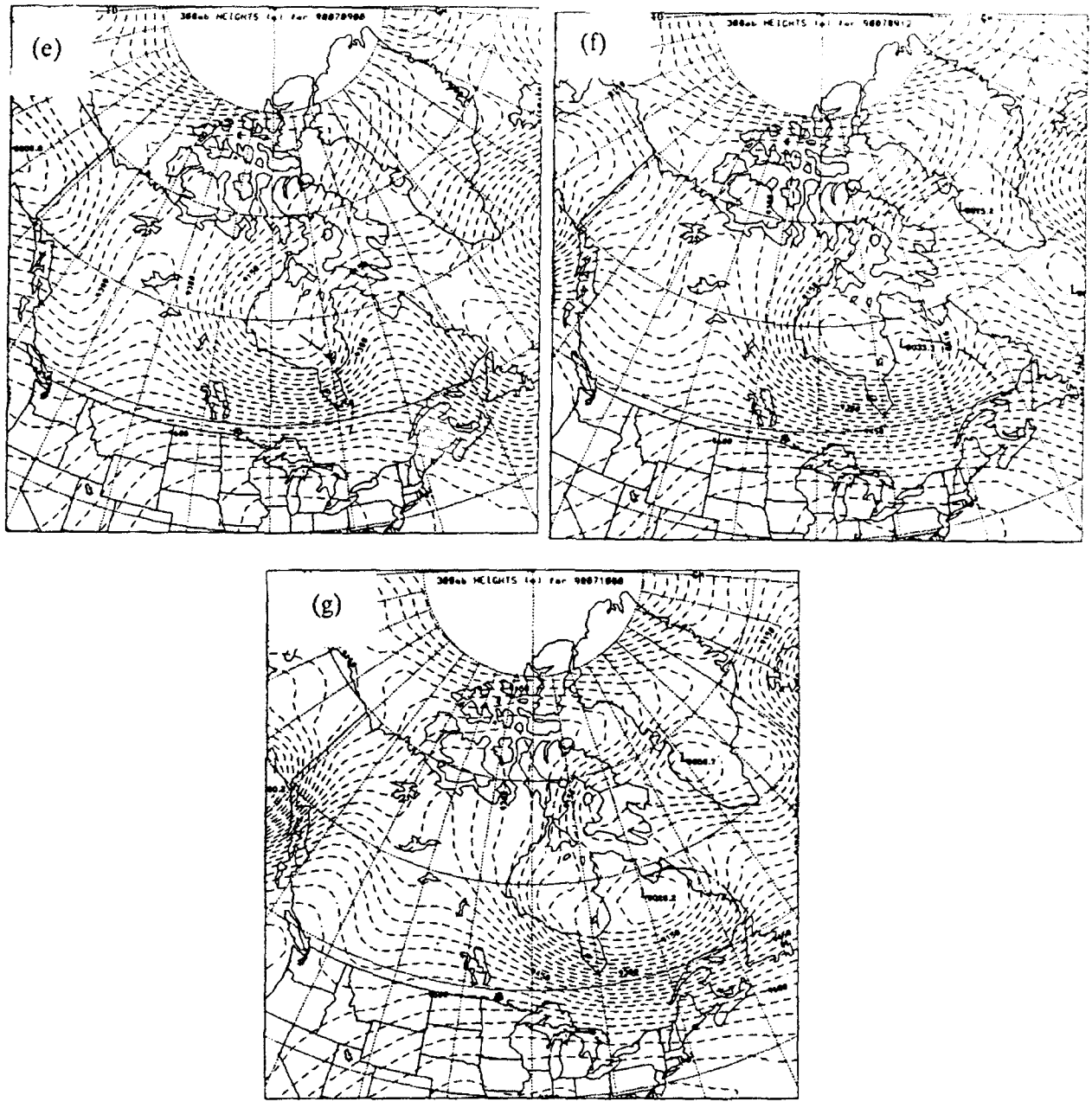

Figure 4.6 300mb pressure heights in m (dashed). Waves interacting to produce a polar vortex. Waves of interest noted by solid line for July 1990 at (a) 7/00Z, (b) 7/12Z, (c) 8/00Z, (d) 8/12Z, (e) 9/00Z, (f) 9/12Z, and (g) 10/00Z.

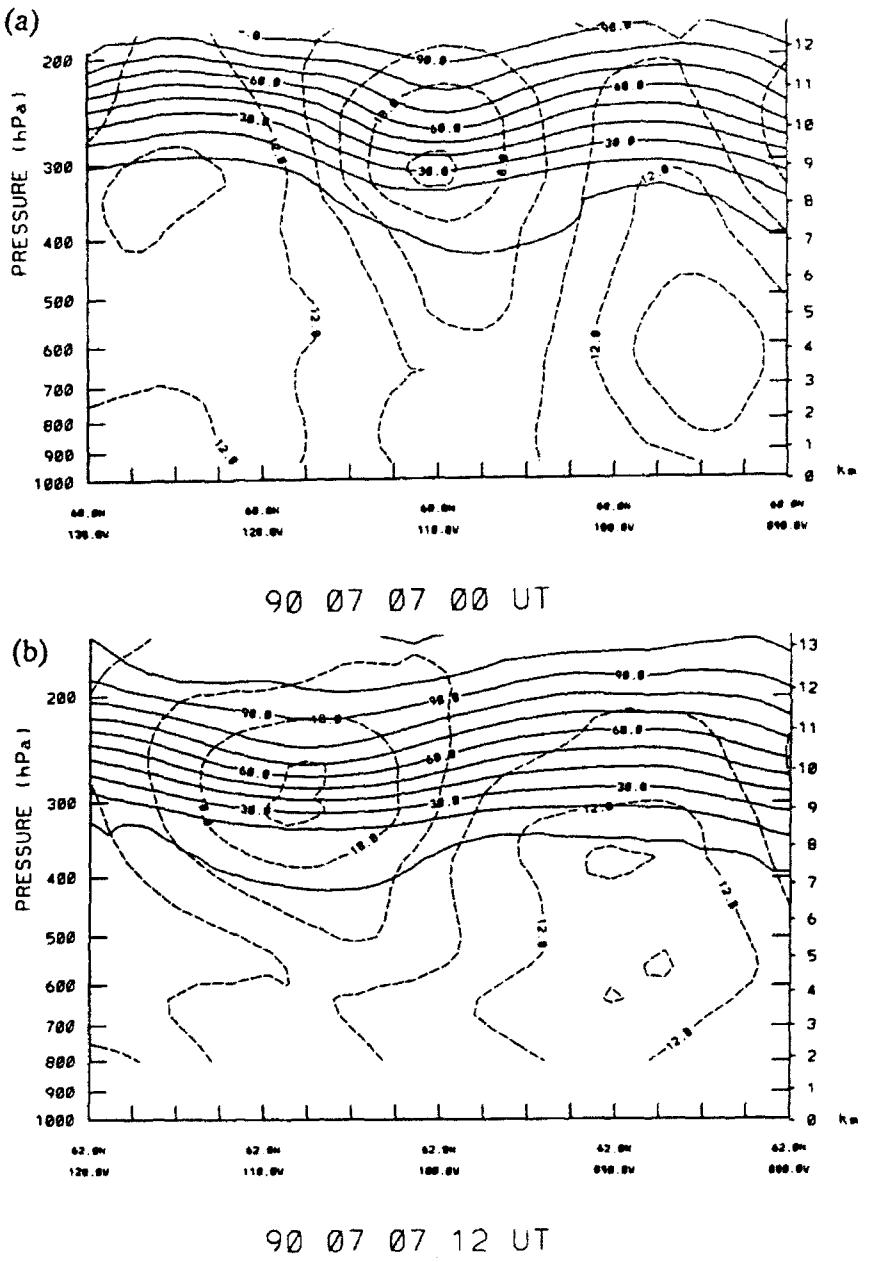

Figure 4.7 Cross-section for potential vorticity in deca PVU (solid) and absolute vorticity in AVU (dashed)in July 1990 at (a) 60N, 130W-90W at 7/00Z;(b) 62N, 120W-80W at 7/12Z;(c) 55N, 120W-90W at 8/00Z;(d) 55N, 110W-70W at 8/12Z;(e) 55N, 120W-80W at 9/00Z;(f) 55N, 90W-60W at 9/12Z.

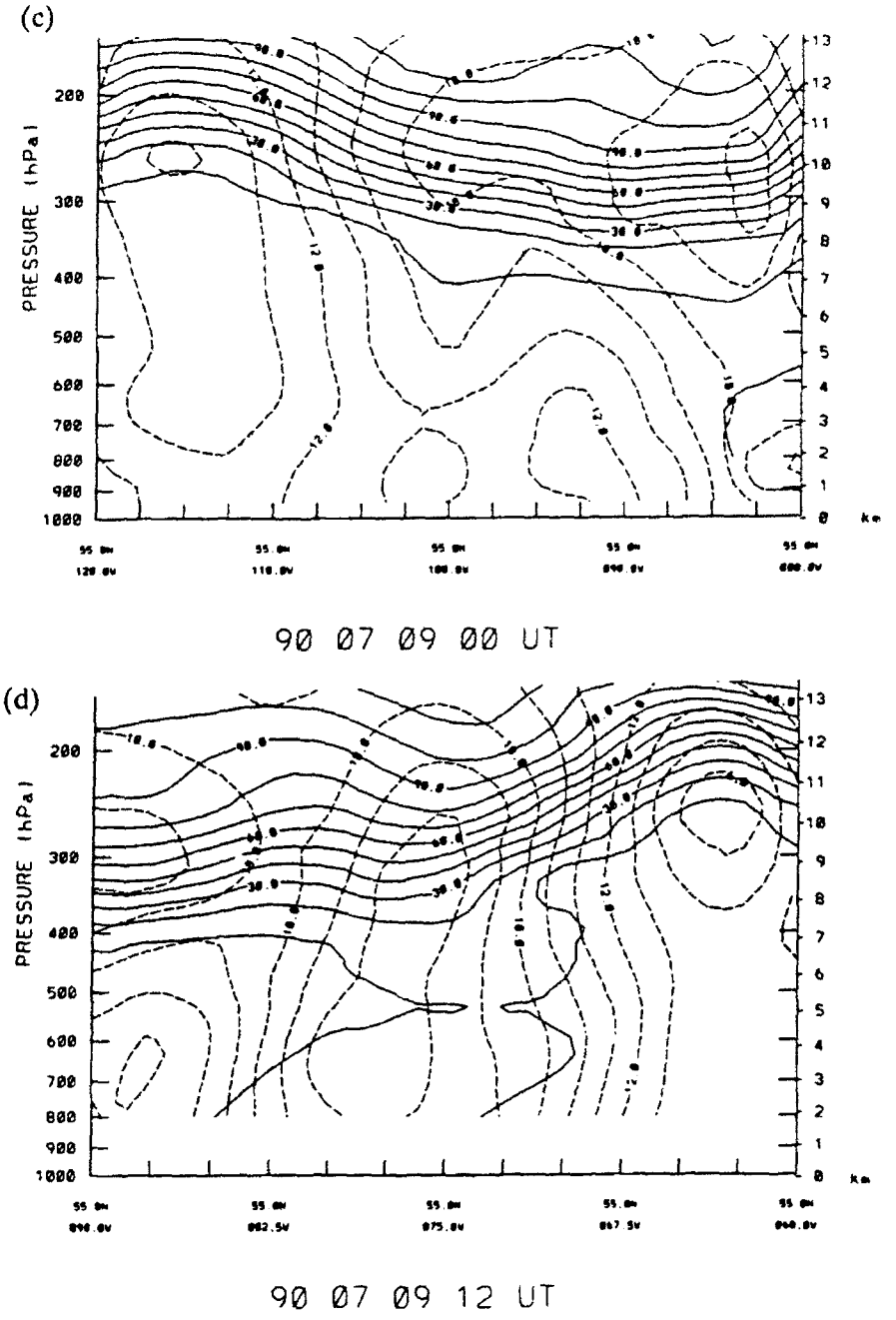

Figure 4.7 Cross-section for potential vorticity in deca PVU (solid) and absolute vorticity in AVU (dashed)in July 1990 at (a) 60N, 130W-90W at 7/00Z;(b) 62N, 120W-80W at 7/12Z;(c) 55N, 120W-90W at 8/00Z;(d) 55N, 110W-70W at 8/12Z;(e) 55N, 120W-80W at 9/00Z;(f) 55N, 90W-60W at 9/12Z.

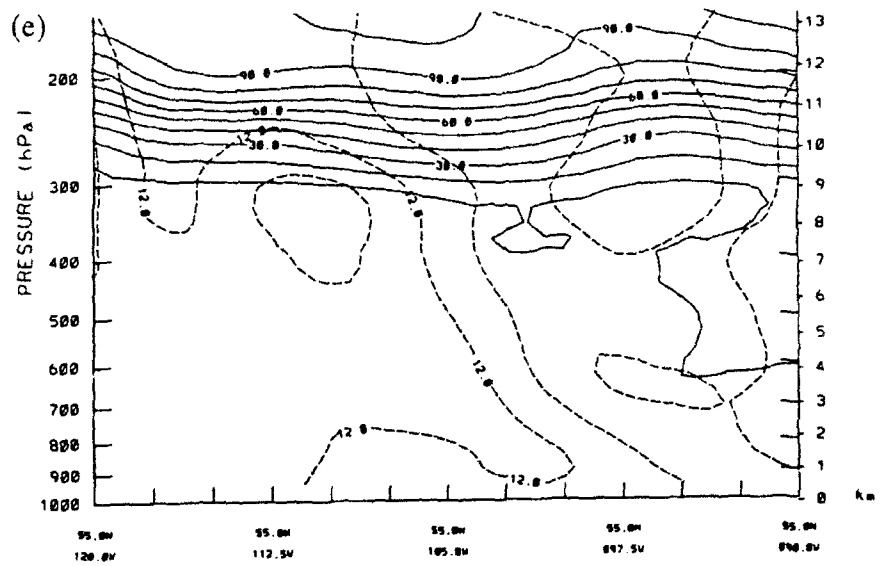

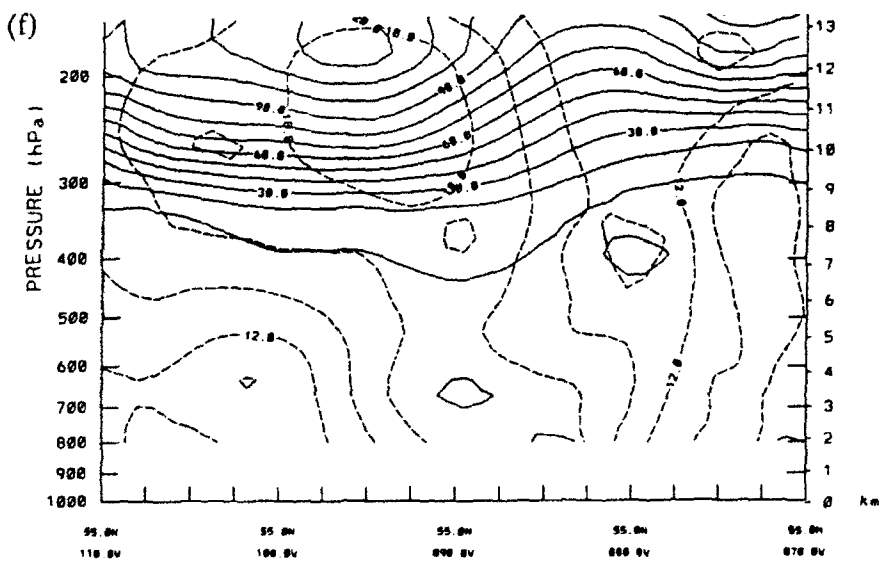

Figure 4.7 Cross-section for potential vorticity in deca PVU (solid) and absolute vorticity in AVU (dashed)in July 1990 at (a) 60N, 130W-90W at 7/00Z;(b) 62N, 120W-80W at 7/12Z;(c) 55N, 120W-90W at 8/00Z;(d) 55N, 110W-70W at 8/12Z;(e) 55N, 120W-80W at 9/00Z;(f) 55N, 90W-60W at 9/12Z.

CHAPTER V

CONCLUSIONS AND RECOMMENDATIONS

Enhancements in tropospheric ozone were found in the Arctic during the Arctic Boundary Layer Experiment (ABLE 3A) have been investigated to determine the origins and physical mechanisms involved. ABLE 3A investigated the sources, sinks, and distribution of trace gases and aerosols during July and August 1988. The area concentrated on included Alaska, Northern Canada and Greenland. The regions of enhanced ozone were obtained from aircraft measurements, lidar soundings, and ozone profiles. Of the 33 Missions, 9 of them served as candidates for major case studies by either having regions of enhanced ozone in the Lidar soundings or enhancements in the *in situ* measurements. Of these 9, 3 were in locations where the back trajectory brought the air over atmospheric sounding sites where the meteorology of the atmosphere could be analyzed in detail. By examining the ozone profiles produced from the lidar and *in situ* measurements, other minor variation from background values of ozone were also noted and investigated. In many of these cases, a simple mechanism of descent of air from aloft could explain the measured values. However, high ozone values (as high as 284 ppbv), compared to a background of 70 ppbv were measured at relatively low altitudes (as low as 4.5

km) during ABLE 3A, which could not be explained in this simple manner. Meteorological analyses of potential vorticity, isentropic trajectories, time-series plots, cross-sections, parcel time-series and total ozone were used to further describe the origins of these high ozone values. These analyses compared and contrasted the behavior of large-scale polar vortex (about 2000 km across) in the Arctic summer. Two cases, on Missions 3 and 8, show how the polar vortices and smaller waves combined to cause tropopause folding and stratospheric-tropospheric exchange of ozone. In contrast, the Mission 19 case documents how the observed ozone enhancement was on the northwest side of a polar vortex. Since ozone had a lifetime of about 40 days (*Jacob et al*, 1992) in the summertime Arctic upper troposphere, ozone was transported long distances. Using isentropic back trajectories and parcel-time series, the origin of the high ozone values was traced to areas of high potential vorticity. From these cases, a meridional structure is proposed for the Arctic summer. Two ideal case scenarios were developed to describe the major contributors to the stratospheric-tropospheric exchange of ozone for the summertime high latitudes - the first being a Rossby wave and a longer wave combining to produce stratospheric-tropospheric exchange; the second being the combination of a polar vortex and a Rossby wave. However, on the hemispheric globe, stratospheric-tropospheric exchange is not limited to these two scenarios. Stratospheric-tropospheric exchange can also occur in many other ways which include the subtropical jet, sinking of air through an anticyclone, thunderstorms and tropical

systems. Even so, the two ideal cases developed here are believed to be responsible for the majority of the stratospheric-tropospheric exchange in the Arctic summertime because of the generally high vertical velocities associated with these tropopause folding mechanisms. These two ideal mechanisms are well described by case studies from the ABLE 3A and ABLE 3B programs.

From case studies completed in this thesis, the flux of exchanged ozone is estimated for areas above 60°N for tropopause folding, high-pressure-induced subsidence, and the relocation of the tropopause during a polar vortex dissipation. These estimates indicate that the dominate source of stratospherically derived ozone is from tropopause relocation in polar vortices.

Further research could be conducted to develop other ways to determine the amount of ozone exchanged and the amount of ozone in the troposphere. The following suggests ideas and questions:

(1) Future research should concentrate on the study of stratospheric/tropospheric exchange of ozone during the dissipation stages of polar vortices. This thesis strongly suggests that this exchange process dominates the stratospheric ozone source term in the Arctic summertime. Because of the large-scale of polar vortices and synoptic scale low pressure systems (≥20 degrees), atmospheric measurements campaigns aimed at testing these results can be made easily, as these features can be easily tracked and followed on weather maps and therefore easily predicted for mission planning.

(2) Estimation of ozone exchange. A method to measure the cross-flux at the tropopause involves taking the method developed in this thesis further. First, the tropopause surface would need to be determined from rawinsonde data. In principle, vertical velocities could then be calculated at all available points. Vertical velocity data and locations would need to be input into a program that converts the nonstandardized data into a gridded product. The mass flux could then be computed directly from the gridded data. With an assumption about ozone's mixing ratio at the tropopause, an estimate could be obtained of mass exchange.

(3) For tropopause folds, future work needs to address how much of the exchanged air returns to the stratosphere?

(4) Future analysis of these type of ozone events should be made from the reference point of the tropopause, since it represents the major atmospheric feature of interest to which atmospheric motion should be related. Potential vorticity and ozone correlations could then be standardized with respect to the tropopause height rather than some arbitrary pressure level or the atmospherically arbitrary reference to height above sea level.

BIBLIOGRAPHY

Austin, J.F. and M.J. Follows, 1991: The Ozone Record at Payerne: An Assessment of the Cross-Tropopause Flux, *Atmos. Environment, 25,* 1873-1880.

Bhartia, P.K., K.F. Klenk, C.K. Wong, D. Gordon, and A.J. Fleig, 1984: Intercomparison of Nimbus 7 SBUV/TOMS total ozone data sets with Dobson and M83 results, *J. Geophys. Res., 89,* 5239-5248.

Billings,W.D., 1987: Carbon balance of Alaskan tundra and taiga ecosystems: Past, present, and future, *Quanti. Sci. Rev., 6,* 165-177.

Blake, D.R., D.F. Hurst, T.W. Smith, W.J. Whipple, T-Y, Chin, N.J. Blake, and F.S. Rowland, 1992: Summertime Measurements of Selected Non-Methane Hydrocarbons and the Artic and Subarctic During the 1988 Artic Boundary Layer Expedition (ABLE 3A), *Journal of Geophysical Resources, 95,* 16,559-16,588.

Blustein, H.B., 1992a: *Synoptic-Dynamic Meteorology in Midlatitudes, 1,* Principles of Kinematics and Dynamics, Oxford University Press, 431p.

Blustein, H.B., 1992b: *Synoptic-Dynamic Meteorology in Midlatitudes, 2,* Observations and Theory of Weather Systems, Oxford University Press, 594p.

Clancy, R.T., M. Callan, and D.W. Rusch, 1992: An Analysis of the TOMS total ozone column as function of tropospheric cloud cover, *Quadrennial Ozone Symposium Abstracts,* International Association for Meteorology and Atmospheric Physcis, International Ozone Commission, Charlottesville, VA, June 4-13, 1992.

Crutzen, P.J., 1971: Ozone production rates in an oxygen, hydrogen, nitrogen-oxide atmosphere, *J. Geophys. Res., 76,* 7311-7327.

Danielsen, E.F.,1961, Trajectories: Isobaric, Isentropic and Actual, *Journal of Meteorology, 18,* 479-486.

Danielsen, E.F., 1968: Stratospheric-Tropospheric Exchange Based on Radioactivity, Ozone and Potential Vorticity, *J. Atmos. Sci., 25,* 502-518.

Danielson, E.F., 1984: Meteorological context for Global Tropospheric Experiments' instrument tests, paper presented to American Geophysical Union, San Francisco, California, December 3-7, 1984, *Eos Trans. AGU, 65,* 834.

Danielson, E.F., and R. Bleck, 1967: Moist isentropic flow and trajectories in a developing wave cyclone, Rep. No. 67-0617, Aif Force Cambridge Res. Lab., Dept. 67-0617, Bedford, MA, 1-34 (NTIS AD 670 847).

Dobson, G.M.B., 1968: Forty-years' Research on Atmospheric Ozone at Oxford: A History, *Applied Optics, 7,3,* 387-405.

Elliot, W.P. and D.J. Gaffen, 1991: On the Utility of Radiosonde Humidity Archives for Climate Studies, *Bulletin American Meteorology Society, 72,* 1507-1517.

Gidel, L.T. and M.A. Shapiro, 1980: General Circulations Model Estimates of the Net Vertical Flux of Ozone in the Lower Stratosphere and the Implications for the Troposphere Ozone Budget, *J. Geophys.Res., 85,* 4049-4058.

Gregory, G.L., B.E. Anderson, L.S. Warren, E.V. Browell, D.R. Bagwell, and C.H. Hudgins, 1992: Tropospheric Ozone and Aeorsol Observations, *J. Geophys. Res., 97, D15,* 16,451-16,472.

Haagenson, P.L., Y.H. Kou, and M. Skumanich, 1987: Tracer Verification of Trajectory Models, *J. Climate and Appl. Meteor., 26,* 410-426.

Haagenson, P.L., and M.L. Shapiro, 1979: Isentropic Trajectories for Deviation of Objectively Analyzed Meteorological Parameters, Tech. Note NCAR/TN-149, National Center for Atmospheric Research, Boulder, CO, 30pp.

Hampson, J., 1965: Chemiluminescent emissions observed in the stratosphere and mesosphere, *Les Problemes Meteorologiques de la Mesosphere,* edited by CNES, Presses Universitaires de France, Paris.

Harriss, R.C., S.C. Wofsy, D.S. Bartlett, M.C. Shipham, D.J. Jacob, J.M. Hoell, R.J. Bendura, J.W. Drewry, R.J. Ncneal, R.J. McNeal, R.L. Navarro, R.N. Gidge, and V.E. Rabine, 1992: The Arctic Boundary Layer Expeditio n (ABLE 3A): July-August 1988, *J. Geophys. Res., 97, D15,* 16,383-16,394

Jacob, D.J., S.M. Fan, S.C. Wofsy, P.A. Spiro, P.S. Bakwin, J.A. Ritter, E.V. Browell, G.L. Gregory, D.R. Fitzjarrald, and K.E. Moore, 1992: Depo sition of Ozone to Tundra, *J. Geophys. Res., 97, D15,* 16,473-16,480.

Kahl, J.D., J.M. Harris, and G.A. Herbert, 1989: Intercomparison of three long-range trajectory models applied to Artic haze, *Tellus, 41,* 524-536.

Kahl, J.D., and P.J. Sampson, 1986: Uncertanity in Trajectory Calculations due to low Resolution Meteorological Data, *J. Clim. and Appl. Meteorol., 25,* 1816-1831.

Kahl, J.D. and P.J. Samson, 1988: Trajectory sensitivity rawinsonde data resolution, *Atmos. Environ., 22,* 1291-1299.

Kelly, K.K., A.F. Tuck, and T. Davies, Wintertime asymmetry of upper troposphere water between the Northern and Southern Hemispheres, *Nature,* 353, 244-247, 1991.

Kerr, J.B. and C.T. McElroy, 1993: Evidence for Large Upward Trends of Ultraviolet-B Radiation Linked to Ozone Depletion, *Science, 262,* 1032-1034.

Koehler, T.L., 1977: A test of seven methods which perform grid to observation interpolations, *Meteorological Applications of Satellite Indirect Soundings II,* NOAA Grant 04-4-158-2, University of Wisconson, 55-65.

Kuo, Y.H., P.L. Haagenson, and J.S. Chang, 1985: The accuracy of air parcel trajectories as revealed by the observing system simulation experiments, *Mon. Wea. Rev., 113,* 1852-1867.

Lamarque, I.F. and P.G. Hess, 1994: Cross-Tropopause Mass Exchange and Potential Vorticity Budget in a Simulated Tropopause Folding, *Journal of Atmospheric Sciences, 51,* 2246-2269.

Levy II, H., 1971: Normal Atmosphere: Large radical and formaldheyde concenrations predicted, *Science, 173,* 141-143.

Molina, M.J. and F.S. Rowland, 1974: Statospheric sink for chlorofluoromethanes: chorine atom catalyzed destruction of ozone, *Nature, 249,* 810-814.

Murphy, D.M. and D.W. Fahey, submitted 1993: An estimate of the flux of stratospheric reactive nitrogen and ozone into the troposphere, *J. Geophys. Res.*

Pedlosky, J., 1979: Geophysical Fluid Dynamics. Springer-Verlag 710.

Post, W.M., W.R. Emanuel, P.J. Zinke, and A.G. Strangenberger, 1982: Soil carbon pools and world life zones, *Nature, 298,* 156-159.

Reed, R.J., 1950: The role of vertical motions in ozone-weather relationships, *J. Meteorol., 7,* 263-267.

Sandholm, S.T. et al, 1992: Summertime Tropospheric Observations Related to N_xO_y Distributions and Partitioning over Alaska: Arctic Boundary Layer Expedition 3A, *J. Geophys. Res., 97, D15,* 16481-16509.

Shapiro, M.A., and T. Hampel, 1987, The Artic Tropopause Fold, *Monthly Weather Review, 115,* 444-454.

Shipham, M., S.A. Bachmeier, and D.R. Cahoon, 1990, Meteorological Conditions During the Summer 1986 CITE 2 Flight Series, *J. Geophys. Res., 95,* 10055-10076.

Singh, H.B., D. Herlth, D. O'Hara, K. Zahnle, J.D. Bradshaw, S.T. Sandho lm, R. Talbot, P.J. Crutzen, and M. Kanakidou, 1992: Relationship of Perozyacetyl Nitrate to Active and Total Odd Nitrogen at Northern High Latitudes: Influence of Resovior Species on NO_x and O_3, *J. Geosphys. Res., 97, D15,* 16,523-16,530.

WMO, 1981: *Basic Synoptic Networks of Observing Stations,* WMO OMM No. 217, WMO Secretariat, Geneva, Switzerland.

WMO, 1985: *Atmospheric Ozone 1985,* WMO Report No. 16, WMO Secretariat, Geneva, Switzerland.

WMO, 1988: *Atmospheric Ozone 1988,* WMO Secretarial, Geneva, Switzerland.